
The mass composition of massive early-type galaxies

Kianusch Mehrgan



Ludwig-Maximilians-Universität

The mass composition of massive early-type galaxies

Kianusch Mehrgan

Dissertation
an der Fakultät Physik
der Ludwig-Maximilians-Universität
München

vorgelegt von
Kianusch Mehrgan
aus München

München, den 07.10.2023

Erstgutachter: P.D. Dr. Roberto Saglia

Zweitgutachter: Prof. Dr. Jochen Weller

Tag der mündlichen Prüfung: 28.11.2023

Contents

Zusammenfassung	ix
Abstract	x
1 Introduction	1
1.1 Galaxy evolution and early-type galaxies (ETGs)	1
1.1.1 Sequencing external galaxies	1
1.1.2 The dichotomy of ETGs	3
1.1.3 Supermassive Black Holes, core formation and ETG evolution . . .	8
1.2 The stellar dynamics of ETGs	15
1.2.1 Stellar kinematical measurements	15
1.2.2 Dynamical modeling	21
1.3 The stellar initial mass function (IMF)	31
1.3.1 IMF probes of other galaxies	33
1.3.2 IMF studies at a crossroads	37
1.4 Aims of this thesis	40
2 A 40-billion solar mass black hole in the extreme core of Holm 15A, the central galaxy of Abell 85	43
3 Detailed shapes of the line-of-sight velocity distributions in massive early-type galaxies from non-parametric spectral models	65
4 Dynamical stellar mass-to-light ratio gradients: Evidence for very centrally concentrated IMF variations in ETGs?	97
5 Conclusions and outlook	137

List of Figures

1.1	Updated Hubble tuning fork sequence from Kormendy & Bender 1996 . . .	2
1.2	Isophotes of cored and coreless (power-law) ETGs	7
1.3	Supermassive black hole scaling relations	10
1.4	Core scouring merger simulation	11
1.5	Illustration of tangential and radial orbits	12
1.6	Orbit anisotropy profiles of cores	12
1.7	Example of kinematic broadening of stellar absorption	16
1.8	Example LOSVD and Gauss-Hermite polynomial	17
1.9	Illustration of higher-order Gauss-Hermite polynomials	22
1.10	Example of a zero-velocity-curve	29
1.11	Example of a surface-of-section	30
1.12	Kroupa, Salpeter and Chabrier IMF	32
1.13	IMF trends over galaxy dispersion	36

Zusammenfassung

Es ist anzunehmen, dass die Vielfalt der Galaxien im lokalen Universum aus sukzessiven Generationen von Galaxienverschmelzungen hervorgegangen ist. Massereiche Ellipsen stehen dabei an der Spitze der Hierarchie der Galaxienverschmelzungen. Außerdem bergen sie die grössten supermassereichen Schwarzen Löcher.

Das Szenario der hierarchischen Verschmelzungen kann viele der beobachteten Eigenschaften von Ellipsen erklären. Dennoch bleibt die genaue Zusammensetzung der Massen in diesen Galaxien schleierhaft. Die Massenfunktion lokaler schwarzer Löcher, und insbesondere ihr oberes Ende, sind nicht bekannt. Auch wissen wir nicht, welcher Anteil der Gesamtmasse einer Galaxie den Sternen und welcher der dunklen Materie zuzuschreiben ist, da es hier stets eine unbekannte Fraktion an stellaren Objekten gibt, welche Masse zur Galaxie beitragen, aber kaum oder gar kein Licht. Auf der einen Seite gibt es eine unbekannte Anzahl an lichtschwachen Zwergsternen, und auf der anderen Seite einen unbekanntes Bruchteil an Sternen, der zu Relikten kollabiert ist. Die ursprüngliche massenfunktion (UMF) der Sterne umfasst diese Information. Verschiedene Studien der UMF haben eine andere UMF in massiven Ellipsen als in weniger massereichen Galaxien wie unserer Milchstraße ermittelt. Doch meistens produzieren verschiedene Methoden widersprüchliche Resultate für dieselben Galaxien.

Auf der Messung nicht-parametrischer Sichtliniengeschwindigkeitsverteilungen (SGV) basierende dynamische Modelle können genutzt werden, um Galaxienmassen zu messen und in einzelne Komponenten zu zerlegen. In dieser Dissertation messe ich die nicht-parametrischen SGV von 9 + 1 Ellipsen bis zur Fluchtgeschwindigkeit des jeweiligen Potentials mit unserem Code WINGIFT. Darauf basierend konstruiere ich für acht der Galaxien Schwarzschild Orbit-Modelle. Dabei präsentiere ich hier die Entdeckung eines von nur vier bisher dynamisch gemessenen Schwarzen Löchern mit $M_{\text{BH}} > 10^{10} M_{\odot}$, sowie zwei empirische Relationen zwischen M_{BH} und der zentralen Flächenhelligkeit, sowie zentralen Oberflächendichte massiver Ellipsen. Mit diesen Relationen lässt sich das obere Ende der Massenfunktion lokaler schwarzer Löcher in der Zukunft gezielt erforschen. Für sieben der Galaxien präsentiere ich dynamische Evidenz für interne Gradienten der UMF. Solche intrinsischen Gradienten der UMF könnten die Diskrepanzen bisheriger auf verschiedenen Methoden basierenden Messungen der UMF lösen. Die gefundenen Gradienten suggerieren, dass sich in den Zentren von Ellipsen sehr kompakte Regionen vorfinden ($r \lesssim 1$ kpc), deren stellare Populationen einen höheren Anteil an entweder lichtschwachen Zwergsternen, oder Relikten vorweisen als es für Populationen im Rest des Universums der Fall ist.

Abstract

It is thought that most galaxies in the local universe are the outcome of several generations of hierarchical mergers of progenitor galaxies. Massive early-type galaxies (ETGs) occupy the top ranks of this hierarchy. They also harbour the biggest supermassive black holes (SMBHS) in the local universe.

The merger framework can explain many of the observed properties of different kinds of ETGs. However, the exact mass compositions of these objects remains elusive: For once, the local SMBH mass function is poorly understood and barely sampled at the high mass end. We also do not know how much galaxy mass is contributed by stars and how much by dark matter, because an unknown fraction of stars are low-luminosity dwarf stars, and another unknown fraction of more massive stars have turned into remnants – both of these contribute a significant amount of mass to galaxies, but little or no light. The stellar initial mass function (IMF) underlying the stellar population(s) of a galaxy encompasses this information. Different studies, using different methods have claimed that the IMF in massive ETGs is different from that of less massive galaxies like the Milky Way. But these results have thus far remained overwhelmingly contradictory on the level of individual galaxies.

Accurate measurements of non-parametric line-of-sight velocity distributions (LOSVDs) in ETGs can be analysed with Schwarzschild orbit models to produce precise galaxy mass decompositions. In this thesis, I measure the full non-parametric shape of LOSVDs all the way to the escape velocity of each galaxy’s gravitation potential for a total of 9 + 1 massive ETGs using our kinematic fitting code WINGFIT. For eight of the galaxies I construct Schwarzschild models based on these kinematics. I present the discovery of one of so far only four SMBHs more massive than $10^{10} M_{\odot}$ with direct dynamical detections, and two new SMBH-host scaling relations between M_{BH} and the central surface brightness, as well as surface mass-density of massive galaxies. In the future, these empirical relations can be used for a targeted sampling of the high mass end of the local SMBH mass function. For seven of the ETGs, I present dynamical evidence for internal radial gradients of the IMF. Such gradients can potentially explain the contradictions between previous IMF measurements from different methods. These measurements suggest that the centers of ETGs contain very spatially concentrated regions ($r \lesssim 1$ kpc) of stellar populations with an enhanced fraction of either low-luminosity dwarfs or remnants relative to stellar populations in the rest of the universe.

Chapter 1

Introduction

1.1 Galaxy evolution and early-type galaxies (ETGs)

1.1.1 Sequencing external galaxies

Astronomers have developed many different classification schemes to categorize galaxies with respect to different morphological frameworks (see Chapter 4.1 of Binney and Merrifield, 1998 for a review). While most these classification schemes made no attempt to endow these categorizations with physical significance – and all are based on the individual judgement of the observer in one way or another – the famous Hubble sequence Hubble (1936); de Vaucouleurs (1959) of galaxies has been particularly popular due to its grouping of galaxies according to (visual) properties which are ostensibly linked to the physics governing the intrinsic structure of these objects. The main aspect of the Hubble sequence is the partition of galaxies into two main types: Galaxies which are smooth, fuzzy and elliptical in apparent shape are designated by the letter E. Galaxies whose main bodies are enormous disks with embedded spiral arms are designated by the letter S. Both types have their own sub-sequence, with the spiral sequence forking into two parallel branches, S and SB, one for “ordinary” spirals and one for barred spirals, where the spiral arms emerge not from the bright center, but from an elongated bar structure piercing the center of the galaxy, as is the case in our own Milky Way galaxy. Both branches are ordered by how tight their spiral arms are wound in three tiers, numerated by the letters a to c, going from galaxies with very tightly wound fuzzy spiral arms to galaxies with very loosely wound but well-defined arms, S[B]a to S[B]c. The sub-sequence for elliptical galaxies, which in the Hubble scheme ranks ellipticals by apparent ellipticity, was later revised by Kormendy and Bender (1996); Faber et al. (1997), introducing a “boxy” and a “disky” shape-sequence to better reflect the physical properties of these galaxies (see below). The revised sequence is shown in the top row of Figure 1.1.

Elliptical galaxies are connected to their spiral-armed counterparts via so-called lenticular galaxies S[B]0, which are similar in appearance to spirals, but their disks have no spiral arms. They have roundish central concentrations of stars. Most spiral-armed galaxies also have more ellipsoidal concentrations of stars in their central regions, called “bulges”

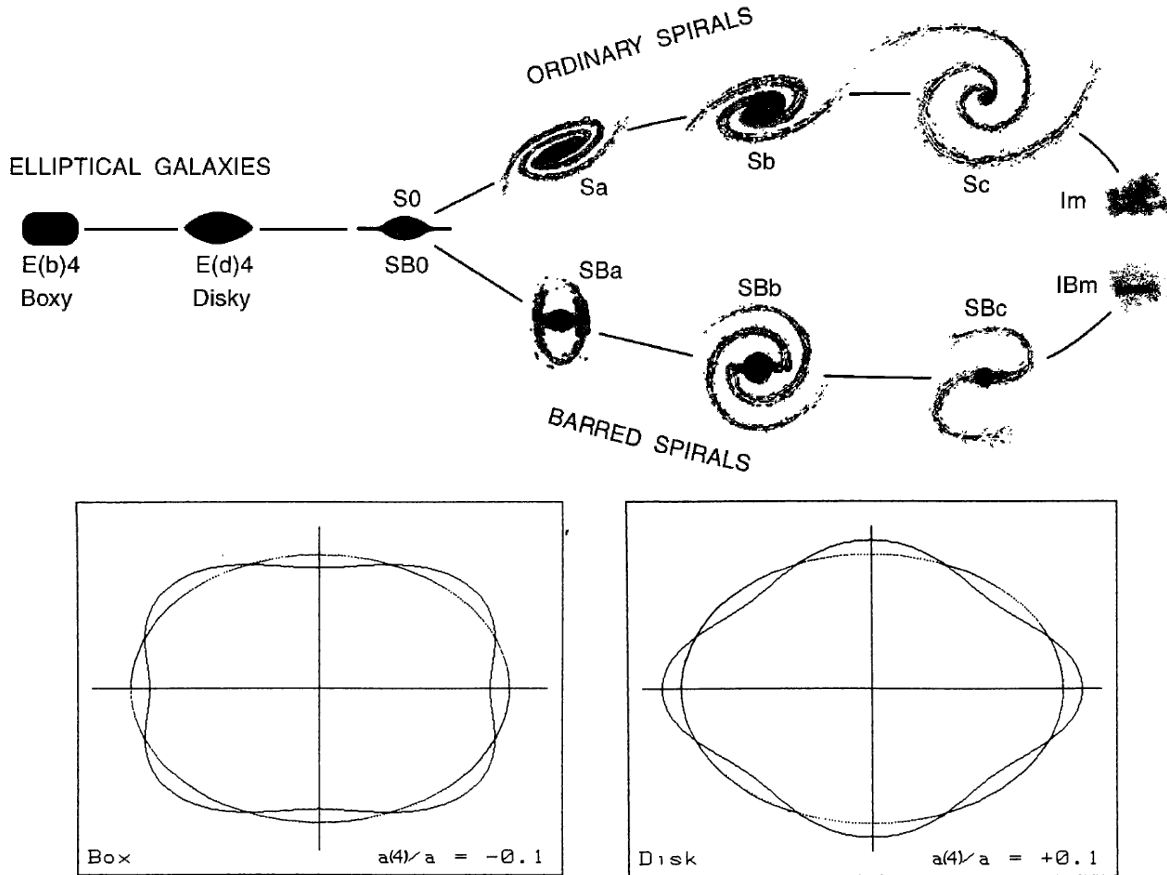


Figure 1.1: Top row: Updated version of the Hubble tuning fork sequence by Kormendy and Bender (1996). This image is taken from Figure 1 of that study. “Im” and “IBm” indicate Magellanic irregulars. Bottom row: Schematic drawings taken from Bender et al. (1988) (their Figure 5) illustrating boxy (left) and diskly (right) deviations from perfect ellipses for an example $a_4/a = \pm 0.1$.

or “pseudo-bulges”. Bulges, unlike pseudo-bulges, appear similar to small ellipticals and are found in S[B]0 and in spirals which are wound more tightly. Thus, when reading the diagram from left-to-right, E-to-S, one could be led to believe that galaxy evolution flows in the same direction. This is why Hubble named the elliptical galaxies “early-type galaxies” (ETG) and their spiral-armed counter parts “late-type galaxies” (LTG). As it turns out, the opposite direction of evolution is closer to the truth: Today it is thought that all galaxies are emergent from hierarchical trees of mergers, interactions and cannibalizations among galaxies which give rise to the different galaxy morphologies which we observe in the local universe. This framework is called hierarchical clustering (White and Rees, 1978; Steinmetz and Navarro, 2002). These clustering hierarchies lead to mergers which break up disks and spiral arms and reassemble their stars in ellipsoidal configurations (Toomre, 1977; Joseph and Wright, 1985; Schweizer, 1990; Kauffmann et al., 1993). Thus, LTG-like

progenitors became ETGs¹. For this reason, nowadays, this terminology has different associations, with “early-type” now referring to the fact that the stars in these galaxies tend to be much older and redder with little or no star formation, whereas their “late-type” counterparts have more diverse stellar populations, with older stars in bulges, but many young, blue stars being born in spiral arms, disks and pseudo-bulges.

The work presented here is centered on ETGs, specifically. While in recent years our understanding of ETGs has become quite comprehensive, in the sense that their relation to the hierarchical clustering framework, as well as their general dynamic and spectroscopic properties have been explored quite thoroughly, there still remain a lot of unanswered questions with respect to the details of their intrinsic mass components and their progenitors. These are the primary concerns of this thesis. In the following I give an overview of our current understanding of ETGs and the pertinent questions that remain.

1.1.2 The dichotomy of ETGs

Disky and Boxy ETGs

In the unrevised Hubble sequence, ETGs are ordered by increasing magnitudes of the apparent ratio of their minor to major axis, b/a , or ellipticity $\epsilon = 1 - b/a$ from perfectly round E0 to strongly ellipsoidal E6 galaxies, whereby En is numbered by $n = 10 \times \epsilon$. While the Hubble sequence is still considered a useful grounded-in-physics classification of galaxies which are LTGs², this can no longer be said of ETGs. Compared to the large body of work which has informed our understanding of ETGs since the introduction of the Hubble sequence (e.g. Kormendy et al., 2009), the Hubble classification is insufficiently linked to actual physics (this issue was notably raised at the 127th symposium of the international astronomical union; Tremaine, 1987). The main issue is that the intrinsic ETG-by-ETG flattening-differences are not in a 1:1 relation to the apparent range of axis-ratios E0-E6, since these are dependent on the inclinations under which these galaxies are viewed (e.g. Sandage et al., 1970; Binney and de Vaucouleurs, 1981). Furthermore, while flattening is often understood as the result of stronger rotation, in ETGs it is also a reflection of the anisotropy of the stellar velocities along different axes within the galaxy.

For these reasons, Kormendy and Bender (1996) and Faber et al. (1997) introduced the revision of the Hubble sequence which I show in Figure 1.1. The revised sequence orders ETGs not by axis ratio, but by velocity anisotropy, in order to create a more physical morphological sequencing of these galaxies. At the heart of the revised sequencing of ETGs lies a dichotomy, sometimes called the “E-E dichotomy”, between two different types of morphology, galaxies whose apparent shape has more “disky” distortions from a perfect

¹One should not make the mistake to think that today’s LTGs are *themselves* the progenitors of ETGs, who were assembled long ago in a different environment at redshifts $z \gtrsim 2$ (e.g. Oser et al., 2010)

²At least to first order. In recent years a dazzling range of complexity in spiral galaxies has been found: small disks in bulges, peanut-shaped bulges for bars, bulges hosting small extra disks, small bars inside small disks inside a bulge and so on (see e.g. Erwin et al., 2021, for some instructive examples). Such complexity can hardly be captured by a simple forking diagram.

elliptical, and those which have more “boxy” distortions. Within these categories, galaxies are ordered by the magnitude of this distortion, ranked from one to four, E(d)1-4 and E(b)1-4, for boxy and disk ETGs, respectively. Below, I elaborate on the details of this dichotomy of ETGs which is fundamental to our understanding of ETG formation.

Considering the formation channel of a particular ETG, in the galaxy clustering framework, the shape of a galaxy is dependent on the morphology of its progenitors and the particular geometries of their mergers. And yet, ETG morphology at first glance appears rather uniform and predictable. An ETG’s size and brightness as parameterized by the size and surface brightness at the effective radius r_e , with corresponding surface brightness I_e , as well as the velocity dispersion σ of the galaxy, all lie on one well-define plane in parameter space:

$$r_e \propto \sigma^{(1.4 \pm 0.15)} I_e^{(-0.9 \pm 0.1)}. \quad (1.1)$$

The plane is called the fundamental plane (FP) of ETGs (e.g. Djorgovski and Davis, 1987; Faber et al., 1987; Bender et al., 1992; Kormendy et al., 2009) and is directly linked to the virial theorem of classical mechanics ³

However, fitting isophotes of surface brightness to galaxy images upon closer inspection reveal that the apparent shapes of ETGs are more complex than mere ellipses: The actual isophotes show small, but still significant distortions from perfect ellipses (e.g Lauer, 1985). This can be put in terms of a Fourier expansion of such isophote distortions δ as a function of azimuthal angle ϕ with respect to the galaxy center:

$$\delta(\phi) = \langle \delta \rangle + \sum_n (a_n \cos(n\phi) + b_n \sin(n\phi)). \quad (1.2)$$

For ETGs, one generally finds four-fold symmetry of such a kind that a_4 is the most characteristic feature defining the distortions, $\delta(\phi) \sim a_4 \cos(4\phi)$ (Though features like a_6 are still necessary for a full description). If $a_4 > 0$, the isophote becomes more “disky” than a perfect ellipse, and if $a_4 < 0$, it becomes more boxy. This is illustrated in the bottom row of Figure 1.1. Generally, a_4 is on the order of one percent of the major axis a . In the Kormendy and Bender (1996) convention, ETGs are ordered by how strongly disk or boxy they are, which is expressed in magnitudes of a_4 , such that these galaxies are ranked E(d)n or E(b)n with $n = 10a_4$.

Since many disk ETGs also host small gas-discs, and spirals host large gas-discs in which their spiral arms are embedded, it is generally thought that the E(d)1-4 sequence lies on a continuum with the S[B]0-S[B]c sequence. As explained earlier, it is thought that ETGs are originated from the mergers of LTG-like progenitors. For the sequence of boxy ETGs E(b) however, there appears to be a genuine dichotomy with the E(d) sequence.

³The FP is linked to the virial theorem governing the average energies in a stable system of particles in a gravitational potential, $2 \langle E_{kin} \rangle = -U \rightarrow M \propto \sigma^2 R$. Assuming that ETGs have overall constant stellar mass-to-light ratios $M/L \sim const.$ (an assumption which I show not to be entirely accurate in Chapter 4), we can use the virial theorem to formulate a chain of proportionalities: $M \propto \sigma^2 R \propto L \propto I \times R^2 \rightarrow R \propto \sigma^2 I^{-1}$. Correcting for the empirical relation $M/L \propto L^{0.32}$ (Cappellari et al., 2007) for ETGs, $R \propto \sigma^{1.2} I^{-0.80}$, which is consistent with the FP within two sigma. The small differences are due to the simplifying assumptions.

As shown in Kormendy and Bender (1996), empirically, a_4/a can be used to separate out galaxies whose stellar motions are dominated by ordered rotation, $|v|/\sigma > 1$ from those which are dominated by random motion, i.e. dispersion, $|v|/\sigma < 1$: Disky ETGs, $a_4 > 0$, are generally dominated by ordered rotation along the major axis, whereas boxy ETGs are supported by random motions and can have significant amounts of minor axis rotation (Bender and Moellenhoff, 1987; Bender et al., 1988). Concerning the latter point, this also means that we can extend this distinction to the intrinsic symmetry of the gravitational potential of these galaxies: disk-like ETGs are overall axisymmetric, while boxy ETGs, $a_4 < 0$, may also show varying degrees of triaxiality which gives rise to minor axis rotation (Franx et al., 1991; Tremblay and Merritt, 1995; de Zeeuw and Franx, 1991).

Emsellem et al. (2007, 2011) expanded on the $|v|/\sigma$ kinematic classification of ETGs by introducing a recipe to classify ETGs by light-weighted averages over extended 2D kinematic fields:

$$\lambda_e \equiv \frac{\langle r_e |v| \rangle}{\langle r_e \sqrt{v^2 + \sigma^2} \rangle}, \quad (1.3)$$

where λ_e is a proxy of the projected angular momentum per unit mass within the effective radius r_e and the averages are 2D light-weighted averages. Plotting λ_e against apparent ellipticity $\epsilon_e = (1 - b/a)$ produces a dichotomy of “slow-rotators” and “fast-rotators”, separated by a line, $\lambda_e = (0.31 \pm 0.11)\sqrt{\epsilon_e}$ with few galaxies in-between. The fast/slow rotator categories for the most part follow the the disk-like/boxy dichotomy.

Finally, slow-rotating boxy galaxies are also overall more luminous ($M_V < -22$ mag), whereas fast-rotating disk-like ETGs are generally less luminous ($M_V > -20.5$ mag). However, the most compelling evidence for a significant dichotomy of ETGs is found in the *central* surface brightness profiles of these galaxies.

Cores and Power-laws

The centers of luminous, boxy ETGs are surprisingly faint. The surface brightness profiles over galactocentric radius ⁴ of most ETGs can be described by a Sérsic law ⁵, $\log I \propto r^{-1/n}$ (Sersic, 1968; Caon et al., 1993), with n being the so-called Sérsic index. However, there are some ETGs whose observed profiles diverge from a simple Sérsic law and which require more complex descriptions: At large radii, for very massive/luminous ETGs, particularly those sitting at the bottom of the large gravitational wells of galaxy clusters, so-called brightest cluster galaxies (BCGs) often have extended stellar envelopes around their main bodies. These are assembled from stars from minor and major mergers (i.e. mergers with small satellite galaxies and mergers between full-sized galaxies) and accretion of surrounding stars. This can for some galaxies raise $I(r)$ at large radii above what would be

⁴more accurately, circularized radius, $r = a*b$, where a and b are the major and minor axes of photometric ellipses

⁵This is a generalization of the famous de Vaucouleurs law (de Vaucouleurs, 1948), $\log I \propto r^{-1/4}$, which can describe many standard ETGs, but has since become outdated relative to the complexity of measured ETG light profiles.

encompassed by a single galaxy-wide Sérsic law (e.g. Kluge et al., 2020; Kluge and Bender, 2023).

At small radii, massive/luminous ETGs also diverge from a single Sérsic law: Typically, on scales of a few parsec to kilo-parsec the light profiles of these galaxies break off from steeper outer Sérsic laws into “cuspy cores”, shallow inner power-laws $I \propto r^{-\gamma}$ with $\gamma \lesssim 0.3$. Conventionally, these are simply called “cores”, even though the “cuspy” specifier, which distinguishes these profiles from analytic cores, $d \log I / \log r = 0$ is more accurate. The light profiles of their less massive/luminous counterparts, by contrast, are almost unbroken towards the smallest resolved radii, $\gamma \gtrsim 0.5$. ETGs without cores are often simply called “power-law” ETGs. Cores are in almost all cases found exclusively in boxy galaxies, whereas central power-laws are associated with disk galaxies. The distinction between cores and power-laws is sharp, nonetheless there is always the possibility of small cores hiding behind instrumental resolution limits of galaxies which have thus far been assumed to be power-laws.

Figure 1.2 illustrates this dichotomy between the central surface brightness profiles of both cored and coreless power-law ETGs. The dichotomy was first suggested by Nieto et al. (1991b), but was later solidified by the photometric measurements of the Hubble Space Telescope (HST) era (Crane et al., 1993; Kormendy et al., 1994; Ferrarese et al., 1994; Lauer et al., 1995; Gebhardt et al., 1996; Faber et al., 1997). Furthermore, Kormendy (1999); Kormendy et al. (2009), showed that “power-laws” are not unbroken, simple Sérsic profiles down to the smallest radii. Instead, close to the study’s resolution limit, in the very center these galaxies have an excesses of light, relative to an overall Sérsic law. This is why the centers of these galaxies are sometimes called “cusps”, forming a cusp/core dichotomy, but this terminology is misleading since the “cores” are technically also cusps, just shallower. The core/power-law convention suffers from the same problem, but is still more common.

For the central $\sim 20''$ of local ETGs, the so-called Nuker-profile (Byun et al., 1996; Lauer et al., 2005, 2007c) can be used to characterize both types of ETGs in order to quantify the properties of their central cores or power-laws:

$$I(r) = I_b 2^{(\beta-\gamma)/\alpha} \left(\frac{r_b}{r}\right)^\gamma \left[1 + \left(\frac{r_b}{r}\right)^\alpha\right]^{(\gamma-\beta)/\alpha}, \quad (1.4)$$

where r_b is the break radius, which for cored profiles designates the spatial extent of the core, and I_b the luminosity at r_b . γ is chiefly the slope of the light profile inside r_b , and β the slope of the profile on the outside. The parameter α regulates the smoothness or abruptness of the transition at r_b . Cores have $\gamma \sim 0.05 - 0.3$.

Later on Graham et al. (2003) and Trujillo et al. (2004b) introduced the core-Sérsic function, which unlike the Nuker law can be used to fit the whole galaxy light profile, because this function includes an outer Sérsic function, in addition to an inner power-law:

$$I(r) = I' \left(1 + \left(\frac{r_b}{r}\right)^\alpha\right)^{\frac{\gamma}{\alpha}} \exp \left[-b_n \left(\frac{r^\alpha + r_\beta^\alpha}{r_e^\alpha}\right)^{\frac{1}{n}}\right], \quad (1.5)$$

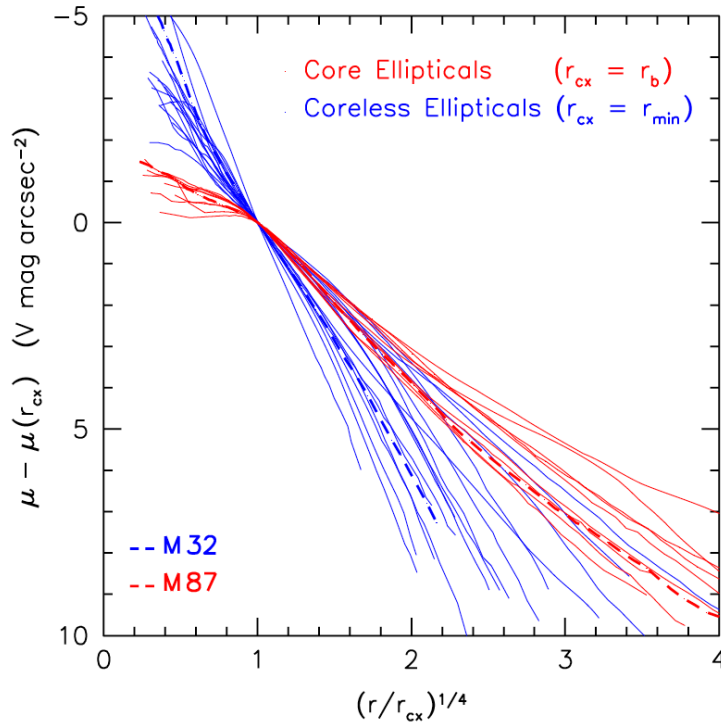


Figure 1.2: Surface brightness profiles over galactocentric radius for cored and coreless (power-law) ETGs from Kormendy (1999). This is Figure 40 of that study. The surface brightness is here shown in units of astronomical magnitudes over arcseconds, $\mu \propto -2.5 \log I$. The radius and profiles are normalized at r_{cx} . This radius is simply the core radius r_b for cored galaxies and the innermost radius up to which a single Sérsic law could describe the profile of the galaxy for the coreless galaxies.

where

$$I' = I_b 2^{-\frac{\gamma}{\alpha}} \exp \left[b_n \left(\frac{2^{\frac{1}{\alpha}} r_b}{r_e} \right)^{\frac{1}{n}} \right], \quad (1.6)$$

carrying on most of the parameters of the Nuker law, but with the addition of the Sérsic index n (b_n is a scaling factor carried over from a normal Sérsic law). The main draw-back of this profile is that it is too rigid, if for example the galaxy is a BCG with an extended stellar envelope. Since this is a profile fit for the whole galaxy this also biases the core parameters r_b , I_b and γ . In Chapter 2, I present a study of the BCG of Abel 85, Holm 15A, whose exact core radius is difficult to define because of the extended stellar envelope which makes the galaxy appear to have an almost unbroken exponential surface brightness profile, $n \sim 1$.

Besides the radius r_b which one can derive from these two profiles to characterize the size of a core, there is also the “cusp-radius” r_γ which functions as a profile-independent core radius. It is defined at the radius where $d \log I / d \log r = -1/2$ (Carollo et al., 1997).

Typically $r_\gamma \sim r_b$, however some caution must be exercised when measuring this radius, as it can in principle apply to any galaxy, including power-law ETGs and even spirals, or any other object, even if there is no actual core. But, as I show in Chapter 2, for some extreme galaxies, the core-transition can be so smooth that r_b is unfit to measure the core size for both a core-Sersic and Nuker profile, and only r_γ is of use.

Cores are of particular interest because their properties correlate with galaxy properties: Cores are larger and less dense in brighter galaxies (e.g. Lauer, 1985; Kormendy, 1985; Nieto et al., 1991a), and as explained above, they are essentially only found in boxy galaxies. While there are different ways to construe the E-E dichotomy, i.e. to tie it to some set of parameters along which ETGs split into two, the core/power-law ETG distinction is especially rooted in physics, as it is *inclination independent*, unlike the fast/slow rotator or boxy/disky distinction.

1.1.3 Supermassive Black Holes, core formation and ETG evolution

It is generally thought that disk and boxy ETGs are the outcome of two types of major mergers. Wet mergers, due to dynamical friction involved between components of gas and between gas and stars, are driven by the dissipation of energy which in turn circularizes orbits, producing an axisymmetric galaxy with isophotes which have disk distortions. Dry mergers by contrast are dissipationless (no gaseous components) and driven by so-called violent relaxation, the process by which a collisionless system consolidates a new dynamical equilibrium in a changing gravitational potential, $dE/dt = \partial\phi/\partial t$. This is associated with a re-distribution of stars in phase-space. In particular, more stars are put on so-called box-orbits, the driving force behind boxy isophote distortions, and the build-up of triaxiality (e.g. Bender and Moellenhoff, 1987; Nieto and Bender, 1989; Hopkins et al., 2009b). Dry mergers can also explain many of the kinematic substructures that are observed in real boxy galaxies, such as decoupled cores, i.e. central regions whose rotation is flipped or misaligned relative to the surrounding galaxy. This translation of the E-E dichotomy into a dry/wet merger dichotomy can also explain the empirical range and trends of galaxy velocity dispersion σ : The Faber-Jackson relation of ETGs $\sigma \propto L^{1/4}$, relating dispersion to galaxy luminosity, *saturates* for the most luminous/massive galaxies (Lauer et al., 2007a; Cappellari et al., 2013a; Kormendy and Bender, 2013). The saturation of the relation can be explained by the superposition of two separate empirical relations for cored and power-law ETGs: $\sigma \propto L^{1/4}$ for power-law ETGs, and the much shallower relation $\sigma \propto L^{1/8}$ for cored ETGs (Kormendy and Bender, 2013) – further evidence for the E-E dichotomy. These differently sloped relations, in turn, can be explained by merger origin: $\sigma \propto L^{1/4}$, the normal Faber-Jackson relation, can be linked back to the virial theorem via empirical scaling relations⁶. Generally, dry, and therefore dissipationless mergers are expected to preserve σ . However, numerical simulations of dry mergers indicate that in the case of

⁶ $\sigma^2 r_e \propto M = M/L \times L$. Using the empirical relations $r_e \propto L^{0.76}$ (Kormendy and Bender, 2012) and $M/L \propto L^{0.32}$ (Cappellari et al., 2007), $\sigma \propto L^{1/3.6}$.

largely 1:1 (mass-wise) and close to head-on mergers, σ increases slightly as in the $\sigma \propto L^{1/8}$ relation (Boylan-Kolchin et al., 2006; Hilz et al., 2012). This can be largely attributed to the build up of radial orbital anisotropy through violent relaxation. But does this also explain why boxy ETGs have cores and disk ETGs do not?

Considering just stars, gas, and dark matter halos, no: Numerical mergers simulations of dry mergers show that existing bright central regions, i.e. power-law-like nucleus, sink to the center of the forming remnant where they become the new bright center. If there are two of them they even form a much larger bright central power-law (e.g. Rantala et al., 2018). For simulations of wet mergers, core-formation is even more suppressed. Here the bright nucleus sinks to the bottom, too, and on top of that, angular momentum transfer and dissipation transport gas to the center of the merger remnant on small timescales, where starbursts are triggered which populate the center with blue, young new stars (e.g. Barnes and Hernquist, 1996; Mihos and Hernquist, 1994; Hopkins et al., 2008, 2009a). Such merger-induced nuclear star bursts have also been observed in nearby mergers (e.g. Kormendy and Sanders, 1992; Joseph and Wright, 1985). This, at least, is fully consistent with the observed unbroken Sérsic profiles with central light excesses in E(d) galaxies. But both formation channels are inconsistent with core-formation or even long-term core-survival.

A way to resolve this issue is to account for the presence of supermassive black holes (SMBHs), black holes with masses $M_{\text{BH}} \sim 10^6 - 10^{10} M_{\odot}$. SMBHs are expected to reside in the centers of most galaxies, and certainly all ETGs (Magorrian et al., 1998). It is unknown how these black holes, or rather their massive progenitors were formed, but they seem to appear at the dawn of galaxy formation: At $z > 2$, and even $z \gtrsim 6$, there exist ultra-luminous point sources ($L \gtrsim 10^{11} L_{\odot}$) called quasars, short for “quasi-stellar radio sources”, which far outshine their host galaxies. The existence of objects so bright and yet so compact can be explained by the accretion of large amounts of mass in the denser ancient universe onto SMBHs and the radiation energy generated thereby. SMBHs are expected to far outlast the current lifetime of the universe, and so they are expected to survive “dormant” and dark in the less turbulent universe of today, in the centers of local galaxies (e.g. Salpeter, 1964; Lynden-Bell, 1969; Kormendy and Richstone, 1995; Richstone et al., 1998; Kormendy and Ho, 2013; Wu et al., 2015). Stellar dynamical modeling of ETGs, which I introduce in Section 1.2, has been used to detect more than a hundred nearby SMBHs by now (see Kormendy and Ho, 2013 and Saglia et al., 2016 for review). The many detections of central SMBHs have also led to the discovery of a number of empirical relations between the properties of host galaxies and the masses of their respective central SMBHs, M_{BH} , such as between M_{BH} and σ , and M_{BH} and bulge/ETG mass and luminosity, M_{Bu} , L_{Bu} (e.g. McConnell and Ma, 2013; Kormendy and Ho, 2013; Saglia et al., 2016). These three relations are shown in the top row of Figure 1.3.

Merger simulations which include central SMBHs, find that the SMBHs of merging galaxies sink to the center of the forming galaxy where they also merge. In doing so, they trigger a process called black hole binary “core-scouring”. This process is illustrated in Figure 1.4. First suggested by Begelman et al. (1980), it involves the ejection of stars from the central regions of the merger remnant – first, during their descent to the center, the

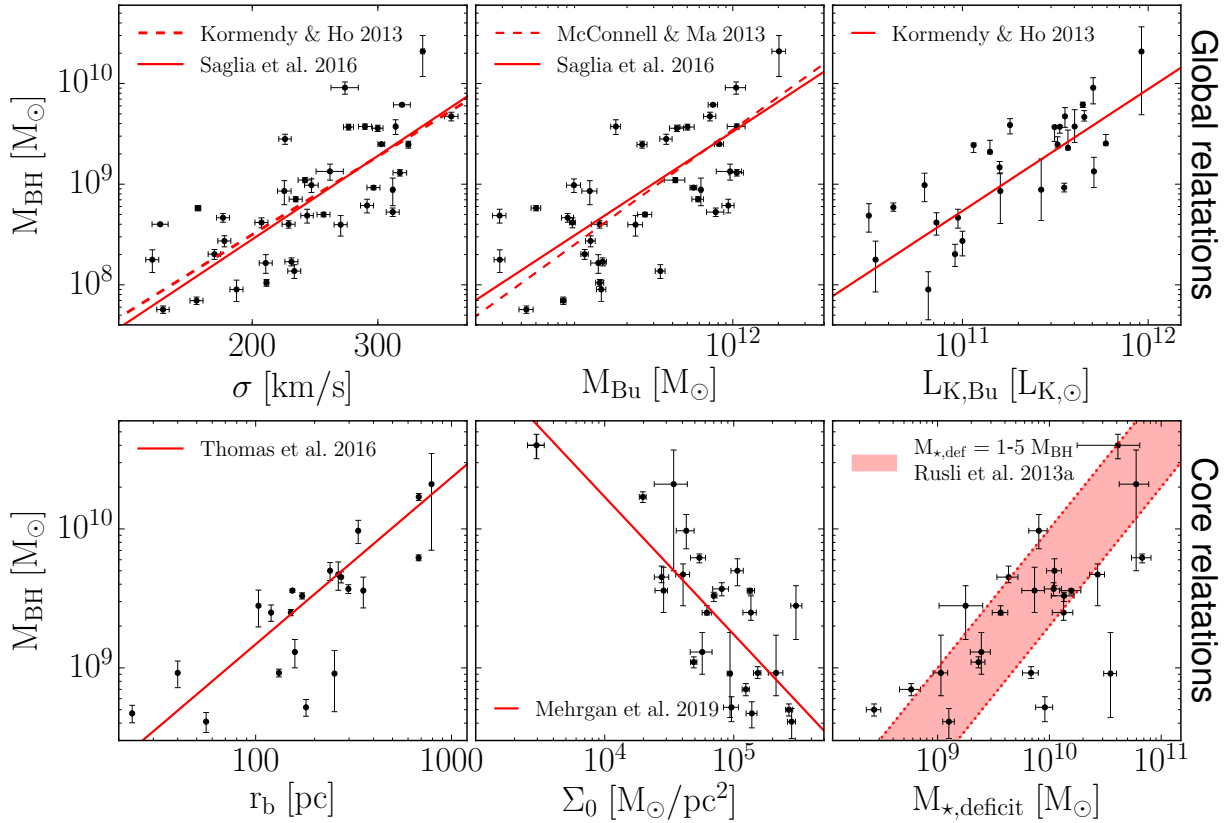


Figure 1.3: Empirical scaling relations between central SMBH mass, M_{BH} and various galaxy properties for exemplary samples of ETGs. The top row shows scaling relations for the *global* galaxy properties velocity dispersion σ , bulge mass M_{Bu} (=stellar mass of the ETG) and K-band bulge luminosity $L_{K,\text{Bu}}$ from Kormendy and Ho (2013); McConnell and Ma (2013); Saglia et al. (2016) for ETGs from Saglia et al. (2016). The bottom row shows scaling relations for the *core* properties core-break radius r_b , stellar surface mass density in the core region Σ_0 and stellar mass deficit of the core $M_{\star,\text{deficit}}$ from Rusli et al. (2013b); Thomas et al. (2016); Mehrgan et al. (2019) for the cored ETGs from these studies.

SMBHs lose angular momentum in the form of kinetic energy to surrounding stars via dynamical friction. Next, the SMBHs become gravitationally bound, and the binary enters short-lived three-body interactions with nearby stars, during which the stars are slingshotted to larger radii, shedding some of the binaries' energy, which facilitates the hardening of the binary. In this manner cores are excavated from the central regions of forming galaxies, which produces light profiles like those observed in real cored galaxies (e.g. Hills and Fullerton, 1980; Ebisuzaki et al., 1991; Makino and Ebisuzaki, 1996; Quinlan, 1996a; Faber et al., 1997; Milosavljević and Merritt, 2001; Volonteri et al., 2003; Milosavljević et al., 2002; Makino and Funato, 2004; Trujillo et al., 2004a; Merritt and Milosavljević, 2005; Merritt, 2006; Merritt et al., 2007; Gualandris and Merritt, 2008; Hopkins et al., 2009b;

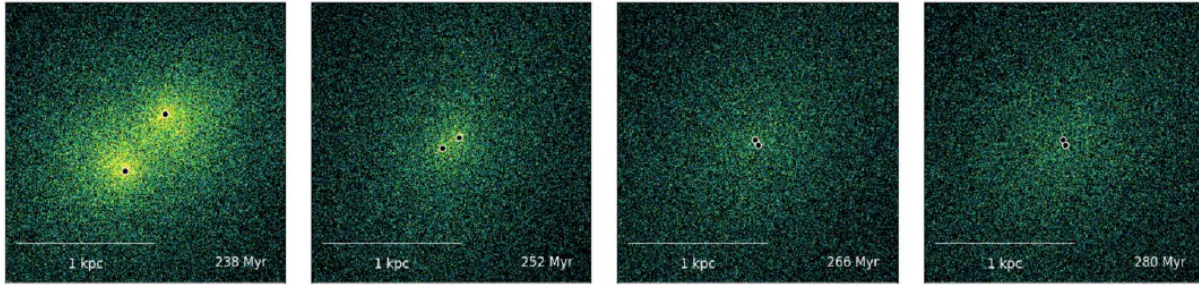


Figure 1.4: Snapshots from ETG-ETG, 1:1 merger simulations from Rantala et al. (2018) (images taken from their Figure 4). The snapshots show the central few kiloparsec of the forming galaxy, where brighter green tones indicate higher concentrations of stars and black disks the central SMBHs of the merging galaxies. From left-to-right, the sequence moves from the initial stages of core scouring to the final hardening of the binary at the simulation’s spatial resolution limit. By that point, the stellar density of the central regions of the remnant has noticeably decreased as the binary SMBHs have slingshotted stars out of the center.

Merritt, 2013; Rusli et al., 2013b; Rantala et al., 2018).

Dynamical evidence of this process is found in the details of the orbital structure of cored galaxies. Stellar dynamical orbit models (see Section 1.2) give us insight into this orbit structure. In particular we can compute radial profiles of the so-called orbital anisotropy parameter

$$\beta = 1 - \frac{\sigma_t^2}{\sigma_r^2}, \quad (1.7)$$

where σ_r is the radial and $\sigma_t = \sqrt{(\sigma_\theta^2 + \sigma_\phi^2)/2}$ is the tangential velocity dispersion, computed from the galaxy-intrinsic dispersions σ_θ and σ_ϕ in the two angular directions. These radial and tangential dispersion measures refer to distributions of stellar motions along orbits with fundamentally different geometries with respect to the galactic center. I here refer to these orbit-groups as radial and tangential orbits. Schematic illustrations of these orbit types are shown in Figure 1.5. Considering the $\beta(r)$ profiles of real cored galaxies, they consistently show a characteristic trend of increasing tangential orbits ($\beta < 0$) inside the core and closer to the very center and increasing radial orbits ($\beta > 0$) outside of the core towards larger radii (e.g. McConnell et al., 2012; Thomas et al., 2014, 2016; Mehrgan et al., 2019). This is also a direct prediction of core-scouring merger simulations (e.g. Quinlan, 1996b; Milosavljević and Merritt, 2001; Rantala et al., 2018, 2019; Frigo et al., 2021): Orbits on more radial trajectories take stars closer to the central SMBH binary than tangential orbits and thus are more likely to be ejected from the core. These observations match up excellently with these predictions in direct comparison of the full $\beta(r)$ profiles (Thomas et al., 2014; Rantala et al., 2018, 2019) as can be seen in Figure 1.6.

Despite everything presented here, thus far, the local black hole mass function is poorly understood, and at the high-mass end, for $M_{\text{BH}} \geq 10^{10} M_\odot$, it is barely sampled at all.

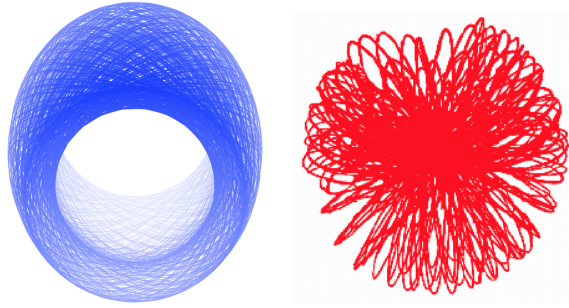


Figure 1.5: Schematic illustration of exemplary tangential (left, blue) and radial (right, red) orbits.

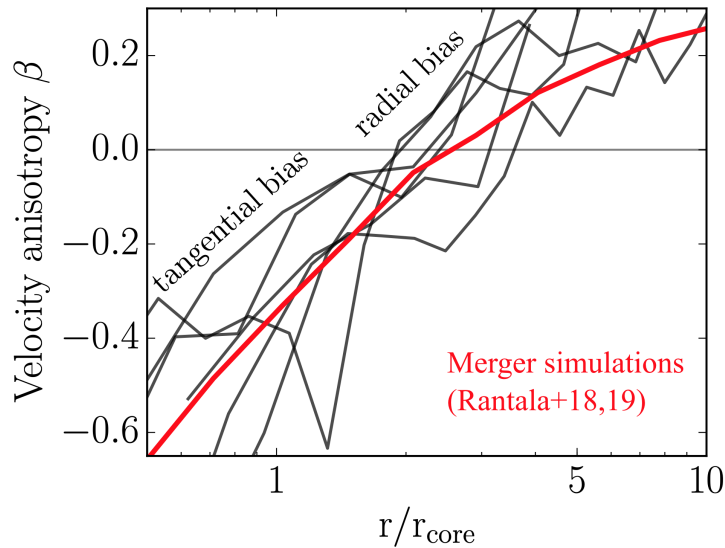


Figure 1.6: The dynamical “fingerprint” of SMBH-binary core-scouring in cored ETGs from Thomas et al. (2014). I show here the velocity anisotropy parameter $\beta(r)$ over radius scaled by core-radius for the ETGs (black) compared to numerical merger simulations with core-scouring from Rantala et al. (2018, 2019) (red). Within and around the core, the orbital distribution becomes more tangentially biased, outside, the radial bias increases.

Indeed, the most established SMBH scaling relation, $M_{\text{BH}} - \sigma$, breaks down at the high-mass end, because dry mergers only grow σ by very little, whereas the masses of the SMBHs simply add up. Fortunately, there are also various empirical relations tying central SMBHs to core properties. I am showing three of these in the bottom row of Figure 1.3. Such relations can be explained via the core-scouring formation channel: There are log-linear relations between M_{BH} and core size, parameterized either by r_b or r_γ , and between M_{BH} and central surface brightness/mass, μ_0 , Σ_0 (for the first time introduced in my study Mehrgan et al., 2019, which I present in Chapter 2). These relations indicate that the

most massive SMBHs reside in the centers of the cores which are largest and faintest/least dense (e.g. Faber et al., 1997; Lauer et al., 2007c; Rusli et al., 2013b; Kormendy and Ho, 2013; Thomas et al., 2016; Mehrgan et al., 2019). Thomas et al. (2016) also showed a 1:1 relation between r_b and r_{SOI} , the radius of the gravitational sphere-of-influence (SOI) of the central SMBH, meaning the galactocentric radius at which the enclosed stellar and DM mass of the galaxy is equal to M_{BH} . The proverbial “smoking gun” for the core-scouring formation channel is the relation between M_{BH} and the central missing light of the core-profile relative to inwards extrapolation of the outer Sérsic light profile, which was first introduced by Kormendy and Bender (2009) (see also Rusli et al., 2013b). This can be translated to a log-linear relation with the missing stellar mass, $M_{\star, \text{deficit}}$. A SMBH binary displaces $M_{\star, \text{deficit}}$ on the order of its own mass per merger. Each merger then increases $M_{\star, \text{deficit}}$ further. Additional scouring from ejected stars falling back into the center of the forming remnant can increase the effectiveness of the scouring process (Gualandris and Merritt, 2008). All of this taken together, leads to the expectation that M_{def} for most galaxies lies between roughly one to five times M_{BH} , which agrees well with observed deficits (Merritt, 2006; Ferrarese et al., 2006; Lauer et al., 2007a; Mehrgan et al., 2019).

The empirical scaling relations between core properties and M_{BH} hold enormous potential for investigating the local black hole mass function, but they are based only on a relatively small number of ETGs, and have previously never been used to select galaxies for dynamical study. It is thus unknown if we can use these relations which are based on very straight-forward observations of photometric properties to find SMBHs in some targeted mass range. In Mehrgan et al. (2019), which I present in Chapter 2, we have for the first time selected a galaxy, Holm 15A, for study specifically because of its extremely large core ($r_\gamma \sim 4 \text{ kpc}$). This lead – as we had anticipated – to the discovery of the most massive dynamically detected SMBH thus far with $(4.0 \pm 0.8) \times 10^{10} M_\odot$, demonstrating the utility of these still young scaling relations for future systematic sampling of the local black hole mass function.

An important question that must be raised is whether or not the E-E dichotomy truly constitutes a “dichotomy” in the stricter sense. Are we just overstating the difference of some individual ETG properties, such as central surface brightness and rotation, whereas the ETGs themselves are on one and the same continuous but forking track of galaxy evolution (like the forking of spiral galaxies into barred and un-barred)? That is, are the progenitors of boxy/cored and disk/power-law ETGs truly different? Naturally, core-scouring would also occur during a wet merger, but the ensuing nuclear star bursts would quickly “cover up” the core. This is why it is often said that the core/power-law dichotomy can be traced back to the outcome of the *last* major merger of each galaxy, since in principle, a previously cored ETG can be turned into a power-law ETG with one or several “unlucky” encounters. However, this is not quite correct, as cored ETGs, are, as stated above, overall more massive than power-law ETGs (if cores could become power-laws “by accident”, why would there be mass segregation?). For this reason Kormendy et al. (2009) also proposed an addendum to the dry-merger-core scenario to better explain why we generally do not find massive galaxies with cores that have been destroyed by chance encounters with gas-rich galaxies: More massive galaxies can hold larger quantities of hot X-ray emitting gas

– gas that has been super-heated by the energetic feedback processes of matter-accreting SMBHs, so-called active galactic nuclei (AGN). In the presence of this medium, gas which could be used for star formation is prevented from collapsing into stars. Indeed, cored ETGs generally contain radio-loud AGN and hold on to hot X-ray emitting gas, whereas power-law ETGs do not. This suggests that also the progenitors of ETGs are mass-segregated, which could speak in favour of a deeper running dichotomy.

Here, however, we still lack knowledge of the stars making up these galaxies: If the stars of the two types formed in radically different environments, their stellar populations could have turned out very different – besides the fact that by now both their populations are red and ageing. This is captured by the so-called stellar initial mass function, which describes the distribution of stellar masses in a stellar population at time of formation. I describe this topic in more detail in Section 1.3. In Chapter 4, I investigate this property of ETGs and present evidence that both more massive power-laws and cored ETGs have in their central regions, on scales of 1 kpc from the respective galaxy center, formed stars in mutually similar ways but with a relative excess of dwarf or giant stars relative to the stellar populations of LTGs such as the Milky Way.

In order to measure both stellar initial mass functions and SMBHs it becomes critical to measure the total masses of ETGs and to decompose them into their principle components.

1.2 The stellar dynamics of ETGs

Stellar dynamical modeling of ETGs is the principal method by which we uncover their intrinsic mass composition. It consists of constructing mass-models for the motions of stars moving in a shared gravitational potential, and optimizing these mass-models from the fits to the kinematics. Stellar kinematics can be recovered from an analysis of galaxy spectroscopy.

1.2.1 Stellar kinematical measurements

The stellar populations of distant galaxies are *unresolved*. This means that the spectra of a galaxy result from the blending of the spectral features of many stars and other light emitting sources along the line-of-sight (LOS).

Spectral feature arise due to the different elements found in the atmospheres of stars and the interstellar medium (ISM). Absorption and emission lines are narrow lines etched into, or on top of, the black body radiation spectrum of stars. The lines are produced by the competing absorption and emission processes of the different and differently abundant elements in the atmospheres of stars and the ISM. Other processes such as the surface gravity of stars also impact the shape of spectral features. The continuum, made up of the blending of individual black body radiation spectra, against which emission and absorption lines appear, can also be impacted by radiation from AGN, which furthermore produce their own broad emission lines from the ionization of gas around the accretion disk of the SMBH.

For the galaxies which are the concern of this thesis, i.e. massive ETGs with very little, or no gas at all, the spectral features consist predominantly of *stellar absorption* lines.

Line-of-sight velocity distributions

Consider an ETG which is observed spectroscopically. Due to its distance, an observed galaxy spectrum \mathcal{G} over wavelength λ is redshifted by the Hubble flow, and relative to that redshift, further redshifted, or blueshifted due to its peculiar velocity. Due to the motions of the stars in the galaxy, their individual spectra are themselves differently red- and blueshifted relative to the overall galaxy redshift by small $\Delta\lambda$, according to their individual LOS velocities, v_{los} ,

$$\frac{v_{\text{los}}}{c} = \frac{\Delta\lambda}{\lambda} \approx \Delta \ln \lambda, \quad (1.8)$$

for the small red/blue shifts found in galaxies. The cumulative blending of the differently-shifted absorption lines of all the stars along some LOS in a galaxy results in a broadening of the absorption lines, producing the observed galaxy spectrum \mathcal{G} . The broadening of stellar absorption lines is illustrated in an example in Figure 1.7. It is advantageous here to introduce a quantity called the “spectral velocity”,

$$u \equiv c \ln \lambda, \quad \mathcal{G}(\lambda) \rightarrow \mathcal{G}(u). \quad (1.9)$$

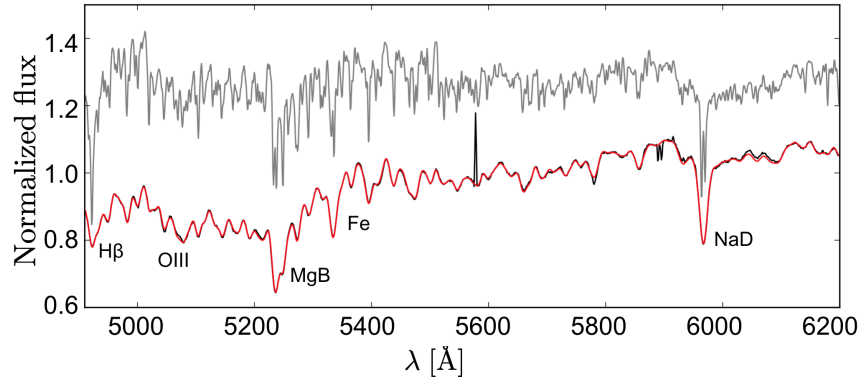


Figure 1.7: Example spectrum and illustration of kinematic broadening over wavelength for a massive ETG (NGC 7619). The continuum of the galaxy spectrum has been removed and the spectrum normalized. The spectrum is shown in black. The grey spectrum on top is a model template for the unbroadened stellar population underlying the galaxy spectrum redshifted to the galaxy redshift (it has also been arbitrarily normalized and shifted in flux for the sake of illustration). The red spectrum is a fit to the galaxy spectrum derived from broadening the template spectrum via a convolution with a LOSVD (shown separately in Figure 1.8). Notable spectral absorption features are indicated in the image. The fit was derived using the so-called WINGFIT spectral fitting code (Thomas et al. in prep.)

Mathematically, the broadening of absorption features can be represented as a convolution of a model of the unbroadened spectrum of a stellar population $\mathcal{T}(u)$, called the “stellar template”, or just “template”, with a broadening function $\mathcal{L}(v_{\text{los}})$:

$$\mathcal{G}(u) = (\mathcal{T} * \mathcal{L})(u) = \int_{v_{\text{los}}} \mathcal{T}(u - v_{\text{los}}) \mathcal{L}(v_{\text{los}}) du \quad (1.10)$$

The broadening function \mathcal{L} is the so-called line-of-sight velocity distribution (LOSVD). An example of such a convolution is shown in Figure 1.7

The most common way to parameterize the LOSVD is with the Gaussian-like Gauss-Hermite series:

$$\mathcal{L}(\mu, h_{3,4,\dots}) = a \cdot e^{-\frac{\mu^2}{2}} (1 + h_3 \mathcal{H}_3(\mu) + h_4 \mathcal{H}_4(\mu) + \dots), \quad (1.11)$$

$$\mu = (v_{\text{los}} - v_{\text{rot}}) / \sigma, \quad (1.12)$$

where

$$\mathcal{H}_i(\mu) = \begin{cases} i! \sum_{j=0}^{\frac{i}{2}} \frac{(-1)^{\frac{i}{2}-j}}{(2j)!(\frac{i}{2}-j)!} (2\mu)^{2j} & \text{if } i \text{ is even} \\ i! \sum_{j=0}^{\frac{i-1}{2}} \frac{(-1)^{\frac{i-1}{2}-j}}{(2j+1)!(\frac{i-1}{2}-j)!} (2\mu)^{2j+1} & \text{if } i \text{ is odd} \end{cases} \quad (1.13)$$

The first term is just a normal Gaussian with amplitude a . For the subsequent terms it is corrected with a sequence of Hermite-polynomials \mathcal{H}_i with coefficients h_i , which are varied

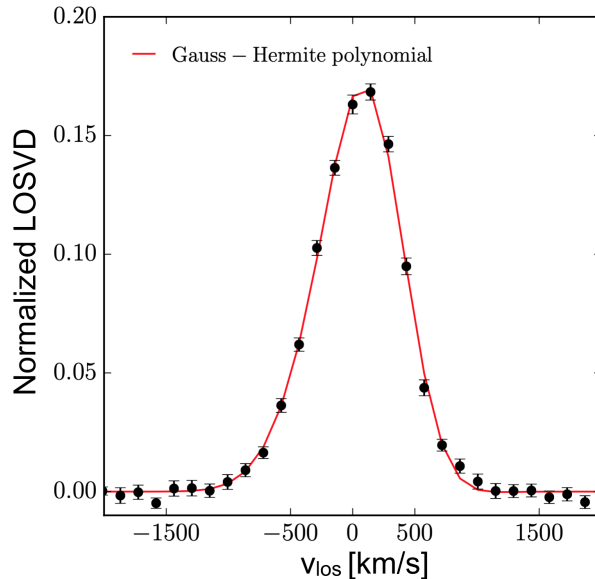


Figure 1.8: Example of an LOSVD which has been recovered non-parametrically (using WINGFIT) (black points with errorbars). *After* recovery, I have fitted the LOSVD with a Gauss-Hermite polynomial of 4th order. The non-parametric LOSVD corresponds to the one from the spectral fit in Figure 1.7.

during the fit, alongside v_{rot} and σ . Frequently in the literature, stellar spectra are fitted with such Gauss-Hermite functions up to h_4 as LOSVD-models, but throughout this thesis I show that it is preferable to determine LOSVDs non-parametrically, and to fit them with Gauss-Hermite functions *a posteriori* to highlight certain kinematic trends where needed. Figure 1.8 shows the non-parametrically determined LOSVD of the galaxy spectrum in Figure 1.7 and a Gauss-Hermite fit to the recovered LOSVD.

Nonetheless, Gauss-Hermite functions often have descriptive utility – v_{rot} and σ , the mean and dispersion of a normal Gaussian, can help us characterize the general rotation and intensity of random motions, or blending of rotation from two sides of the galaxy (making one broad envelope of two narrower Gaussians). In the beginning of stellar kinematic analysis, a Gaussian was all that was fitted. The functions of the higher-order Gauss-Hermite moments h_3 and h_4 are illustrated in Figure 1.9. Hermite orders beyond this are essentially extensions of the trends generated by these even and odd order coefficients to larger velocities. Therefore I here focus on h_3 and h_4 . However, in Mehrgan et al. (2023a), I show that at least sixth or eight order polynomials should be used to capture the full shape of the LOSVD of many ETGs. This is presented in Chapter 3 (see also Krajnović et al., 2015; Veale et al., 2018; Quenneville et al., 2022; Thater et al., 2022).

h_3 and higher order odd Hermite coefficients primarily govern the axisymmetric features of a LOSVD. Expanding a Gaussian with a non-zero h_3 skews the LOSVD asymmetrically in one direction: On the one side from the LOSVD peak, the tail of the distribution gets slightly lifted, on the other suppressed. The LOSVD-peak also moves slightly in the di-

rection of the suppressed side of the LOSVD. Gauss-Hermite polynomials with $v_{\text{rot}} - h_3$ anticorrelation (illustrated in the left-hand panel of Figure 1.8), produce a good representation of the projection of stellar motions along a LOS that is dominated by ordered rotation. Along such a LOS, the LOSVD is not perfectly symmetric about v_{rot} . In the case of only circular or close-to circular orbits, orbits which are intercepted perfectly tangentially by the LOS produce the largest projected velocities. Other intercepted orbits are intercepted at an angle and project to smaller v_{los} . At the same time, these orbits also necessarily lie at larger distances from the center and thus carry less light. Therefore, the LOSVD abruptly terminates at a largest velocity on the side of v_{rot} , and has a trailing tail of smaller velocities on the opposite side. Typically, the circular velocity of orbits vary, and a varying number of orbits are more radial. In this case, the LOSVD-signal on the side of rotation terminates smoothly, and the LOSVD can be described by a Gauss-Hermite polynomial with $v_{\text{rot}} - h_3$ anticorrelation.

The descriptive function of h_4 is related to the orbital anisotropy along the LOS. Random motions, i.e. radial orbits, produce large velocities on both sides of the peak of the LOSVD. For a LOS through the center of the galaxy, more tangential orbits largely project to zero or smaller velocities, because they are intercepted perpendicular to the direction of the circular velocity. However, real observations are limited by finite spatial resolutions and atmospheric seeing, which redistributes light from off-center lines-of-sight to the center. For these lines-of-sight, close to the center, but not thorough it, non-zero velocities can be generated along the LOS even from circular orbits, as they are not be intercepted perpendicularly. If the mass profile of the galaxy becomes steeper in the center, these velocities become larger. This poses a conundrum: Is a given LOSVD broader because the mass profile is steeper or because there are more stars on radial orbits? This problem is called the mass-anisotropy degeneracy, and h_4 was introduced to stellar kinematic fitting to resolve it (Binney and Mamon, 1982; Dejonghe and Merritt, 1992; van der Marel and Franx, 1993; Gerhard, 1993; Merritt and Saha, 1993; Bender et al., 1994). If the galaxy is more radially anisotropic along the LOS, the high-velocity tails of the LOSVD will have stronger signal, what we in Mehrgan et al. (2023a) dubbed LOSVD-“wings”. This LOSVD shape can be produced by a Gauss-Hermite polynomial with a positive h_4 , as seen in the right-hand panel of Figure 1.9. If there is less radial anisotropy or even tangential anisotropy along the LOS, the LOSVD has suppressed wings, and might even become flat-topped. The latter happens because of two sides of rotation from tangential orbits blurring together. This shape can be described by a negative- h_4 Gauss-Hermite LOSVD (see Figure 1.9).

However, it is important to emphasize that h_3 and h_4 are not in a 1:1 relation to these physical aspects of galaxies. If a LOSVD associated with a LOS dominated by strong rotation has a kinematic component that produces extra-light at the prograde wing of the LOSVD, h_3 can become very small. Similarly, a LOSVD might have a broad flat-topped trunk from tangential anisotropy at the same time as it has wings. As a result, h_4 might be positive, despite tangential anisotropy. I present a few such complex LOSVDs in Chapters 2 and 3.

Template mismatch

A significant issue facing us for the measurement of stellar kinematics is the determination of the template \mathcal{T} . The stars in ETGs are overall different than those in the MW: redder, older and more metal-rich on average. Yet, when we are looking for a template to represent the underlying stellar population of an ETG we either have to use observed stellar spectra from the MW, or synthetic spectra, which underlie various model assumptions. One way or another, it is very likely that any kinematic fit of an ETG suffers from some degree of so-called template mismatch – the mismatch between our model of the underlying stellar population of a galaxy and its actual intrinsic, to us unresolved, stellar population. This causes a variety of distortions of the recovery of the LOSVD. These distortions can also in part, but not sufficiently, be described by biases in h_3 and h_4 . LOSVDs can be overall more asymmetrically distorted or have a more symmetric excess or suppression of wing-light due to template mismatch. I simulate, illustrate and explain the mechanism behind, and the various manifestations of template mismatch distortions of the LOSVD in great detail in Mehrgan et al. (2023a) which is presented in Chapter 3. There, I also describe strategies that can be applied to minimize the effects of template mismatch.

Methods

I here briefly describe some of the methods that can be used to recover the LOSVD from ETGs. I focus only on those methods which appear in the subsequent chapters of this thesis, particularly Chapters 2 and 3. Most other methods however, are similar to one of each of the methods described here.

Considering Equation 1.10, the most natural way to recover the LOSVD seems to be a deconvolution via a Fourier transformation of the spectra:

$$\tilde{\mathcal{L}}(k) \propto \frac{\tilde{\mathcal{G}}(k)}{\tilde{\mathcal{T}}(k)}, \quad (1.14)$$

where the tilde signs indicate Fourier transformations. The LOSVD can be derived by performing an inverse Fourier transformation. In practice, this approach becomes problematic: In order to perform the deconvolution, the continua of both \mathcal{G} and \mathcal{T} need to be subtracted. This, however, results in a loss of information of the low frequency signal of the LOSVD. For the high frequency signal, the ratio of $\tilde{\mathcal{G}}(k)$ and $\tilde{\mathcal{T}}(k)$ greatly amplifies some of the noise in the data as both terms become very small for larger k . The end result is that in the best case scenario this can yield enough kinematic information to fit a simple Gaussian to the signal, but both higher-order Gauss-Hermite moments, and the non-parametric LOSVD are too distorted for utility (This is illustrated in Figure 11.2 of Binney and Merrifield, 1998).

More indirect approaches for recovering the LOSVD produce more detailed kinematics. Bender (1990) introduced the Fourier correlation quotient (FCQ) which can recover the non-parametric shape of the LOSVD. Here the LOSVD is not recovered through a deconvolution of the spectrum with the template directly, but of the *peak* of the cross-correlation

of the spectrum and the template with the *peak* of the auto-correlation of the template with itself:

$$\tilde{\mathcal{L}}(k) \propto \frac{\tilde{K}_{\mathcal{G},\mathcal{T},peak}(k)}{\tilde{K}_{\mathcal{T},\mathcal{T},peak}(k)}, \quad (1.15)$$

$$\tilde{K}_{\mathcal{G},\mathcal{T}}(k) = \tilde{\mathcal{G}}(k)\tilde{\mathcal{T}}^*(k) \quad (1.16)$$

$$\tilde{K}_{\mathcal{T},\mathcal{T}}(k) = \tilde{\mathcal{T}}(k)\tilde{\mathcal{T}}^*(k). \quad (1.17)$$

With this approach, most of the problems of the straight-forward deconvolution of the spectra are mitigated (though some loss of signal from the removal of the continua, deconvolution and inverse Fourier transformation are inevitable). Moreover, by isolating the peaks of the correlation functions, $\tilde{K}_{\mathcal{G},\mathcal{T},peak}$ and $\tilde{K}_{\mathcal{T},\mathcal{T},peak}$ from $\tilde{K}_{\mathcal{G},\mathcal{T}}$ and $\tilde{K}_{\mathcal{T},\mathcal{T}}$ (the cut-off around the peak is set by the smallest distance between absorption lines of \mathcal{G}), the effects of template mismatch on at least the lower moments of the LOSVD are removed from the equation. The disadvantages of this method are that FCQ cannot be used with spectral masks (see below), and requires the spectral features of the underlying stellar spectrum to be intrinsically *narrow* prior kinematic broadening. While this is generally the case for atomic absorption lines, molecular spectral features are *intrinsically broadened*. For such spectral features, the FCQ method breaks down.

Other methods sidestep the issue of recovering the LOSVD through deconvolution entirely. The popular Penalized Pixel-Fitting method (pPXF, Cappellari, 2017), as well as our novel pixel-fitting code WINGFIT (Thomas et al. in prep.) optimize the χ^2 of a model-spectrum \mathcal{S} fitted to the galaxy spectrum \mathcal{G} :

$$\mathcal{S} = \left(\sum_n w_n \mathcal{T}_n \right) * \mathcal{L}, \quad (1.18)$$

where \mathcal{T}_n are a *number of* different templates, with different weights w_n . These weights are, alongside the LOSVD \mathcal{L} , optimized in the fit via a Levenberg-Marquardt algorithm. Such methods can also be used for kinematic fits to intrinsically broadened molecular lines, unlike FCQ. Moreover, a much more complex template for the stellar population, $\mathcal{T} = \sum_n w_n \mathcal{T}_n$ can be determined in the fit. For pPXF, the LOSVD is parameterized by a Gauss-Hermite polynomial of a chosen order, whereby the parameters v_{rot} , σ , h_3 , h_4, \dots are optimized in the fit alongside the templates. This, however, is insufficient for very detailed dynamic analyses of galaxies (Lipka and Thomas, 2021; Neureiter et al., 2021). WINGFIT, by contrast, like FCQ, fits a non-parametric LOSVD. This LOSVD consists of a signal-histogram with velocity-bin-widths set by the spectral velocity resolution Δu of the data. This histogram is filled with signal during the fit-optimization. Naturally, some smoothing is needed to produce a usable LOSVD, which is always the case for non-parametric methods. For the latest version of WINGFIT (which I use in Chapter 3), the best smoothing is determined with a data-driven optimisation method that is based on a generalisation of the classical Akaike Information Criterion (AIC) Thomas and Lipka

(2022), and applies a smoothing penalty to the model. Therefore the fit optimizes not merely the χ^2 to the spectrum, but also takes the so-called “effective degrees of freedom” m_{eff} of the LOSVD into account, $\text{AIC}_p = \chi^2 + 2 \times m_{\text{eff}}$.

m_{eff} is calculated directly from the data by computing different noisy LOSVD realizations – bootstrap LOSVDs – from Gaussian noise based on the statistical uncertainties of the kinematic data. These bootstrap LOSVD realizations are then re-fitted by the model at a given LOSVD-smoothing and compared against the original fits to compute m_{eff} :

$$m_{\text{eff}} = 1/N_{\text{boot}} \sum_b^{N_{\text{boot}}} \sum_n^N \frac{1}{(\Delta\mathcal{L}^n)^2} \cdot (\mathcal{M}_{\text{boot}}^{b,n} - \mathcal{M}_{\text{fid}}^n)(\mathcal{L}_{\text{boot}}^{b,n} - \mathcal{M}_{\text{fid}}^n) \quad (1.19)$$

here $\Delta\mathcal{L}^n$ is the statistical uncertainty of the n -th LOSVD velocity bin, $\mathcal{M}_{\text{boot}}$ and \mathcal{M}_{fid} the smoothed-model-LOSVD for the bootstrap and the original unsmoothed LOSVD $\mathcal{L}_{\text{boot}}$ respectively.

To match the continuum of \mathcal{G} , polynomials, in this case Legendre polynomials are multiplied and/or added to the model \mathcal{S} . If there are emission lines or other independent kinematic components they may also be fitted with their own kinematics and templates, turning Equation 1.18 into a matrix multiplication with $T_n, w_n \rightarrow T_{n,j}, w_{n,j}$ and $\mathcal{L} \rightarrow \mathcal{L}_j$ for kinematic components j . Alternatively, emission lines may just be masked during the fits. Real spectra are also never uncontaminated by spectral artefacts, such as emission/absorption from earths atmosphere, the MW or the ISM, or simply systematics from the detector or data reduction. Such issues can also be seen in the example spectrum in Figure 1.7, where the strong oxygen 5577 Å emission line from earth’s atmosphere is clearly visible. Around 5850 – 5890 Å, to the left of the NaD absorption feature, one can see a small residual doublet-feature, which is in fact NaD absorption from the MW. On the right side of the galactic NaD, around 5850 – 5890 Å there also appear to be some issues with matching the continuum of the data. FCQ can only be applied to continuous spectral intervals, which means that these problematic regions cannot simply be masked in the fit – the fitting interval has to be chosen to exclude them, or the associated contaminating features need to be subtracted prior to the fit. For pixel-fitting methods like pPXF and WINGIFIT such problematic regions can simply be masked during the fit, as was also done in Figure 1.7. In Chapters 2 and 3 I present a more detailed explanation of the treatment of galaxy spectra for kinematic fitting.

1.2.2 Dynamical modeling

The motions of luminous components in galaxies originate from gravitational forces. Therefore, they constrain the underlying mass distributions of galaxies.

In spiral galaxies the situation can often be rather simple: Instead of looking at the movement of their stars, we can look at their large discs which are made up of cold atomic hydrogen. Simple kinematic measurements from the emission lines produced by a disc can be used to directly infer the circular velocity of the disk, v_{circ} ⁷ This immediately yields

⁷Such emission lines can be fitted with just a Gaussian. The mean velocity of that Gaussian, v_{rot} is

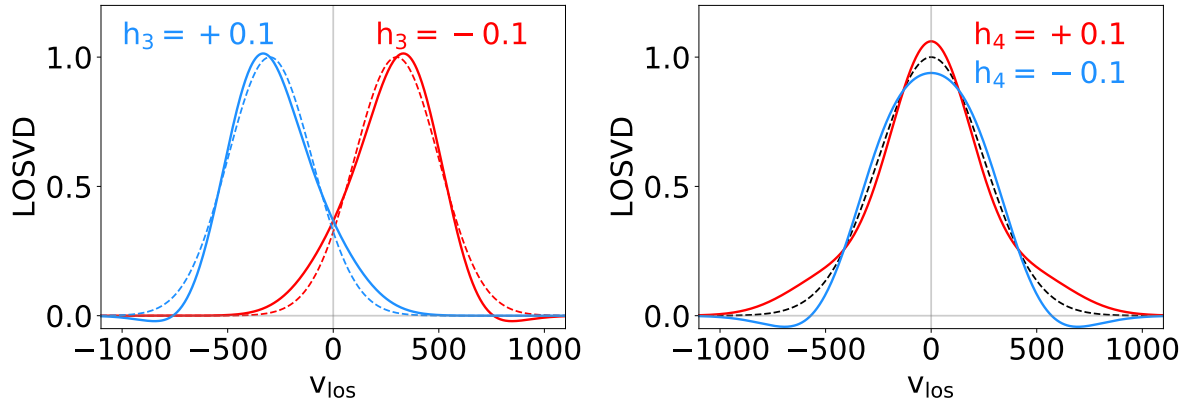


Figure 1.9: Illustrations of the effect of higher-order Gauss-Hermite polynomials on the LOSVD. Left: Two normal Gaussians (equivalent to $h_3 = h_4 = \dots = h_n = 0$) with $\sigma = 200$ km/s at $v_{\text{rot}} = -300$ km/s and $v_{\text{rot}} = +300$ km/s, shown as dashed red and dashed blue lines. In solid red and solid blue are shown Gauss-Hermite polynomials with the same v_{rot} and σ , but $h_3 = +0.1$ and $h_3 = -0.1$ (the signs of each v_{rot} and h_3 pair are opposite). Right: The same exercise with one normal Gaussian with $\sigma = 240$ km/s at $v_{\text{rot}} = 0$ km/s, shown in dashed black. In solid red and solid blue are shown versions of this LOSVD with $h_4 \pm 0.1$.

the mass distribution at a radius r_i :

$$v_{\text{circ}}^2(r_i) \propto \frac{M(r \leq r_i)}{r_i}. \quad (1.20)$$

For ETGs, things are not so straight forward. ETGs only have gas discs at the low-mass end (see the previous section) and these also tend to be very small. Instead, ETGs are truly three-dimensional objects whose luminous parts are overwhelmingly made up only of stars. If we consider a star moving through an ETG with some initial velocity v , after crossing the galaxy once, the change of its square velocity through randomly oriented chance encounters with other stars can be estimated to be

$$\frac{\Delta v^2}{v^2} \approx \frac{0.1 \ln N}{N}, \quad (1.21)$$

where N is number of stars in the galaxy (Binney and Tremaine, 2008, equations 1.28-1.38). The number of crossings that it would take to change the initial (square) velocity of the star by order of itself through the cumulative effect of perturbations from two-body gravitational interactions with other stars is simply $n_{\text{relax}} \simeq v^2/\Delta v^2$. The time it would take for this to occur, is then

then the projection of v_{circ} along the LOS. Since such discs are circular, as are all the motions within, the disks apparent ellipticity ϵ can directly yield an inclination i , with which we can project $v_{\text{rot}} \cos(i) = v_{\text{circ}}$. If the disc is perfectly face-on, no kinematic measurement is possible since all the velocities are intercepted perpendicular to the LOS.

$$t_{\text{relax}} = n_{\text{relax}} \times t_{\text{cross}} \simeq \frac{N}{0.1 \ln N} t_{\text{cross}}, \quad (1.22)$$

Where t_{cross} is the time of one galaxy crossing $\sim r_e/v$. This time is called the two-body relaxation time. For a typical ETG with $N \sim 10^{11}$ stars, $r_e \sim 10$ kpc, even for a very high stellar velocity of $v = 500$ km/s, the relaxation time is more than a factor 10^7 larger than the age of the universe. This means ETGs are effectively collisionless systems and we can treat the cumulative gravitational potential of all N stars in the galaxy as one smooth, continuous potential $\phi(\vec{r})$ which governs the motions of each star. Violent relaxation, which occurs in dry mergers, continuously redistributes the energies and angular momenta of stars in phase-space, but only as long as the gravitational potential is changing as a function of time, $dE/dt = \partial\phi/\partial t$. Once the potential has stabilised due to phase-mixing, violent relaxation stops, and the orbital trajectories of the stars in the galaxy “freeze out” as they are in that moment (since t_{relax} is so enormous). As a consequence, when an ETG is formed from a merger, it is usually *anisotropic*. Furthermore, we cannot compute the distribution of the stars in phase-space from first principles. Our only option is to model and test many different model gravitational potentials and orbital configurations to best fit observed properties of real ETGs.

Collisionless Boltzmann equation in a steady-state system

Following the hundreds of billions of stars in a galaxy on their orbits is impossible. Therefore we instead look at *probability functions*. The distribution function (DF) of stars in an ETG – the probability of finding a star within some interval $d\vec{r}$, $d\vec{v}$ is stated as

$$f(\vec{x}, \vec{v}, t) d^3r d^3v. \quad (1.23)$$

Naturally, the probability function has to be conserved over the whole galaxy and we can adapt the continuity equation of fluid mass from fluid dynamics for the DF:

$$\frac{\partial f}{\partial t} + \frac{\partial}{\partial V}(f\dot{V}) = 0, \quad (1.24)$$

where V is a six-dimensional volume element in phase-space $V \equiv (\vec{r}, \vec{v})$. We can rewrite the second term on the left side of the equation as

$$\frac{\partial}{\partial \vec{r}}(f\dot{\vec{r}}) + \frac{\partial}{\partial \vec{v}}(f\dot{\vec{v}}), \quad (1.25)$$

and apply the Hamiltonian equations:

$$\frac{\partial}{\partial \vec{r}} \left(f \frac{\partial H}{\partial \vec{v}} \right) + \frac{\partial}{\partial \vec{v}} \left(f \left(-\frac{\partial H}{\partial \vec{r}} \right) \right) = \quad (1.26)$$

$$\frac{\partial^2 H}{\partial \vec{r} \partial \vec{v}} f + \frac{\partial H}{\partial \vec{v}} \frac{\partial f}{\partial \vec{r}} - \frac{\partial^2 H}{\partial \vec{v} \partial \vec{r}} f - \frac{\partial H}{\partial \vec{r}} \frac{\partial f}{\partial \vec{v}} = \quad (1.27)$$

$$\frac{\partial H}{\partial \vec{v}} \frac{\partial f}{\partial \vec{r}} - \frac{\partial H}{\partial \vec{r}} \frac{\partial f}{\partial \vec{v}}, \quad (1.28)$$

where in the last line we made use of the equality $\frac{\partial^2 H}{\partial \vec{r} \partial \vec{v}} = \frac{\partial^2 H}{\partial \vec{v} \partial \vec{r}}$. Substituting in the Hamiltonian for a gravitational system, $H = 1/2\vec{v}^2 + \phi$, and plugging everything back into Equation 1.24, we derive the collisionless Boltzmann equation (CBE):

$$\frac{\partial f}{\partial t} + \vec{v} \nabla f - \nabla \phi \frac{\partial f}{\partial \vec{v}} = 0, \quad (1.29)$$

where we use the nabla operator $\nabla = \partial/\partial \vec{r}$ for the sake of convention. We can use Poisson's equation to relate everything to an underlying mass distribution, the mass density ρ :

$$\nabla^2 \phi = 4\pi\rho. \quad (1.30)$$

Knowing the DF, we can compute essentially any observable of an ETG by integrating over different regions of phase-space. For instance, we can derived the LOSVD at a LOS through some (x_i, y_i) along z ,

$$\mathcal{L}(x_i, y_i, v_z, t) = \int f(\vec{r}_i, \vec{v}_i, t) dv_x dv_y dz, \quad (1.31)$$

and the phase-space density,

$$\nu(\vec{r}, t) = \int f(\vec{r}, \vec{v}, t) d^3v. \quad (1.32)$$

This density can be normalized to the total luminosity of a galaxy, which makes it essentially equal to a luminosity density. Multiplying this with a mass-to-light ratio Υ for the stars yields a stellar mass density $\rho_\star = \Upsilon \times \nu$, which we plug into the Poisson equation (see Equation 1.30) to derive a gravitational potential. As such, Equations 1.24 - 1.32 represent a self-consistent set of equations which we can solve for f to fit the kinematics of an ETGs. However, real galaxies *are not self-consistent*. To fully describe ETGs, a model for the dark matter (DM) halo and a central SMBH point-mass are also needed:

$$\rho(\vec{r}) = \rho_\star(\vec{r}) + M_{\text{BH}}\delta(\vec{r}) + \rho_{\text{DM}}(\vec{r}). \quad (1.33)$$

Hence, we need to try out different model-mass potentials to find the one which can best fit the data of an ETG.

Jean's equations

One way to approach this issue is by approximation: Instead of determining the DF itself, one can make use of the so-called Jean's⁸ equations.

In order to derive the Jean's equations, we will consider the CBE (see Equation 1.29) for different axes x_i (with x_i being the x,y, or z-axis) and derive the zeroth and first order moments of the equation. This means we take the integral $\int(\text{CBE})d^3v$ (zeroth order) and

⁸The name is derived from the fact that James H. Jeans was the first to apply these equations to stellar dynamics (Jeans, 1919)

$\int v_j \times (\text{CBE}) dv^3$ (first order). A summary of the calculation of these integrals can be found in Binney and Tremaine (2008, Equation 4.204 - 4.209). The zeroth order is

$$\frac{\partial \nu}{\partial t} + \frac{\partial(\nu \bar{v}_i)}{\partial x_i} = 0, \quad (1.34)$$

which is once again an analogue of the continuity equation from fluid dynamics, where $\bar{v}_i = 1/\nu \int v_i f d^3v$. Similarly, the first order,

$$\nu \frac{\partial \bar{v}_j}{\partial t} - \nu \bar{v}_i \frac{\partial v_j}{\partial x_i} = -\nu \frac{\partial \phi}{\partial x_j} - \frac{\partial(\nu \sigma_{ij}^2)}{\partial x_i}, \quad (1.35)$$

is akin to Euler's equation of fluid flow, where $\sigma_{ij}^2 = \overline{v_i v_j} - \bar{v}_i \cdot \bar{v}_j$ is the velocity dispersion tensor, which characterizes the stress applied to the stellar motions via the stress tensor $-\nu \sigma_{ij}^2$.

The Jeans modeling technique, and its most popular implementation, Jeans anisotropic modeling (JAM; Cappellari et al., 2007; Cappellari, 2008), consists of using galaxy images to constrain ν , and then fit the observed stellar kinematics by solving the Jeans equations, Equations (1.34 and 1.35) for the different axes, x , y and z .

However, the method is dependent on making assumptions about the intrinsic geometry of a galaxy, because there are more parameters than equations (three x_i plus six σ_{ij} equals nine parameters versus four Jeans equations). More importantly, since this method is not based on recovering the DF, the solutions to the Jeans equations *need not be physical*.

The majority of existing dynamical models of ETGs are currently based on this technique – with the shortcomings described above. Throughout this study, however, I use the Schwarzschild orbit modeling technique, which is less dependent on geometric assumptions and only produces *physical* solutions since it recovers the DF.

Schwarzschild orbit modeling

In the following I only consider ETGs which are steady-state systems, so that $\partial f / \partial t = 0$ and $f \equiv f(\vec{r}, \vec{v})$. The Schwarzschild orbit modeling technique rests on two fundamental theorems governing steady-state systems, the Jean's theorem and the time-averages theorem.

Jean's theorem states that for steady-state systems, all trajectories through phase-space are fully described by integrals of motion I_n . Along these trajectories *the phase-space density is constant*. Such trajectories are orbits. This means that the DF f depends on \vec{r} and \vec{v} only via I_n , and that the DF is a superposition of orbits:

$$f(\vec{r}, \vec{v}) \rightarrow f(I_1, I_2, \dots, I_n) \approx \sum_i f_i \delta(I_1 - I_{1,i}) \delta(I_2 - I_{2,i}) \dots \delta(I_n - I_{n,i}), \quad (1.36)$$

where f_i and $I_{n,i}$ are constant density phase-space contributions and integrals of motion of individual orbits i . Schwarzschild (1979) showed that superpositions of orbits from sampling sets of I_n can indeed be used to construct steady-state, model-galaxy configurations which are solutions to the CBE. Therefore, we can find a good approximation of the DF of

a stationary galaxy of any shape by modeling the evolution of tens of *thousands* of orbits, instead of the motions of hundreds of *billions* of individual stars. This is well within the realm of computational feasibility and laid the foundations for the Schwarzschild modeling technique.

The basic idea is to sample the DF f by launching enough orbits (I_1, I_2, \dots, I_n) in a model potential (generated by a model mass distribution ρ) to sufficiently fill out the phase-space (plausibly) covered by a galaxy. The galaxy is segmented into spatial cells K_j . Most orbits evolve in phase-space. Thus, orbits need to be modelled sufficiently long, i.e. over enough time steps Δt , that they show their regularity. As orbits move around in phase-space we record the fractions of time Δt_j they spend in each cell K_j . For a steady-state system one can take advantage of the so-called time-average theorem:

$$\frac{dV}{V} = \frac{dt}{T}, \quad (1.37)$$

where V is the total six dimensional phase-space volume covered by an orbit and T the time integration period. Since all observable properties of a system governed by a DF f are simply integrals along different sub-volumes in phase-space (see e.g. Equations 1.31 and 1.32), we can sum up the amount of time spent by all generated orbits in some cell K_j as a fraction of T to determine the amount of light of the galaxy associated with K_j . Similarly, by storing all local orbital velocities \vec{v}_i weighted by their fractional time spend in K_j , we can generate the intrinsic velocity distribution in K_j . From this, internal kinematic properties like the velocity anisotropy parameter β (see Equation 1.7) can be derived. Projecting the intrinsic velocity distributions along the line of sight yields model-LOSVDs. Thus, we can optimise the mass model (as described in Equation 1.33) by iteratively formulating different mass models, generating orbits (I_1, I_2, \dots, I_n) for the corresponding potential until we have densely filled out the phase-space of the galaxy (see below) and then fitting the observed LOSVDs of an ETG with model LOSVDs, minimizing

$$\chi^2 = \sum_z \sum_i \frac{(\mathcal{L}^{\text{obs}}(x_i, y_i, v_{\text{los}} \equiv v_z) - \mathcal{L}^{\text{model}}(x_i, y_i, v_z))^2}{\Delta \mathcal{L}^{\text{obs}}(x_i, y_i, v_{\text{los}})^2}, \quad (1.38)$$

where $\mathcal{L}^{\text{obs}}(x_i, y_i, v_{\text{los}})$ and $\Delta \mathcal{L}^{\text{obs}}(x_i, y_i, v_{\text{los}})$ are the observed LOSVD with statistical uncertainties at (x_i, y_i) on the plane of the sky, the z -axis of the model is pointing along the LOS, and $\mathcal{L}^{\text{model}}$ are the LOSVDs of the tested-for mass/orbit model. We improve this approach by adopting the model-selection approach of Thomas and Lipka (2022). Analogously to what is discussed in Equation 1.19, we minimize $\text{AIC}_p = \chi^2 + 2 \times m_{\text{eff}}$ ⁹. Selecting best-fit models in terms of minimum AIC_p allows for a more unbiased recovery of the mass model (Lipka and Thomas, 2021; de Nicola et al., 2022; Neureiter et al., 2023a). As for the mass-model parameterization (see Equation 1.33), the most common approach

⁹For Mehrgan et al. (2019), which I present in Chapter 2, this method was not yet available, neither for the determination of kinematics nor dynamic modeling. However, I use this method for Mehrgan et al. (2023a), as well as for the dynamical models presented in Mehrgan et al. (in press 2023b) (Chapters 3 and 4, respectively)

today is to use a spherical or generalized Navarro-Frenk-White profile from cosmological N-body simulations by Navarro et al. (1996) and Zhao (1996), for the DM-profile ρ_{DM} . More details are given in Chapter 2. The generalized profile is determined by three parameters, the DM density at 10 kpc, ρ_{10} , a scale radius r_s and a power-law slope γ of the distribution. As for the stellar mass density $\rho_\star = \Upsilon \times \nu$ (see Equation 1.32)), until recently a single constant stellar mass-to-light ratio Υ for an entire galaxy was used for almost all dynamical models in the literature. However, in Mehrgan et al. (in press 2023b, see Chapter 4), I present new Schwarzschild models which utilize spatially variable $\Upsilon(r)$. Nonetheless, together with the mass of the central SMBH, M_{BH} , the typical mass-profile determination thus entails the optimization of up-to around five model-parameters, depending on the approach.

In the simplest case, a spherical potential, the integrals of motions are simply the total energy E and angular momentum \vec{L} . Early on spherical Schwarzschild models have been used to fit the LOSVDs of a number ETGs (e.g. Richstone and Tremaine, 1984; Rix et al., 1997). With improving computational capabilities, more generalized, axisymmetric Schwarzschild modeling became feasible (Richstone and Tremaine, 1988; Gebhardt et al., 2003; Thomas et al., 2004; Siopis et al., 2009). Axisymmetric potentials support three integrals of motion, E , L_z and I_3 . I_3 is a non-classical integral which cannot be determined analytically. However, it can be sampled implicitly, by explicitly modeling initial orbital conditions (see below). Triaxial potentials are even more difficult: Here orbits are described by only one classical integral of motion E , but two non-classical integrals I_2 and I_3 . Nonetheless, Triaxial Schwarzschild models are also now available (e.g. van den Bosch et al., 2008; Neureiter et al., 2021; Quenneville et al., 2022; Liepold et al., 2023). We see here a steady progression towards describing real ETGs as accurately as possible. However, triaxial Schwarzschild modeling is still computationally very challenging, and it is not feasible to model larger samples of galaxies in this way. Instead, it is more suited for extended analysis of individual ETGs. Therefore, I here use axisymmetric Schwarzschild models. Axisymmetric Schwarzschild models may be a robust approximation even for triaxial galaxies. The best example of this is the determination of the SMBH mass of M87 by Gebhardt and Thomas (2009) using axisymmetric Schwarzschild modeling, $M_{\text{BH}} = (6.4 \pm 0.4) \times 10^9 M_\odot$, which was later confirmed by direct imaging of the shadow of the SMBH by observations with the Event Horizon telescope ($M_{\text{BH}} = (6.5 \pm 0.8) \times 10^9 M_\odot$, Event Horizon Telescope Collaboration et al. 2019).

Sampling integrals of motion

In Chapters 2 and 3, I make use of the axisymmetric Schwarzschild modeling approach of Thomas et al. (2004). Therefore, I briefly outline how (E, L_z, I_3) are sampled in this approach. Further details can also be found in Richstone and Tremaine (1988); Gebhardt et al. (2003); Siopis et al. (2009).

In an axisymmetric potential $\phi = \phi(r, \theta)$, we can reduce the 3D motions of stars to 2D motions – orbits are generated in the meridional plane and later “smeared out” over the azimuth angle $\psi \in [0, 2\pi]$. In this approach, the motion of a star on an orbit with energy

E , and angular momentum L_z can be described by

$$E = H = \frac{1}{2}(v_\theta^2 + v_r^2 + \frac{L_z^2}{r^2 \cos^2 \theta}) + \phi(r, \theta). \quad (1.39)$$

From any position in four dimensional phase-space \vec{w} , the trajectory through phase-space can be calculated using the Hamiltonian equations and integrating the next step of the trajectory from \vec{w} at time t to \vec{w}' at $t' = t + \Delta t$ with a fourth-order Runge-Kutta integrator. In this manner we launch orbits in a fixed $\phi(r, \theta)$ and follow them for 80 crossings with the equatorial plane (Thomas et al., 2004). At a given (E, L_z) each orbital trajectory is determined by a set of four launch-parameters $(r, \theta, v_r, v_\theta)$. By necessity, every regular orbit in the potential is fully described by the integrals of motion (E, L_z, I_3) . Therefore, we sample (E, L_z, I_3) *indirectly*, by sampling sets of (E, L_z) , and generating orbits for each set with different launch-parameters $(r, \theta, v_r, v_\theta)$. Thus the dynamical problem reduces to finding the right sets of these four parameters at each (E, L_z) to map out the phase-space covered by the galaxy (i.e. the DF) with orbits.

The sampling of (E, L_z) is straight forward. For every radius r_i and r_j with $r_i > r_j$ on the equatorial plane, there is at least one equatorial orbit (E, L_z) that has these radii as its apocenter and pericenter, $r_{apo} = r_i$, and $r_{peri} = r_j$. Hence, we iterate through pairs of grid values (r_i, r_j) to derive a sufficiently dense sampling of (E, L_z) .

For any given (E, L_z) , all possible orbit trajectories are bounded by the so-called zero-velocity-curve (ZVC), along which $v_\theta = v_r = 0$, $E = L_z^2/(2r^2 \cos^2 \theta) + \phi(r, \theta)$. The ZVC at every (E, L_z) determines the boundary between physically permitted and forbidden regions for trajectories. Except for circular orbits in the equatorial plane, all orbits touch the ZVC at least twice. This is illustrated in Figure 1.10. Any orbit that goes over the equatorial plane touches the ZVC, turns around, and punches through the equatorial plane, touches the ZVC on the other side, punches back up through the equatorial plane and so on. As the orbit evolves, there can be many impacts on the equatorial plane. If for each impact, the radius r on the equatorial plane and radial velocity v_r of the equatorial crossing are stored and plotted on a (r, v_r) diagram, orbits generate characteristic “invariant curves” on the this surface-of-section (SOS). I show an example SOS for an orbit model in Figure 1.11. For astrophysically relevant cases of axisymmetric potentials, the SOS encompasses all possible orbit shapes with a given (E, L_z) . Thus, a (indirect) sampling of I_3 that is dense enough to be representative of the sub-volume of the DF associated with this (E, L_z) , should densely fill out the SOS (bounded by the maximum r and v_r at this E and L_z) with imprints.

For each (E, L_z) , we launch orbits from the ZVC at the intersections of the meridional rays of the modeling grid with the ZVC, thereby determining r and θ of the launches. Per the definition of the ZVC, the velocities at these points, $v_r = v_\theta = 0$. We therefore start the orbits from their turning-points, and store the resulting imprints on the SOS. In the next step, we determine the most sparsely filled region on the SOS, and launch the next orbit from the SOS coordinates $(r_i, v_{r,i})$, that are the most distant from all invariant curves which were produced so far. Since these orbits are launched from the equatorial

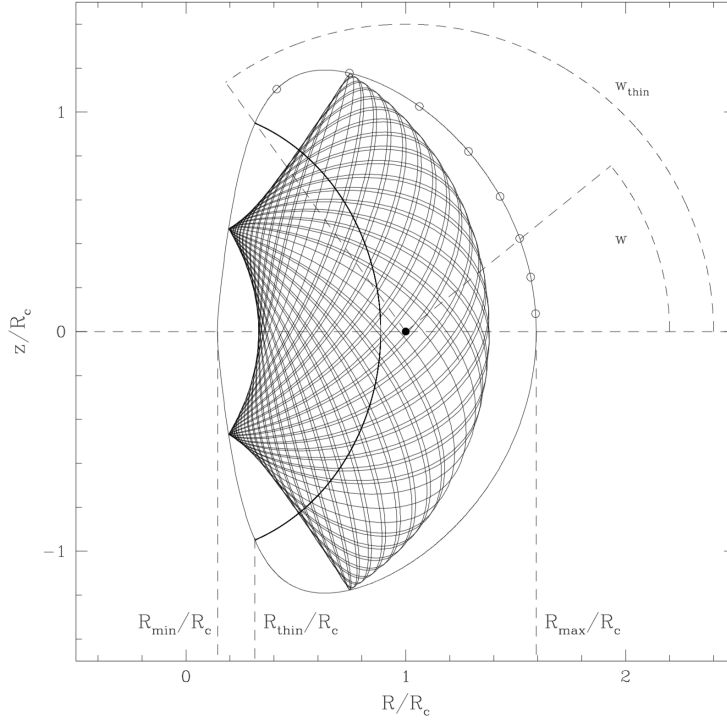


Figure 1.10: Example of the zero-velocity-curve (ZVC, black vertical oval shape). The ZVC is shown for a pair (E, L_z) , which produces an equatorial circular orbit with radius R_c . The z -axis is perpendicular to the equatorial plane. The circular orbit (black dot) does not touch the ZVC. Open circles on the ZVC show possible intercepts of orbits with the ZVC, which are characterized by different angles. Two orbits are shown, an evolving orbit at the intercept angle w which hits the ZVC at four different points and one at w_{thin} , a so-called thin-tube orbit which intercepts with the ZVC only at two locations. This Figure is taken from Cretton et al. (1999).

plane $\theta = 0$. v_θ at each launch-point is determined from the other coordinates:

$$v_{\theta,i} = \sqrt{2(E - \phi(r_i, 0)) - \frac{L_z^2}{r_i^2} - v_{r,i}^2}. \quad (1.40)$$

The new imprints generated by this orbit are again stored on the SOS, and this process is repeated iteratively until the SOS is representatively sampled. By doing this for each (E, L_z) , the full set of (E, L_z, I_3) is sampled sufficiently dense to produce a complete DF. The generated orbit library is then used to fit the data-LOSVDs. For each mass-model a full orbit library is generated in the manner outlined above. Mass models are then optimized with respect to the fits to the LOSVDs (see Equation 1.38).

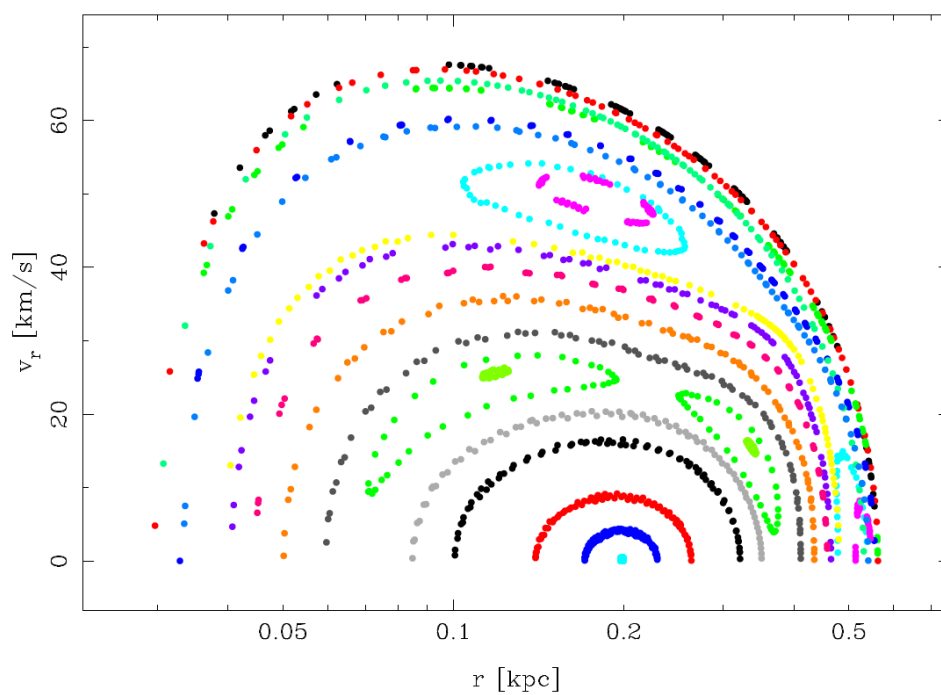


Figure 1.11: Example of surface-of-section (SOS) for a simple orbit-model. Every same-colored imprint belongs to the same orbit. This image is taken from Thomas et al. (2004).

1.3 The stellar initial mass function (IMF)

One of the fundamental uncertainties in our understanding of ETGs is the separation of the mass contributions of stars from those of DM to the total galaxy potential. Not knowing the amount of mass associated with stellar populations in galaxies, we cannot directly probe DM matter halos on spatial scales on the order of r_e (e.g. Cappellari et al., 2007; Thomas et al., 2011; Rusli et al., 2013a), and we are missing a critical piece in our understanding of galaxy formation and evolution. The difficulty is that we a) do not know how many stars in a galaxy have become remnants over the course of the evolutionary history of the galaxy, and b) we cannot fully constrain the amount of low luminosity dwarf stars. Both these types of objects carry a significant portion of the galactic stellar mass, but contribute little or no observable light.

Salpeter (1955) analyzed star counts of nearby stellar populations and found that the associated distribution function $\psi(L)$ roughly corresponds to a two-part power-law: At lower stellar luminosities star counts fall slowly with luminosity, with fainter stars being more numerous, while at luminosities brighter than a limiting luminosity L_{limit} , star counts fall much more rapidly with brightness, with the power-law slope of the distribution function becoming roughly three times as steep. The point of slope change corresponds to the beginning of the magnitude range of stars on the giant branch. The diagram was interpreted as a scenario in which luminous main-sequence stars towards brighter luminosities, past L_{limit} , reach a point where more and more stars had time to burn through the hydrogen in their cores, leave the main sequence, and enter their giant phase. Of these, a fraction growing with luminosity have turned into remnants, leaving the graph all together, as they “go dark”. This causes a steeper falling off of the star counts towards brighter luminosities. To investigate the stellar evolution history implied in this graph, Salpeter constructed a function termed the “original mass function”, later known as the stellar initial mass function (IMF). This function is introduced as the probability function of forming stars within different stellar mass M_\star -intervals underlying all star formation events which produced the observed stellar populations, which he connected to the local luminosity function:

$$\log \psi(L, M_\star) = \begin{cases} \log(\eta(L, M_\star)) - \log(M_\star/L \cdot L_{\text{limit}}/M_{\star, \text{limit}}) & \text{if } L > L_{\text{limit}} \\ \log(\eta(L, M_\star)) & \text{if } L < L_{\text{limit}}, \end{cases} \quad (1.41)$$

where,

$$\log(\eta(L, M_\star)) \propto \text{IMF}(M_\star) \cdot \frac{d \log(M_\star)}{d \log(L)}, \quad (1.42)$$

describes the “original luminosity function”. Inspecting these equations we can see that the IMF is ultimately the driving factor of the local observed stellar luminosity distribution, with the right hand term on the right side of Equation 1.41 for $L > L_{\text{limit}}$ removing stars which have since the time from birth to today “gone dark”. Using the local star counts from the Milky Way (MW), Salpeter found that between $0.5M_\odot$ and $100M_\odot$, the IMF can be described by a single power law with slope $x = 2.3$ (see Figure 1.12). Using this IMF, Salpeter estimated that the amount of stellar mass converted to remnants (which he had

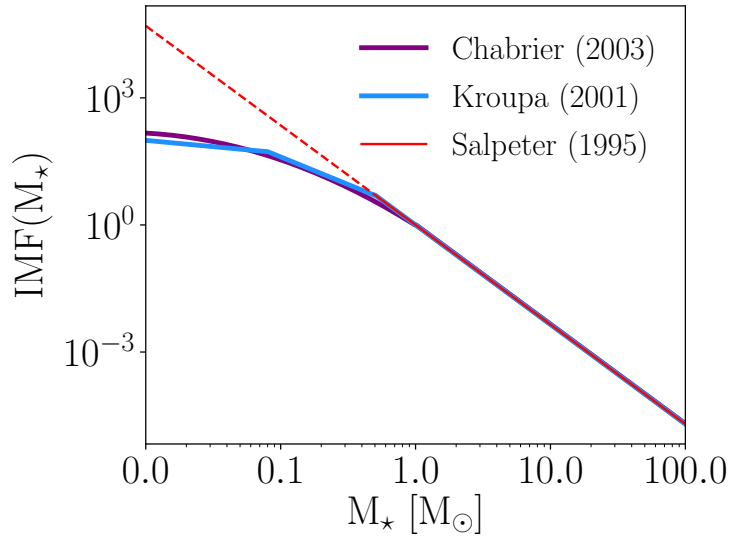


Figure 1.12: Stellar initial mass function (IMF) derived from local star counts by Salpeter (1955); Kroupa (2001); Chabrier (2003).

erroneously assumed to be made up entirely of gas) was of the order of the total stellar mass observed in today’s stellar population.

The seminal works of Kroupa (2001) and Chabrier (2003) have expanded the analysis of local star counts, particularly to low-mass dwarfs, and found that the Galactic IMF breaks at least two times for masses smaller than $0.5M_{\odot}$ into a multi-component power-law while remaining consistent with a single-slope Salpeter IMF above this stellar mass (see Figure 1.12). The net-effect of this modification of the Salpeter IMF is that the Kroupa and Chabrier IMFs reduce the number of low-luminosity dwarf stars. The distribution of low luminosity dwarfs essentially remains unchanged from the IMF, as these stars are longer-lived than the typical age of galaxies. Therefore the slope modification drives down the stellar mass-to-light ratio Υ of the stellar population.

In recent years, numerous studies have found stellar distributions consistent with a Kroupa or Chabrier IMF across multiple differing environments (in terms of age, metallicity, star formation, galactocentric distance, etc.) in the MW (Kroupa, 2002; Bastian et al., 2010). It is important to note that stars from the low-mass and high-mass ends of the IMF cannot be counted simultaneously for the same stellar population – giant stars turn into remnants on time-scales which are generally shorter than the formation time of dwarf stars. This means that the proposed MW IMF is a patchwork of IMF slopes in different mass-intervals derived from several differently aged stellar populations.

Nonetheless, these findings raise the question if the IMF – i.e. the way in which stars of different masses are produced in star formation events, which has been linked to the competitive interplay of gravito-turbulent fragmentation and radiation feedback in collapsing molecular clouds (Hennebelle and Chabrier, 2008; Krumholz, 2011; Hopkins, 2012) – is *universal* to all stellar populations and all galaxies.

An increased presence of either low luminosity dwarf stars or remnants increases the stellar mass-to-light ratio Υ and vice versa. Knowledge of the IMF can uncover the exact shape of DM profiles of galaxies on scales of r_e : One can use measurements of the age and metallicity of a galaxy’s stellar population to determine the stellar mass-to-light ratio that the population would have for a certain IMF, Υ_{IMF} . Using Υ_{IMF} one can determine the stellar mass of the galaxy, $M_\star = L_{galaxy} \times \Upsilon_{IMF}$. From the point-of-view of galaxy dynamics, outside the SOI of the central SMBH, the DM mass profile would become the only unaccounted for driver of the observed stellar motions. Schwarzschild dynamical models of ETGs with one less model parameter and the most crucial mass-degeneracy broken, could be used to determine very accurate DM profiles within r_e , even non-parametrically. Furthermore, the IMF informs essentially every part of galaxy evolution in addition to stellar mass, such as star formation rates, stellar feedback, and heavy element production (e.g. Kennicutt, 1998; Bastian et al., 2010).

Henceforth, I use the terms “Kroupa IMF”, “Chabrier IMF” and “MW IMF” interchangeably as is common practice in the field of galaxy evolution.

1.3.1 IMF probes of other galaxies

Individual star counts, as done in the MW, the Large and Small Magellanic Clouds, and other dwarf galaxies, are infeasible in distant galaxies. There, the stellar populations are *unresolved*. Hence, different methods have to be used to extract the IMF information from the observed stellar light.

Constraints on the shape of the IMF in distant galaxies can be derived from observations of the photoionization properties of stellar populations in star-forming regions. This entails measuring the luminosity of H α emission lines. Excluding AGNs, H α emission is produced solely by massive, hot O and B stars, which are in any case short-lived. This means that H α is directly tied to averaged star formation rates and the high-mass ($M_\star > 1M_\odot$) slope of the IMF. Kennicutt (1983) showed that different underlying IMFs distinguish themselves on the galaxy color – $\log(\text{H}\alpha\text{EW})$ plane, where H α EW is the equivalent width of the observed H α emission. Large surveys of galaxies using this method by Hoversten and Glazebrook (2008) and Gunawardhana et al. (2011), comparing $\log(\text{H}\alpha\text{EW})$ to $g - r$ color, have found that the IMF($M_\star > 1M_\odot$) is only Salpeter/Kroupa-like for galaxies of similar mass as the MW, but shallower for more massive galaxies (producing more giants/remnants) and steeper (producing less giants/remnants) for less massive galaxies. The main disadvantage of this method, besides modeling assumptions about the galaxy star formation history, is that it only applies to LTGs and other less massive galaxies with disks. It cannot provide constraints on the high-mass end of the IMF of gas-free massive ETGs.

The two dominant techniques that have established themselves for probing massive ETGs are stellar population modeling and measurements of the (enclosed) galactic mass, via stellar dynamics and lensing:

Stellar population modeling: Stellar population modeling (e.g. Vazdekis et al., 1996; Maraston, 1998; Thomas et al., 2003; Vazdekis et al., 2012; Ricciardelli et al., 2012; La Barbera et al., 2013; Spiniello et al., 2014; Conroy, 2013; Conroy et al., 2018; Maraston

et al., 2020) avoids the issue of deconvolving luminous and dark matter along the LOS by modeling the stellar spectral features of galaxies. Here, IMF probes entail an analysis of absorption features which are sensitive to the surface gravity of stars and thus can be used to determine the ratio of dwarf-to-giant stars in the stellar population, which constrains the slope of the IMF at low masses. The most commonly used spectral features here are the Na I doublet at 8190 Å, the TiO feature at 8860 Å, as well as FeH, or the so-called Wingford-band at 9916 Å. Increasing line strengths of these features are associated with larger amounts of dwarf stars. Such spectral indices are fitted individually, or as part of full spectral fitting, with model-spectra from single stellar population (SSPs) synthesis libraries, whereby the IMF, as well as the age of the stellar population, metallicity, star formation history, dust, gas etc. are fit-parameters changing the shape of the model spectra. From the best-fit model a stellar mass-to-light ratio Υ^{SSP} can be derived. One important drawback of this method is that it can only probe the low-mass end of the IMF in ETGs, as without replenishment from star formation, most stars on the high-mass end of the distribution have turned into remnants by the time of observation, becoming invisible to stellar population models.

Stellar dynamics & lensing: Both stellar dynamics and gravitational lensing can be used to constrain the total mass-to-light ratio M^{tot}/L within some aperture. In particular advantageous circumstances one may even combine both stellar dynamical modeling and lensing for stronger constraints on M^{tot}/L . The issue is that these types of probes – measurements of the gravitational potential of a galaxy – do not in principle distinguish between mass contributions from stars, the DM halo and central SMBH, which may all be lined up along the line of sight. As described in the previous section (see Equation 1.33), the mass decomposition of dynamical models is the result of model assumptions, such as that DM does not follow the stars, or that it has the profile-shape of a generalized NFW halo. Υ^{dyn} , the dynamical stellar mass-to-light ratio, is always determined relative to a particular DM-model. The same is true of gravitational lensing, which only maps lensing arcs and shears onto enclosed mass according to general relativity. To derive Υ^{lens} , a DM model has to be subtracted. Typically, for probes of the stellar mass-to-light ratio, using these gravitational measurements, one tries to focus on the centers of galaxies within r_e , as here the mass-contribution of the DM component is drowned out by the stars. Though within the SOI of the central SMBH, the stellar mass becomes more difficult to separate from M_{BH} . What these gravitational measurements can in any case do, is to provide upper limits for Υ , which can be used to exclude IMFs which would produce Υ in excess of M^{tot}/L , i.e to exclude IMFs which would produce such a high amount of dwarfs or remnants that the mass of the galaxy would not be compatible with the measured gravitational potential. Furthermore, unlike SSP probes, these probes can still measure stars which have turned into remnants. Thus, they can also probe the high-mass end of the IMF, even at the same time as the low-mass end, though without the possibility of separating the two based on dynamics alone.

For both approaches, it is useful to characterise the IMF probes by a mass normalization factor α of the stellar mass-to-light ratio relative to a reference $\Upsilon_{ref}^{\text{SSP}}$ with a reference IMF, $\alpha \equiv \Upsilon/\Upsilon_{ref}^{\text{SSP}}$. Typically the reference value is taken for a Kroupa or Salpeter IMF,

depending on the study. I here use a Kroupa IMF, Υ_{Kroupa}^{SSP} as reference and transform all mass normalization factors from the various studies, according to $\Upsilon_{Salpeter}^{SSP}/\Upsilon_{Kroupa}^{SSP} = 1.55$.

Galaxy-by-galaxy variation of the IMF

Different methods, including those described above, have found that most LTGs are not consistent with a mass-normalization significantly above a MW IMF (de Jong and Bell, 2001; Kassin et al., 2006; Bershadsky et al., 2011; Brewer et al., 2012) in agreement with the proposed IMF universality. By contrast, even dynamical probes of ETGs which did not include any model for the DM component (de Zeeuw et al., 2002; Emsellem et al., 2004; Cappellari et al., 2007) found $(M/L)^{dyn}$ to vary relative to a Kroupa IMF Υ_{Kroupa}^{SSP} , indicating that either the IMF or DM halo-shapes varied from galaxy to galaxy.

An important next step came with dynamical studies of Coma cluster galaxies (Thomas et al., 2007, 2009, 2011) and the BCG of Abell 262 (Wegner et al., 2012), as well as the SLACS survey (Treu et al., 2010; Auger et al., 2010). All of these studies used standard spherical NFW profiles for their halo models to disentangle the contribution of stars, Υ^{dyn} from DM. They found galaxy-by-galaxy variation of the mass normalization α , which also correlated with σ (see Figure 1.13). For most galaxies with $\sigma \gtrsim 250$ km/s, they found a Salpeter- or super-Salpeter level α . The measurements of the SLACS group were based on a combination of constraints from both dynamical models and gravitational lensing. However, their dynamical models only fitted a single central velocity dispersion σ from SDSS per galaxy and consisted of simple spherical Jeans models which assumed that the ETGs were fully isotropic. By contrast, Thomas et al. (2007, 2009, 2011) and Wegner et al. (2012) used axisymmetric Schwarzschild models to fit fourth order Gauss-Hermite LOSVDs from long-slit data along the galaxies' major and minor axes.

This was followed by the ATLAS^{3D} project Cappellari et al. (2012, 2013c,b), which analysed a large sample of 260 ETGs using the JAM modeling technique (Cappellari et al., 2007; Cappellari, 2008), which takes into account galaxy morphology more accurately than the spherical Jeans models of the SLACS group, by using velocity ellipsoids in cylindrical coordinates with variable anisotropy for modelling the stellar component. They also used 2D stellar kinematic constraints from integral field unit (IFU) observations covering the galaxies up to roughly r_e . On the other hand, JAM models like all methods based on the Jeans equations, do not recover galaxy DFs (see Section 1.2.2) and are therefore not necessarily physical. Furthermore, they only used simple Gaussian kinematics as input to their models (only v_{rot} and σ). Nonetheless, the ATLAS^{3D} project corroborated the results of previous IMF probes by also finding a trend of α with σ_e , with galaxies on average going from Kroupa-level to Salpeter-level and beyond with increasing σ_e (see Figure 1.13).

Later on, Posacki et al. (2015) updated the results of the SLACS group from spherical Jeans models to JAM modeling, bringing them to a similar standard as the ATLAS^{3D} galaxies with the goal of combining both data sets. The log-linear $\alpha - \sigma_e$ relation is overall steeper for the more massive SLACS galaxies. Both data sets together produce a parabola-like relation in logarithmic units with σ_e (see Figure 1.13), which has since become one of the standard reference points for galaxy-gravitational IMF probes of ETGs.

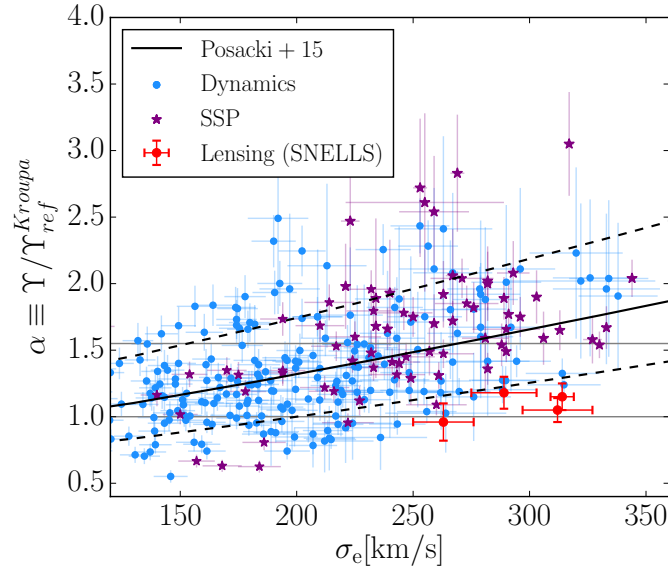


Figure 1.13: Mass normalization factor α relative to a Kroupa IMF against dispersion within r_e for stellar dynamics (from SLACS and ATLAS^{3D}, Posacki et al., 2015; Cappellari et al., 2013b), stellar population modeling (from Conroy and van Dokkum, 2012 and MASSIVE, Gu et al., 2022) and SNELLS lensing measurements (Smith et al., 2015; Newman et al., 2017). The $\alpha - \sigma_e$ relation from Posacki et al. (2015) (solid black curve), is shown with its 1σ uncertainties (dashed black curves). In the literature thus far, dynamics and SSP modeling seem to produce broadly consistent results whereas the SNELLS lensing measurements imply a different, more MW-like IMF trend in massive ETGs.

For massive ETGs which have dispersions $\sigma_e \gtrsim 250$ km/s, it predicts a mass normalization $\alpha \gtrsim 2$ above MW-level (with a statistical scatter of 0.12 dex). However, all dynamical measurements mentioned thus far (and the majority that exist in the literature) assumed that Υ is spatially constant in all ETGs. In Mehrgan et al. (in press 2023b, see Chapter 4), I show that if ETGs have intrinsic gradients of Υ with $\Upsilon(r)$ increasing towards the center, constant- Υ models overestimate the overall α of galaxies.

Efforts were made to narrow the fraction of the detected mass excess which was really DM, i.e. to determine if the apparent non-universality of the IMF was actually a non-universality of DM halos. All the studies above found only small DM matter fractions $\lesssim 20\%$ within r_e . Cappellari et al. (2013b) also tried generalized NFW halos with a variable central DM-density slope (Zhao, 1996), and found that their results were largely invariant against the DM-density slope (due to the low mass contribution of the halo, relative to the stars for all models). Lensing studies of massive ETGs found Salpeter or super-Salpeter α using generalized NFW models even for those galaxies where they found concentrated central DM cusps (e.g. Spiniello et al., 2011; Sonnenfeld et al., 2015; Oldham and Auger, 2018b). Notably, Sonnenfeld et al. (2019) studied a rare massive ETG with two concentric Einstein rings, which put stronger constraints on the inner shape of the DM

distribution and still found a Salpeter-level mass-normalization. Though it is unclear if generalized NFW halos, which the latter study also used, describe the true density profiles of DM halos.

At the same time as mass probes converged on a comprehensive picture of IMF variation, stellar population probes of the centers of ETGs also found similar trends of the IMF with σ_e (van Dokkum and Conroy, 2010, 2011, 2012; Smith et al., 2012; Conroy and van Dokkum, 2012; Conroy et al., 2014; Ferreras et al., 2013; La Barbera et al., 2013). This convergence can also be seen in Figure 1.13. Several studies furthermore found α to increase with [Mg/Fe] -enrichment, in addition to σ_e (e.g. Conroy and van Dokkum, 2012; Parikh et al., 2018). These stellar population studies necessarily focused on the low-mass end of the IMF, i.e. dwarfs, since they cannot detect the dark remnants of giant stars from the high-mass end of the IMF. However, in principle, above-Kroupa level mass normalizations for the dynamics and lensing based measurements could also originate from the IMF being different from a Kroupa IMF in a variety of different mass-intervals, e.g. the stellar mass could be driven up by black holes from a relative excess of higher-mass stars having turned into remnants. However, van Dokkum and Conroy (2010) showed that in many existing SSP measurements the mass excess above MW-level is driven by spectral signals of stars on the low-mass end, with low luminosity dwarf stars making up roughly 60 – 80% of the stellar mass. For this reason, referring to excesses of the mass-normalization above a Kroupa IMF as “bottom-heavy” has become ubiquitous in IMF studies. Nonetheless, in Chapter 4, I discuss the possibility of the “top-heaviness” of the IMF, i.e. the IMF producing more remnants than a Kroupa/Salpeter IMF.

Since the IMF probes of the Coma cluster, SLACS and ATLAS^{3D} projects have been published, more evidence from all three methods has been accumulated for the IMF becoming more bottom-heavy with ETG mass, including from the CALIFA survey (Lyubenova et al., 2016) which uses all three methods. Besides the correlation with mass and [Mg/Fe], the bottom-heaviness of the IMF has been found to correlate with metallicity (Martín-Navarro et al., 2015b; Li et al., 2017; van Dokkum et al., 2017; Parikh et al., 2018), and orbit structure (Poci et al., 2022).

1.3.2 IMF studies at a crossroads

Does this mean we can simply use the α trends above to estimate an ETG’s IMF based on its σ , [Mg/Fe], metallicity etc, and then derive a ready-made Υ ? As of yet, this is not the case, as a number of pertinent problems remain with this framework.

To begin with, the galaxy-to-galaxy scatter in these measurements is still quite considerable (also clearly visible in Figure 1.13). More significantly, IMF variation is under tension from recent lensing constraints, including strong lensing measurements which exclude above-MW-level α for several very massive galaxies with $\sigma > 250$ kms from the SNELLS and MNELLS surveys (Smith et al., 2015; Newman et al., 2017; Collier et al., 2018, 2020), as well as a survey of 23 massive lensed ETGs by Sonnenfeld et al. (2019). The SNELLS and MNELLS studies used DM-profiles of similar galaxies from the EAGLE cosmological simulation. On the scales which they probed with lensing, $\sim 1 - 2$ kpc, this

produced DM fractions of around 20%. Yet, even with no DM, i.e. absorbing all DM into the stellar mass-to-light Υ^{lens} , their measured $\langle \alpha \rangle \sim 1.3$ is well below the expected value $\alpha \gtrsim 2$ from the Posacki et al. (2015) relation. The SLACS lensing galaxies had smaller assumed DM fractions, and yet, even correcting for this difference, SLACS α -values do not go below Salpeter for galaxies in the SNELLS and MNELLS mass range. Either the SLACS galaxies have an even higher DM fraction than assumed for the SNELLS and MNELLS survey, or one, or both of the opposing studies are in some way biased.

A similar and more pressing tension comes from the fact that despite producing complementary overall trends, on the level of individual galaxies, the published stellar population measurements of α often do not agree with the stellar dynamical measurements – worse yet, they often do not even *correlate*, meaning that this is unlikely to be simply an effect of insufficient dynamic disentanglement of stars and DM (Smith, 2014; McDermid et al., 2014). This issue remains prevalent and thus far largely unresolved, suggesting that either stellar population, or dynamical/lensing methods, or both are biased in some way.

Davis and McDermid (2017) derived dynamical IMF probes from resolved gas kinematics of nuclear disks in ATLAS^{3D} galaxies and found that their gas-dynamical IMF probe was in agreement with their stellar dynamics, but not with their SSP models, suggesting the issue lying with the latter. They confirmed the presence of galaxy-to-galaxy variation of the IMF, but contrary to previous studies, could not correlate this variation with any dynamic or stellar population properties.

An exception to this issue is Zieleniewski et al. (2017), who measured α -values for four Coma cluster galaxies with SSP modeling. Their SSP modeling results were in agreement with published dynamical results. However, three of the four galaxies in this study pointed towards a MW IMF, despite these ETGs being in the high- σ range where previous studies suggested a bottom-heavy IMF.

Lyubenova et al. (2016) of the CALIFA project have suggested that the existing tensions between many dynamical and SSP measurements could at least be partially alleviated by correcting for aperture limitations, as apertures from stellar population modeling are often confined to small galactocentric radii $\sim r_e/8$, whereas dynamical models tend to cover more or all of the galaxy up to r_e . The aperture difference could be particularly relevant if galaxies have internal, radial gradients of the IMF. Indeed, Bernardi et al. (2018); Domínguez Sánchez et al. (2019) demonstrated that IMF gradients could – in theory – bridge the gap between the measurement differences.

Such internal gradients of the IMF are at least conceptually plausible. Internal gradients of increasing metallicity, age, color and starburst activity in ETGs have long been known. Meanwhile, the outskirts of ETGs are thought to originate from the accumulated stars from minor mergers and stripping of smaller galaxies. In such objects, star formation is less extreme and the IMF therefore expected to be MW-like, which existing IMF probes have also suggested. Consequently, if bottom-heaviness is measured in the center of an ETG, we expect galactocentric radial gradients of α converging on Kroupa towards r_e . The centers of ETGs are generally highly enriched in [Mg/Fe], which is typically associated with rapid starbursts. The correlation of [Mg/Fe] with α has so far also been found to be tighter than with σ_e . If the IMF is indeed different in the centers ETGs, this necessitates

that the conditions of the originating star formation events were different, too.

A number of studies have measured radial variation of α using stellar population models (Martín-Navarro et al., 2015a; van Dokkum et al., 2017; Parikh et al., 2018; La Barbera et al., 2019; Domínguez Sánchez et al., 2019). These studies suggest that IMF gradients are confined to spatial scales on the order of r_e , with the IMF being Kroupa-like at the largest radii and becoming increasingly bottom heavy with decreasing radius, with values up to $\alpha \sim 2.5$ in the very center.

Among the few dynamical and lensing studies of such gradients that exist, similar trends of the IMF with galactocentric radius have been found in the massive ETGs M87 (Oldham and Auger, 2018a; Li et al., 2020), the lensing galaxy ESO 325-G004 Collett et al. (2018), as well as for several lensing galaxies from the samples of Oldham and Auger (2018b) and Newman et al. (2015).

Nonetheless, the claim that intrinsic IMF gradients can indeed resolve the tension between different methods has not yet been demonstrated. In Chapter 4, I investigate this claim using axisymmetric Schwarzschild models with Υ -gradients.

1.4 Aims of this thesis

The hierarchical merger framework can convincingly explain many of the observed properties of ETGs, in particular the E-E dichotomy and the existence of shallow surface brightness cores. Nonetheless, there remain a number of important gaps in our understanding of the exact the mass compositions of ETGs and how these fit into the merger framework (see below). This thesis is concerned with addressing these issues using recent advancements in the measurement of non-parametric stellar kinematics and Schwarzschild dynamical modeling. These advances have been shown to be vital to break many known degeneracies of the dynamical mass decomposition of ETGs (Neureiter et al., 2021; Lipka and Thomas, 2021; de Nicola et al., 2022). The chapters of this thesis are focused on different components of the mass-decomposition of massive ETGs:

SMBHs and cores: The distribution of Quasar luminosities at the dawn of galaxy formation $z > 2$, as well as empirical scaling relations in the local universe suggest a distribution of SMBHs within 300 Mpc with only a dozen to few hundred of SMBHs with masses $> 10^{10} M_{\odot}$ (Lauer et al., 2007b; Rusli et al., 2013b) – so called “ultramassive” black holes (UMBHs). The large uncertainties reflect our poor understanding of the local SMBH mass-function. Empirical scaling relations between M_{BH} and core properties predict the most massive black holes in the largest and faintest cores, and that the core radius roughly corresponds to the SOI of the central SMBH. While these relations have enormous potential for the sampling of the local black hole mass function, their utility for targeting ETGs for their (predicted) M_{BH} had thus far not been tested. Here, I kinematically and dynamically analyse a massive ETG, Holm 15A, which was for the first time selected specifically for its extreme core properties, namely a 4 kpc large core which is the faintest core detected thus far, pointing to an exceptionally large SMBH. I also compare this galaxy’s complex orbit structure to state-of-the-art numerical merger simulations and establish two new SMBH-core scaling relations. This is presented in Chapter 2. The chapter was originally published in Mehrgan et al. (2019).

Stars & DM: The separation of the mass contributions of stars and DM in ETGs is difficult, as the stars have their own “dark” contributions in the form of low luminosity dwarf stars and remnants. The information about the distribution of these dark stellar components is contained in the IMF. Late-type and dwarf galaxies appear to be comprised of stars which were generated with the same, universal IMF. However, in dynamical models, massive ETGs are often consistent with IMFs which produce many more giant or dwarf stars (e.g. Posacki et al., 2015) Stellar population models seem to point in the same direction (e.g. Conroy and van Dokkum, 2012), but for individual galaxies the results from different methods are mostly contradictory (Smith, 2014; McDermid et al., 2014). A number of lensing measurements of massive ETGs also explicitly exclude the bottom-heavier IMFs which are claimed for massive ETGs (Smith et al., 2015; Newman et al., 2017; Collier et al., 2018, 2020). Thus far, trends of the IMF mass normalisation α from dynamics are mostly based on dynamical models which often a) do not determine the DF of the galaxies, i.e. are not necessarily physical, b) only use Gauss-Hermite or even just simple Gaussian parameterizations of the LOSVD instead of using the full non-parametric LOSVD, and c)

assume spatially constant stellar mass-to-light ratios Υ . Internal gradients of the IMF could potentially explain the mismatch between IMF probes from different methods (Bernardi et al., 2018; Domínguez Sánchez et al., 2019; Lyubenova et al., 2016). But this has not been systematically investigated in the literature. In Chapters 3 and 4, I analyse a sample of nine massive ETGs with the aim of measuring radial gradients of the Υ , and by extension, the IMF. Chapter 3 deals with the derivation of non-parametric kinematics for these ETGs using WINGFIT with the the AIC_p model selection approach of Thomas and Lipka (2022). This includes simulating many of the problems which plague most kinematic fitting and finding effective strategies of dealing with them. The chapter was published in Mehrgan et al. (2023a). In Mehrgan et al. (in press 2023b), presented in Chapter 4, I generate axisymmetric Schwarzschild dynamical models based on the non-parametric kinematics of seven of the galaxies. These models make use of the AIC_p model selection approach, and allow for gradients of the stellar mass-to-light ratio Υ in order to investigate for internal gradients of the IMF.

I summarize the results of this thesis in Chapter 5. There, I also provide an outlook for future investigations of the mass composition of massive ETGs in light of these results.

Chapter 2

A 40-billion solar mass black hole in the extreme core of Holm 15A, the central galaxy of Abell 85

Bibliographic information

Kianusch Mehrgan, Jens Thomas, Roberto Saglia, Ximena Mazzalay, Peter Erwin, Ralf Bender, Matthias Kluge, and Maximilian Fabricius – A 40 Billion Solar-mass Black Hole in the Extreme Core of Holm 15A, the Central Galaxy of Abell 85, 2019, ApJ, 887,2045.

DOI: [10.3847/1538-4357/ab5856](https://doi.org/10.3847/1538-4357/ab5856).

Author's contribution

As first author, I wrote all sections of this manuscript, with exception of Section 5.5 and Appendix C, which were written by Jens Thomas, and Appendix A.2 which was written by Peter Erwin. I generated all figures besides Figures 3, 16 and 17 (generated by Peter Erwin), and Figure 20 (generated by Jens Thomas). Jens Thomas provided important support to this work in the form of frequent discussions, ideas, and revisions of text. Roberto Saglia provided further valuable corrections and discussions. This project was based on MUSE observations of Holm 15A from ESO program 099.B-0193(A), P.I. Jens Thomas. Mathias Kluge provided Wendelstein Wide Field Imager photometry for this galaxy and all other BCGs whose light profiles are shown in the study. I performed the 1D analysis of the Wendelstein images, whereas Peter Erwin performed the 2D analysis. I performed the deprojection of the imaging data of the galaxy. Moreover, I reduced the MUSE observations from the the raw data to the final datacube and performed the full kinematic analysis with pPXF and our kinematic fitting code WINGFIT, which was not yet named at the time of the publication of the manuscript. FCQ comparison-kinematics were

produced by Ralf Bender. Based on the WINGFIT kinematic analysis, I generated the dynamical models of the galaxy using our group's axisymmetric Schwarzschild modeling code. Moreover, I derived the new core-scaling laws which we introduce in this study, $M_{BH} - \mu_{V,0}$ and $M_{BH} - \Sigma_0$, and compared our dynamical models of Holm 15A with the 1st and 2nd generation merger N-body simulations from Rantala et al. (2018, 2019). All authors provided feedback for the final version of the manuscript.

Copyright notice

©2019 ApJ

reprinted on pages 45 - 63.



A 40 Billion Solar-mass Black Hole in the Extreme Core of Holm 15A, the Central Galaxy of Abell 85

Kianusch Mehrgan^{1,2} , Jens Thomas^{1,2} , Roberto Saglia^{1,2} , Ximena Mazzalay^{1,2}, Peter Erwin^{1,2} , Ralf Bender^{1,2} ,
Matthias Kluge^{1,2} , and Maximilian Fabricius^{1,2}

¹ Max-Planck-Institut für extraterrestrische Physik, Giessenbachstrasse, D-85748 Garching, Germany; kmehrgan@mpe.mpg.de

² Universitäts-Sternwarte München, Scheinerstrasse 1, D-81679 München, Germany

Received 2019 July 24; revised 2019 November 13; accepted 2019 November 15; published 2019 December 19

Abstract

Holm 15A, the brightest cluster galaxy of the galaxy cluster Abell 85, has an ultradiffuse central region, ~ 2 mag fainter than the faintest depleted core of any early-type galaxy (ETG) that has been dynamically modeled in detail. We use orbit-based, axisymmetric Schwarzschild models to analyze the stellar kinematics of Holm 15A from new high-resolution, wide-field spectral observations obtained with the Multi-Unit Spectroscopic Explorer at the Very Large Telescope. We find a supermassive black hole with a mass of $(4.0 \pm 0.80) \times 10^{10} M_{\odot}$ at the center of Holm 15A. This is the most massive black hole with a direct dynamical detection in the local universe. We find that the distribution of stellar orbits is increasingly biased toward tangential motions inside the core. However, the tangential bias is less than that in other cored elliptical galaxies. We compare Holm 15A with N -body simulations of mergers between galaxies with black holes and find that the observed amount of tangential anisotropy and the shape of the light profile are consistent with a formation scenario where Holm 15A is the remnant of a merger between two ETGs with pre-existing depleted cores. We find that black hole masses in cored galaxies, including Holm 15A, scale inversely with the central stellar surface brightness and mass density. These correlations are independent of a specific parameterization of the light profile.

Unified Astronomy Thesaurus concepts: Galaxy bulges (578); Galaxy dynamics (591); Galaxy evolution (594); Galaxy formation (595); Galaxy kinematics (602); Galaxy mergers (608); Galaxy photometry (611); Galaxy mass distribution (606); Galaxy dark matter halos (1880); Orbits (1184); Supermassive black holes (1663); Scaling relations (2031)

1. Introduction

Holm 15A is the brightest cluster galaxy (BCG) of Abell 85. It is a very luminous ($M_V = -24.8$ mag; Kluge et al. 2019) early-type galaxy (ETG) with a high stellar mass of $M_{\star} \gtrsim 2 \times 10^{12} M_{\odot}$. The rotational velocity of Holm 15A is $v_{\text{rot}} \lesssim 40 \text{ km s}^{-1}$ and small compared to the velocity dispersion $\sigma \sim 350 \text{ km s}^{-1}$. This is very common among massive ETGs (e.g., Emsellem et al. 2011; Cappellari 2016; Veale et al. 2017). Despite its high overall luminosity, Holm 15A has one of the faintest known central regions of any massive galaxy.

Figure 1 compares Holm 15A’s observed light profile with Nuker models of the centers of cored ETGs from the Lauer et al. (2007a) sample, core-Sérsic models of cored ETGs with existing dynamical models from Rusli et al. (2013a) and Thomas et al. (2016), as well as nonparametric light profiles of BCGs from Kluge et al. (2019). Evidently, at radii $r \gtrsim 30$ kpc, Holm 15A’s surface-brightness profile is characterized by a local Sérsic index $n \gtrsim 4$, typical for massive ETGs and BCGs. Holm 15A is very bright though: only a handful of other BCGs have a higher surface brightness outside the central region ($r \gtrsim 5$ kpc).

It is all the more striking then how faint the center of Holm 15A is compared to ETGs from all three samples, BCG or not. Indeed, among the 88 core galaxies in the Lauer et al. (2007a) sample, the faintest center is still ~ 0.5 mag arcsec⁻² brighter than the center of Holm 15A. Among galaxies with detailed dynamical models, the difference is even larger: ~ 2 mag arcsec⁻² (Rusli et al. 2013b; Thomas et al. 2016; see Figure 1).

Such diffuse, shallow central surface-brightness regions are commonly referred to as “cores” and have been observed in massive ETGs for a long time (e.g., Kormendy 1985; Lauer 1985; Faber et al. 1987). As methods for the dynamical detection of supermassive black holes (SMBHs) of ETGs have grown more sophisticated in recent years, several tight scaling relations between core properties and central black holes have been established. In particular, the most massive black holes in the local universe are expected to be found in the centers of the largest, faintest cores (e.g., Faber et al. 1997; Lauer et al. 2007a; Kormendy & Ho 2013; Rusli et al. 2013a; Thomas et al. 2016).

The contemporary view of the formation of cores in massive ETGs is that their observed properties are best explained via so-called black hole binary “core scouring.” Core scouring is driven by the hardening of an SMBH binary naturally formed during dissipationless mergers between ETGs, which are thought to dominate the late growth processes of massive galaxies (e.g., Khochfar & Burkert 2003; Boylan-Kolchin et al. 2006; De Lucia et al. 2006; Naab et al. 2006; Oser et al. 2010). Gravitational slingshots eject stars on predominantly radial orbits from the center of the remnant galaxy, producing a cored central light profile (e.g., Begelman et al. 1980; Hills & Fullerton 1980; Ebisuzaki et al. 1991; Milosavljević & Merritt 2001; Volonteri et al. 2003; Trujillo et al. 2004; Merritt & Milosavljević 2005; Merritt 2006, 2013; Rusli et al. 2013a; Rantala et al. 2018). This core-formation channel can explain the fundamental characteristics of core galaxies: (1) the observed uniform tangentially biased orbit structure in cores (Milosavljević & Merritt 2001; Thomas et al. 2014; Rantala et al. 2018) and

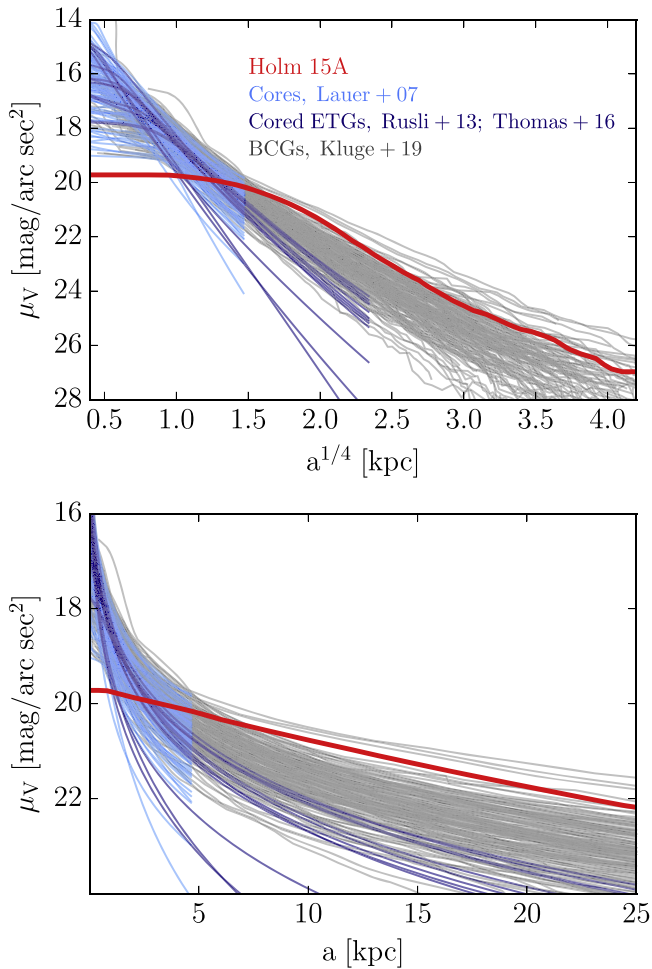


Figure 1. V-band surface-brightness profile of Holm 15A compared to the central 5 kpc of Nuker models of cored ETGs from Lauer et al. (2007a; light blue), core-Sérsic models of cored ETGs with dynamical SMBH detections from Rusli et al. (2013a) and Thomas et al. (2016; dark blue), as well as observed light profiles of the 170 local BCGs from Kluge et al. (2019; gray) over the major axis. Holm 15A’s light profile has been shifted from the g' band assuming $g - V = 0.45$ mag (Kluge et al. 2019), a K-correction of 0.13 mag, cosmological dimming of 0.23 mag, and a galactic extinction of $A_g = 0.125$ mag.

(2) the various core-specific scaling relations between the black hole mass, core size, size of the gravitational sphere of influence (SOI), and “missing” light compared to the inwards extrapolation of the steeper outer light profile (from which the core “breaks”; Lauer et al. 2007b; Kormendy & Bender 2009; Kormendy & Ho 2013; Rusli et al. 2013a; Thomas et al. 2016; Rantala et al. 2018).

From a radius of $r \sim 15$ kpc inwards down to the smallest resolved scales, the light profile of Holm 15A is almost exponential (lower panel of Figure 1). Bonfini et al. (2015) and Madrid & Donzelli (2016) interpreted this as evidence against a large core in Holm 15A. However, as Figure 1 shows, Holm 15A fits perfectly into the homology of cored BCGs/ETGs. Hopkins et al. (2009) suggested that nearly exponential surface-brightness profiles on kiloparsec scales could be ubiquitous among core galaxies as a relic of merger-induced star formation bursts in early evolutionary phases prior to the actual core formation. In their analysis, Hopkins et al. (2009) assumed that the SOI of the black hole binary is much smaller than the spatial scale relevant for these “extra-light” regions. In fact, their fits including exponential components often do not

well represent the actual core region. We now know that the sizes of the cores are almost identical to the SOI radii of the central black holes (Thomas et al. 2016). The core of Holm 15A has a size of 3–5 kpc (see Figure 1, Section 2, and also López-Cruz et al. 2014), on a similar scale to the previously largest known core in IC 1101, $r_b = 4.2$ kpc (Dullo et al. 2017). Hence, the expected SOI is so large that it interferes with the spatial scale of potential extra-light. The only other galaxy that seems to be dominated by a nearly exponential behavior in its entire inner region may be NGC 1600 (see Hopkins et al. 2009). NGC 1600 has a large SOI radius of 1.2 kpc as well. There are many processes that influence the final inner light profile of massive galaxies, like dynamical interactions between stars and the SMBH binary, early star formation episodes, active galactic nucleus (AGN) feedback, etc. While these processes have been studied individually (in different levels of detail; e.g., Merritt 2006; Hopkins et al. 2009; Teysier et al. 2011; Martizzi et al. 2012, 2013; Choi et al. 2018; Rantala et al. 2018, 2019), we currently lack simulations that include all these processes in a consistent manner. The black hole binary core-scouring process, which is likely dominant in core formation has now been studied in great detail, including the effects of different merger histories on the stellar density profile and stellar orbits in the core (Rantala et al. 2018, 2019). Here, we use dynamical models based on new spectroscopic observations with the Multi-Unit Spectroscopic Explorer (MUSE) IFU³ to determine the mass of the central black hole and the distribution of central stellar orbits in Holm 15A. Our goal is to shed light on possible formation scenarios for the galaxy’s extreme core.

This paper is structured as follows: Section 2 describes the new i -band photometry of Holm 15A obtained with the Fraunhofer Telescope at the Wendelstein Observatory, as well as additional images generated from our MUSE data. Section 3 details the MUSE spectroscopy and stellar kinematics derived from them. The dynamical models and results based on the photometry and kinematics are presented in Section 4. In Section 5, we discuss these results and their implications, in particular in view of predictions from N -body simulations. We summarize our conclusions about Holm 15A in Section 6.

We use the *Planck* Λ CDM (Planck Collaboration et al. 2018) cosmological model, $H_0 = 67.4$ and $\Omega_M = 0.315$. The redshift of Holm 15A, $z = 0.055$, then corresponds to a luminosity distance of $D_L = 252.8$ Mpc and an angular diameter distance of $D_A = 227.2$ Mpc ($1'' = 1.10$ kpc).

2. Photometry

We used two image sources for our photometric analysis of Holm 15A. The first is an i -band image obtained with the Fraunhofer Telescope at the Wendelstein observatory using the Wendelstein Wide Field Imager (WWFI; Kosyra et al. 2014). While a g' -band image was also available, the i -band image had significantly better seeing (Moffat FWHM from fits to multiple stars = $0''.86$ versus $1''.8$ for the g' -band image). The isophote analysis of this image is the basis for the 3D deprojection that we use to constrain the dynamical models (Section 2.1). We also used this image to analyze the core region and estimate the “missing light” in the center of Holm 15A (Section 2.2).

³ Based on observations collected at the European Organisation for Astronomical Research in the Southern Hemisphere under ESO program 099.B-0193(A).

The second source is an image created from the MUSE data cube, which we used to analyze Holm 15A for the presence of dust or color gradients which could potentially affect the deprojection (Section 2.3; also see Section 3.2 for the spectroscopic analysis).

2.1. *Wendelstein Image: Reduction and PSF-deconvolved Light Profile*

Holm 15A is part of the sample of 170 local BCGs that were observed by Kluge et al. (2019) with the WWFI. The light profiles derived for these BCGs provide a unique photometric database, reaching down to an unprecedented deep limiting surface brightness of ~ 30 mag arcsec $^{-2}$ in the g' band (Kluge et al. 2019; see Figure 1). The data cover a field of $49' \times 52'$ (pixel size $0''.2/\text{pixel}$) around Holm 15A, which corresponds to a projected area of roughly 10 Mpc 2 . The radial surface-brightness profile was measured by fitting ellipses to the galaxy’s isophotes, while allowing for higher-order deviations from perfect ellipses, using the code from Bender & Moellenhoff (1987). To increase the spatial resolution in the inner parts of the galaxy, the central $\sim 1' \times 1'$ of the image has been point-spread function (PSF) deconvolved using 40 iterations of the Richardson–Lucy method (Lucy 1974). The 2D convolution is performed on images regenerated from previously performed isophote analyses. The radial light profile from this PSF deconvolution is the basis of our 3D deprojection that we use to constrain the dynamical models of Holm 15A. A detailed description of the observations and data reduction can be found in Kluge et al. (2019).

2.2. *Core Radius and Missing Light of Holm 15A*

The core radii of massive galaxies are typically described by either the core-break radius r_b of a “Nuker” (Lauer et al. 1995) or core-Sérsic profile (Graham et al. 2003; Trujillo et al. 2004), or by the “cusp radius” r_γ , the radius where $d \log I / d \log r = -1/2$. The cusp radius only requires that a galaxy’s light profile becomes shallow in the central parts. This is clearly the case in Holm 15A, and the cusp radius is well defined: $r_\gamma = 3''.7 \pm 0''.10$ (4.11 ± 0.11 kpc). The semimajor axis length of the corresponding isophote is $a_\gamma = 4''.1 \pm 0''.10$, consistent with López-Cruz et al. (2014). In contrast, the concept of a core-break radius implies—in addition to central shallowness—a distinct change of the light profile from its behavior outside of r_b to a different behavior interior to r_b . As we will discuss here, the light profile of Holm 15A does not exhibit a clear and distinct change but continuously flattens to the smallest observed radii.

The surface-brightness distribution of Holm 15A out to $r < 200''$ (or $\mu_i < 26$ mag arcsec $^{-2}$) can be represented fairly well by the sum of two Sérsic functions, where the inner component is nearly exponential with Sérsic index $n_1 = 1.26$ and $r_{e,1} = 15.81$ kpc and the outer component follows roughly a de Vaucouleurs profile with $n_2 = 4.21$ and $r_{e,2} = 208.1$ kpc (Kluge et al. 2019). A more complex model composed as the sum of a core-Sérsic plus a Sérsic function improves the fit in the core region slightly. The break radius of this model, $r_b = 8''.96$ (see model cSS in Table 2 of Appendix A.1) is roughly consistent with the radius of the maximum curvature of the observed light profile. However, the Sérsic parameters of the core-Sérsic component are very different from the inner Sérsic component of the model by Kluge et al. (2019) quoted above. The “steep” Sérsic index $n_1 = 5.24$, together with the

fact that $r_{e,1} < r_b$, undermines the intended meaning of r_b as a “break radius” and of n_1 and $r_{e,1}$ as the local Sérsic approximation to the light outside of the core. Indeed, the corresponding Sérsic part of the model does not trace the observed light profile anywhere in the inner regions of the galaxy.

To investigate this a little further, we also tried an alternative fitting approach where we separate the determination of the core parameters from the two Sérsic components: we start by fitting the sum of two (coreless) Sérsic components to the surface-brightness profile outside of the core, i.e., outside of a minimum radius r_{\min} . Then, in the second step, we repeat the fit, now including also the data inside r_{\min} but now we only vary the core parameters in the fit, while holding the inner and outer Sérsic components n_1 , $r_{e,1}$ and n_2 , $r_{e,2}$, and $\mu_{e,2}$ fixed. In this way, we determine the Sérsic parameters before the core parameters and force the Sérsic components to approximate the light profile outside of r_{\min} . We tried a range of different r_{\min} . Below $r_{\min} < r_\gamma \sim 4''$ (i.e., inside the core), the inner components n_1 and $r_{e,1}$ are affected too much by the core region itself. Above $r_{\min} = 12''$, the light profile is already so steep that we are far outside the core, and the models, even after fitting the core parameters, no longer provide good fits. For $r_{\min} = 4''\text{--}12''$, these two-step fits represent the data very well. Moreover, in all the two-step fits, we found $r_b < r_e$ and $r_b \sim r_\gamma$, as expected (see models cSS($r_{\min} = 4$) and cSS($r_{\min} = 12$) in Table 2). The Sérsic components approach the Sérsic+Sérsic model of Kluge et al. (2019) in the limit of small r_{\min} . However, the fits did not converge to a stable set of parameters. We found both the Sérsic index n_1 of the inner component and r_b to systematically increase with r_{\min} (see Table 2 and Figure 2).

All these results led us to conclude that the galaxy does not exhibit a clear break radius inside of which the light profile follows a power law and outside of which it can be characterized by a single local Sérsic index n over a range that is more extended than a few arcseconds. Fitting the inner parts of the 1D light profile of Holm 15A with a Nuker profile confirmed this finding. Again, we could not derive a stable break radius and r_b turned out to be a monotonic function of the maximum radius out to which we extended the fit (we tried $r_{\max} = 10''\text{--}70''$; see Table 2).

Finally, we also performed a 2D multicomponent fit to the entire i -band Wendelstein image of Holm 15A using IMFIT (Erwin 2015; see Appendix A.2). This yielded a stable set of core parameters. However, in the 2D analysis, allowing for a broken inner profile with a power-law core with $r_b = 2''.57$ did not improve the fit significantly over a central, pure Sérsic component with $n \sim 1$.

Holm 15A evidently continues the homology of cores observed in less extreme ellipticals in the sense of having a faint center with a shallow surface-brightness profile (see Figure 1). But, as our attempts to identify a clear break radius have shown, the core region in Holm 15A is not as sharply separated from the outer parts of the galaxy as it is in other core galaxies with a more prominent break in the light profile. Because of this, even though both r_b and r_γ have been shown to follow tight scaling relations with M_{BH} in other core galaxies (e.g., Lauer et al. 2007b; Thomas et al. 2016), we will only consider the cusp radius of Holm 15A in the rest of the paper.

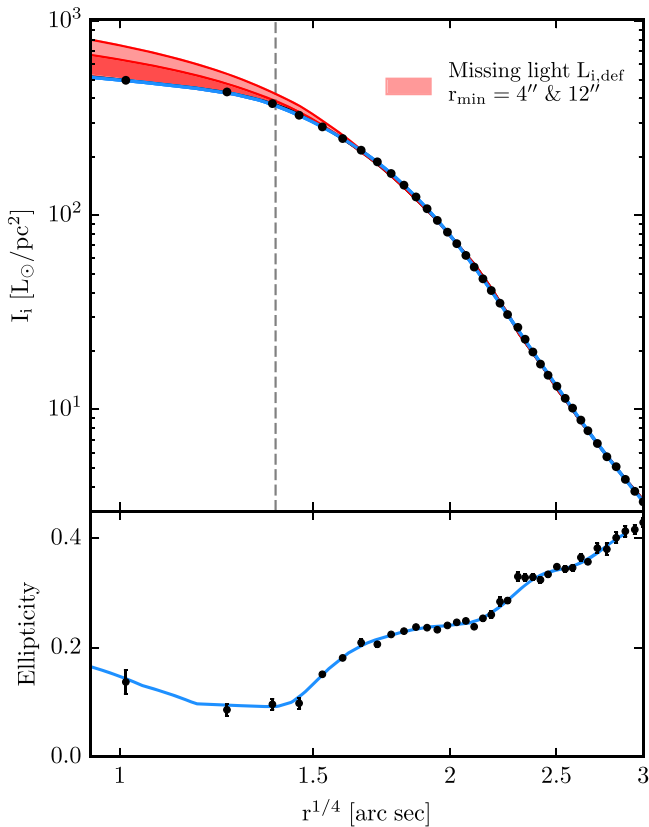


Figure 2. Top: deconvolved i -band light profile of Holm 15A (corrected for extinction and cosmological dimming; black dots) and inwards extrapolation of outer Sérsic components from multicomponent (core-)Sérsic models to the light profile from large radii ($r_{\max} \sim 200''$) to inner radii of $r_{\min} = 4''$ and $r_{\min} = 12''$ (red lines). Red areas indicate the missing light relative to Holm 15A’s depleted, shallow core for both models. Bottom: ellipticity from ellipse fits to the isophotes of Holm 15A. Blue lines indicate the projection of our 3D deprojection of the 2D Wendelstein image.

The shallowness of the inner light profile still allows the estimation of the amount of “missing light.” From the above-described models $\text{cSS}(r_{\min} = 4)$ and $\text{cSS}(r_{\min} = 12)$ (see Table 2), we find $L_{i,\text{def}} = (2.75 \pm 2.22) \times 10^{10} L_{i,\odot}$, which we will later use in Section 5.1 to estimate the mass of stars ejected from the center via core scouring. The estimated missing light is illustrated in Figure 2.

2.3. MUSE Images: No Evidence for Dust or Color Gradients

To investigate whether dust extinction might distort the isophotes and to check for color gradients indicative of a change in the stellar populations, we also generated images from the MUSE data cube. This has two advantages. First, the MUSE observations have (slightly) better seeing than the Wendelstein i -band image: in the “red” image (see below for definition), we measured $\text{FWHM} = 0''.72$ from the two point sources in the image. Second, when collapsing the data cube, we can choose wavelength ranges that explicitly exclude emission, which is important because we do detect regions of line emission within Holm 15A (see below).

We use the spectral region 7300–8500 Å to create a largely emission-line-free “red” image and the spectral region 4750–5500 Å for its “blue” counterpart. The ratio of the blue and red MUSE images is shown in the right-hand panel of Figure 3, and it shows no evidence for either dust lanes or significant color gradients.

2.4. 3D Deprojection

In order to constrain the distribution of stars in our dynamical model of Holm 15A (see Section 4), we create a 3D deprojection of the luminosity density from our deconvolved 2D Wendelstein image. The algorithm that we use to achieve this enables us to find a 3D nonparametric axisymmetric luminosity density distribution $\nu(\mathbf{r})$ consistent with the 2D input surface-brightness distribution and an assumed inclination angle i . As can be seen in Figure 2, Holm 15A is for the most part relatively round, but flattens significantly to an ellipticity $\varepsilon \sim 0.4$ at radii $\gtrsim 100''$. In the axisymmetric case, this limits possible viewing angles to be close to edge on, which is why we assume $i = 90^\circ$. The algorithm utilizes a penalized log-likelihood function and is detailed in Magorrian (1999). As Figure 2 shows, the resulting axisymmetric luminosity density distribution reproduces the relevant observed photometric features almost perfectly.

3. MUSE Spectroscopy: Stellar Kinematics of Holm 15A

3.1. MUSE Observations and Data Reduction

We obtained wide-field spectroscopic data of Holm 15A with MUSE at the Very Large Telescope at Paranal on 2017 November 16 and 2018 August 10. At $z = 0.055$, MUSE covers several important absorption features such as $\text{H}\beta$, the Mgb region, Na I, several Fe absorption features, and the Ca II triplet.

Our observations were carried out over the course of two nights and consist of three observational blocks of two dithered 1200 s exposures of Holm 15A plus one 300 s long exposure of the sky in between each. All observations, including the sky-field offset, cover an approximately $1' \times 1'$ field of view (FOV) composed of 24 combined integral field units (IFUs).

We performed the data reduction using version 2.8.5 of the standard Esoreflex MUSE pipeline supplied by ESO (Freudling et al. 2013). The pipeline runs several recipes on both exposures such as flat-field and wavelength calibrations and returns a combined data cube, covering the optical domain from about 4800 to 9400 Å with a spectral resolution of 1.25 Å. We sampled the cube in spaxels of $0''.4 \times 0''.4$, which at the redshift of the galaxy ($z = 0.055$) corresponds to approximately $400 \text{ pc} \times 400 \text{ pc}$ per pixel. As previously mentioned, we measure a PSF with $\text{FWHM} = 0''.71$ for the MUSE image.

Sky emissions were removed separately from all galaxy exposures using the sky field from offset sky exposures, taking into account the instrumental line spread function for each IFU.

3.2. Treatment of Spectra and Derivation of (Parametric) Stellar Kinematics

For our study of Holm 15A, we initially used the MUSE absorption spectra to derive spatially resolved, 2D stellar kinematics parameterized by the rotational velocity v_{rot} , velocity dispersion σ , and higher-order Gauss–Hermite coefficients h_3 and h_4 of the line-of-sight velocity distribution (LOSVD). For the dynamical modeling, we use nonparametric LOSVDs that were derived following a set of equivalent steps (see Section 3.3).

To achieve a balance between a precise measure of the kinematics in the core and an overall high spatial resolution, we aim for a target signal-to-noise ratio (S/N) of at least ~ 50 per pixel in each spectrum. To achieve this, we spatially bin the

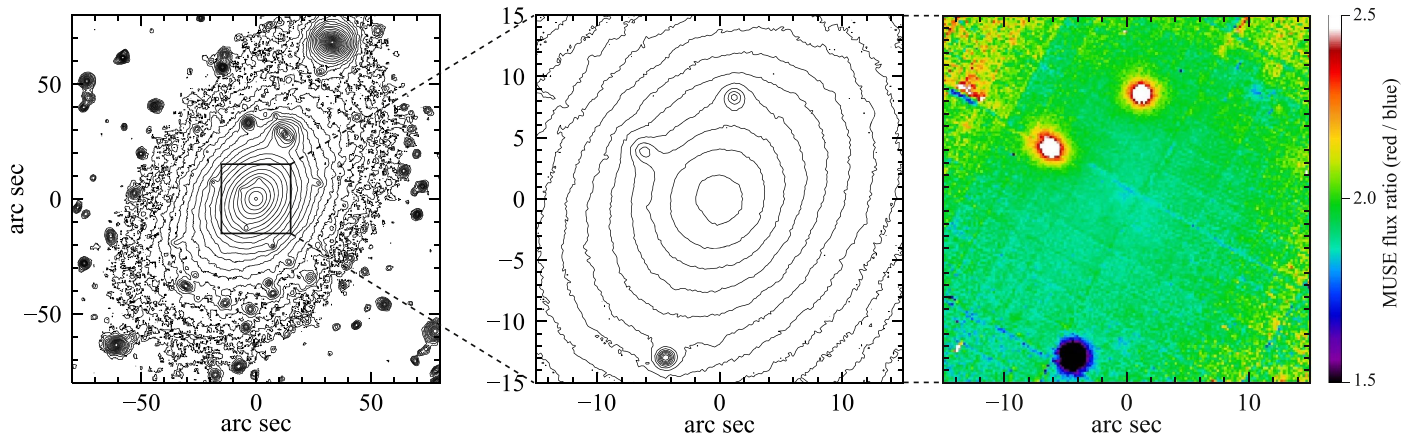


Figure 3. Holm 15A isophotes and central color map. Left: logarithmically scaled isophotes for our Wendelstein *i*-band image (median-smoothed with an 11 pixel wide box). Middle: isophotes for the MUSE red image (extracted from data cube using 7300–8500 Å). Right: color map from the ratio of MUSE blue (4750–5500 Å) and red images. No evidence for dust lanes or a color gradient in the central region of the galaxy can be seen.

data cube using the Voronoi tessellation method of Cappellari & Copin (2003). Pixels belonging to foreground sources such as galaxies or AGNs are removed from the data before binning.

At the center of the galaxy ($r \leq 5$ kpc), the spatial resolution of the Voronoi bins turns out to be $0''.4$ – $0''.8$ (roughly 400–800 pc) for an $S/N \sim 50$. We here define the radius of the gravitational SOI of the black hole as the radius where the enclosed mass $M(\leq r_{\text{SOI}}) \equiv M_{\text{BH}}$. By integrating the deprojected 3D luminosity density and assuming a range of plausible stellar mass-to-light ratios, between Υ_* = 4 and 6, we estimated the enclosed mass of the galaxy. For the lowest expected black hole mass for a galaxy of this mass and velocity dispersion, $M_{\text{BH}} \sim 3 \times 10^9 M_{\odot}$ (using the mean expected values from the $M_{\text{BH}}-\sigma$, $M_{\text{BH}}-r_{\text{SOI}}$ scaling relations from ETGs from McConnell & Ma 2013; Saglia et al. 2016), the enclosed stellar mass equals M_{BH} at $r_{\text{SOI}} \sim 1''.6$. Because our PSF and spatial binning resolution are both on the order of $0''.8$ we ensure that we can resolve the expected SOI with a diameter of $2 \times 1''.6 = 3''.2$ by a factor ≥ 4 . However, the extreme core properties of Holm 15A actually point to an SMBH with $M_{\text{BH}} \sim 10^{11} M_{\odot}$ (based on $M_{\text{BH}}-r_{\text{SOI}}$ scaling relations from Lauer et al. 2007b and Thomas et al. 2016), whose SOI radius would be roughly $r_{\text{SOI}} \sim 4''$ – $5''$ —a factor > 10 above our resolution limit. If the dark matter halo is included in the modeling, this resolution is sufficient for a robust black hole mass determination (Rusli et al. 2013b).

In total, we obtain 421 spatial bins, of which 145 bins are located inside the central $5''$. For the purpose of our subsequent dynamical modeling of the galaxy, we divided the spatial bins of our MUSE FOV into four quadrants, q1–q4, in such a way that quadrant membership is determined by which side of the major and minor axes the center of each bin is located on.

Parametric LOSVDs for each bin were obtained by fitting the stellar absorption lines of the galaxy with Penalized Pixel-Fitting (pPXF; Cappellari 2017) implemented in Python 2.7. pPXF convolves a weighted sum of template stellar spectra, in this case the MILES library (Sánchez-Blázquez et al. 2006) with a Gauss–Hermite LOSVD in order to fit the absorption features. Optionally, emission-line features of ionized gas are fit simultaneously, with a separate set of templates and LOSVDs. Figure 4 shows an example of a (parametric) kinematic fit to the spectral features of Holm 15A with pPXF for a bin located roughly $0''.5$ from the center of the galaxy (best fit to the stellar component: $v_{\text{rot}} = -1.59 \pm 8.04$ km s^{-1} relative to the systemic

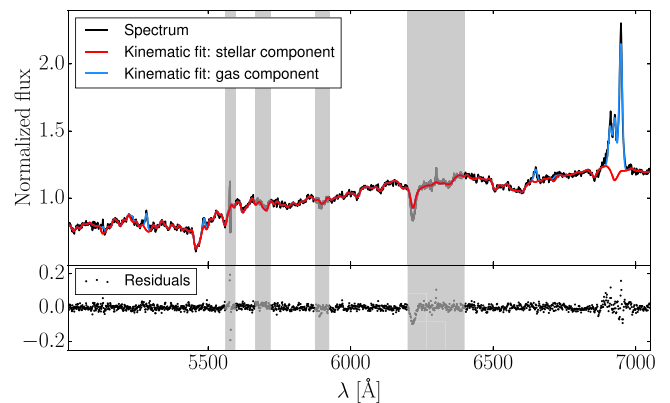


Figure 4. Stellar kinematic fit with pPXF (red) to a normalized spectrum of Holm 15A (black) with corresponding residuals (black points, lower panel). Emission lines from ionized gas are fit simultaneously (blue). Spectral regions masked during the fit are shown as gray shaded areas.

velocity of the galaxy, $\sigma = 342 \pm 9.71$ km s^{-1} , $h_3 = 0.025 \pm 0.015$, $h_4 = 0.062 \pm 0.018$).

Several bins within the central 5 kpc region of the galaxy—primarily in the southeastern regions—contain emission lines from ionized gas, most notably $H\alpha$, $H\beta$, $[\text{O III}]$ 5007 Å, $[\text{N I}]$ 5199 Å, and $[\text{N II}]$ 6583 Å (see Figure 4), which we fitted with the emission-line-fitting routine of pPXF, though we do not consider their kinematics in this study. Figure 5 shows the measured emission-line flux for $H\alpha$, $H\beta$, $[\text{O III}]$, and $[\text{N II}]$. The average flux ratios $\log([\text{O III}]/H\beta) = 0.09 \pm 0.26$ and $\log([\text{N II}]/H\alpha) = 0.48 \pm 0.12$ of emission lines with $S/N > 3$ are associated with LINER-type emission (Kauffmann et al. 2003), which is quite typical for cool-core clusters. Of the ~ 100 brightest X-ray clusters, Abell 85’s cool core has the 14th strongest cooling flow (Chen et al. 2007). The spatial extent of this LINER-type emission (~ 4 – 5 kpc) suggests it could be related to ionized cooling-flow filaments (e.g., Ferland et al. 2008, 2009; O’grea et al. 2010). This was already previously noted by McDonald et al. (2010), who found that it coincided with a similarly extended region of X-ray emission associated with cooling flows.

By contaminating some absorption features such as $H\beta$, the gas emission increases the uncertainties of the kinematic fits in some bins. As we will show in Section 4, this contamination of mostly central spectra slightly increases the uncertainty of

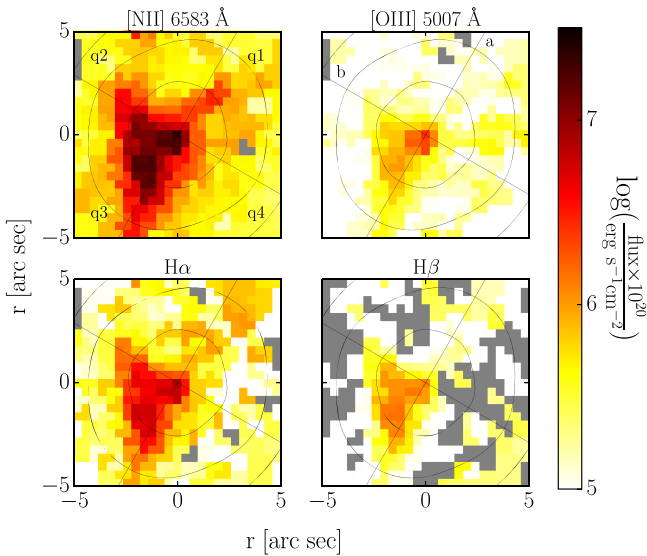


Figure 5. Logarithmic flux of emission lines [N II], [O III], $H\alpha$, and $H\beta$ from ionized gas located within the central regions of the galaxy. Gray areas indicate bins for which no meaningful emission-line fit could be derived. Photometric i -band isophotes are shown in black. Axes a and b (black lines) correspond to the major and minor axes of the galaxy, respectively. The center of the galaxy coincides with the peak of the emission-line flux.

M_{BH} , but has little impact on the global stellar mass-to-light ratio Υ_* and the shape of the dark matter halo.

At redshift $z = 0.055$, the strong oxygen 5577 \AA sky emission line lies on top of the 5270 \AA Fe feature. Because this line is difficult to remove, the Esoreflex sky subtraction left strong residuals in this region, effectively rendering it unusable for fitting. We noted a few additional systematic residuals which may be related to sky subtraction or telluric correction issues as well. In order to minimize possible systematics in the LOSVDs, we defined a single mask that we used for all spectra throughout the entire galaxy. We consistently mask all wavelength regions that are possibly affected by any systematic issues.

We performed our kinematic fits over the spectral interval between 5010 and 7050 \AA . Including spectral regions bluer than 5010 \AA resulted in lower-quality fits and a constant bias in h_3 , indicative of template mismatch. Spectral regions redder than 7050 \AA were badly affected by sky lines and were therefore omitted. In particular, we could not derive meaningful kinematics in the [Ca II] triplet region.

We also used a sixth-order multiplicative polynomial and an additive constant in the fit. The former allows for the correction of errors in the flux calibration, while the latter is typically used to correct over- or underestimations of the continuum during sky correction. We also made use of the sigma-clipping and bias-factor options. The value of the bias factor— 0.2 in our case—was determined from testing pPXF on Monte Carlo simulations of model spectra.

A subset of stellar template spectra for the fit was selected as follows: we fitted a mean spectrum of all bins of the galaxy with the full set of 985 MILES library templates. All binned spectra were corrected for the systematic velocity of the galaxy, as well as their respective rotational velocities. All spectra were normalized to one before averaging. We set both the third-order Gauss–Hermite coefficient h_3 and the additive constant to zero in order to avoid template mismatch (which can result in biases in these parameters). With these restrictions, pPXF assigned

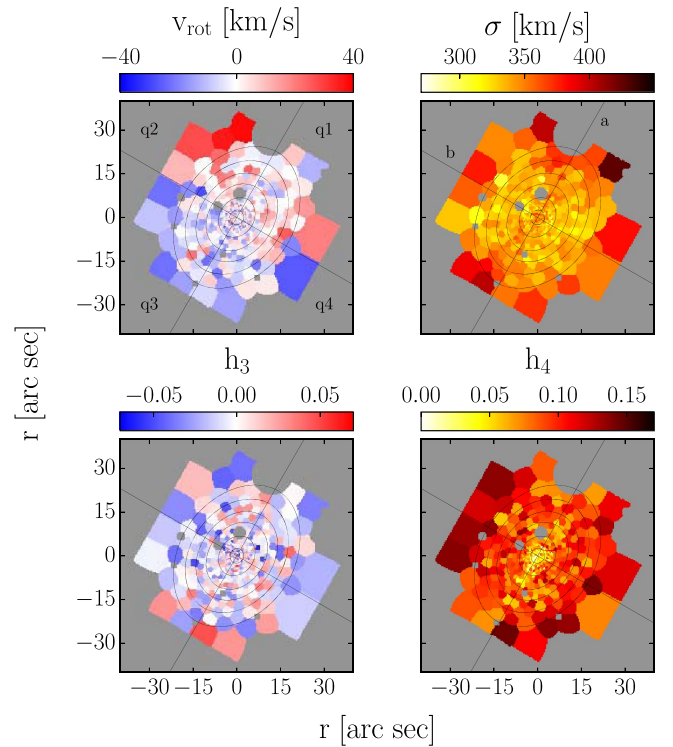


Figure 6. From top to bottom, left to right: kinematic maps of the rotational velocity v_{rot} , velocity dispersion σ , and the higher-order Gauss–Hermite coefficients h_3 and h_4 over the MUSE FOV. The systematic velocity of the galaxy has been subtracted in the kinematic map of v_{rot} . Ellipse fits to i -band isophotes are drawn in black; axes a and b (black lines) correspond to the major and minor axes of the galaxy, respectively.

nonzero weights exclusively to a set of 16 templates with a wide variety of luminosity classes but limited to spectral types G, K, and M, in good agreement with the uniformly red color of the galaxy (Section 2). We used this subset of stars from the MILES library as templates for fitting the galaxy’s absorption features in all Voronoi bins.

The parameterized kinematics in the interval between 5010 and 7050 \AA over the MUSE FOV are shown in Figure 6. As can be seen in the figure, we measure a weak rotation signal of less than 40 km s^{-1} , which is only faintly reciprocated in h_3 —the rotation is likely too weak for an anticorrelated signal in this parameter to be detectable. The velocity dispersion σ peaks in the central regions ($r < 2 \text{ kpc}$) at $\sim 350 \text{ km s}^{-1}$, stays somewhat constant at $\sim 330 \text{ km s}^{-1}$ throughout most of the FOV, and finally starts to rise again at the edges of the MUSE FOV up to $\gtrsim 370 \text{ km s}^{-1}$. Our measured velocity dispersions are similar to those of Fogarty et al. (2014). Our h_4 kinematic profile starts out at ~ 0.07 within 2 kpc and rises to $\gtrsim 0.1$ toward the edges of the FOV. In Appendix B.1, we compare the kinematics of Holm 15A to those of massive ETGs from the MASSIVE survey. The corresponding statistical uncertainties are shown in Figure 7. Uncertainties were determined from Monte Carlo simulations on model spectra of the galaxy, i.e., refitting best-fit spectral models with 100 different noise realizations, the noise being drawn from a Gaussian distribution with a dispersion corresponding to the local S/N, which is measured directly from each spectrum. We note that the distribution of uncertainties is spatially asymmetric between central bins across quadrants—central kinematics in q3 have overall larger uncertainties than those in the other quadrants.

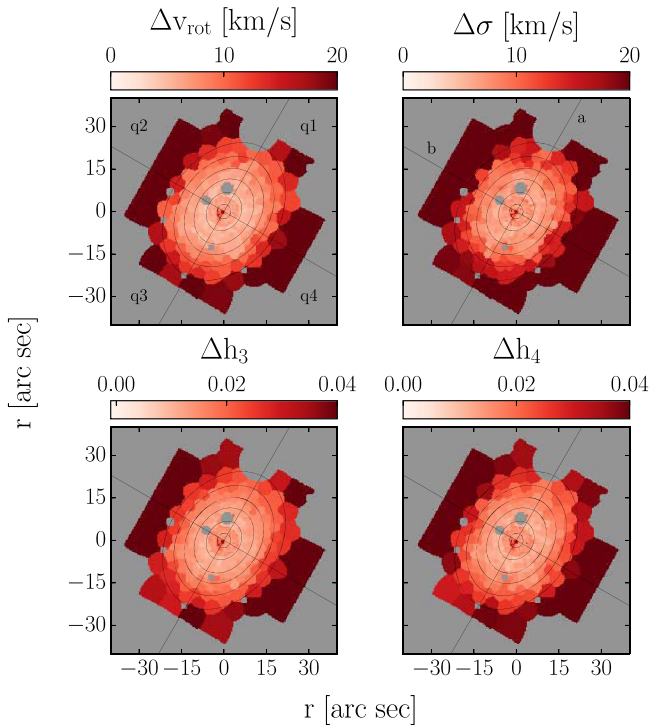


Figure 7. Maps of statistical uncertainties corresponding to the parameters of the kinematic maps of Figure 6.

This is in agreement with the distribution of emission-line flux between quadrants (see Figure 5), i.e., q3 seems to be affected worse by uncertainties introduced by gas contamination of absorption features. However, as we will show in Section 4, including q3 in our dynamical modeling did not produce any larger systematic offset in our best-fit parameters relative to the other quadrants.

3.3. Nonparametric LOSVDs

In our dynamical modeling of Holm 15A, we set out to achieve a precise mass measurement of the galaxy, which makes the parametric representation of the stellar kinematics in Figure 6 problematic: large values of σ and $h_4 > 0$ over the entire FOV result in the escape velocity of the galaxy, v_{esc} being practically infinite everywhere. Because v_{esc} depends directly on the gravitational potential, we try to measure it as accurately as possible.

To obtain LOSVDs with more realistic v_{esc} , we use our own kinematic extraction code (J. Thomas et al. 2019, in preparation) which operates in a similar way to pPXF but minimizes the χ^2 over all spectral pixels by utilizing a Levenberg–Marquardt algorithm to fit a template broadened with a nonparametric LOSVD to the absorption features of a galaxy.

We use the same setup of template stars, and additive and multiplicative polynomials as described above. Emission lines are masked for each spectrum individually, according to their respective widths (spectral regions within $4 \times \sigma_{\text{gas}}$ are masked for each emission line) and positions as determined with the pPXF emission-line fit. The nonparametric LOSVDs mainly differ from the parametric ones in the high-velocity tails, as demonstrated for an example bin of Holm 15A in Figure 8. While the width of the LOSVD ($\sigma = 338 \pm 9.57 \text{ km s}^{-1}$ with our own code and $\sigma = 328 \pm 10.7 \text{ km s}^{-1}$ with pPXF), as well as its global shape, is similar for both methods, the

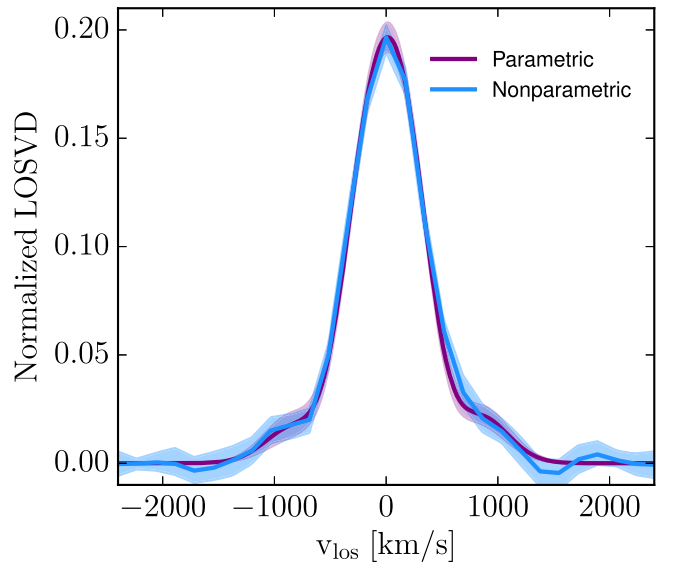


Figure 8. Example LOSVDs from the central regions of q4 originating from two different methods: one determined parametrically with pPXF (purple) and the other nonparametrically with our own code (blue). The shaded envelopes indicate statistical uncertainties.

nonparametric LOSVDs provide a more realistic sampling of the LOSVD and noise at large projected velocities. Therefore, for our dynamical study of Holm 15A, we use the nonparametric LOSVDs. Radial profiles comparing both parametric and nonparametric kinematics for all bins in our study are presented in Appendix B.2.

4. Schwarzschild Dynamical Modeling of Holm 15A

4.1. Dynamical Models

We dynamically modeled Holm 15A under the assumption of axisymmetry. The lack of unambiguous, obvious isopotential distortions (see Section 2) and the overall symmetry of the observed kinematic profiles (see Section 3.2) imply that Holm 15A is generally consistent with an axially symmetric stellar distribution.

The dynamical models in this study were constructed using an updated version of our axisymmetric Schwarzschild orbital superposition code. We will here only briefly summarize the key features of our implementation and refer to previous publications for more in depth descriptions (Richstone & Tremaine 1988; Gebhardt et al. 2003; Thomas et al. 2004; Siopis et al. 2009).

Schwarzschild dynamical modeling is based on the calculation of stellar orbital distributions in a fixed gravitational potential as a solution to the collisionless Boltzmann equation (Schwarzschild 1979). Any orbit can be fully described by three integrals of motion: the classical integrals E and L_z (in the axisymmetric case) plus a nonclassical integral I_3 (in most astrophysically relevant cases). Sampling values of this set of integrals of motion (E, L_z, I_3) allows us to create an orbit library in a given gravitational potential Φ whose distribution function $f(\mathbf{r}, \mathbf{v})$ satisfies the collisionless Boltzmann equation.

In order to determine Φ , we assume that the density distribution of Holm 15A can be described by

$$\rho(r, \theta) = \rho_*(r, \theta) + M_{\text{BH}}\delta(r) + \rho_{\text{DM}}(r), \quad (1)$$

Table 1

Results of Schwarzschild Dynamical Modeling of Holm 15A. Best-fit Values were Derived as the Mean of the Independent Fits to the Four Quadrants

Schwarzschild Model Parameter	Best-fit Value	Units
M_{BH}	(4.0 ± 0.80)	$10^{10} M_{\odot}$
Υ_* (<i>i</i> band)	4.5 ± 0.19	
DM Halo:		
ρ_{10}	(1.0 ± 0.10)	$10^7 \frac{M_{\odot}}{\text{kpc}^3}$
$\log r_s$	(2.4 ± 0.29)	$\log \frac{r}{\text{kpc}}$
γ	0.35 ± 0.26	

Note. The quoted uncertainties are derived from the variation between quadrants.

which we insert into Poisson’s equation. ρ_* is linked to the three-dimensional deprojection $\nu(r, \theta)$ of the observed *i*-band surface brightness (see Section 2) via the stellar (*i*-band) mass-to-light ratio, $\rho_*(r, \theta) = \Upsilon_* \cdot \nu(r, \theta)$, assuming a spatially constant stellar Υ_* . In addition to the mass of the central black hole M_{BH} , the model admits the inclusion of a dark matter (DM) halo $\rho_{\text{DM}}(r)$. Here, we chose a generalized Navarro–Frenck–White halo derived from cosmological *N*-body simulations (Navarro et al. 1996; Zhao 1996):

$$\rho_{\text{DM}}(r) = \frac{\rho_0}{\left(1 + \frac{r}{r_s}\right)^{3-\gamma} \left(\frac{r}{r_s}\right)^{\gamma}}, \quad (2)$$

with

$$\rho_0 = \rho_{10} \left(1 + 10 \frac{\text{kpc}}{r_s}\right)^{3-\gamma} \left(10 \frac{\text{kpc}}{r_s}\right)^{\gamma}, \quad (3)$$

where ρ_{10} is the DM density at 10 kpc, r_s , the scale radius of the halo and γ the inner slope of the DM density profile.

For a given Φ , we sample thousands of representative initial orbital conditions, implicitly varying all the integrals of motion E , L_z , and I_3 , and including individual orbital phase-space volumes (Thomas et al. 2004). For Holm 15A, we stored LOSVDs in 29 velocity bins adapted to the velocity dispersion of the galaxy, with one LOSVD associated with each of the 421 spatial bins of our FOV, meaning our models fitted roughly a total of 3000 velocity bins per quadrant.

We use the NOMAD optimization software (Audet & Dennis 2006; Le Digabel 2011; Audet & Hare 2017) to find the set of mass parameters M_{BH} , Υ_* , ρ_{10} , r_s , and γ that yields the best fit to the observed kinematics.

4.2. Results

The most important result from our dynamical modeling is the detection of an SMBH with $M_{\text{BH}} = (4.0 \pm 0.80) \times 10^{10} M_{\odot}$ in Holm 15A. The associated SOI of this SMBH is $r_{\text{SOI}} = 3.8 \pm 0.37$ kpc ($3''5 \pm 0''34$). Even though the galaxy is more than 200 Mpc away, we spatially resolve the SOI by a factor of 10. In fact, ~ 100 out of our 421 LOSVDs sample the SOI of the galaxy. The modeling results for the black hole, stellar mass-to-light ratio, and DM halo parameters are summarized in Table 1. $\Delta\chi^2$ curves for M_{BH} , Υ_* , and ρ_{10} from all four quadrants are shown in Figure 9. The figure shows that none of the four quadrants stands out and yields a significantly different result than the others. While the black

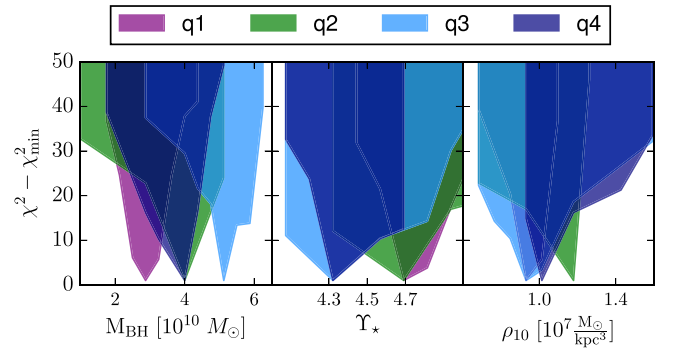


Figure 9. From left to right: χ^2 for the minimization curves of our dynamical modeling for the parameters M_{BH} , Υ_* , and ρ_{10} . Each quadrant (q1–q4) was modeled separately. The variation between their respective χ^2 curves is treated as representative of the inherent systematic and statistical uncertainties of each measurement.

hole mass in q3 (where the gas emission in the spectra is most prominent) is slightly larger than in the other quadrants, this offset is not significant. By computing the dynamical quantities separately for each quadrant and estimating the uncertainties from these four nearly independent measurements, we implicitly include any residual systematics (like, e.g., from the gas emission) in our error budget. Fits to the kinematics of one quadrant of Holm 15A parameterized by v_{rot} , σ , $h3$, and $h4$ of our best-fit model are shown in Figure 10. They show that our best-fit model can successfully reproduce the observed kinematics of the galaxy. For the nonparametric kinematics, our best-fit model reaches a reduced χ^2 of 0.8–0.9 for each quadrant.

We had previously also acquired spectroscopy of Holm 15A from the McDonald Observatory using the low-resolution mode ($\sigma \sim 25 \text{ km s}^{-1}$) of the IFU spectrograph VIRUS-W (Fabricius et al. 2012). Stellar kinematics for these independent data were derived by applying the Fourier correlation method (FCQ) by Bender (1990) in the wavelength interval between 4500 and 6250 Å, using a sparser spatial sampling (Figure 10, blue) and circular spatial binning. This entirely independent measurement of the stellar kinematics in Holm 15A is consistent with the MUSE kinematics. We note that, on average, values of h_4 and σ appear to be slightly lower for FCQ (likely due to a different smoothing method). Therefore, as a consistency check, we ran a second set of dynamical models using only the VIRUS-W kinematics and found the same results within the errors. Because the MUSE data have better spatial resolution and higher S/N, we will only discuss the results derived from the MUSE data in the remainder of this paper.

Finally, an example comparison between an observed and modeled LOSVD and a discussion of the importance of the LOSVD wings can be found in Appendix C.

5. Discussion

With $M_{\text{BH}} = (4.0 \pm 0.80) \times 10^{10} M_{\odot}$, the SMBH at the center of Holm 15A is the most massive dynamically determined black hole so far. It is a factor of 2 larger than the SMBHs in NGC 4889 (McConnell et al. 2012), with $M_{\text{BH}} = (2.1 \pm 0.99) \times 10^{10} M_{\odot}$, and NGC 1600, with $M_{\text{BH}} = (1.7 \pm 0.15) \times 10^{10} M_{\odot}$ (Thomas et al. 2016). Quasar luminosities at higher redshifts and current determinations of local SMBH scaling relations give an expected black hole

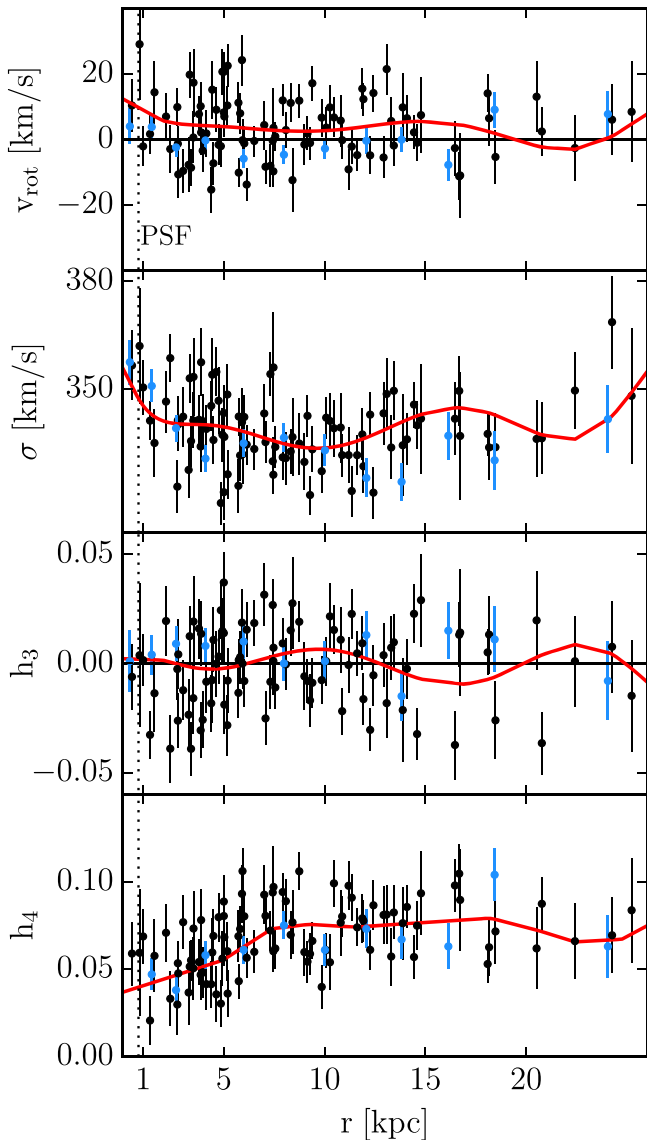


Figure 10. The Gauss-Hermite moments measured from the MUSE spectra (black points) compared to the best-fitting model (red). Shown are (from top to bottom) v_{rot} , σ , h_3 , and h_4 of quadrant q4. Note that the model was fit to the full nonparametric LOSVDs. The Gauss-Hermite moments are only used for illustrative purposes here. The figure also includes Gauss-Hermite moments measured independently on VIRUS-W spectra using the FCQ method (blue).

cumulative space density ranging from half a dozen up to a few hundred SMBHs with $M_{\text{BH}} \gtrsim 10^{10} M_{\odot}$ out to $z \leq 0.055$ (e.g., Lauer et al. 2007b; Rusli et al. 2013b). Hence, circumstances for the formation of a 40 billion solar-mass SMBH are probably rare, but the central structure of the Coma cluster serves as an example that they do exist. As stated above, NGC 4889, one of the two central galaxies of Coma, contains an SMBH of $M_{\text{BH}} = 2.1 \times 10^{10} M_{\odot}$. The other galaxy, NGC 4874, has a very extended classical shallow power-law surface-brightness core with a size of $r_b = 1.7$ kpc (Lauer et al. 2007a). This suggests an SMBH with a mass of $M_{\text{BH}} \sim 2 \times 10^{10} M_{\odot}$ (using the core scaling relations of Thomas et al. 2016). Both galaxies are interacting and will eventually merge (e.g., Arnaboldi et al. 2006; Gerhard et al. 2007). This will produce a BCG at the center of the Coma cluster which will very likely have an SMBH in the same mass range as Holm 15A has now.

In the following sections, we will discuss the observational and theoretical evidence for the merger origin of Holm 15A, as well as attempt to unravel some specific details of the merger history.

5.1. SMBH Scaling Relations: Evidence for Dissipationless Merging

The SMBH of Holm 15A is not only the most massive one to date, it is also four to nine times larger than expected given the galaxy’s stellar mass, $M_{\text{Bu}} = (2.5 \pm 0.64) \times 10^{12} M_{\odot}$, and the galaxy’s stellar velocity dispersion, $\sigma = (346 \pm 12.5) \text{ km s}^{-1}$ (see Figure 11(a)).

It has been previously noted that the $M_{\text{BH}}-\sigma$ relation may become shallow out at the high-mass end, due to dry merging becoming the dominant growth process at the high-mass end. Because dry (major) mergers grow σ only slowly (e.g., Lauer et al. 2007b; Naab et al. 2009) but simply sum over the central SMBH masses of the merging galaxies, such mergers will move galaxies toward “overmassive” M_{BH} at a given σ (e.g., Lauer et al. 2007b; Kormendy & Bender 2013). Correspondingly, massive core galaxies follow an $M_{\text{BH}}-\sigma$ relation that is steeper and slightly offset (toward larger values of M_{BH}) compared to less massive, cuspy galaxies (see Saglia et al. 2016 and McConnell & Ma 2013). Despite the fact that we here already consider the $M_{\text{BH}}-\sigma$ relation of core galaxies, Holm 15A is still almost an order-of-magnitude offset in M_{BH} (see Figure 11(a)). This might be indicative of an especially extensive dry merging period.

One could expect the $M_{\text{BH}}-M_{\text{Bu}}$ relation to be tighter at the high-mass end, because $M_{\text{BH}}/M_{\text{Bu}}$ is conserved in dry mergers. Holm 15A, however, is also a strong outlier from this relation (M_{BH} is roughly four times larger than expected from M_{Bu} ; see Figure 11(b)). The ratio between M_{BH} and M_{Bu} is typically $\lesssim 0.5\%$ for cored ETG and typically $\lesssim 1\%$ when considering all ETGs below a stellar mass of $< 10^{13} M_{\odot}$, irrespective of central morphology (Kormendy & Ho 2013). Holm 15A, however, hosts a black hole that contains close to 2% of the total stellar mass of the galaxy. A similar high ratio as been found in NGC 1600 (Thomas et al. 2016). This might suggest that the progenitor galaxies of Holm 15A were different from typical massive ETGs at $z \sim 0$. Studies of the evolution of $M_{\text{BH}}/M_{\text{Bu}}$ since $z \sim 3$ in active galaxies suggest that the ratio scales like $(1+z)^{0.7-1.4}$ (e.g., Decarli et al. 2010; Merloni et al. 2010; Bennert et al. 2011). Depending on which $M_{\text{BH}}-M_{\text{Bu}}$ relation is used (all central morphologies or cores only), we can estimate that Holm 15A’s progenitors might have formed early, at $z \gtrsim 1$ or 2.

In Figure 11(b), we only consider scaling relations based on dynamical bulge masses to avoid systematics related to assumptions about the initial stellar mass function (IMF). We will touch on this again in Section 5.6.

Kluge et al. (2019) showed that BCGs and ETGs in general follow different scaling relations between total luminosity, size, and effective surface brightness. This would also translate into different SMBH scaling relations. Bogdán et al. (2018) suggested that BCGs follow steeper $M_{\text{BH}}-\sigma$ and $M_{\text{BH}}-M_{\text{Bu}}$ relations (see Figures 11(a) and (b)). Holm 15A is closer to these BCG-centric scaling relations. In fact, it happens to fall onto the corresponding $M_{\text{BH}}-M_{\text{Bu}}$ relations and is offset from the corresponding $M_{\text{BH}}-\sigma$ relations by about a factor of 2. This could indicate that the galaxy formed from a dissipationless,

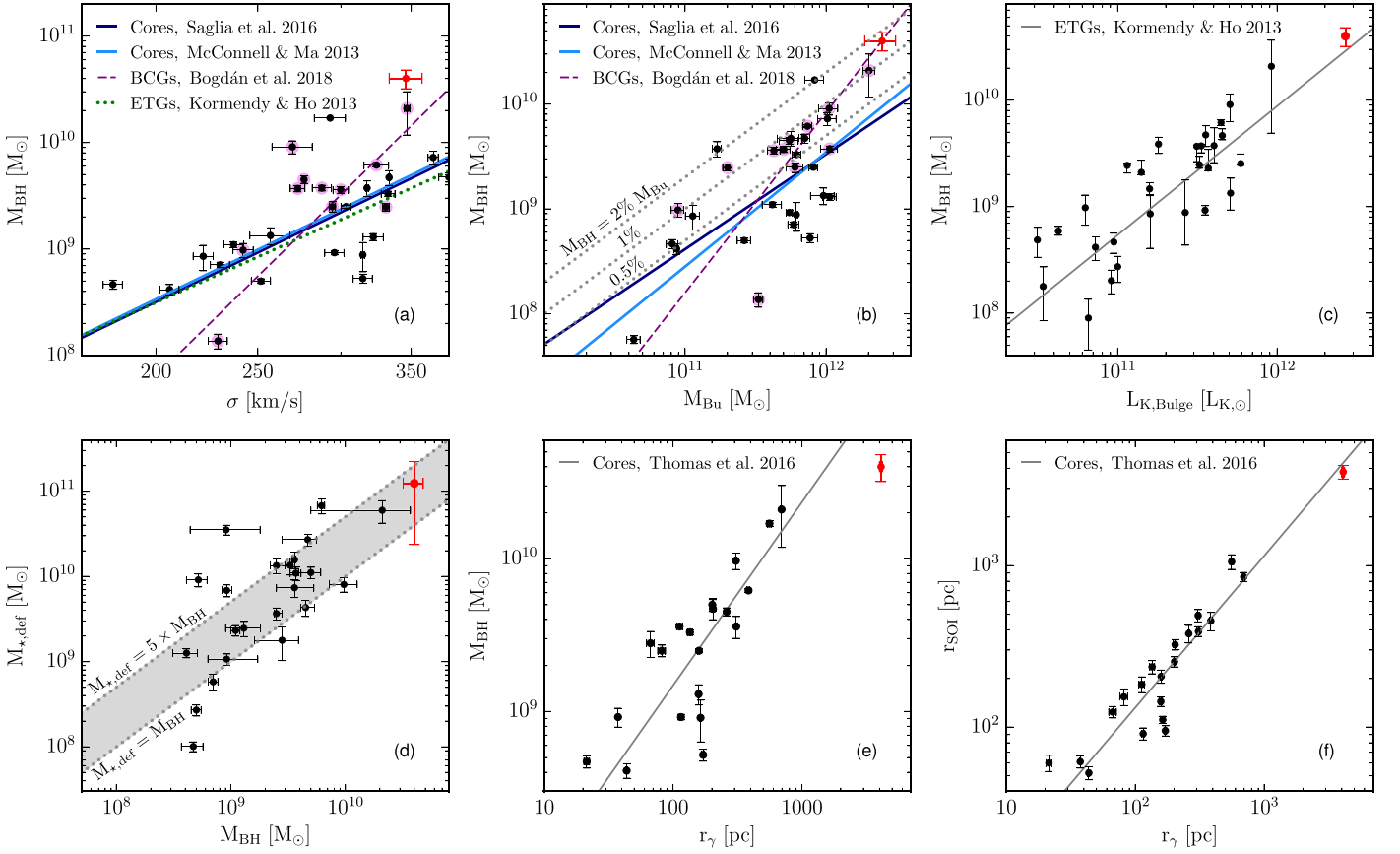


Figure 11. Holm 15A (red) compared to other ETGs, cores, and BCGs (black) on SMBH scaling relations. (a) and (b) Holm 15A compared to cored ETGs listed in Saglia et al. (2016) with respect to the global galaxy scaling relations, (a) $M_{\text{BH}}-\sigma$ and (b) $M_{\text{BH}}-M_{\text{Bu}}$. Solid lines show the linear relations for cored ETGs from Saglia et al. (2016) and McConnell & Ma (2013). Dashed and dotted lines indicate scaling relations for ETGs in general (cored or not) from Kormendy & Ho (2013) and BCGs only from Bogdán et al. (2018). ETGs identified as BCGs in Bogdán et al. (2018) are enhanced by purple halos around their symbols. (c) Holm 15A’s directly measured (3KK) K -band luminosity L_K compared to ETGs from Kormendy & Ho (2013) on the global galaxy scaling relation $M_{\text{BH}}-L_K$. The line shows the linear relation from Kormendy & Ho (2013). (d) Core-mass deficits $M_{*,\text{def}}$ of cored ETGs from Rusli et al. (2013a) and Holm 15A. (e) and (f) Holm 15A compared to cored ETGs from Thomas et al. (2016) and Rusli et al. (2013a, 2013b) with respect to the core-specific scaling relations, (e) $M_{\text{BH}}-r_\gamma$ and (f) $r_{\text{SOI}}-r_\gamma$. The lines show the linear relations from Thomas et al. (2016). The figure includes the uncertainties of r_γ , but they are generally smaller than the symbol size.

(roughly) equal-mass BCG merger, though the scatter in the relations is large.

We note that the total stellar mass of Holm 15A is estimated based on the assumption that the stellar mass-to-light ratio is constant out to a region that is almost 10 times larger than the FOV of our kinematic observations. Therefore, in Figure 11(c), we also compare Holm 15A’s K -band luminosity L_K to the $M_{\text{BH}}-L_K$ relation of Kormendy & Ho (2013). L_K was measured from an image that extends out to ~ 250 kpc and that was obtained with the three-channel imager at the Wendelstein 2 m Telescope (3KK; Lang-Bardl et al. 2010, 2016). Holm 15A follows the $M_{\text{BH}}-L_K$ correlation better than the $M_{\text{BH}}-M_{\text{Bu}}$ relation.

5.2. Scaling Relations of Core Properties: Similarity with Other Core Galaxies

Dissipationless mergers between ETGs involve binary black hole core scouring and, hence, result in depleted, low-surface-brightness cores. As already mentioned above, core galaxies follow specific scaling relations between the core size, missing light, and black hole mass (Lauer et al. 2007a; Rusli et al. 2013a) and the radius of the SOI (Thomas et al. 2016). Simulations have shown that these relations can be explained by the black hole binary model (Rantala et al. 2018). In

Figure 11(d), we show the central stellar mass deficits from Rusli et al. (2013a) together with Holm 15A. The mass deficit in Holm 15A is $M_{*,\text{def}} = (1.24 \pm 1.00) \times 10^{11} M_\odot$, based on the dynamical stellar mass-to-light ratio and $L_{i,\text{def}}$ derived in Section 2.2. This roughly corresponds to 0.5–5.5 times the black hole mass, similar to the mass deficits in many other core galaxies.

In Figure 11(e), we compare the core size of Holm 15A to other galaxies. As described in Section 2.2, we use the cusp radius r_γ here. Compared to the galaxies of Rusli et al. (2013a, 2013b) and Thomas et al. (2016), the core in Holm 15A is roughly a factor of 2.5 larger than expected for the mass of its black hole. Such an offset could be explained, for example, if Holm 15A experienced an early phase of rapid evolution with an enhanced merger rate. It could well be then that not only a binary black hole was involved in the formation of its core, but possibly a more complicated system of multiple black holes. Theory suggests that core-scouring efficiency is significantly enhanced by multiple black holes and that cores grow much larger (Kulkarni & Loeb 2012). We will revisit this issue in Section 5.4. In Figure 11(f), we compare r_γ with the radius of the SOI, r_{SOI} . Despite being offset on the $M_{\text{BH}}-r_\gamma$ relation, the cusp radius is consistent with the correlations between core-size measurements and r_{SOI} in other core galaxies

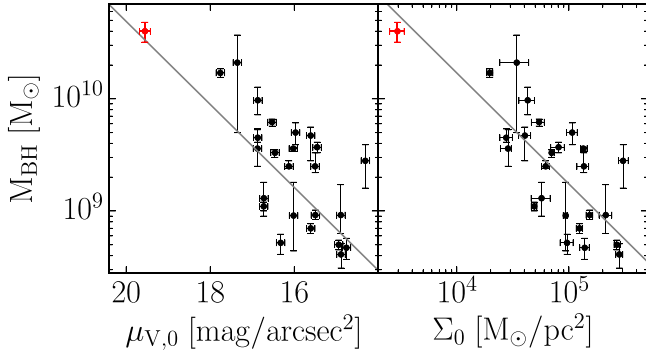


Figure 12. The central V-band surface brightness $\mu_{V,0}$ (left) and stellar surface mass density Σ_0 (right) vs. M_{BH} for Holm 15A (red) and cored ETGs from Rusli et al. (2013a, 2013b) and NGC 1600 (Thomas et al. 2016; black). All values of $\mu_{V,0}$ and Σ_0 relate directly to the observed light profiles themselves. The line shows the best-fit linear relation.

5.3. A New Correlation between Black Hole Mass and Core Surface Brightness

Cores in massive ETGs obey a strong homology in that the central surface brightness correlates inversely with the size of the core (Dullo & Graham 2014; Faber et al. 1997; Lauer et al. 2007b). This, together with the scaling between M_{BH} and core size, implies a potential scaling between M_{BH} and the central surface brightness μ_0 in cores. An equivalent argument can be made for a correlation between M_{BH} and the central stellar surface mass density Σ_0 . We show these correlations in Figure 12 for the galaxy sample of Rusli et al. (2013b), NGC 1600 (Thomas et al. 2016), and Holm 15A. We used the uncertainties for the stellar mass-to-light ratios and black hole masses listed in Rusli et al. (2013a, 2013b) and Thomas et al. (2016) and assumed rather conservative uncertainties of $0.1 \text{ mag arcsec}^{-2}$ for the light profiles. Our best-fit linear relations were determined following the approach to linear regression from Kelly (2007; using the Python package `linmix` by Meyers 2015) with errors in both M_{BH} and $\mu_{V,0}$, Σ_0 :

$$\log(M_{\text{BH}}/M_{\odot}) = (0.37 \pm 0.07)\mu_{V,0} \text{mag}^{-1} \text{arcsec}^2 + (3.29 \pm 0.37) \quad (4)$$

$$\log(M_{\text{BH}}/M_{\odot}) = (-0.99 \pm 0.19)\log(\Sigma_0/M_{\odot} \text{pc}^{-2}) + (14.19 \pm 0.09). \quad (5)$$

The $M_{\text{BH}}-\mu_{V,0}$ relation has an intrinsic scatter $\epsilon = 0.32 \pm 0.07$. Similarly, the $M_{\text{BH}}-\Sigma_0$ relation has an intrinsic scatter of 0.30 ± 0.07 . Values of Σ_0 were calculated from the surface brightness at the spatial resolution limit for each galaxy and their corresponding dynamical stellar mass-to-light ratios (Rusli et al. 2013a, 2013b; Thomas et al. 2016). Values for both $\mu_{V,0}$ and Σ_0 were determined using the observed light profiles of each core galaxy. Holm 15A has the lowest central stellar surface brightness/mass, $\mu_{V,0} = 19.9 \pm 0.13 \text{ mag arcsec}^{-2}$, $\Sigma_0 = (3.0 \pm 0.40) \times 10^3 M_{\odot} \text{pc}^2$ of all core galaxies with dynamical black hole mass measurements (see Figure 12). Nonetheless, Holm 15A is fully consistent with the homology established by other core galaxies.⁴ All of the above evidence points to the fact that the core

⁴ The listed relations were determined including Holm 15A, but the relations change only marginally and within the listed uncertainties when we exclude the galaxy.

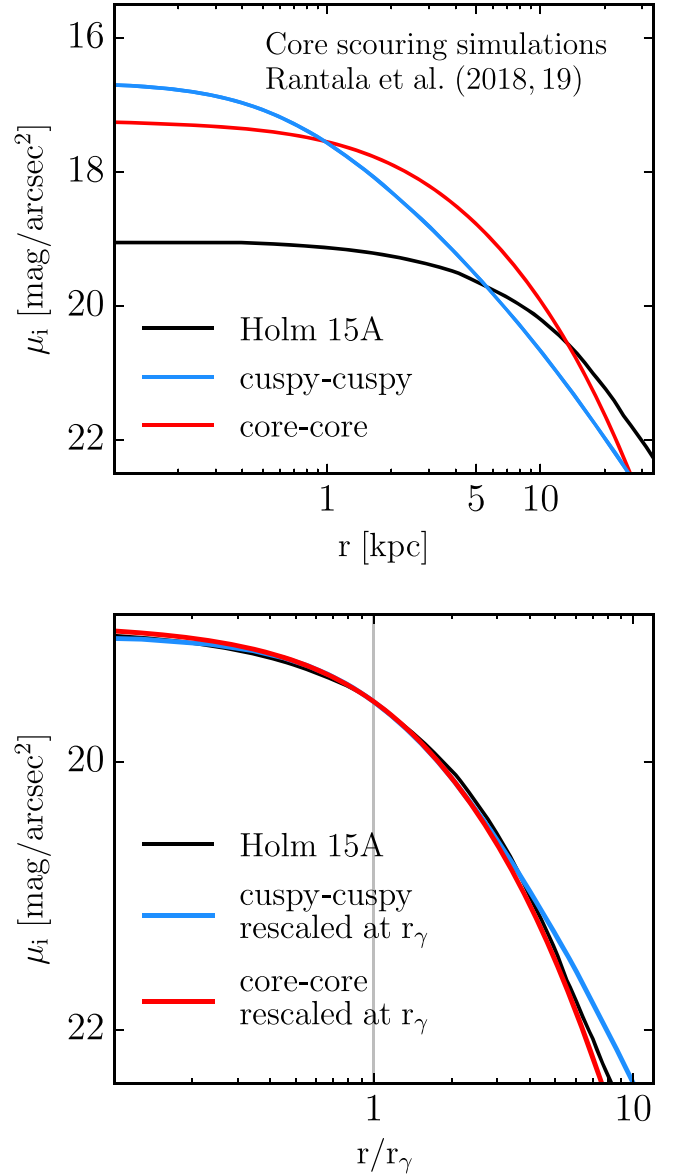


Figure 13. Top panel: i -band surface-brightness profile of $\mu(r)$ of Holm 15A (black) compared to the remnants of numerical merger simulations with core scouring. The blue profile shows a merger between two cuspy galaxies with a final black hole mass of $M_{\text{BH}} = 1.7 \times 10^{10} M_{\odot}$, roughly half of the black hole mass observed in Holm 15A. The red profile is the result of remerging this remnant with itself, doubling the mass of the central black hole to $M_{\text{BH}} = 3.4 \times 10^{10} M_{\odot}$. Bottom panel: Holm 15A compared to the remnant surface-brightness profiles scaled to the value $\mu(r \equiv r_{\gamma})$ of Holm 15A.

in Holm 15A was formed by the same physical process as cores in other massive ETGs, i.e., by a black hole binary.

5.4. N-body Merger Simulations: Evidence for a Merger between Two Core Galaxies

We will now discuss what the specific photometric and orbital dynamical properties of Holm 15A may tell us about its merger history.

In Figure 13, we compare the light profile of Holm 15A with the N -body merger simulations of Rantala et al. (2018, 2019). These simulations study the outcome of a dissipationless merger between two early-type progenitor galaxies, both with central black holes. The simulations follow the dynamical

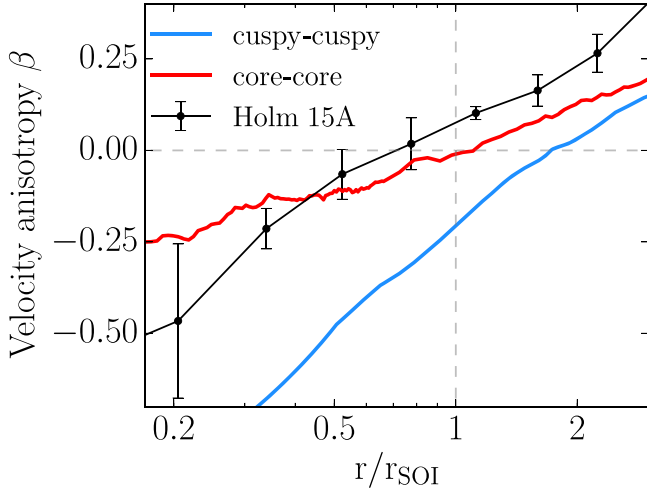


Figure 14. Anisotropy profile $\beta(r)$ of our best-fit dynamical model of Holm 15A averaged over four quadrants compared to numerical merger simulations of binary black hole core scouring from Figure 13, in the same colors as before. Radii are scaled by r_{SOI} .

interaction between the black hole binary that temporarily forms at the center of the remnant galaxy and the surrounding stars with high accuracy. The figure demonstrates that mergers between cuspy progenitors (i.e., mergers between originally coreless progenitor galaxies) lead to slightly different light profiles than do mergers between galaxies that already had cores. The light profile of Holm 15A, in fact, looks very similar to the second type of merger, i.e., between two already cored galaxies⁵ (Figure 13).

The evidence in favor of a core–core merger from the light profile is consistent with the evidence from the orbit distribution that we find in Holm 15A. Figure 14 shows the radial profile of the anisotropy parameter

$$\beta = 1 - \frac{\sigma_t^2}{\sigma_r^2}, \quad (6)$$

where σ_r is the radial and $\sigma_t = \sqrt{(\sigma_\theta^2 + \sigma_\phi^2)}/2$ is the tangential velocity dispersion, computed from the dispersions σ_θ and σ_ϕ in the two angular directions. The figure also includes the results from numerical N -body simulations. It is known that core scouring results in an orbital distribution that is biased increasingly toward tangential orbits ($\beta < 0$) inside the SOI of the black hole as $r \rightarrow 0$ and increasingly toward radial orbits ($\beta > 0$) outside of it, toward larger radii (e.g., Quinlan & Hernquist 1997; Milosavljević & Merritt 2001; Rantala et al. 2018). Tangential anisotropy around SMBHs has been observed in systems of various masses and morphologies (e.g., Verolme et al. 2002; Gebhardt et al. 2003; Houghton et al. 2006; Shapiro et al. 2006; Gebhardt & Thomas 2009; Gültekin et al. 2009; Krajnović et al. 2009; Siopis et al. 2009; Shen & Gebhardt 2010; van den Bosch & de Zeeuw 2010; Gebhardt et al. 2011; Schulze & Gebhardt 2011; McConnell et al. 2012; Walsh et al. 2015; Thomas et al. 2016; Feldmeier-Krause et al. 2017). In core galaxies,

⁵ At roughly $8 \times r_\gamma \sim 40$ kpc (for Holm 15A), the surface brightness of the rescaled core–core remnant drops faster than the that Holm 15A. This could be due to the fact that the merger simulations do not include an extended cD halo. Photometric studies of Holm 15A (e.g., Kluge et al. 2019; Donzelli et al. 2011) suggest an extended stellar envelope starting at $r \gtrsim 35$ kpc. At radii $< 8 \times r_\gamma$, the core–core remnant is remarkably similar to Holm 15A.

specifically, the measured anisotropy is extremely homogeneous and intimately linked to the core region and follows very closely the prediction of N -body merger simulations (Thomas et al. 2014).

In Holm 15A, we see the same behavior: a change from outer radial anisotropy to inner tangential motions roughly at the SOI radius (which is similar to the core size; see Figure 11(f)). The evidence for this comes from the wings of the observed LOSVDs (see Appendix C). However, the central anisotropy in Holm 15A is milder than observed in other core galaxies, which follow the “cuspy–cuspy” line in Figure 14 (Rantala et al. 2018). This difference is actually expected if the direct progenitors of Holm 15A were not cuspy power-law ellipticals but galaxies that already had cores. In the latter case, the anisotropy in the center is predicted to be very similar to the observed orbital structure of Holm 15A (Rantala et al. 2019).⁶

Because cores grow with each merger generation, a core–core merger scenario would plausibly explain the fact that the central region of Holm 15A is fainter than the centers of $\gtrsim 97\%$ of the 164 local ETGs in Lauer et al. (2007a), despite the fact that the galaxy is more luminous than $\gtrsim 90\%$ of the sample ($M_V = -23.8 \pm 0.1$; López-Cruz et al. 2014; see also Figure 12). It would also explain the large core size of Holm 15A. Moreover, it could even provide a reason for Holm 15A’s large cusp radius (Figure 11(e)): in the merger simulation during the core–core merger, M_{BH} doubled while the core radius (described either by r_b or r_γ) roughly tripled in size. This would suggest that in successive core-scouring events, the core grows faster than the central black hole. Similarly, for a sequence of five smaller core scourings due to minor mergers, the remnant also “outgrew” its black hole by a similar factor.

In the merger case, Holm 15A represents a dynamically very evolved galaxy that is possibly one merger generation ahead of cored galaxies like NGC 4874 and NGC 4889 at the center of the Coma cluster. As we showed in the previous subsection, Holm 15A’s high $M_{\text{BH}}/M_{\text{Bu}}$ ratio of $\sim 2\%$ might indicate that the galaxy’s progenitors had already formed at redshifts larger than 1 or 2 and/or that its progenitors were themselves BCGs. Abell 85 has one of the strongest cool cores among X-ray bright clusters (Chen et al. 2007) and is strongly BCG dominated, with Bautz–Morgan morphological type I (Hudson et al. 2010), such that the central parts of the main cluster in fact might have been subject to a slightly accelerated evolution at some point in the past. Previous X-ray studies of Abell 85 had already suggested that the measured temperature and metallicity maps of the cluster were compatible with an intense merger history (e.g., Durret et al. 2005; McDonald et al. 2010).

5.5. Alternative Formation Scenario via AGN Feedback?

Even though the merger scenario provides a consistent explanation for the central light profile shape of the galaxy, the orbital structure, and how both are connected to the mass of the central black hole, we briefly discuss whether the interaction between an AGN and the surrounding stars could serve as an alternative core-formation scenario.

⁶ In the N -body simulations, the final anisotropy profile of an equal-mass core–core merger is very similar to that of the final orbit distribution after a sequence of minor mergers (Rantala et al. 2019). However, the light profile of Holm 15A is more similar to the core–core merger than to the remnant after repeated minor mergers. Further simulations covering a wider range of initial conditions are needed to confirm the connection between anisotropy, profile shape, and merger history.

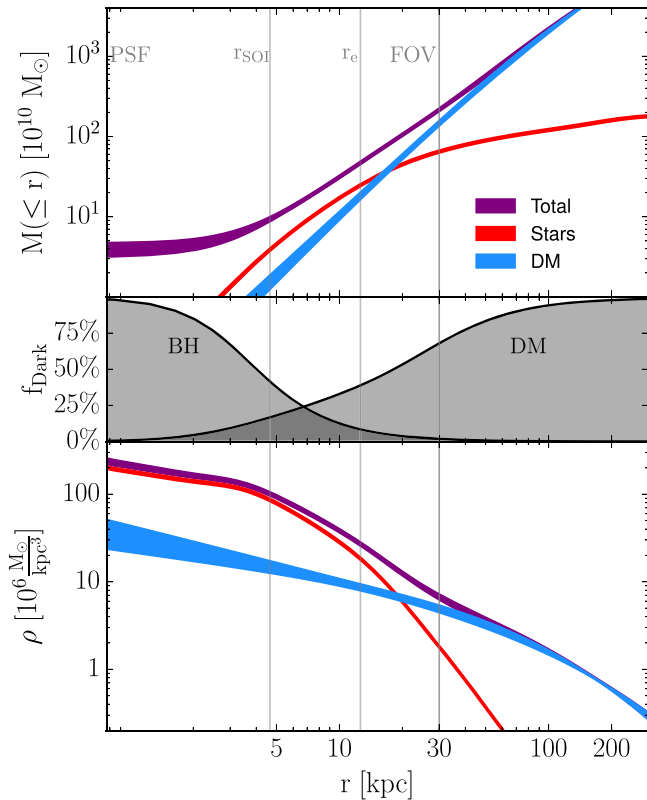


Figure 15. Top panel: enclosed mass profile of the best-fit dynamical model of Holm 15A, separated into total (including black hole; purple), stellar (red), and DM (blue) mass. The broadness of the profiles indicates the variation of best-fit models between the quadrants. The middle panel indicates the fraction of nonluminous mass, i.e., the black hole and DM halo, with respect to the total enclosed mass at a given radius for the best-fit model. The bottom panel shows, correspondingly, the stellar, DM, and total density distributions.

In recent simulations, AGN outflows have been observed to trigger fluctuations of the local gravitational potential, which irreversibly transfer energy to the dark matter and stellar components (Teyssier et al. 2011; Martizzi et al. 2012, 2013; Choi et al. 2018). These simulations produced exponential light profiles, which resemble the cores of ETGs in the sense discussed in the introduction: the central surface brightness is low and the slope of the central surface-brightness profile is shallow. In fact, based on the black hole fundamental plane, it has been argued that many black holes in the BCGs of cool-core clusters could be more massive than predicted by the classical black hole scaling relations, and many would actually be expected to have masses $M_{\text{BH}} > 10^{10} M_{\odot}$ (Phipps et al. 2019; Hlavacek-Larrondo et al. 2012). We are still lacking numerical simulations that study in quantitative detail the effect of AGN feedback on the stellar light distribution and orbital structure. The information contained in the actual orbits of the stars might turn out to be crucial to distinguish between different core-formation scenarios.

5.6. Dark Matter Halo and Stellar Mass-to-light Ratio

Figure 15 shows the underlying stellar, dark matter, and total enclosed mass and density profiles of our best-fit dynamical model of Holm 15A. Apart from the 20% variation in M_{BH} , the quadrants of the galaxy produce a consistent overall mass and density profile.

Using simple stellar population models (Thomas et al. 2003; Maraston & Strömbäck 2011), we find that Holm 15A has a marginally supersolar metallicity, $[Z/H] = 0.08 \pm 0.05$, and is strongly α -enhanced, $[\alpha/\text{Fe}] = 0.25 \pm 0.03$. Assuming a Kroupa stellar IMF, we find a stellar mass-to-light ratio of $\Upsilon_{\text{SSP,Kroupa}} = 2.7 \pm 0.30$ (i band) using methods from either Maraston & Strömbäck (2011) or Conroy et al. (2017). The large $\sim 20\%$ uncertainty of this value is due to the difficulty in determining the age of the stars. Formally, our SSP models fitted stellar ages that exceed the age of the universe. The value of $\Upsilon_{\text{SSP,Kroupa}}$ and its uncertainty are derived from “manually” varying stellar ages between 10 Gyr and 13.8 Gyr while fixing elemental abundances.

Our dynamical mass-to-light ratio of $\Upsilon_{\star} = 4.5 \pm 0.19$ is roughly twice as large as the SSP ratio ($\Upsilon_{\star}/\Upsilon_{\text{SSP,Kroupa}} = 1.7 \pm 0.20$). This is a continuation of a growing trend among recent mass-to-light ratio measurements in massive ETGs from dynamics, lensing, and spectroscopy often finding values larger than predicted by SSP models adopting a Kroupa stellar IMF, $\Upsilon_{\star}/\Upsilon_{\text{SSP,Kroupa}} \gtrsim 1.6$ (e.g., Auger et al. 2010; Treu et al. 2010; Spiniello et al. 2011; Thomas et al. 2011; Cappellari et al. 2012; Conroy & van Dokkum 2012; Tortora et al. 2014; Conroy et al. 2017; Alton et al. 2018; Parikh et al. 2018). This offset is roughly consistent with a mass-to-light ratio implied by a Salpeter-like IMF or might suggest that DM traces the stars. Our stellar-dynamical mass-to-light ratio is based on the assumption that all mass tracing the galaxy’s light profile belongs to the stars of the galaxy. In this case, when parameterizing the inner DM halo as $\rho_{\text{DM}} \sim r^{-\eta}$, we find $\eta = 0.45 \pm 0.16$ out to roughly 50 kpc. This is substantially shallower than predicted by numerical simulations of cold dark matter, $\eta \geq 1$ (e.g., Navarro et al. 1996, 1997; Moore et al. 1998). Combined stellar kinematics and weak & strong lensing studies of local BCGs previously found $\rho_{\text{DM}} \sim r^{-0.5}$ on scales comparable to the effective radius (e.g., Sand et al. 2004, 2008; Newman et al. 2013).

Within the core region, the fraction of DM is $\lesssim 20\%$. However, under the assumption of a Kroupa IMF and that DM traces stars, the fraction of DM within the core region would be roughly 50%, while in the former scenario, equality between the enclosed stellar and DM mass is reached only at $r_{\text{eq}} = 33 \pm 2.5$ kpc (the stellar mass density profile reaches equality with the DM density profile at 28 ± 0.10 kpc). In both scenarios, the mass density distribution of the stars in our best-fit model has a slope similar to that of the distribution of DM inside the core, $\rho_{\text{total}} \sim r^{-0.5}$.

We note that some massive galaxies seem consistent with a low-mass IMF (e.g., Thomas et al. 2016; Collier et al. 2018) and that some fine-tuning is required to consistently combine masses from multiple constraints like lensing, dynamics, or spectroscopy (e.g., Newman et al. 2017). Dynamical and lensing constraints, in general, become model dependent when stars and DM trace each other closely (e.g., Thomas et al. 2011).

6. Summary and Conclusions

We have observed Holm 15A, the BCG of the cool-core galaxy cluster Abell 85, with MUSE. Our observations reveal a galaxy with little rotation ($v_{\text{rot}} < 40 \text{ km s}^{-1}$) and a nearly constant velocity dispersion of $\sigma = 340 \text{ km s}^{-1}$. Toward the center and toward large radii, the velocity dispersion increases slightly.

We use orbit-based, axisymmetric Schwarzschild models to analyze the dynamical structure of Holm 15A and compare them to recent high-resolution N -body simulations of mergers between ETG galaxies that host black holes. Our results indicate the following:

1. Holm 15A hosts a $(4.0 \pm 0.8) \times 10^{10} M_{\odot}$ SMBH at its center, the most massive black hole directly detected via stellar dynamics so far. The black hole constitutes close to 2% of the total stellar mass of the galaxy.
2. Inside of the gravitational SOI of the black hole, $r_{\text{SOI}} = 3.8 \pm 0.37$ kpc, the orbital distribution becomes increasingly tangentially anisotropic. However, the anisotropy inside the core is less tangential than in other big elliptical galaxies with depleted cores.
3. The galaxy’s light profile and the observed mild orbital anisotropy both match remarkably well with predictions from N -body simulations of a merger between two elliptical galaxies that already had depleted cores.
4. The SMBH is roughly nine times larger than expected from the $M_{\text{BH}}-\sigma$ relation and four times larger than expected from the stellar mass of the galaxy when compared to other cored ETGs. However, the offsets are smaller when compared to other BCGs.
5. In core galaxies, black hole masses scale inversely with the central stellar surface brightness μ_0 and central stellar mass density Σ_0 —including in Holm 15A. We show this correlation here for the first time.
6. Even in extreme instances of core formation like in Holm 15A, the core-specific relations $M_{\text{BH}}-\Sigma_0$, $M_{\text{BH}}-\mu_0$, and $r_{\text{SOI}}-r_{\gamma}$, as well as the global galactic relation $M_{\text{BH}}-L_K$ still seem to hold. But the details of the light profile and orbital anisotropy contain valuable information about the specific formation path.
7. Assuming that all the mass that follows the light is stellar, we infer a bottom-heavy IMF, $\Upsilon_{*} = 4.5 \pm 0.19$ (i band), and the inner power-law slope of the DM density distribution to be $\eta = 0.45 \pm 0.16$. Equality between enclosed stellar and DM mass is reached at 33 ± 2.5 kpc. Assuming a Kroupa IMF, $\Upsilon_{\text{SSP,Kroupa}} = 2.7 \pm 0.3$, and DM tracing stars, we infer $\eta \sim 1$ outside of the core and a DM fraction of nearly 50% within the core.

We plan to extend our analysis of the galaxy to triaxial Schwarzschild models. This will allow us to investigate potential systematics related to symmetry assumptions in the modeling and related to possible substructure near the very center of the galaxy.

Our results suggest that the exact shape of the central light profile as well as the details of the distribution of stellar orbits in the center contain valuable information about the merging history of very massive galaxies. For example, extreme instances of core formation could potentially lead to remnant surface-brightness profiles diverging from the typical core-Sérsic profiles of “classical” cored galaxies. Hydrodynamical cosmological simulations have also produced large stellar and DM cores through AGN feedback. It will be interesting to compare the anisotropy profiles predicted by these simulations with measurements in observed galaxies. More extensive simulations are also required to investigate in detail the effect of core scouring under different initial conditions of the progenitor galaxies and on the DM halo.

The SMBH of Holm 15A is a candidate system for direct imaging of its SOI. The photon ring radius is $\sqrt{27} GM_{\text{BH}}/c^2 = 2100 \pm 410$ au. At redshift $z = 0.055$, this corresponds to an area spanning $18 \pm 3.7 \mu\text{as}$ on the sky, only slightly smaller than the current minimum angular resolution of the Event Horizon Telescope, 25 mas (Event Horizon Telescope Collaboration et al. 2019).

We acknowledge the support by the DFG Cluster of Excellence “Origin and Structure of the Universe.” The dynamical models have been done on the computing facilities of the Computational Center for Particle and Astrophysics (C2PAP), and we are grateful for the support by A. Krukau and F. Beaujean through the C2PAP. We are grateful to Hans Böhringer for valuable discussions and suggestions.

Appendix A

Parametric Analysis of Wendelstein Photometry

A.1. 1D Analysis of the Wendelstein Image

The best-fit parameters of the various models we fit to the 1D i -band Wendelstein image of Holm 15A in Section 2.2 are shown in Table 2. In the table, the parameters of the different models are separated into components: parameters of the core-Sérsic function $I_{\text{CS}}(r_b, n, \alpha, \gamma, n_1, r_{e,1})$ (see Equation (2) from Rusli et al. 2013a), outer Sérsic function $I_{\text{S}}(n_2, \mu_{e,2}, r_{e,2})$ (see the outer Sérsic components in the Sérsic+Sérsic models from Kluge et al. 2019; Equations (11) and (12)), and Nuker function $I_{\text{N}}(r_b, n, \alpha, \beta, \gamma)$ (see Equation (10) from Lauer et al. 2007b).

A.2. 2D Analysis of the Wendelstein Image

As described in Section 2.2, a detailed investigation of the 1D light profile of Holm 15A did not provide strong evidence for a break radius that separates the inner core from the rest of the galaxy. Here, we describe in detail our 2D fits to the i -band image using IMFIT (Erwin 2015). Our goal in performing these fits was to better understand the structure of the unusual core region of Holm 15A, in particular, whether or not a 2D analysis including the ellipticity structure of the galaxy would help in constraining the size of the galaxy’s core.

To have a fully independent analysis, we created ellipse fits to the Wendelstein image using the IRAF task “ellipse” (Carter 1978; Jedrzejewski 1987), complementary to our analysis in Section 2. The surface-brightness profile and isophote shape measurements out to $250''$ (see Figure 16) are fully compatible with the results from the other method (see Figures 1 and 2).

Beyond about $140''$, the position angle twists by about 90° , and the ellipticity drops from ~ 0.4 to ~ 0.2 (see Figure 16). Meanwhile, the centers of the fitted ellipses begin varying by as much as $\sim 15''$. It is not clear how much of this represents a real change in the isophotes, e.g., if this is related to a transition to intracluster light, or how much is simply an artifact of the increasingly low S/N. We therefore confine our 2D fitting to $a < 140''$. In the interval between $3''$ and at least $100''$, the position angle is remarkably stable, suggesting that Holm 15A might be close to rotational symmetry.

Toward the very center, the change in position angle implies that the isophotes start rotating but at the same time the galaxy becomes significantly rounder.

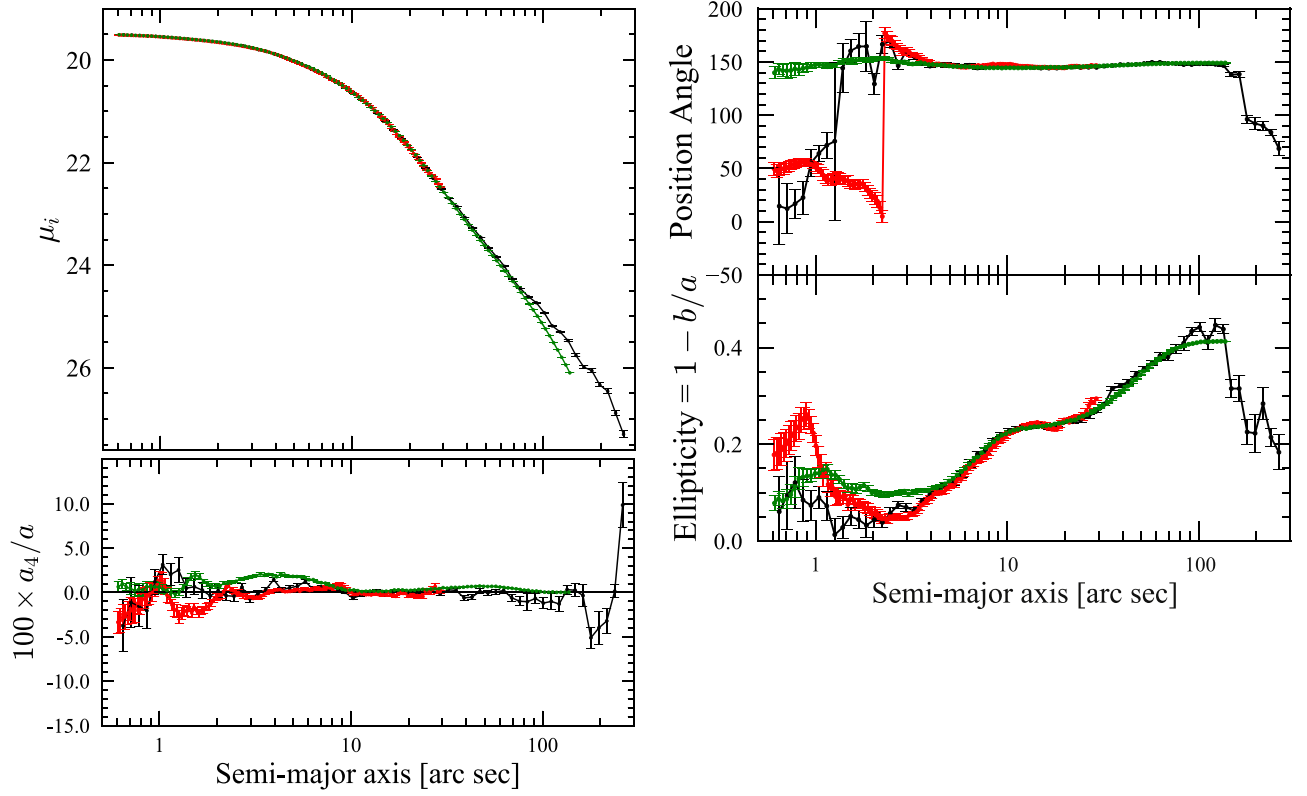


Figure 16. Ellipse fits to the isophotes of Holm 15A for our *i*-band Wendelstein image (black), the red image extracted from our MUSE data cube (red), and the best-fitting 2D model image (green). From top to bottom, left to right, the panels show *i*-band surface brightness, position angle, ellipticity, $a_4/a = \sqrt{b/a} * \cos 4\theta$ parameter vs. semimajor axis on a logarithmic scale. The logarithmic scale is shown for the sake of completeness and complementary to the $r^{1/4}$ and linear scale of Figure 1.

Table 2

Parameters of Our Best-fit Models to the 1D *i*-band Wendelstein Image of Holm 15A, Separated into Components: cSS: Core-Sérsic+(outer) Sérsic Fit to the Light Profile out to $200''$ with All Parameters Fit Simultaneously

Model	Parameter	cSS	cSS($r_{\max} = 4''$)	cSS($r_{\max} = 12''$)	$N(r_{\max} = 20'')$	$N(r_{\max} = 70'')$	Units
Core-Sérsic	r_b	8.96	3.72	5.52	arcsec
	μ_b	20.6	20.1	20.1	mag arcsec ⁻²
	α	1.71	7.96	2.65	
	γ	0.09	0.00	0.13	
	n_1	5.24	1.38	2.52	
	$r_{e,1}$	5.20	14.4	14.9			
Outer Sérsic	n_2	2.90	5.37	3.30	
	$\mu_{e,2}$	28.7	28.6	28.8	mag arcsec ⁻²
	$r_{e,2}$	917.0	647.3	952.5	arcsec
Nuker	r_b	11.09	8.16	arcsec
	μ_b	20.9	20.45	mag arcsec ⁻²
	α	1.50	2.30	
	β	2.66	2.1	
	γ	0.06	0.15	

Note. cSS($r_{\max} = 4''$): Core-Sérsic+(outer) Sérsic fit to the light profile out to $200''$ but with the parameters fit in two steps as described in Section 2.2 with $r_{\max} = 4''$. cSS($r_{\max} = 12''$): same as the previous model, but with $r_{\max} = 12''$. $N(r_{\max} = 20''$): Nuker profile fit to the the data within $r_{\max} = 20''$ with all five parameters simultaneously. $N(r_{\max} = 70''$): same as the previous model, but with $r_{\max} = 70''$.

Because the region of the core is close to circular, the actual isophotes do not show any visible twists or distortions (Figure 17(a)).

We find that fitting the image with an inner Sérsic function that is near-exponential in shape, with a Sérsic index of $n = 0.99$ and an outer Sérsic component with $n = 1.48$, results

in a good fit to the Wendelstein data. The inner component is consistent with the Sérsic+Sérsic model listed in Kluge et al. (2019), though the outer Sérsic index is smaller. It is also smaller than for our core-Sérsic+Sérsic models from Section 2.2 (see Table 2). It is however consistent with models from Donzelli et al. (2011), who found that Holm 15A's

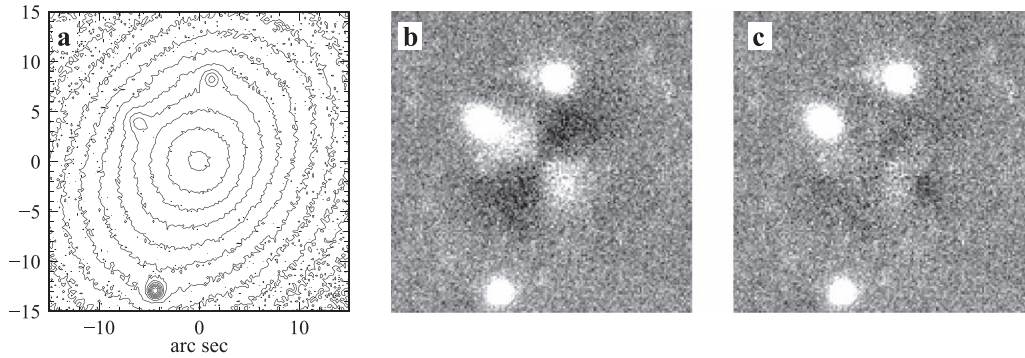


Figure 17. Data and residuals for 2D fits. (a) Inner isophotes for Wendelstein *i*-band image of Holm 15A; peak galaxy intensity is ≈ 700 counts/pixel. (b) Residuals for the core-Sérsic+Sérsic model (data – model), plotted on a linear scale from -25 (black) to $+25$ (white) counts/pixel. (c) Same as for panel b, but for the core-Sérsic+Sérsic+GaussianRing3D model.

R-band light profile is well fit by the sum of two exponential functions (i.e., equivalent to a Sérsic+Sérsic model, with both $n \sim 1$). Similar results were obtained from the 2D analysis of a CFHT *r*-band image by Bonfini et al. (2015).

However, replacing the inner, exponential-like Sérsic component with a core-Sérsic component did not significantly improve the quality of the fit relative to the coreless model. This reflects the radial trend of the observed light profile shown in the bottom panel of Figure 1—the central light profile of Holm 15 is approximately exponential up to $\sim 25''$.

Nonetheless, there was still a distinct, bilobed excess in the residual image from the both the double-Sérsic and the core-Sérsic+Sérsic fit, on a scale of $a \sim 4''$ (Figure 17(b)). We therefore experimented with adding additional components to the model. The best result was with the GaussianRing3D function of IMFIT, which performs line-of-sight integration for an inclined ring with a Gaussian radial density and an exponential vertical density. The final result was a fit with central residuals, which were almost completely lacking in any systematics (see Figure 17(c)). The “ring” component has a semimajor axis of $4.1''$, a position angle of 53° —almost perpendicular to the Sérsic components—and is intrinsically circular, viewed at an inclination of 68° . We also note that this may be consistent with the extra Gaussian-like Sérsic component (with $n = 0.3$)—with a position angle of $\sim 55^\circ$ —which Bonfini et al. (2015) added to their 2D fits as a “corrective” component. We emphasize that this is a purely empirically chosen function which produces approximately the right excess light to minimize the residuals; it is not necessarily evidence for an actual inclined ring. The parameters of the best-fit 2D model are listed in Table 3.

In summary, while the 2D analysis provides somewhat more stable fit parameters, it confirms the results from Section 2.2, in particular the lack of a clear break radius. In the 2D analysis, we assume a spatially constant flattening for each individual component. This might imply that the components simply trace the structure of the ellipticity profile of the galaxy and this, in turn, could explain why the parameters of the 2D fits turn out to be more stable than those in the 1D analysis. It is not clear at the moment how much or which physical information is encoded in the ellipticity profile of the galaxies. Likewise, it is not clear how physically significant the extra-light ring might be, which has a total luminosity comparable to the expected amount of stars ejected from the center by an SMBH binary, i.e., the extra light is of a similar order $\sim 0.5 \times 10^{10} L_\odot$ to the missing light determined in Section 2.2. Comparing the

Table 3
Best-fit IMFIT Model for the *i*-band Image of Holm 15A

Component	Parameter	Value	Units
Core-Sérsic	PA	141.9 ± 0.2	deg
	ϵ	0.187 ± 0.002	
	n	0.965 ± 0.005	
	I_b	20.040 ± 0.012	mag arcsec $^{-2}$
	r_e	12.87 ± 0.04	arcsec
	r_b	2.57 ± 0.05	arcsec
	α	12.15 ± 4.1	
Sérsic	γ	0.096 ± 0.007	
	PA	149.0 ± 0.1	deg
	ϵ	0.413 ± 0.003	
	n	1.69 ± 0.03	
GaussianRing3D	I_e	24.035 ± 0.016	mag arcsec $^{-2}$
	r_e	60.67 ± 0.48	arcsec
GaussianRing3D	PA	52.1 ± 0.9	deg
	inclination	81.8 ± 1.5	deg
	J_0	1.08 ± 0.03	counts pixel $^{-3}$
	a	4.37 ± 0.07	arcsec
	σ	1.76 ± 0.05	arcsec
	h_z	2.78 ± 0.10	arcseconds

Note. Column 1: component used in fit. Column 2: parameter. Column 3: best-fit value for parameter and $1-\sigma$ confidence limits from 200 rounds of bootstrap resampling. Column 4: units. Note that for the GaussianRing3D component, we fixed the ring PA and ellipticity to both be zero, so these are not listed in the table.

distribution of stars in Holm 15A to that of other cored ETGs (see Figure 1) makes clear that Holm 15A is not only characterized by an extreme deficit of light in the inner core but also by an excess of light adjacent to the core. This light “excess,” however, extends well beyond the extra-light ring (roughly out to $20''$).

Appendix B Stellar Kinematics

B.1. Kinematics of Holm 15A Compared to MASSIVE Survey ETGs

To better understand Holm 15A’s place among other known massive ETGs, we will compare its stellar kinematics to ETGs from the MASSIVE survey (Ma et al. 2014 and subsequent MASSIVE survey papers).

Characterizing Holm 15A’s velocity dispersion profile, $\sigma(r)$ (see Section 3.2) by fitting a combined power-law profile as

suggested by Veale et al. (2018) in their study of the 90 ETGs of the MASSIVE survey, we find an inner logarithmic slope $\gamma_{\text{inner}} = -0.017 \pm 0.007$ of the σ profile at ~ 2 kpc and an outer logarithmic slope $\gamma_{\text{outer}} = 0.029 \pm 0.009$ at ~ 20 kpc. Roughly 90% of BCGs in the MASSIVE survey have $\gamma_{\text{inner}} \leq 0$ and $\sim 60\%$ with $\gamma_{\text{outer}} \geq 0$. Moreover, for the 11 most massive BCGs in their sample with $M_* \sim 10^{12} M_{\odot}$, $\gamma_{\text{inner}} \leq 0$, and $\gamma_{\text{outer}} \geq 0$ for all except one. The scatter in γ_{inner} and γ_{outer} between these 11 most massive BCGs is quite high, $\bar{\gamma}_{\text{inner}} = -0.040 \pm 0.055$ and $\bar{\gamma}_{\text{outer}} = 0.088 \pm 0.084$. Nonetheless, statistically, their overall rather flat $\sigma(r)$ profiles are similar to the one in Holm 15A, even though the galaxy's average velocity dispersion within one effective radius $\sigma_e \sim 340 \text{ km s}^{-1}$ is slightly higher compared to these BCGs $\sim 300 \text{ km s}^{-1}$.

The parameter h_4 in our measured kinematic profile starts out at ~ 0.07 within 2 kpc and rises to $\gtrsim 0.1$ along the major axis toward the edges of the MUSE FOV. All 11 of the most massive MASSIVE BCGs share this trend of $h_4 > 0$ over their respective radial coverage and all but one have positive h_4 gradients toward larger radii. Similarly as with σ , average values for h_4 within r_e are larger for Holm 15A, $h_{4,e} \sim 0.08$, than for those other BCGs where $h_{4,e} \lesssim 0.06$. Essentially all galaxies in the MASSIVE sample with $h_{4,e} > 0.05$ (BCG or not) have within the central 2 kpc supersolar $[\alpha/\text{Fe}] > 0.2$ and

most galaxies with $h_{4,e} > 0$ have $[\text{Fe}/\text{H}] \leq 0$ (Greene et al. 2019).

Using stellar population models of Lick indices (Thomas et al. 2003; Maraston & Strömbäck 2011), we find abundance ratios in good agreement with those in Holm 15A: $[\alpha/\text{Fe}] = 0.25 \pm 0.03$ and $[\text{Fe}/\text{H}] = -0.011 \pm 0.008$.

Overall, we find stellar kinematics in Holm 15A similar to those of other known massive ETGs. Indeed, from a stellar kinematic point of view, we find no indication that Holm 15A is anything other than a higher-mass extrapolation of known massive ETGs in the local universe, the vast majority of which is cored (e.g., Lauer et al. 2007a; Kormendy & Ho 2013; Krajnović et al. 2013).

B.2. Nonparametric Kinematics Compared to Gauss–Hermite Polynomials

We compare the nonparametric stellar kinematics we measured with our own code with those derived parametrically with pPXF. This is illustrated in Figure 18 for all bins of our FOV (i.e., LOSVDs from all quadrants). Both kinematic profiles are, for the purpose of illustration, parameterized via Gaussian times third- to fourth-order Gauss–Hermite polynomials. As the distribution of differences in the right column of the figure show, both methods agree within their uncertainties.

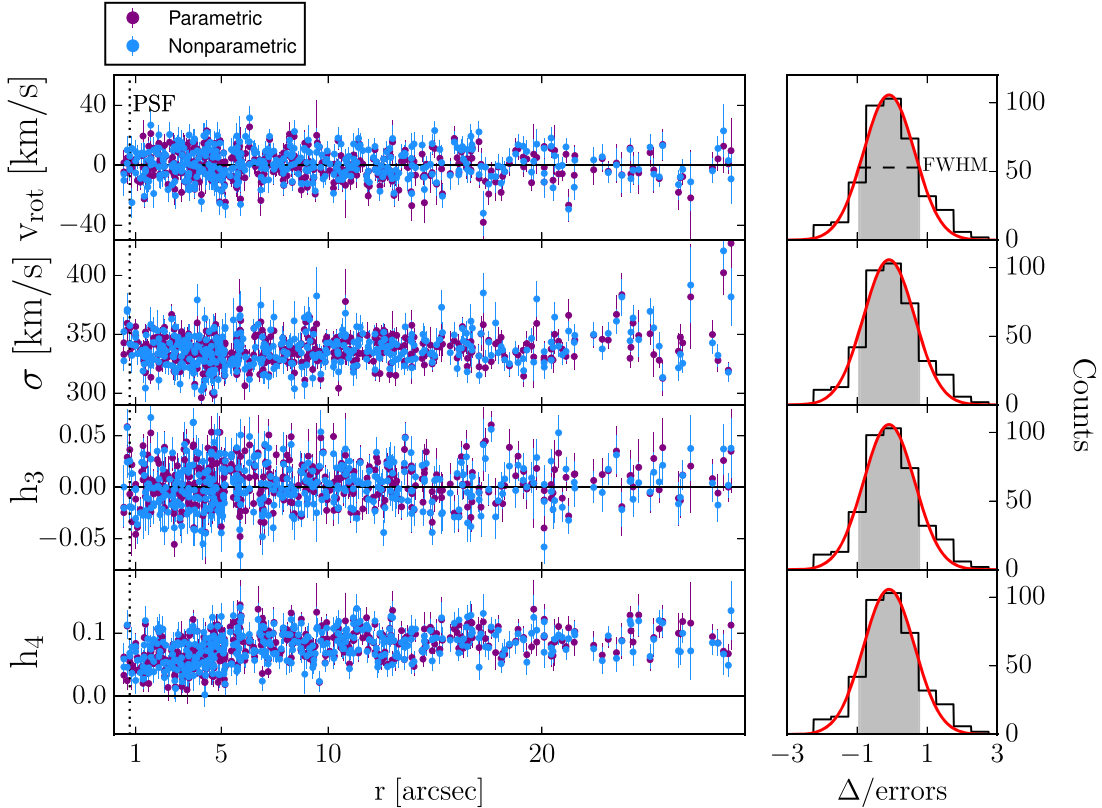


Figure 18. Left column: resulting kinematic profiles over radius of the two kinematic measurements performed in this study, one using pPXF (purple points) and one with our own nonparametric code (blue points). Panels show, from top to bottom, radial profiles for v_{rot} , σ , h_3 , and h_4 , including statistical uncertainties. For this plot, nonparametric LOSVDs were fitted with a Gaussian times third- to fourth-order Gauss–Hermite polynomials. In our final modeling, nonparametric LOSVDs are used, but these parameters still allow us to showcase the kinematic structure of Holm 15A. Right column, from top to bottom: corresponding distributions of the difference Δ (black) between pPXF and nonparametric LOSVD Gauss–Hermite parameters over the statistical uncertainties of the pPXF values. Each distribution is fit with a Gaussian (red) with the FWHM of each distribution indicated by gray shaded areas.

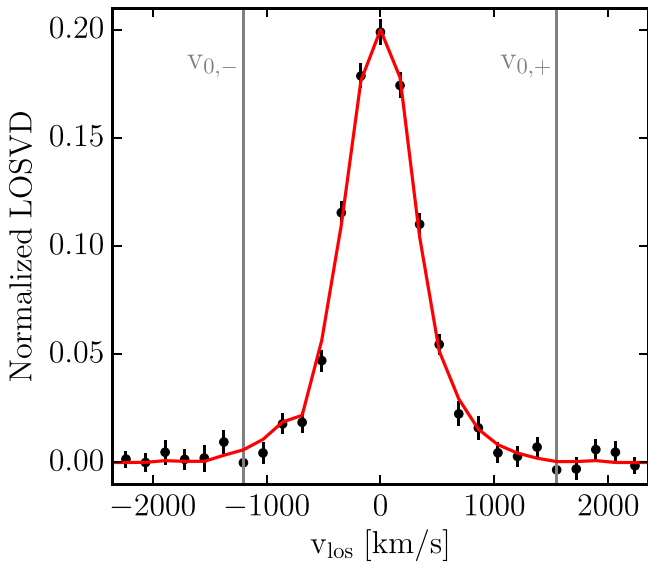


Figure 19. Example of a nonparametric fit of our dynamical model (red line) to a nonparametric LOSVD from the center of Holm 15A (black points). The cutoff velocities of the LOSVD are marked as gray, vertical lines.

Appendix C

Nonparametric Dynamical Modeling: Escape Velocities

Here, we will briefly discuss the connection between the wings of the observed LOSVDs on the one side and the mass distribution and orbital structure on the other. Figure 19 shows an example of a nonparametric LOSVD measured near the center of Holm 15A together with the corresponding LOSVD from our best-fit dynamical model. We define the cutoff velocity v_0 of any LOSVD as the mean $v_0 = (v_{0,+} + v_{0,-})/2$. If v_{peak} denotes the line-of-sight velocity at which the LOSVD peaks, then $v_{0,+}$ is the smallest zero of the LOSVD for $v_{\text{los}} > v_{\text{peak}}$, and $v_{0,-}$ is the absolute value of the largest zero of the LOSVD for $v_{\text{los}} < v_{\text{peak}}$, respectively. For Holm 15A, this definition is sufficient as there is almost no detectable rotation, and the LOSVDs are largely symmetric with respect to v_{peak} . For the LOSVDs in Figure 19, we measure $v_0 \sim 1375 \text{ km s}^{-1}$.

Figure 20 shows all the measured cutoff velocities v_0 from our MUSE observations together with the escape velocity curves $v_{\text{esc}}(r)$ of the four best-fit models for the four quadrants of the galaxy. Here, we define v_{esc} relative to the maximum radius that is sampled by the orbit library. The uncertainties of the cutoff velocities are measured via the difference between values of v_0 determined from $\text{LOSVD}(v_{\text{los}}) + \Delta\text{LOSVD}(v_{\text{los}})$ and $\text{LOSVD}(v_{\text{los}}) - \Delta\text{LOSVD}(v_{\text{los}})$. Outside the core ($r \gtrsim 5 \text{ kpc}$), the best-fit $v_{\text{esc}}(r)$ curves follow closely the maximum observed cutoff velocities v_0 . This is expected in a radially anisotropic system where a significant number of stars is populated on weakly bound, radially extended orbits. The less bound and the more radial the orbit is, the closer the orbital velocity gets to v_{esc} . Indeed, outside the core region, our best-fit models become increasingly radially anisotropic (see Figure 14).

The situation changes toward the center of the galaxy, where the gravitational well is deepest. The observed cutoff velocities decrease at small radii, whereas the escape velocity necessarily increases. This can only be explained as an anisotropy effect: inside the SOI of the central black hole (indicated by the vertical line), the orbit distribution becomes tangential (see

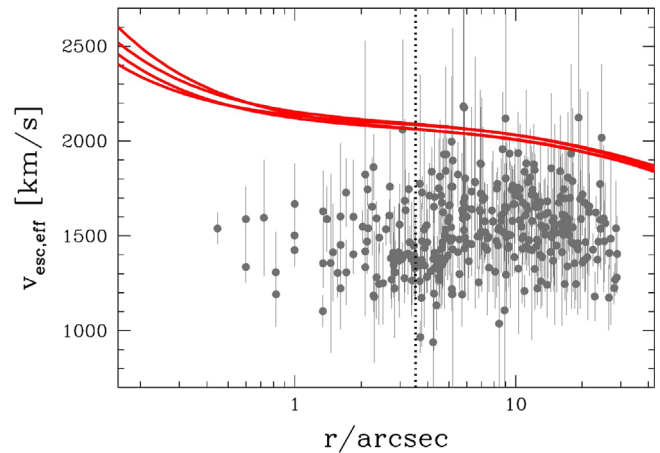


Figure 20. Effective escape velocities measured for every LOSVD of our FOV (gray points) and the escape velocities of the gravitational potential of our best-fit dynamical model of Holm 15A (four red lines, one for each quadrant) vs. radius. The vertical dotted line indicates the SOI of the black hole.

Figure 14). Because only stars on the most radial orbits can move with velocities up to the escape velocity and those stars are missing, the LOSVDs no longer extend to v_{esc} but vanish at smaller velocities.

The uncertainties in the observed cutoff velocities are large (due to the noise in the wings of the LOSVDs). This is indicated by the large scatter in values of v_0 . However, the figure clearly demonstrates the importance of the information contained in the wings of the LOSVDs for both the gravitational potential as well as for the orbital structure.

ORCID iDs

Kianusch Mehrgan <https://orcid.org/0000-0002-9821-3535>
 Jens Thomas <https://orcid.org/0000-0003-2868-9244>
 Roberto Saglia <https://orcid.org/0000-0003-0378-7032>
 Peter Erwin <https://orcid.org/0000-0003-4588-9555>
 Ralf Bender <https://orcid.org/0000-0001-7179-0626>
 Matthias Kluge <https://orcid.org/0000-0002-9618-2552>
 Maximilian Fabricius <https://orcid.org/0000-0002-7025-6058>

References

- Alton, P. D., Smith, R. J., & Lucey, J. R. 2018, *MNRAS*, **478**, 4464
 Arnaboldi, M., Gerhard, O., Freeman, K. C., et al. 2006, in IAU Symp. 234, Planetary Nebulae in our Galaxy and Beyond, ed. M. J. Barlow & R. H. Méndez (Cambridge: Cambridge Univ. Press), 337
 Audet, C., & Dennis, J., Jr. 2006, *SJCO*, **17**, 188
 Audet, C., & Hare, W. 2017, *Derivative-Free and Blackbox Optimization* (Berlin: Springer), 302
 Auger, M. W., Treu, T., Gavazzi, R., et al. 2010, *ApJL*, **721**, L163
 Begelman, M. C., Blandford, R. D., & Rees, M. J. 1980, *Natur*, **287**, 307
 Bender, R. 1990, *A&A*, **229**, 441
 Bender, R., & Moellenhoff, C. 1987, *A&A*, **177**, 71
 Bennert, V. N., Auger, M. W., Treu, T., Woo, J.-H., & Malkan, M. A. 2011, *ApJ*, **742**, 107
 Bogdán, Á., Lovisari, L., Volonteri, M., & Dubois, Y. 2018, *ApJ*, **852**, 131
 Bonfini, P., Dullo, B. T., & Graham, A. W. 2015, *ApJ*, **807**, 136
 Boylan-Kolchin, M., Ma, C.-P., & Quataert, E. 2006, *MNRAS*, **369**, 1081
 Cappellari, M. 2016, *ARA&A*, **54**, 597
 Cappellari, M. 2017, *MNRAS*, **466**, 798
 Cappellari, M., & Copin, Y. 2003, *MNRAS*, **342**, 345
 Cappellari, M., McDermid, R. M., Alatalo, K., et al. 2012, *Natur*, **484**, 485
 Carter, D. 1978, *MNRAS*, **182**, 797
 Chen, Y., Reiprich, T. H., Böhringer, H., Ikebe, Y., & Zhang, Y. Y. 2007, *A&A*, **466**, 805

- Choi, E., Somerville, R. S., Ostriker, J. P., Naab, T., & Hirschmann, M. 2018, *ApJ*, **866**, 91
- Collier, W. P., Smith, R. J., & Lucey, J. R. 2018, *MNRAS*, **478**, 1595
- Conroy, C., & van Dokkum, P. G. 2012, *ApJ*, **760**, 71
- Conroy, C., van Dokkum, P. G., & Villaume, A. 2017, *ApJ*, **837**, 166
- De Lucia, G., Springel, V., White, S. D. M., Croton, D., & Kauffmann, G. 2006, *MNRAS*, **366**, 499
- Decarli, R., Falomo, R., Treves, A., et al. 2010, *MNRAS*, **402**, 2453
- Donzelli, C. J., Muriel, H., & Madrid, J. P. 2011, *ApJS*, **195**, 15
- Dullo, B. T., & Graham, A. W. 2014, *MNRAS*, **444**, 2700
- Dullo, B. T., Graham, A. W., & Knapen, J. H. 2017, *MNRAS*, **471**, 2321
- Durret, F., Lima Neto, G. B., & Forman, W. 2005, *A&A*, **432**, 809
- Ebisuzaki, T., Makino, J., & Okumura, S. K. 1991, *Natur*, **354**, 212
- Emsellem, E., Cappellari, M., Krajnović, D., et al. 2011, *MNRAS*, **414**, 888
- Erwin, P. 2015, *ApJ*, **799**, 226
- Event Horizon Telescope Collaboration, Akiyama, K., Alberdi, A., et al. 2019, *ApJL*, **875**, L4
- Faber, S. M., Dressler, A., Davies, R. L., et al. 1987, in *Nearly Normal Galaxies. From the Planck Time to the Present*, ed. S. M. Faber (New York: Springer), 175
- Faber, S. M., Tremaine, S., Ajhar, E. A., et al. 1997, *AJ*, **114**, 1771
- Fabricius, M. H., Grupp, F., Bender, R., et al. 2012, *Proc. SPIE*, **8446**, 84465K
- Feldmeier-Krause, A., Zhu, L., Neumayer, N., et al. 2017, *MNRAS*, **466**, 4040
- Ferland, G. J., Fabian, A. C., Hatch, N. A., et al. 2008, *MNRAS*, **386**, L72
- Ferland, G. J., Fabian, A. C., Hatch, N. A., et al. 2009, *MNRAS*, **392**, 1475
- Fogarty, L. M. R., Scott, N., Owers, M. S., et al. 2014, *MNRAS*, **443**, 485
- Freudling, W., Romaniello, M., Bramich, D. M., et al. 2013, *A&A*, **559**, A96
- Gebhardt, K., Adams, J., Richstone, D., et al. 2011, *ApJ*, **729**, 119
- Gebhardt, K., & Thomas, J. 2009, *ApJ*, **700**, 1690
- Gebhardt, K., Richstone, D., Tremaine, S., et al. 2003, *ApJ*, **583**, 92
- Gerhard, O., Arnaboldi, M., Freeman, K. C., et al. 2007, *A&A*, **468**, 815
- Graham, A. W., Erwin, P., Trujillo, I., & Asensio Ramos, A. 2003, *AJ*, **125**, 2951
- Greene, J. E., Veale, M., Ma, C.-P., et al. 2019, *ApJ*, **874**, 66
- Gültekin, K., Richstone, D. O., Gebhardt, K., et al. 2009, *ApJ*, **695**, 1577
- Hills, J. G., & Fullerton, L. W. 1980, *AJ*, **85**, 1281
- Hlavacek-Larrondo, J., Fabian, A. C., Edge, A. C., & Hogan, M. T. 2012, *MNRAS*, **424**, 224
- Hopkins, P. F., Lauer, T. R., Cox, T. J., Hernquist, L., & Kormendy, J. 2009, *ApJS*, **181**, 486
- Houghton, R. C. W., Magorrian, J., Sarzi, M., et al. 2006, *MNRAS*, **367**, 2
- Hudson, D. S., Mittal, R., Reiprich, T. H., et al. 2010, *A&A*, **513**, A37
- Jedrzejewski, R. I. 1987, *MNRAS*, **226**, 747
- Kauffmann, G., Heckman, T. M., Tremonti, C., et al. 2003, *MNRAS*, **346**, 1055
- Kelly, B. C. 2007, *ApJ*, **665**, 1489
- Khochfar, S., & Burkert, A. 2003, *ApJL*, **597**, L117
- Kluge, M., Neureiter, B., Riffesser, A., et al. 2019, arXiv:1908.08544
- Kormendy, J. 1985, *ApJL*, **292**, L9
- Kormendy, J., & Bender, R. 2009, *ApJL*, **691**, L142
- Kormendy, J., & Bender, R. 2013, *ApJL*, **769**, L5
- Kormendy, J., & Ho, L. C. 2013, *ARA&A*, **51**, 511
- Kosyra, R., Gössl, C., Hopp, U., et al. 2014, *ExA*, **38**, 213
- Krajnović, D., McDermid, R. M., Cappellari, M., & Davies, R. L. 2009, *MNRAS*, **399**, 1839
- Krajnović, D., Karick, A. M., Davies, R. L., et al. 2013, *MNRAS*, **433**, 2812
- Kulkarni, G., & Loeb, A. 2012, *MNRAS*, **422**, 1306
- Lang-Bardl, F., Hodapp, K., Jacobson, S., et al. 2010, *Proc. SPIE*, **7735**, 77353Q
- Lang-Bardl, F., Bender, R., Goessl, C., et al. 2016, *Proc. SPIE*, **9908**, 990844
- Lauer, T. R. 1985, *ApJ*, **292**, 104
- Lauer, T. R., Ajhar, E. A., Byun, Y.-I., et al. 1995, *AJ*, **110**, 2622
- Lauer, T. R., Gebhardt, K., Faber, S. M., et al. 2007a, *ApJ*, **664**, 226
- Lauer, T. R., Faber, S. M., Richstone, D., et al. 2007b, *ApJ*, **662**, 808
- Le Digabel, S. 2011, *ACM Transactions on Mathematical Software*, **37**, 1
- López-Cruz, O., Añorve, C., Birkinshaw, M., et al. 2014, *ApJL*, **795**, L31
- Lucy, L. B. 1974, *AJ*, **79**, 745
- Ma, C.-P., Greene, J. E., McConnell, N., et al. 2014, *ApJ*, **795**, 158
- Madrid, J. P., & Donzelli, C. J. 2016, *ApJ*, **819**, 50
- Magorrian, J. 1999, *MNRAS*, **302**, 530
- Maraston, C., & Strömbäck, G. 2011, *MNRAS*, **418**, 2785
- Martizzi, D., Teyssier, R., & Moore, B. 2013, *MNRAS*, **432**, 1947
- Martizzi, D., Teyssier, R., Moore, B., & Wentz, T. 2012, *MNRAS*, **422**, 3081
- McConnell, N. J., & Ma, C.-P. 2013, *ApJ*, **764**, 184
- McConnell, N. J., Ma, C.-P., Murphy, J. D., et al. 2012, *ApJ*, **756**, 179
- McDonald, M., Veilleux, S., Rupke, D. S. N., & Mushotzky, R. 2010, *ApJ*, **721**, 1262
- Merloni, A., Bongiorno, A., Bolzonella, M., et al. 2010, *ApJ*, **708**, 137
- Merritt, D. 2006, *ApJ*, **648**, 976
- Merritt, D. 2013, *Dynamics and Evolution of Galactic Nuclei* (Princeton, NJ: Princeton Univ. Press)
- Merritt, D., & Milosavljević, M. 2005, *LRR*, **8**, 8
- Meyers, J. 2015, linmix, <https://github.com/jmeyers314/linmix>, GitHub
- Milosavljević, M., & Merritt, D. 2001, *ApJ*, **563**, 34
- Moore, B., Governato, F., Quinn, T., Stadel, J., & Lake, G. 1998, *ApJL*, **499**, L5
- Naab, T., Johansson, P. H., & Ostriker, J. P. 2009, *ApJL*, **699**, L178
- Naab, T., Khochfar, S., & Burkert, A. 2006, *ApJL*, **636**, L81
- Navarro, J. F., Frenk, C. S., & White, S. D. M. 1996, *ApJ*, **462**, 563
- Navarro, J. F., Frenk, C. S., & White, S. D. M. 1997, *ApJ*, **490**, 493
- Newman, A. B., Smith, R. J., Conroy, C., Villaume, A., & van Dokkum, P. 2017, *ApJ*, **845**, 157
- Newman, A. B., Treu, T., Ellis, R. S., & Sand, D. J. 2013, *ApJ*, **765**, 25
- Ogrea, G. A., Hatch, N. A., Simionescu, A., et al. 2010, *MNRAS*, **406**, 354
- Oser, L., Ostriker, J. P., Naab, T., Johansson, P. H., & Burkert, A. 2010, *ApJ*, **725**, 2312
- Parikh, T., Thomas, D., Maraston, C., et al. 2018, *MNRAS*, **477**, 3954
- Phipps, F., Bogdán, Á., Lovisari, L., et al. 2019, *ApJ*, **875**, 141
- Planck Collaboration, Aghanim, N., Akrami, Y., et al. 2018, arXiv:1807.06209
- Quinlan, G. D., & Hernquist, L. 1997, *NewA*, **2**, 533
- Rantala, A., Johansson, P. H., Naab, T., Thomas, J., & Frigo, M. 2018, *ApJ*, **864**, 113
- Rantala, A., Johansson, P. H., Naab, T., Thomas, J., & Frigo, M. 2019, *ApJL*, **872**, L17
- Richstone, D. O., & Tremaine, S. 1988, *ApJ*, **327**, 82
- Rusli, S. P., Erwin, P., Saglia, R. P., et al. 2013a, *AJ*, **146**, 160
- Rusli, S. P., Thomas, J., Saglia, R. P., et al. 2013b, *AJ*, **146**, 45
- Saglia, R. P., Opitsch, M., Erwin, P., et al. 2016, *ApJ*, **818**, 47
- Sánchez-Blázquez, P., Peletier, R. F., Jiménez-Vicente, J., et al. 2006, *MNRAS*, **371**, 703
- Sand, D. J., Treu, T., Ellis, R. S., Smith, G. P., & Kneib, J.-P. 2008, *ApJ*, **674**, 711
- Sand, D. J., Treu, T., Smith, G. P., & Ellis, R. S. 2004, *ApJ*, **604**, 88
- Schulze, A., & Gebhardt, K. 2011, *ApJ*, **729**, 21
- Schwarzschild, M. 1979, *ApJ*, **232**, 236
- Shapiro, K. L., Cappellari, M., de Zeeuw, T., et al. 2006, *MNRAS*, **370**, 559
- Shen, J., & Gebhardt, K. 2010, *ApJ*, **711**, 484
- Siopis, C., Gebhardt, K., Lauer, T. R., et al. 2009, *ApJ*, **693**, 946
- Spiniello, C., Koopmans, L. V. E., Trager, S. C., Czoske, O., & Treu, T. 2011, *MNRAS*, **417**, 3000
- Teyssier, R., Moore, B., Martizzi, D., Dubois, Y., & Mayer, L. 2011, *MNRAS*, **414**, 195
- Thomas, D., Maraston, C., & Bender, R. 2003, *MNRAS*, **339**, 897
- Thomas, J., Ma, C.-P., McConnell, N. J., et al. 2016, *Natur*, **532**, 340
- Thomas, J., Saglia, R. P., Bender, R., Erwin, P., & Fabricius, M. 2014, *ApJ*, **782**, 39
- Thomas, J., Saglia, R. P., Bender, R., et al. 2004, *MNRAS*, **353**, 391
- Thomas, J., Saglia, R. P., Bender, R., et al. 2011, *MNRAS*, **415**, 545
- Tortora, C., Napolitano, N. R., Saglia, R. P., et al. 2014, *MNRAS*, **445**, 162
- Treu, T., Auger, M. W., Koopmans, L. V. E., et al. 2010, *ApJ*, **709**, 1195
- Trujillo, I., Erwin, P., Asensio Ramos, A., & Graham, A. W. 2004, *AJ*, **127**, 1917
- van den Bosch, R. C. E., & de Zeeuw, P. T. 2010, *MNRAS*, **401**, 1770
- Veale, M., Ma, C.-P., Greene, J. E., et al. 2018, *MNRAS*, **473**, 5446
- Veale, M., Ma, C.-P., Thomas, J., et al. 2017, *MNRAS*, **464**, 356
- Verolme, E. K., Cappellari, M., Copin, Y., et al. 2002, *MNRAS*, **335**, 517
- Volonteri, M., Haardt, F., & Madau, P. 2003, *ApJ*, **582**, 559
- Walsh, J. L., van den Bosch, R. C. E., Gebhardt, K., et al. 2015, *ApJ*, **808**, 183
- Zhao, H. 1996, *MNRAS*, **278**, 488

2. A 40-billion solar mass black hole in the extreme core of Holm 15A, the
64 central galaxy of Abell 85

Chapter 3

Detailed shapes of the line-of-sight velocity distributions in massive early-type galaxies from non-parametric spectral models

Bibliographic information

Kianusch Mehrgan, Jens Thomas, Roberto Saglia, Taniya Parikh, and Ralf Bender – Detailed Shapes of the Line-of-sight Velocity Distributions in Massive Early-type Galaxies from Nonparametric Spectral Models, *ApJ*, Volume 948, Issue 2, id.79, 30 pp.

DOI: 10.3847/1538-4357/acbf2e.

Author's contribution

As first author, I wrote all sections of the manuscript myself, with the exception of Section 2.4 which was written by Jens Thomas. All figures appearing in the study were generated by myself. Jens Thomas provided important support to this work in the form of frequent discussions, ideas, and revisions of text. Roberto Saglia provided further valuable corrections and discussions. The sample of nine ETGs was selected for observation with MUSE under ESO program 095.B-0624(A), P.I. Jens Thomas. I reduced the MUSE observations from the the raw data to the final datacubes for all nine galaxies and performed the full non-parametric kinematic analysis for each, as well as all tests appearing in this study. I developed the template selection and kinematic fitting strategy presented here. These methods were based on extensive mock-testing with simulated galaxy-spectra which I generated together with Jens Thomas. To this end, Taniya Parikh provided me with her setup of *alf*. Finally, I classified the galaxies according to the fast/slow rotator

convention of Emsellem et al. (2007, 2011) and performed the analysis of the the higher order Gauss-Hermite moments of the final kinematics. All authors provided feedback for the final version of the manuscript.

Copyright notice

©2023 ApJ

reprinted on pages 67 - 96.



Detailed Shapes of the Line-of-sight Velocity Distributions in Massive Early-type Galaxies from Nonparametric Spectral Models

Kianusch Mehrgan^{1,2} , Jens Thomas^{1,2} , Roberto Saglia^{1,2} , Taniya Parikh¹ , and Ralf Bender^{1,2} ¹Max-Planck-Institut für extraterrestrische Physik, Giessenbachstrasse, D-85748 Garching, Germany; kmehrgan@mpe.mpg.de²Universitäts-Sternwarte München, Scheinerstrasse 1, D-81679 München, Germany

Received 2022 September 16; revised 2023 January 31; accepted 2023 February 23; published 2023 May 9

Abstract

We present the first systematic study of the detailed shapes of the line-of-sight velocity distributions (LOSVDs) in nine massive early-type galaxies (ETGs) using the novel nonparametric modeling code WINGFIT. High-signal spectral observations with the Multi-Unit Spectroscopic Explorer (MUSE) at the Very Large Telescope allow us to measure between 40 and 400 individual LOSVDs in each galaxy at a signal-to-noise ratio level better than 100 per spectral bin and to trace the LOSVDs all the way out to the highest stellar velocities. We extensively discuss potential LOSVD distortions due to template mismatch and strategies to avoid them. Our analysis uncovers a plethora of complex, large-scale kinematic structures for the shapes of the LOSVDs. Most notably, in the centers of all ETGs in our sample, we detect faint, broad LOSVD “wings” extending the line-of-sight velocities, v_{los} , well beyond 3σ to $v_{\text{los}} \sim \pm 1000\text{--}1500 \text{ km s}^{-1}$ on both sides of the peak of the LOSVDs. These wings likely originate from point-spread function effects and contain velocity information about the very central unresolved regions of the galaxies. In several galaxies, we detect wings of similar shape also toward the outer parts of the MUSE field of view. We propose that these wings originate from faint halos of loosely bound stars around the ETGs, similar to the cluster-bound stellar envelopes found around many brightest cluster galaxies.

Unified Astronomy Thesaurus concepts: [Elliptical galaxies \(456\)](#); [Stellar kinematics \(1608\)](#); [Galaxy dark matter halos \(1880\)](#); [Supermassive black holes \(1663\)](#); [Galaxy spectroscopy \(2171\)](#); [Galaxy structure \(622\)](#)

1. Introduction

Stellar kinematics from spectroscopic observations hold many interesting clues on the internal structure of galaxies. It has long been known that the angular momentum content of early-type galaxies (ETGs) varies as a function of mass. Less massive ETGs are strongly rotating, while the most massive elliptical galaxies are mostly slowly rotating systems. This encodes basic information about the main aspects of the evolution of these galaxies (e.g., the dominance of dissipational versus dissipationless processes). In addition, stellar kinematics contains the fundamental information required for dynamical modeling, i.e., to uncover properties of the principle components of these galaxies, meaning the mass of the central supermassive black hole (SMBH), the stellar mass-to-light ratio, the shape of the dark matter (DM) halo, and the stellar orbital anisotropy profiles, all at once. Various dynamical modeling methods have been developed, based on velocity moments or on orbits, or even on particles (Schwarzschild 1979; Syer & Tremaine 1996; Cretton et al. 1999; Gebhardt et al. 2000; Siopis & Kandrup 2000; Thomas et al. 2004; de Lorenzi et al. 2007; Cappellari 2008; van den Bosch et al. 2008; Napolitano et al. 2011; Rusli et al. 2013a; Thomas et al. 2014; Mehrgan et al. 2019; Cappellari 2020; Jethwa et al. 2020; Vasiliev & Valluri 2020; Quenneville et al. 2021, 2022). The widely used Schwarzschild orbit superposition method in particular has recently seen several important advancements (de Nicola et al. 2020; Liepold et al. 2020; Lipka & Thomas 2021;

Neureiter et al. 2021; Thomas & Lipka 2022; de Nicola et al. 2022; Neureither et al. 2023).

The stellar kinematics of an ETG manifests in the line-of-sight velocity distribution (LOSVD) of stars in the galaxy, which is obtained from the broadening and shifting of stellar absorption features due to the Doppler shifts of stars in projected motion along the line of sight, blended together. A simple Gaussian parameterization of the LOSVD fails to capture the subtle difference between velocity contributions from stellar orbital anisotropy and those from steeper mass profiles (Binney & Mamon 1982; Dejonghe & Merritt 1992). For this reason, a Gauss–Hermite series expansion is often used to parameterize the LOSVDs (Gerhard 1993; Merritt & Saha 1993; van der Marel & Franx 1993; Bender et al. 1994). Already the lowest-order coefficients that describe deviations from a purely Gaussian LOSVD (e.g., h_4) contain valuable information required to solve the mass–anisotropy degeneracy. Recently, also higher orders beyond h_4 have gained more interest (Krajnović et al. 2015; Veale et al. 2018; Quenneville et al. 2022; Thater et al. 2022).

In principle, even more information can be obtained from stellar absorption features. For example, one of the most important methods, the Fourier correlation quotient (FCQ) method (Bender 1990), produces in principle nonparametric LOSVDs, and other codes for nonparametric LOSVD reconstructions have been developed as well (Gebhardt et al. 2002; Pinkney et al. 2003; Houghton et al. 2006; Fabricius et al. 2014; Falcón-Barroso & Martig 2021). Detailed knowledge about the LOSVD shapes is currently of particular importance because recent developments in Schwarzschild dynamical modeling have shown that a surprisingly high level of accuracy and precision can be reached given adequate kinematic data (Lipka & Thomas 2021; Neureiter et al. 2021, 2023; de Nicola et al. 2022). Pushing the limits of the kinematic information



Original content from this work may be used under the terms of the [Creative Commons Attribution 4.0 licence](#). Any further distribution of this work must maintain attribution to the author(s) and the title of the work, journal citation and DOI.

that we can extract from galactic spectra is therefore important to achieve mass measurements with a precision necessary, for example, to unlock the stellar initial mass function (IMF) of ETGs and to understand its seeming variation between ETGs (and probably also within individual galaxies), which is one of the most important missing puzzle pieces of galaxy formation (e.g., Rusli et al. 2011; Spiniello et al. 2011; Cappellari et al. 2012; Parikh et al. 2018).

In Mehrgan et al. (2019) we used our new spectral fitting code WINGFIT (J. Thomas et al. 2023, in preparation) to recover nonparametric LOSVDs for the brightest cluster galaxy (BCG) of A85, Holm 15A, all the way to the cutoff velocity (where the LOSVD signal goes to zero), which provides a lower limit for the escape velocity of the potential (Mehrgan et al. 2019). Our dynamical modeling of the LOSVDs showed that the radial profile of the cutoff velocity of the nonparametric LOSVDs provided an important constraint on the anisotropy profile of the galaxy—which, in turn, provided constraints on its formation history from major mergers, illustrating the importance and advantages of fitting the *full* shape of the LOSVD. However, improved knowledge about the LOSVDs in galaxies is not only interesting from the point of view of high-precision dynamical modeling. In Holm15A, for example, the measured cutoff velocities were very high, $v_{\text{esc}} \gtrsim 1500 \text{ km s}^{-1}$, extending the tails of the distribution in the form of faint “wings.” Here, the LOSVDs indicated a faint component in velocity space that seems separated from the galaxy, which could correspond to a weakly bound, faint, large-scale stellar envelope surrounding the BCG, similar to the kinematic evidence in the central galaxy of A2199, NGC 6166 (e.g., Bender et al. 2015). Indeed, our photometric decomposition of Holm15A suggested such an outer envelope as is evident for many other BCGs, illustrating the amount of detail stored in the tails of the velocity distribution—detail, that, using a simple Gaussian or even fourth-order Gauss–Hermite parameterization, would have been partially or entirely lost to us.

Therefore, we here conduct the first systematic investigation of nonparametrically determined LOSVD shapes in a sample of ETGs. This sample consists of nine ETGs, for which we acquired high-resolution, wide-field spectral observations from the Multi-Unit Spectroscopic Explorer (MUSE). The ETGs are part of a larger sample of galaxies that have been previously analyzed for their photometric, kinematic, and dynamical properties using different instruments in previous publications (Rusli et al. 2011, 2013a, 2013b; Thomas et al. 2014; Mazzalay et al. 2016; Erwin et al. 2018). In subsequent publications, we will use the nonparametric LOSVDs from the present study to construct new Schwarzschild orbital dynamical models with stellar mass-to-light ratio gradients in order to investigate the IMF (including possible radial gradients) and the details of stellar orbital system and DM halos, including their triaxiality (K. Mehrgan et al. 2023, in preparation; Neureiter et al. 2023; Parikh et al. 2023; J. Thomas et al. 2023, in preparation).

We have structured our study as follows. Section 2 details our observations and treatment of the MUSE spectroscopy for the sample galaxies and also briefly introduces WINGFIT. Since we are trying to achieve previously unattained levels of accuracy for the shape of LOSVD, we performed detailed mock tests using synthetic mock galaxy spectra to, in Section 3, explore the distorting effects of so-called template mismatch and, in Section 4, to stress-test the setup and approach with which we here treat the sample galaxies. Section 5 presents the

Table 1
MUSE Data Set of ETGs

Galaxy	Date(s) of Obs.	No. OBs	T_{exp} (s)	PA (deg)	PSF (FWHM) (arcsec)
NGC 0307	07.09	1	1800 + 300	82	2.10
NGC 1332	07.09	1	1800 + 300	114	2.12
NGC 1407	07.09	1	1800 + 300	40	1.93
NGC 4751	13.08	1	1800 + 300	175	1.59
NGC 5328	10, 11.08	2	4800 + 600	85	1.28
NGC 5419	08.08	2	4800 + 600	78	1.56
NGC 5516	11.08	1	2800 + 300	0	2.00
NGC 6861	16.06	1	1800 + 300	142	0.75
NGC 7619	18.08	1	1800 + 300	30	2.00

Note. All date(s) of observation relate to the year 2015. The number of observational blocks (OBs) describes the number of object-sky-object exposure sequences, as described in Section 2.1. For NGC 4751 two OBs were performed, on the 08.08 and 13.08 of 2015, but for the former both object exposures were taken with bad sky transparency conditions (thin cirrus) and were therefore not used in the final analysis. Exposure times, T_{exp} , are listed as object plus sky exposure times, $T_{\text{exp, total, object}} + T_{\text{exp, total, sky}}$, where total exposure times are the sum of all individual object or sky exposure times from all OBs. The position angles (PA) of the observations were chosen such that they are aligned with the major axes of the galaxies as determined from previous photometric observations (Rusli et al. 2013a, 2013b; Mazzalay et al. 2016; Erwin et al. 2018). Values of the FWHM of the PSF were measured directly from point sources found in either the object or sky exposures of the galaxies, except for NGC 0307, NGC 1332, and NGC 7619, where we found no such sources and therefore used measurements from the ESO DIMM instead.

results of our kinematic fits, which are discussed and interpreted as to their physical origin in Section 6. Finally, we sum up our results and conclusions in Section 7, where we also propose further necessary investigations in order to fully understand the kinematic structures we discovered in the nonparametric shapes of the LOSVDs of the ETGs.

2. Kinematic Data and Fitting Code

2.1. MUSE Observations and Data Reduction

We obtained wide-field spectroscopic data of nine ETGs from MUSE at the Very Large Telescope (VLT) at Paranal between 2015 June and September.³ The galaxies and general information on their observations, such as dates of observation, exposure times, and seeing conditions, are listed in Table 1.

Observations were carried out in one or two observational blocks (OBs), each consisting of two dithered object exposures plus one sky exposure in between. Individual object exposures were adapted to each object (900–1200 s long); the sky exposures were always 300 s long. The MUSE field of view (FOV) covers approximately $1' \times 1'$ on the sky, which encompasses the effective radius, r_e , of each galaxy in our sample (see Table 2).

We performed the reduction of the MUSE data for all nine galaxies using version 2.9.1 of the standard ESOreflex MUSE pipeline supplied by ESO (Freudling et al. 2013). The pipeline runs several recipes on all exposures such as flat-field and wavelength calibrations and returns combined data cubes,

³ Observations were collected at the European Organisation for Astronomical Research in the Southern Hemisphere under ESO program 099.B-0193(A), P.I. J. Thomas.

Table 2
General, Kinematic, and Morphological Properties of the Sample Galaxies

Galaxy	D (Mpc)	M_V (mag)	Cored	r_e (arcsec)	$\sigma_{e/2}$ (km s $^{-1}$)	σ_e (km s $^{-1}$)	σ_0 (km s $^{-1}$)	$\lambda_{e/2}$	λ_e	$\epsilon_{e/2}$	ϵ_e	Rotator
NGC 0307	52.8	−20.8	no	4.8	213.5	190.5	218.2	0.33	0.43	0.36	0.37	fast
NGC 1332	22.3	−21.5	no	28.0	263.1	...	334.2	0.37	...	0.31	...	fast
NGC 1407	28.1	−22.7	yes	70.33	258.9	...	300.8	0.09	...	0.05	...	interm.
NGC 4751	26.9	−20.8	no	22.76	249.0	219.3	382.8	0.64	0.69	0.51	0.53	fast
NGC 5328	64.1	−22.8	yes	22.2	306.7	291.3	333.5	0.06	0.15	0.31	0.31	slow
NGC 5419	56.2	−23.1	yes	43.4	309.6	...	347.7	0.04	...	0.20	...	slow
NGC 5516	58.4	−22.9	yes	22.1	283.8	274.2	315.8	0.08	0.07	0.16	0.17	slow
NGC 6861	27.3	−21.4	no	17.7	294.2	275.5	414.6	0.55	0.57	0.42	0.43	fast
NGC 7619	51.5	−22.9	yes	36.9	270.8	...	333.0	0.14	...	0.26	...	interm.

Note. We have adopted the distance, absolute V -band magnitude, presence/absence of a core, effective radius r_e , and ellipticity ϵ from previous publications: from Rusli et al. (2011) in the case of NGC 1332, Mazzalay et al. (2016) for NGC 5419, Erwin et al. (2018) for NGC 0307, and Rusli et al. (2013a, 2013b) and Thomas et al. (2014) for the rest. All distances except NGC 1332 and NGC 5328 are determined from values that were each determined from the respective radial velocity (HyperLEDA), corrected for the infall velocity of the Local Group into the Virgo Cluster. Distance values for NGC 1332 and NGC 5328 were taken from the SBF survey of galaxy distances (Tonry et al. 2001), after a Cepheid zero-point correction of -0.06 mag (Mei et al. 2005). Based on the new stellar kinematics presented here, the stellar velocity dispersion and angular momentum per unit mass (Emsellem et al. 2007) within one r_e , σ_e , and λ_e and within half of r_e , $\sigma_{e/2}$, and $\lambda_{e/2}$ are luminosity-weighted averages over elliptical apertures following the guidelines laid out by Emsellem et al. (2007, 2011). Luminosity-weighted averages of the ellipticity, ϵ_e and $\epsilon_{e/2}$, also follow the same procedure but are based on photometry originating from the studies listed above. The central velocity dispersion, σ_0 , is a luminosity-weighted average over a circular region within a radius equal to the FWHM of the PSF. For NGC 0307 and NGC 1332 we used $B - V$ color of RC3.

covering the optical domain from about 4800 to 9400 Å with a spectral resolution of 1.25 Å. At the redshifts of the galaxies in our sample, $z \sim 0.005$ – 0.015 , this wavelength range covers several stellar absorption features important for the recovery of stellar kinematics such as $H\beta$, the Mg b region, and several Fe lines, particularly those at 5270 and 5335 Å.

Sky emissions were removed separately from all galaxy exposures using the sky field from offset sky exposures, taking into account the instrumental line-spread function (LSF) for each of the 24 integral field units (IFUs) that MUSE consists of. While the correction of telluric absorption features is fully covered by the standard Esoreflex pipeline, we noticed that for all galaxies the telluric spectrum, which is derived from observations of a telluric standard star, was scaled by a too-large factor resulting in a correction where the division by the telluric spectrum left strong residuals on the galaxies’ spectra. This was particularly significant in the telluric absorption region between ~ 7590 and 7710 Å. To obtain a better telluric correction, we decided to optimize the scale factor for the telluric standard-star spectrum manually such as to minimize the residuals in the strong telluric absorption region between ~ 7590 and 7710 Å of the corrected spectrum with respect to the continuum on both sides of this region. For two galaxies (NGC 7619 and NGC 5328) we also used *Molecfit* (Kausch et al. 2015; Smette et al. 2015), a software tool for the correction of telluric absorption features developed by ESO, to do the telluric correction. We found that *Molecfit* produced comparable results and therefore continued to manually optimize the scaling factors for the ESO-provided telluric standard stars.

We resampled all data cubes to a spaxel size of $0''.4 \times 0''.4$, which at the respective redshifts of the galaxies corresponds to spatial resolutions of approximately 40–120 pc. In cases where we found point sources such as active galactic nuclei or stars in the object or sky exposures we estimated the FWHM of the point-spread function (PSF) for our observations directly from their broadening; otherwise, we used the seeing measurement of the ESO Differential Image Motion Monitor (ESO DIMM;

Sarazin & Roddier 1990) at the VLT. The FWHM of the PSF ranges between $\sim 0''.8$ and $2''.2$ for our sample.

2.2. Spatial Binning

We spatially binned the MUSE data cubes of the nine galaxies using the Voronoi tessellation method of Cappellari & Copin (2003) for a target signal-to-noise ratio (S/N) of 150 per spectral bin between ~ 4800 and 5500 Å. In this way we also achieved an $S/N > 100$ in every spectral bin over the entire MUSE wavelength range (except for spectral bins where strong skyline residuals persisted in the data reduction steps of Section 2.1). For the calculation of the S/N of the spectral bins for the spatial binning, we used the variance $\sigma^2(x, y, \lambda)$, which is generated alongside the spectroscopic data by the Esoreflex pipeline as a secondary slice of the product data cube. Pixels belonging to foreground sources such as other galaxies, AGNs, or stars were removed from the data before binning. This resulted in 60–400 spatial bins for each galaxy.

2.3. Morphological Properties of the Sample Galaxies

Kormendy & Bender (1996) and Faber et al. (1997) introduced a sequencing of ETGs into two types as a refinement of the historical Hubble classification scheme: (1) luminous/massive ETGs with shallow central surface brightness cores, boxy isophotes, and little rotation; and (2) less luminous/massive ETGs with steep central power-law surface brightness profiles, disk-like isophotes, and significant rotational support. There are more properties and studies of these two types, for which we refer to the review of Lauer (2012). To give a first brief overview of our sample galaxies based just on our spectroscopic MUSE data, we have classified our ETGs into the slow/fast rotator categories of Emsellem et al. (2007, 2011) in Table 2.

We calculate the λ parameter for the slow/fast rotator classification using the spectroscopic data out to $r_e/2$ (or out to r_e if the data allow). In total our sample includes four fast rotators, three slow rotators, and two “intermediate” cases. The last ones are very close to the dividing line between slow and

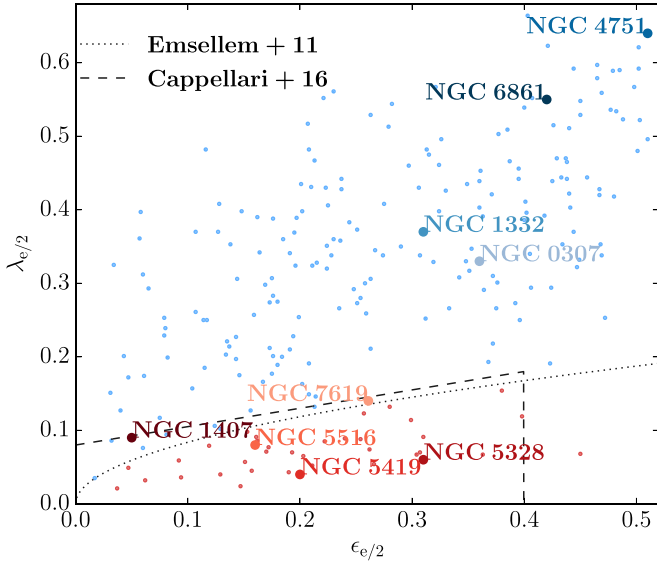


Figure 1. Apparent angular momentum λ per unit mass and ellipticity ϵ measured at half the effective radius for the nine sample galaxies (large circles) compared to ETGs from Emsellem et al. (2011; small circles), including the old and revised dividing line (Emsellem et al. 2011 and Cappellari 2016, respectively) between slow rotators (red circles) and fast rotators (blue circles). NGC 1407 and NGC 7619, which we refer to as “intermediate” rotators in the text, are here grouped in with slow rotators.

fast rotators from Emsellem et al. (2011) and to the revised line from Cappellari (2016) (see Figure 1). As we will argue later, these two galaxies are dynamically much more similar to slow rotators than to fast rotators. All slow and intermediate rotators in our sample have depleted stellar cores in their light profiles (Rusli et al. 2013b). At least two of these galaxies seem to have kinematical misalignments and/or kinematically decoupled cores. We will provide a more detailed discussion of the kinematical structure of the galaxies below (Section 6).

2.4. Nonparametric LOSVD Fitting

We will perform the main part of our kinematic analysis using WINGFIT, a new spectral fitting code that allows us to derive LOSVDs in a nonparametric fashion (J. Thomas et al. 2023, in preparation). In WINGFIT, the spectral model \mathcal{S} is composed as

$$\mathcal{S} = \left[\sum_{j=1}^{N_c} \left(\sum_{i=1}^{N_j} w_{ij} \mathcal{T}_{ij} \right) * \mathcal{L}_j \right] \times \left[\sum_{l=1}^{N_m} d_l \mathcal{M}_l \right] + \sum_{k=0}^{N_a} b_k \mathcal{A}_k. \quad (1)$$

\mathcal{T}_{ij} are template spectra that are superimposed to construct N_c kinematical components with different LOSVDs \mathcal{L}_j . For elliptical galaxies a typical model will have a single stellar kinematical component composed of one or several template stellar spectra convolved with the LOSVD of the stars \mathcal{L} . If emission lines are present, one or more additional kinematical components can be added, for example, composed of template spectra with the respective emission lines and associated with separate \mathcal{L} to derive the kinematics of the respective gas component. In more complex galaxies with several distinct stellar populations that have different kinematics one can also use more than one stellar kinematical component. \mathcal{A}_l and \mathcal{M}_l are Legendre polynomials of order l that can be included in the model in order to account for additive spectral components or

flux calibration uncertainties. In this paper we will use WINGFIT only in the nonparametric mode, where the LOSVDs \mathcal{L}_j are modeled in a nonparametric fashion. To this end, each LOSVD is represented by its values at N_{vel} line-of-sight velocities, equally spaced between a minimum and maximum velocity. The width of the velocity bins is determined by the resolution of the data spectrum. In this study we sample the LOSVDs over $N_{\text{vel}} = 87$ velocity bins within $-2900 \text{ km s}^{-1} < v_{\text{los}} < 2900 \text{ km s}^{-1}$, which covers more than $\pm 6\sigma_{\text{max}}$ even in the galaxies where the maximum velocity dispersion is $\sigma_{\text{max}} \sim 400 \text{ km s}^{-1}$. The sole exception is the galaxy NGC 0307, where a sampling between $-1500 \text{ km s}^{-1} < v_{\text{los}} < 1500 \text{ km s}^{-1}$ or $N_{\text{vel}} = 47$, respectively, is sufficient owing to its low velocity dispersion.

The free parameters of the galaxy model are the template weights w_{ij} , the LOSVDs \mathcal{L}_j , and the polynomial coefficients d_l and b_k . The code utilizes a Levenberg–Marquardt algorithm to minimize the χ^2 over all spectral pixels of a model stellar spectrum relative to the data. In the nonparametric mode—which we will consider in this paper—the code uses a penalty function that minimizes the second derivative of the LOSVD to reject physically implausible solutions. The code uses a data-driven optimization method that is based on a generalization of the classical Akaike information criterion (Thomas & Lipka 2022). The smoothing penalty and the method to determine its optimal strength individually for each spectrum in each Voronoi bin are exactly the same as described in Equation (3) of Thomas & Lipka (2022). A full description of the code will be given in J. Thomas et al. (2023, in preparation).

Since this is the first systematic investigation of nonparametrically determined LOSVD shapes in a sample of massive elliptical galaxies, it is important to carefully investigate how well the LOSVDs of the stars can be recovered and which potential systematic issues could affect the results. For the data in our sample (e.g., assuming the MUSE spectral coverage and the S/N used in our binned spectra) we show in Section 4.3.1 that the nonparametric LOSVD recovery in principle works without bias if the exact template spectrum is used. In this case, the LOSVD recovery is largely independent of the fitting setup. This means that the recovery is independent of the particular wavelength region used in the fit, it is independent of one or more spectral regions being masked and excluded from the fit or not, and it is independent of whether or not additive or multiplicative polynomials have been used in the fit.

In general, however, it is unrealistic to assume that the exact stellar mix is available as a template spectrum for the fit. This is particularly true for the fits in this study, since we use the MILES library of *empirical* stellar spectra from stars in the Milky Way—i.e., from an environment very different from our target ETGs. In the next two sections, we discuss results of a number of mock tests aimed at investigating how template mismatch can affect the shapes of LOSVDs in observed galaxies. We put particular emphasis on the question of which setup (wavelength region, masks, template selection, usage of polynomials) is the best given the fact that some template mismatch is almost unavoidable. The analysis of the galaxies will be presented in Section 5.

3. LOSVD Distortions Induced by Template Mismatch

The “naive” approach to spectral fitting would be to simply minimize the residuals of the fit to the spectrum. We here leave aside the question of how to find the optimal trade-off

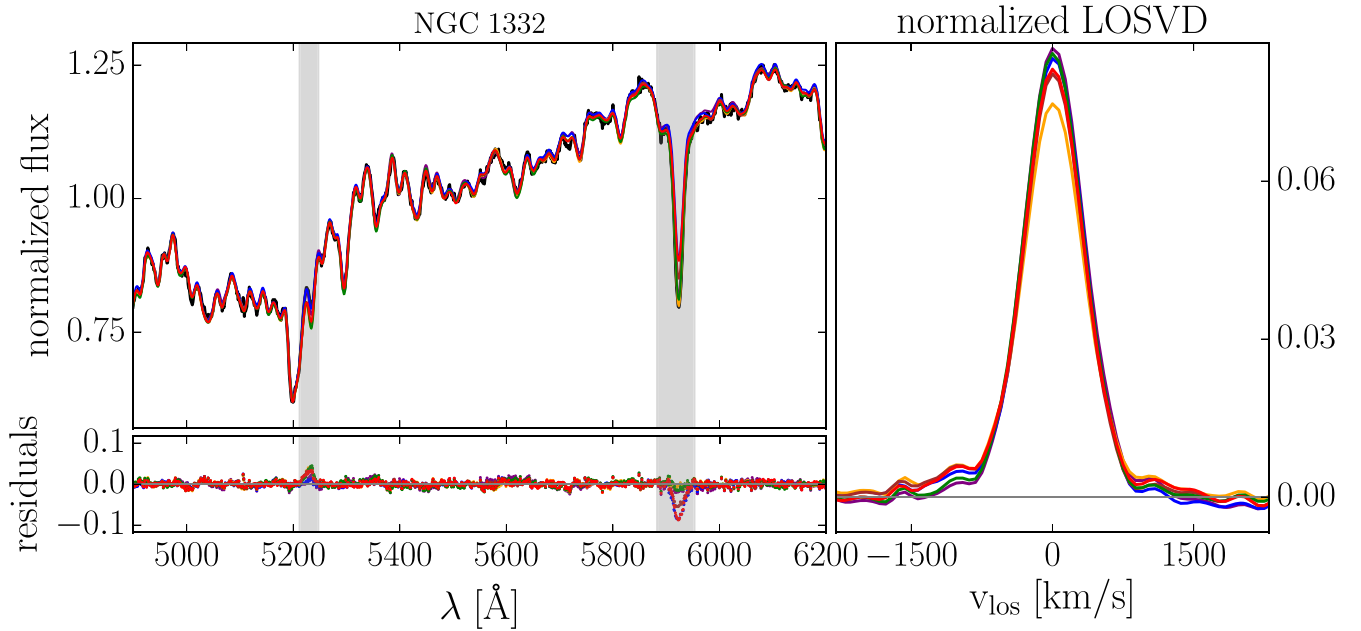


Figure 2. Top left: a spectrum measured near the center of NGC 1332 (black) fitted with different models (colored lines), with different orders of additive and multiplicative polynomials, as well as spectral masking with WINGFIT, using a template set of around 30 (mostly K-type) MILES stars. The spectral models are very similar; hence, in spectral intervals where only one color is visible, the models overlap. The residuals are shown in the bottom left panel, in the same colors. Gray shaded areas indicate spectral regions that were masked during the fit for some models—one mask concerning potential [N I] emission around 5250 Å, and the other, NaD, around 5950 Å. All models shown in the figure are detailed in Table 3. The right panel shows the nonparametric LOSVDs determined from the fits (same colors as fits to the spectrum). The line-of-sight velocities v_{los} are relative to the systemic velocity of the galaxy.

between smoothing and goodness of fit (see Thomas & Lipka 2022; J. Thomas et al. 2023, in preparation). Beyond this, the fit can often be improved by tweaking the fitting setup: the number of template stellar spectra used, the orders of additive and multiplicative polynomials, and spectral regions that are masked or excluded from the fit. Typically, the fit to the spectrum will remain very similar for most setups, but the recovered LOSVD, particularly at large projected velocities, may differ. While for many purposes the detailed shapes of the high-velocity tails of galaxy LOSVDs may not be important, they certainly are for accurate and precise dynamical modeling (de Nicola et al. 2022; Neureiter et al. 2023).

Figure 2 and the complementary Table 3 show several example fits with different setups for the same central bin of NGC 1332. For many setups, we encounter LOSVDs that consist of a relatively narrow central component and a weaker but very broad additional component that extends to large line-of-sight velocities v_{los} and that is most strongly affected by variations of the fitting setup. We will henceforth refer to these broad components as “wings”—a faint, high-velocity structure on both sides of the peak of the LOSVD that extends well beyond 3σ (i.e., typically to $v_{\text{los}} \sim \pm 1000\text{--}1500 \text{ km s}^{-1}$).

Increasing the orders of the additive and multiplicative polynomials, as well as the spectral masking applied to the spectrum, improves the rms to the spectrum. Therefore, setups with higher orders of polynomials and more spectral masking seem favorable. However, given the strong impact on the wing component, the question is: which setup allows for the most robust recovery of LOSVDs, avoiding both over- and under-prediction of the stellar light in various velocity regions, in particular at the tails of the distribution?

Table 3
Setup Parameters and rms of the Fits to the Data of the Models Shown in Figure 2

Color	Add. Polynomial	Mult. Polynomial	Spectral Masks	rms [10^{-3}]
brown	8	8	[N I], NaD	5.72
red	1	12	[N I], NaD	5.85
blue	4	8	[N I]	6.04
orange	8	4	[N I]	6.22
green	0	4	[N I], NaD	7.32
purple	0	1		8.06

Note. Models are identified by their color-coding in the figure. The spectral models are very similar; hence, in spectral intervals where only one color is visible in the figure, the models overlap. The setup parameters include the orders of the additive and multiplicative polynomials used in the fit, as well as the spectral features that were masked.

3.1. LOSVD Distortions due to Line Strength Mismatch in a Single Isolated Line

To illustrate the basic mechanism by which LOSVD shapes and template mismatch can interfere, we start with fits around the strong and relatively isolated NaD feature. We use *alf* (v2.1) to create a synthetic template star spectrum with solar abundances. We also create a mock galaxy spectrum by convolving this stellar spectrum with a simple Gaussian LOSVD.⁴ Then, we simulate template mismatch by creating two additional mock galaxy spectra, based on the same Gaussian LOSVD, but modifying the abundance of [Na/H] by ± 0.2 dex relative to solar. The fits of these two mocks with the unmodified, solar abundance template star and the resulting

⁴ The specifics of how we create mocks and templates in this section are detailed in Appendix A.

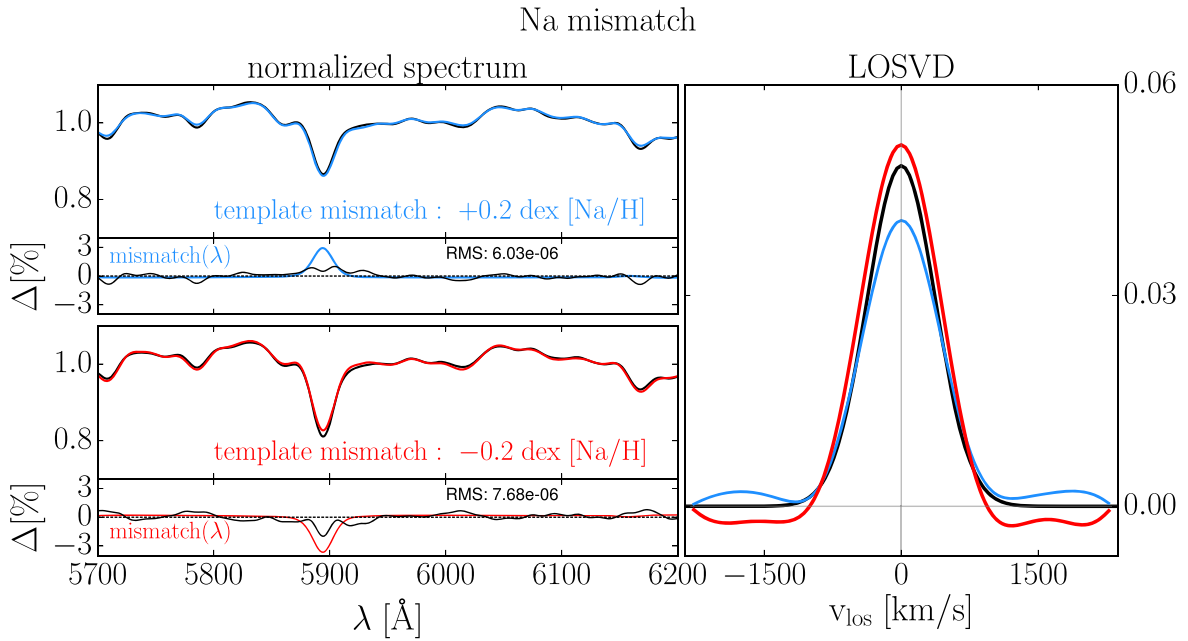


Figure 3. Fits to a mock spectrum with artificially induced template mismatch, with respect to the elemental abundance of Na. The left column shows the mock (black) that has been Na reduced (top) or Na enhanced (bottom) relative to the original mock (dashed black). Fits to the modified mocks using the unmodified template are shown in blue and red for reduced and enhanced elemental abundances, respectively. In the right panel, we show, in the same color-coding, the LOSVD recoveries that have been distorted by template mismatch compared to the true LOSVD (dashed black). Below either spectrum we indicate the template mismatch of different absorption features via the residuals between the modified and unmodified mock. No additive or multiplicative polynomials were used during the fit.

distortions of the recovered LOSVDs are shown in Figure 3. To keep things simple at first, we use no multiplicative or additive polynomials during the fits and fit noise-free spectra.

The Gaussian input LOSVD, per definition, has no wings. However, fitting the NaD feature with a template that is overabundant in $[\text{Na}/\text{H}]$ (achieved by using the solar template to fit the mock spectrum with subsolar $[\text{Na}/\text{H}]$) produces a wingy LOSVD (blue). The opposite is true for the fit where the template is underabundant in $[\text{Na}/\text{H}]$ and the recovered LOSVD has “negative” wings. This result is intuitive: After convolution with a wingy LOSVD, the absorption feature of the template star appears weaker. After convolution with an LOSVD with “negative” wings, instead, the absorption feature appears stronger than in the unconvolved template.

When simply fitting an isolated feature, template mismatch can only occur in the form of this mismatch in the line strength. As we will show in the following, various combinations of over- or underabundances in different elements can lead to more complicated net distortions of the recovered LOSVDs.

3.2. The Origin of Asymmetric and Symmetric LOSVD Distortions

We performed a number of similar mock tests with controlled template mismatch in particular for Mg and Fe. These are the elements associated with the most predominant absorption features (besides NaD) within the wavelength interval 4800–6200 Å that we finally decided to use for our stellar kinematic analysis (Section 5). Gauss–Hermite parameterizations of the resulting distorted LOSVDs (including the NaD mock-test described above) are listed in Table 4. We fit up to the eighth order, which is sufficient for the LOSVD shapes we deal with here.

To start with, we generated four mocks by increasing and decreasing the abundances of $[\text{Mg}/\text{H}]$ and $[\text{Fe}/\text{H}]$ individually,

each by ± 0.2 dex. As with the Na test, we performed the first set of tests without the use of additive or multiplicative polynomials. It should be noted that some of the related fits, particularly those for Mg mismatch, are so poor that we would not accept them for any observed spectrum. However, we here intentionally probe exaggerated template mismatch in order to highlight certain trends of the recovery of the LOSVD. Later on, in Section 4, we will describe tests that involve more realistic amounts of template mismatch.

The distortions of the exact Gaussian input LOSVD are primarily *asymmetric* in the case of Mg: the fitted LOSVDs have a (positive) wing on one side of the peak and a dip (or “negative” wing) on the other (Figure 4 top). This type of asymmetric template mismatch has long been known and manifests itself in a bias of the third-order Gauss–Hermite coefficient h_3 (Bender et al. 1994). Note, however, that for the fit with too strong Mg (see Table 4) the h_3 of the resulting distorted LOSVD—or equivalently the recovery mismatch Δh_3 —is quite small, $\Delta h_3 = 0.007$. It is actually similar to the value for the near-symmetric LOSVDs from the equivalent Na mismatch test, $\Delta h_3 = 0.008$. The difference between the cases only becomes apparent when looking at the sequence of higher-order odd Hermite coefficients. In the Mg test (asymmetric LOSVD) also the next higher-order moments are nonzero: $\Delta h_3 = 0.007$, $\Delta h_5 = 0.032$, $\Delta h_7 = 0.033$. Instead, for the Na case (more symmetric LOSVD) the odd higher-order moments add little beyond the third order: $\Delta h_5 = 0.003$, $\Delta h_7 = 0$. Relying solely on h_3 and h_4 to describe the shape of the LOSVD is sometimes not sufficient, and an unambiguous characterization of the LOSVD distortions requires a sequence of odd Hermite coefficients (which often have the same sign).

Compared to Mg, distortions caused by template mismatch in Fe are more *symmetric* (as can also be seen from a comparison of the sequence of higher-order odd moments in Table 4). Indeed, the LOSVDs recovered from fits with a

Table 4
Gauss–Hermite Coefficients of LOSVDs Recovered Simulating Different Forms of Template Mismatch

Mismatch	Na ▲	Na ▼	Mg ▲	Mg ▼	Fe ▲	Fe ▼	Mg/Fe ▲	Mg/Fe ▼	Mg/Fe ^{mpoly} ▲	Mg/Fe ^{mpoly} ▼
Δh_3	0.008	−0.010	0.007	−0.016	−0.004	0.001	0.015	0.002	−0.003	−0.003
Δh_5	0.003	−0.005	0.032	−0.032	−0.014	0.016	0.038	0.001	0.008	−0.001
Δh_7	0.000	0.001	0.033	−0.033	−0.018	0.022	0.034	0.002	0.009	0.000
Δh_4	−0.003	−0.067	−0.023	−0.007	0.014	−0.042	0.019	0.012	0.036	0.069
Δh_6	0.038	−0.04	0.003	−0.008	0.017	−0.023	0.037	0.019	0.038	0.055
Δh_8	0.050	−0.039	0.025	−0.032	−0.002	−0.017	0.044	0.017	0.036	0.045

Note. While the true input LOSVD is purely Gaussian, the recovered LOSVDs are distorted depending on the template mismatch. We parameterize the distortion by fitting the recovered LOSVDs with eighth-order Gauss–Hermite polynomials. We group the Hermite moments into even- and odd-order moments. Since the input LOSVD is Gaussian in every case ($h_i = 0$; $i = 3, 4, \dots$), the Hermite parameter h_i of this fit is a measure of the recovery mismatch, and we denote it by Δh_i . Upward-pointing triangles indicate that the associated elemental abundance of the template spectrum is too low relative to the mock spectrum. Downward-pointing triangles indicate template mismatch in the opposite direction. Mg/Fe^{mpoly} refers to the mismatch tests presented in Figure 5, wherein multiplicative polynomials were used in the recovery of the LOSVD. We here only list the distorting effects of the fit with multiplicative polynomials, as those of the fit with additive polynomials are virtually identical.

template that is over- or underabundant in [Fe/H] relative to the mock galaxy spectrum show both positive and negative distortions on the same side ($v_{\text{los}} > 0$; Figure 4, middle).

Next, we modified both [Fe/H] and [Mg/H] at the same time. To mimic a template that is α -deficient (which in this limited wavelength range translates to a too low [Mg/Fe]), we set [Mg/H] to -0.1 dex and [Fe/H] to -0.2 dex. When doing so, the fit with this template yields an LOSVD distorted in such a way that even though the LOSVD is almost perfectly symmetric ($\Delta h_{3,5,7} \sim 0$) it displays smooth artificial wings. When we try to change the ratio in the opposite direction, to mimic a template that is α -enhanced relative to the galaxy ([Mg/H] = -0.3 , [Fe/H] = -0.1), the fitted LOSVD becomes strongly asymmetric again, with the largest $|\Delta h_{3,5,7}|$ distortions of all tests, producing only one wing on one side (Figure 4, bottom).

This variety of distortion patterns in the recovered LOSVDs (e.g., asymmetric versus symmetric) can be understood by comparing the degree to which the template mismatch is either localized or spread out across the fitted wavelength interval. After all, the LOSVD, by design, affects every absorption feature within the wavelength range in the same way. This means that a mismatch pattern that repeats over the whole fitted wavelength region in a similar fashion can be compensated for by modifications of the LOSVD shape.

For example, when we change [Fe/H], the depths of multiple absorption features between ~ 5200 and 5450 \AA are modified to a roughly similar degree, leading to the many regular ups and downs in the mismatch pattern shown in the little panels below each panel with a spectrum in Figure 4. For the test where we additionally enhanced [Mg/H], this similarity between the line strength differences of the template and the mock spectrum even extends to Mg b , such that almost all absorption features in the fitted wavelength interval are too shallow by a similar amount (Figure 4, bottom). In these cases, the recovered LOSVDs show relatively symmetric distortions. The most symmetric case is the one we described last: here the LOSVD shows very smooth and symmetric wings that make the fit to the spectrum appear quite good even though both the template and the LOSVD are wrong. By raising or lowering the signal on both sides of the inner, main part of the LOSVD, all the absorption features of the fitted model collectively become

shallower or deeper, respectively (by the mechanism described in Section 3.1).

Such symmetric template mismatch, scarcely ever mentioned, has already been noted in observations by Bender et al. (1994), who found that template mismatch biased their measurements not only of h_3 but also of h_4 . We can expand on this and say that symmetric template mismatch biases the sequence of even-order moments, $h_{4,6,8,\dots}$, in the same direction (as with asymmetric template mismatch for the odd-order moments).

In the remaining cases shown in Figure 4 the mismatch pattern is very inhomogeneous over the fitted wavelength region and, in fact, mostly localized (around Mg b). In these cases, the recovered LOSVD gets asymmetrically distorted. The fitting optimization process has to seek a solution compensating for the local template mismatch, e.g., by distorting the LOSVD. However, at the same time, the freedom in compromising the LOSVD shape to improve the fit is limited by the fact that all other features in the fit region do not need a compensation (or need a different one, e.g., in the opposite direction). If a single feature is particularly dominant in the spectrum (and the continuum on both sides of the feature is particularly smooth and featureless—e.g., as discussed above with NaD), this compromise can exceptionally result in symmetric LOSVD distortions as described above. Typically, however, the LOSVD settles for a shape that is asymmetrically distorted. Moreover, in comparison to nonlocalized template mismatch, the improvements in the fit achieved by deforming the LOSVD are very limited when the mismatch is localized and the residuals remain relatively large.

The predominant distortion effect of template mismatch appears to be positive or negative wing signals. Nonetheless, the dispersion σ for all template mismatch mock tests conducted in this study is biased *high*. For the tests in this section the average σ mismatch is $\sim 10\%$. For tests with more realistic amounts of template mismatch, which we encounter in Section 4, this bias is $\sim 1\%–5\%$.

3.3. Polynomials Can Amplify the Effect of Template Mismatch

The quality of the fits in the previous subsection is often lacking, particularly for those mock tests with more spectrally localized template mismatch. These fits can be improved

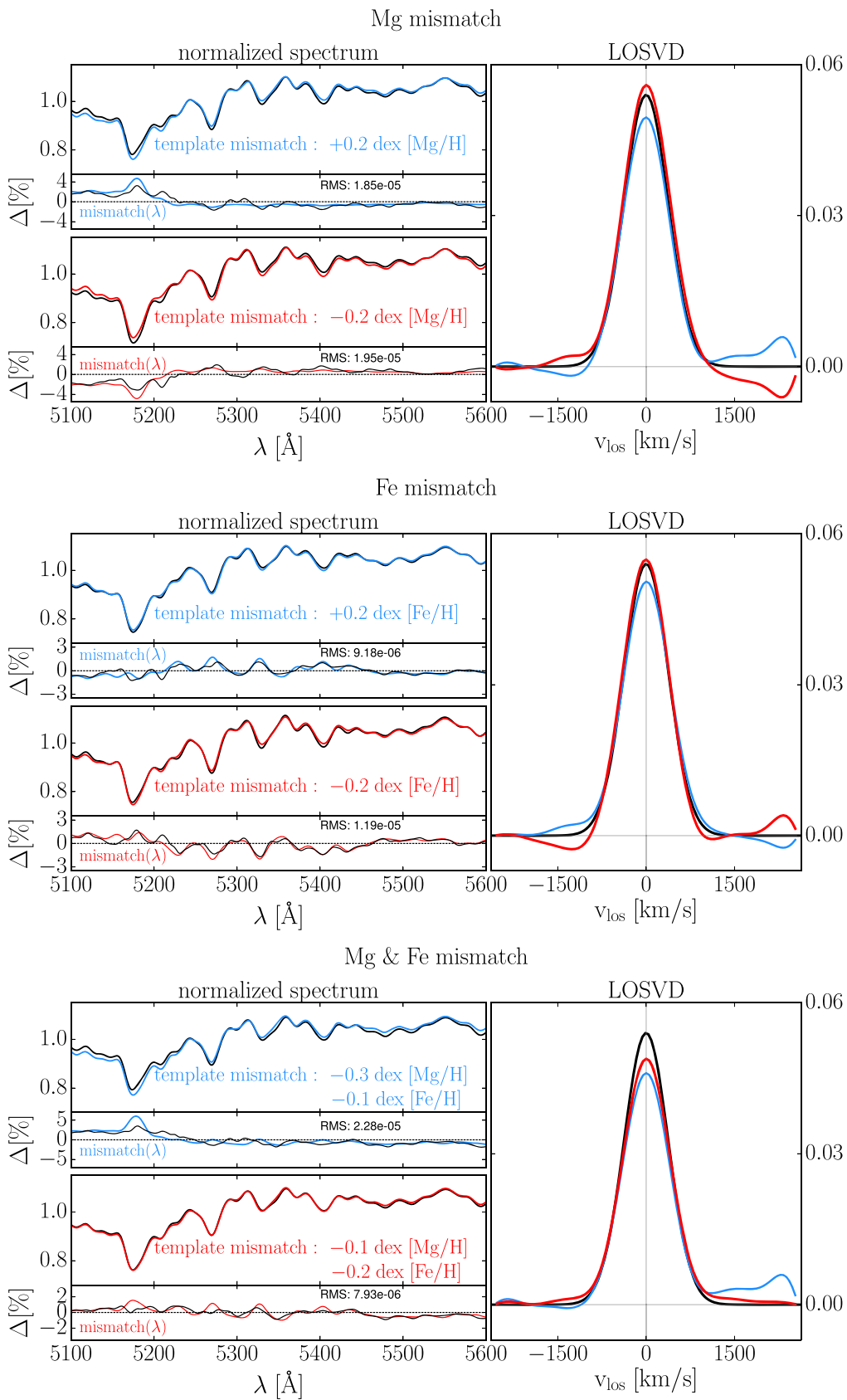


Figure 4. Test for artificially induced template mismatch, with respect to the elemental abundance of Mg, Fe, and Mg and Fe simultaneously, analogous to the Na mismatch tests from Figure 3.

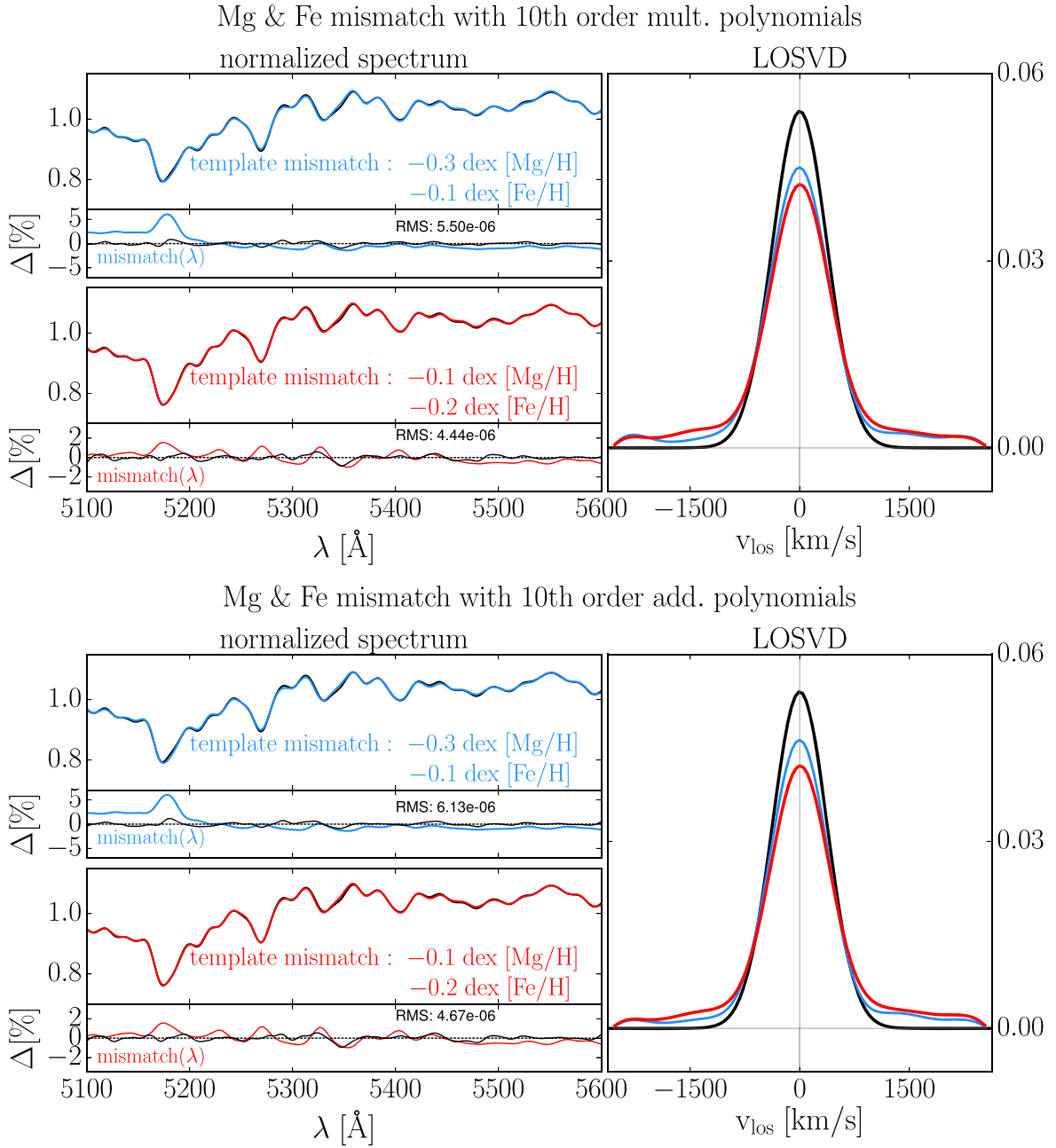


Figure 5. Test for artificially induced template mismatch, with respect to the elemental abundance of Mg and Fe simultaneously, in analogy to the Na mismatch tests from Figures 3 and 4, but with the use of additive/multiplicative polynomials. The ways in which these polynomials change the shape of the effective template during the fit are indicated in black in the mismatch panels: here we compare the spectral difference between the modified and unmodified mock after the use of the polynomials, to highlight how the polynomials interfere with template mismatch to produce even further distorted LOSVDs.

substantially by the use of polynomials, which is standard practice for stellar kinematics. This however, turns out to be problematic for the recovery of the LOSVD shape. Figure 5 shows again fits with mismatched [Mg/Fe] like the ones in the bottom panel of Figure 4. However, this time we also use additive and multiplicative polynomials in the fit. To clearly highlight the trend in the LOSVD recovery, we use polynomials with an order up to 10.

The result for the positive [Mg/Fe] mismatch mock (blue) is particularly concerning: The use of either type of polynomials increased the quality of the fit from unacceptable ($\text{rms} = 2.3 \times 10^{-5}$) to a level that would be considered more than

sufficient in case of an observed spectrum ($\text{rms} \sim 0.6 \times 10^{-5}$). At the same time, however, while removing almost any asymmetry from the recovered LOSVDs (compare with Figure 4), the usage of the polynomials raised strong wings. This is also evident in the Gauss–Hermite parameterization, where $|\Delta h_{3,5,7}|$ decrease while $\Delta h_{4,6,8}$ increase.

What happens here is that the freedom provided by the polynomials is used by the code to homogenize the template mismatch in different spectral regions. If this is possible, then symmetric LOSVD distortions can be used to collectively compensate for the mismatch (as described above). Together, this leads to a significant improvement of the fit. However, the

LOSVD shape develops a bias toward extended wings. This can be seen for the much more uniform template mismatch mock test after the application of polynomials.

Furthermore, even for the mismatch test where the template is underabundant in [Mg/Fe] (red), the already-symmetric distortions of the LOSVD become more pronounced through the use of polynomials. The additive/multiplicative polynomials modify the effective template such that template mismatch in Mg *b* and the Fe features is actually increased. However, it is increased in such a way that at the same time the mismatch is homogenized over the wavelength region such that in combination with a respectively distorted LOSVD the fit to the spectrum becomes overall much better ($\text{rms} = 0.8 \times 10^{-5}$ versus 0.5×10^{-5}). Again, the LOSVD distortion consists of strong artificial wings (compare with Figure 4), producing the largest values of $h_{4,6,8}$ so far.

These tests demonstrate that polynomials should be used with care. For both tests, the fit to the spectrum became significantly better, but at the expense of strong LOSVD distortions. Hence, when template mismatch could be an issue, a too-liberal use of polynomials can lead to biased LOSVD shapes. Without template mismatch, polynomials do not lead to biases (Section 4.3.1).

As we will explain at the start of the next section, this tendency of polynomials to exacerbate template mismatch in such a way that symmetric wings are overproduced in the fitted LOSVDs is potentially dangerous, not least because it is harder to identify than template mismatch that leads to asymmetric LOSVD distortions.

4. Fitting Strategy to Minimize the Effects of Template Mismatch

As we have demonstrated in the previous section, template mismatch can induce asymmetric and symmetric distortions of the recovered LOSVDs.

Asymmetric distortions are less problematic. For galaxies that are in dynamical equilibrium, in the absence of template mismatch, stars on the same orbits but on opposite sides of the center of the galaxy will be seen moving along the line of sight with velocities $\pm v_{\text{los}}$, i.e., with the same absolute value but opposite signs. Hence, an asymmetric bias in the shape of the LOSVD over any spatial region that is axi- or point-symmetric about the center of the galaxy can be recognized as template mismatch (e.g., Bender et al. 1994).

Similarly, LOSVD distortions that produce symmetric, negative wings can always easily be identified as template mismatch because a negative LOSVD signal is unphysical.

More problematic are symmetric distortions that produce positive-signal wings, because they lead to a kind of “hidden” template mismatch. It is “hidden” because the fit to the spectrum in these cases is usually quite good (e.g., in the polynomial tests in Section 3.3), while at the same time the resulting LOSVD shapes are consistent with LOSVD shapes that can occur in real dynamical systems (via, e.g., radial anisotropy or variations in the circular velocity curve; see Section 6). Hence, in this case, the form of the LOSVD itself does not allow one to judge whether it is distorted by template mismatch or not. This type of template mismatch is therefore potentially dangerous.

We now turn to the question whether one can modify the setup of the fits in such a way that any influence of template mismatch is at least minimized.

4.1. Strategy to Reduce Template Mismatch

Assuming that the galaxies in our sample are in dynamic equilibrium, we argue that asymmetric template mismatch can be efficiently suppressed by the selection of appropriate template stars.

To this end, we section the MUSE FOV into half a dozen to a dozen elliptical annuli and add together spaxels that fall within each annulus, with spaxels near the boundary of the FOV added to the outermost annulus. Pixels that are contaminated by foreground sources such as other galaxies, AGNs, or stars are removed before this process. For reasons of symmetry we also removed all pixels from the FOV that were point-symmetrical to these contaminated pixels. Then, we individually fit each of the resulting spectra with all ~ 1000 stars of the MILES library simultaneously, with an LOSVD that we constrain to be symmetric around $v_{\text{los}} = 0$ during the fit, and then select those templates that are assigned a nonzero weight as the final template (sub)set for all Voronoi bins whose centers lie within the annulus in question for the final kinematic analysis. Typically, this approach to template optimization yields optimized template sets of roughly 20–30 MILES templates per elliptical annulus or mock. These empirical templates serve as an approximation of the underlying stellar mix in the spectra encompassed by the corresponding annulus. In the actual fits to the individual spectra in the annulus the weights of the empirical templates are allowed to vary freely. During the selection, we use the same wavelength interval and spectral masks as in our final fits.

4.2. Strategy to Reduce LOSVD Distortions

Since we use MILES stars to fit the massive ETGs in our sample, we cannot exclude some residual template mismatch, even after the careful selection of templates. The above tests have demonstrated that in such a situation one should minimize the use of polynomials (Section 3.3).

In principle, additive polynomials are only required in a fit if there is an actual additive component in the spectrum, which typically means an AGN and would thus only apply to the central few arcseconds of a galaxy. In that case, for those central spectra, the lowest possible order of additive polynomials should be used. Fortunately, in the case of our galaxies, there was no evidence for significant AGN activity (Rusli et al. 2011, 2013a, 2013b; Thomas et al. 2014; Mazzalay et al. 2016; Erwin et al. 2018), and all central spectra could be fit sufficiently well without the use of additive polynomials (see Section 5). Therefore, we disabled the use of additive polynomials entirely.

By contrast, fitting observed galaxy spectra entirely without the use of multiplicative polynomials as well is unrealistic given residual imperfections in the data reduction process, e.g., in the flux calibration of the observations. Typically, even very extensively flux-calibrated spectra, such as our MUSE data, cannot be fitted properly without multiplicative polynomials. To optimize the usage of the polynomials, we tried to determine the largest multiplicative polynomial order that still allows for an unbiased recovery of the true LOSVD structure. The mock tests presented later in this section indicate that a multiplicative polynomial of fourth order is best for our data and fit range (see Figure 8). It is likely that the optimal polynomial order depends on the specific data at hand, the fitted wavelength interval, the type and mass of galaxy, etc.

Table 5
Parameters of Mock Spectra: Stellar Population Parameters of the *alf*-generated Synthetic Templates and Gaussian Parameters of the LOSVD

Mock	Template				LOSVD				
	[Z/H] (dex)	[Mg/H] (dex)	[Fe/H] (dex)	[Na/H] (dex)	v_1 (km s $^{-1}$)	σ_1 (km s $^{-1}$)	w_2	v_2 (km s $^{-1}$)	σ_2 (km s $^{-1}$)
Deep features + wings	0.233	0.231	-0.064	0.523	120	370	0.3	0	900
Shallow features + Gaussian	0.206	0.190	-0.139	0.456	123	374	0.0
Solar abundance + Gaussian	0.0	0.0	0.0	0.0	123	374	0.0

Note. For the the LOSVD, v_1 , σ_1 are parameters of the dominant kinematic component, while v_2 , σ_2 belong to a secondary component with relative weight w_2 . The total LOSVD is the weighted sum of the two components, with $w_1 \equiv 1 - w_2$.

Concerning the wavelength interval that we fit, MILES in principle allows us to model the entire region 4700–7000 Å. In the mock tests above, we only focused on isolated or a few features, but including more absorption features in the fit increases the constraints on the shape of the LOSVD. Unfortunately, the MUSE range includes multiple spectral regions contaminated by under- or over-subtracted skylines, regions in which the detector is affected by other instrumental issues, and sometimes strong emission lines from ionized gas, such as H α . All these systematics can distort the recovered LOSVD shapes. We tried a variety of different setups, before settling for the wavelength region between \sim 4800 and 6200 Å. This interval includes H β , the Mg *b* triplet, several strong Fe absorption lines, and the NaD absorption feature. Our approach involves minimal spectral masking. The specific spectral masks and wavelength limits vary from galaxy to galaxy and are determined according to a strategy that is detailed in Appendix B. For the setup test in this section the spectral masking was chosen to recover the shape of the LOSVD without additional distortions from different model spectra after adding to them mock emission lines for H β , [O III] λ 5007, and [N I] λ 5199 (with $v_{\text{rot}} = 200$ km s $^{-1}$, $\sigma = 150$ km s $^{-1}$).⁵

Notably, we did not mask the NaD feature for our best setup. Masking the NaD absorption feature often resulted in worse recoveries of the LOSVD (Section 6.5).

4.3. Verification of the Setup

In order to verify our fitting approach, we finally describe a set of targeted mock tests where we explicitly try to mimic the conditions under which we fit real massive ETGs and try to answer the question of how much we can trust the shape of the recovered LOSVDs. For these final tests we again created mocks based on synthetic stellar template spectra using *alf* and different LOSVD shapes. We fitted these with exactly the setup that we used for the observed galaxies to obtain an estimate of the expected scatter (and potential biases) in the measurements.

“*Deep Features + Wings*”: First, we set out to create a mock spectrum that is representative of the type of galactic spectra in

⁵ Historically, emission lines were often removed from galaxy spectra, instead of spectrally masked. This, however, can bias the shape of the LOSVD if the emission is not removed correctly. Nonetheless, we also tested this approach by fitting different models with added emission lines using the in-built multicomponent fitting capabilities of WINGFIT, using a simple Gaussian for the emission-line component, and eighth-order Gauss–Hermite polynomials for the stellar component. Then, in the next step we refitted the mocks again with only a stellar component and two different treatments of the emission lines: spectral masking and subtraction of the emission-line models from the two-component fits. We found that the recoveries were of similar quality, though always slightly better in the case of spectral masking, the latter typically having a factor 1.1–1.2 advantage in terms of rms to the input LOSVD. Therefore, we here only use spectral masking.

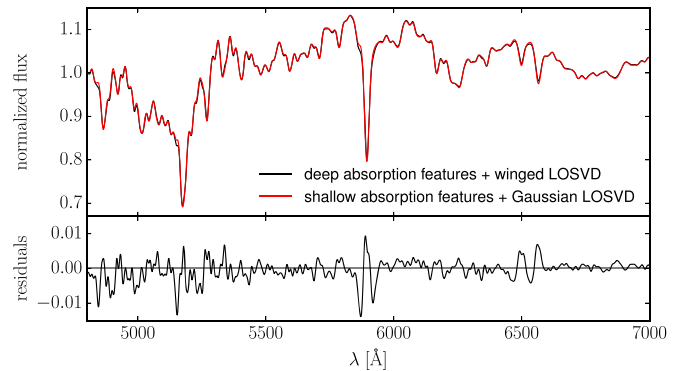


Figure 6. Deep features + wings mock (black) compared to the shallow features + Gaussian mock (red). While the mocks are based on different LOSVDs, the templates were adapted to make the resulting mock spectra as similar as possible. Differences in individual pixels are typically smaller than 1%.

the centers of our ETGs where we measured the most significant LOSVD wings. To this end, we first derived a stellar population model from a fit with a fourth-order Gauss–Hermite LOSVD to the central regions of NGC 1332 using *alf*. A detailed description of our stellar population fitting procedure for the sample galaxies will be given in a different publication (Parikh et al. 2023). Next, we generated a galaxy mock spectrum based on these stellar population parameters and an LOSVD with typical wings extending to $v_{\text{los}} \sim \pm 1700$ km s $^{-1}$. The latter was constructed as the weighted sum of two Gaussians, one narrower component for carrying most of the signal of the distribution and one broader Gaussian component for the wings (see the parameters in Table 5).

In the following, we will refer to this mock by the shorthand DEEP.

“*Shallow Features + Gaussian*”: In order to investigate how well we can recover the LOSVD shape despite the danger of “hidden” template mismatch, we attempted to find a combination of a wingless LOSVD and a different template stellar spectrum that—together—combine into a spectrum that resembles the DEEP mock as closely as possible. Therefore, we derived an alternative stellar population model by fitting the DEEP mock with *alf*, constraining the LOSVD to have a Gaussian shape. In this way, we forced *alf* to implicitly construct a stellar template spectrum that fits the mock under the constraint of a wingless, Gaussian LOSVD. The resulting model served as the second mock for our mock tests, which we will refer to by the shorthand SHALLOW.

It is shown in Figure 6 in comparison with the DEEP mock. As can be ascertained from Table 5, the LOSVD of the mock is essentially just the primary component of the DEEP mock,

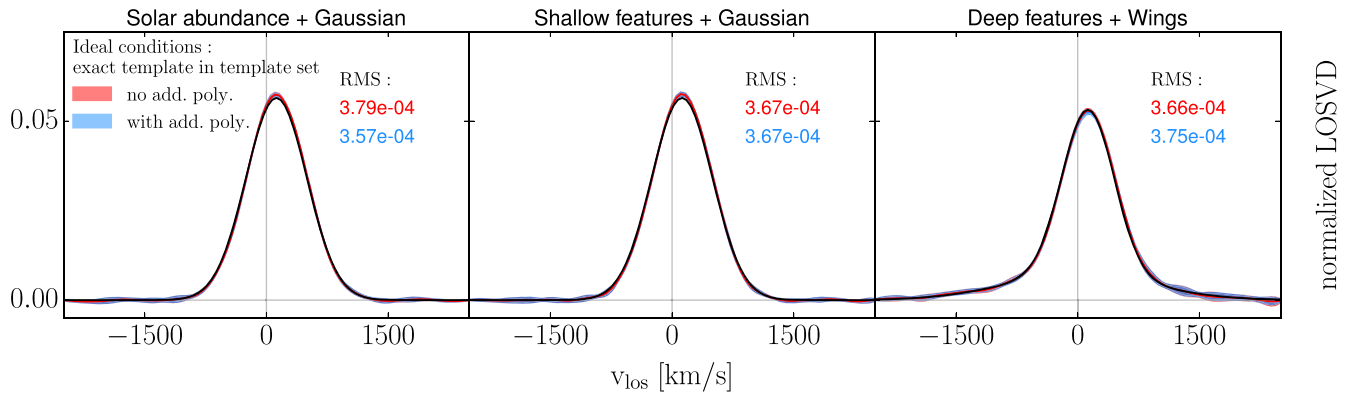


Figure 7. Nonparametric WINGFIT recoveries of the LOSVDs of the SOLAR mock (left column), the DEEP mock (middle column), and the SHALLOW mock (right column). All input LOSVDs are shown in black. As an example for setup invariance of the recovery we show recoveries performed with and without the use of additive polynomials (blue and red shaded, respectively). The barely visible width of the lines indicates the spread of the recoveries from 10 different noise realizations.

without the secondary wing component. The main difference from the latter mock in terms of the chemical abundances is the reduced $[\text{Fe}/\text{H}]$ and $[\text{Mg}/\text{H}]$ (as expected from the discussion in Section 3), resulting in intrinsically shallower features that nonetheless, after both underlying spectra are convolved with their respective LOSVDs, appear to be almost equally deep. Indeed, we tried to provoke as much degeneracy between the models as possible: while the underlying population of the DEEP mock was 12.8 Gyr, a still plausible age, we allowed the age of the underlying population of the SHALLOW mock to assume even unphysical values, for the sake of imitating the DEEP mock as closely as possible, resulting in a stellar population age of 15 Gyr.

“*Solar Abundance + Gaussian*”: Finally, we created a reference model whose stellar populations were purposefully easy to approximate with our empirical MILES templates, by convolving a solar abundance template (generated by setting all abundance ratios to zero, but keeping the age of the underlying population of the DEEP mock) with the same Gaussian LOSVD as for the SHALLOW mock. The shorthand for this mock in the following will be SOLAR.

We generated 10 noisy realizations of each mock assuming an $S/N = 150$ (as in our MUSE data). We fitted all mock data sets with WINGFIT and averaged the resulting LOSVDs in each velocity bin and determined the scatter.

4.3.1. LOSVD Recovery in the Absence of Template Mismatch

As a preliminary first test, we fitted the three mocks with nonparametric LOSVDs using an “ideal” template set consisting of the three synthetic templates underlying the mocks. In this way, for each of the three mocks, one out of the three candidate templates in the template set was always the “true,” exact template of that mock.

The LOSVD recoveries are shown in Figure 7. We tried a variety of different combinations of spectral regions for the fit, spectral masking, and use/order of multiplicative and/or additive polynomials during the fit and found that the results remained invariant under these alterations: in all cases, the recovery of the LOSVD was successful, irrespective of the LOSVD shape, and in each fit the correct template was picked from the template set, while the templates belonging to the other two mocks were ignored.

4.3.2. LOSVD Recovery under Realistic Conditions

We now turn to the results under realistic conditions, i.e., when fitting with the MILES library.

SOLAR: as expected, the recovery of the solar abundance mock with the MILES stars does not pose any problems or biases. The LOSVD recovery is essentially as good as under ideal conditions with the correct template stellar spectrum (Figure 8 left). And, like the ideal fits that used the “real” template, the fit result is largely setup invariant, i.e., it does not depend on the selected wavelength range, spectral masking, or use of polynomials.

DEEP and SHALLOW: The most interesting question is whether we can discriminate between the LOSVD shapes underlying the mocks with the intrinsically shallow and deep features, respectively, even though the mocks were created in such a way as to make them appear as similar as possible. As Figure 8 shows, the recovery is indeed surprisingly good. The fits clearly reveal the different intrinsic LOSVD shapes underlying the two mocks. While the rms between the true LOSVD and the reconstructed one did increase compared to the ideal situation with known template spectra, it is for both mocks still very low. In terms of an eighth-order Gauss–Hermite parameterization, both the asymmetric and symmetric distortions of the LOSVD of the SHALLOW mock are negligible, $\Delta h_{3,5,7} < 0.01$, $\Delta h_{4,6,8} < 0.005$. Fitting the two-component DEEP LOSVD with an eighth-order Gauss–Hermite polynomial and comparing the sequence of even-order Hermite moments as a representation of the strong wings, $h_4 = 0.067$, $h_6 = 0.033$, $h_8 = 0.024$, with those of the recovery, $h_4 = 0.063$, $h_6 = 0.017$, $h_8 = 0.006$, we can see that the recovery overall is quite successful, but it becomes less accurate with increasing order. In terms of the actual nonparametric shape of the LOSVD, this amounts to a very slight overprediction of the LOSVD signal between $v_{\text{los}} = \pm 500$ and $\pm 1500 \text{ km s}^{-1}$ and an even smaller underprediction of the LOSVD signal beyond $v_{\text{los}} = \pm 1500 \text{ km s}^{-1}$. There is also a small bias in σ of $\Delta\sigma \sim 1\%$ for the SHALLOW mock and $\Delta\sigma \sim 5\%$ for the WINGS mock. Overall, however, the recovered LOSVD is consistent with the input model within the statistical uncertainties.

The results of these tests are representative for the line strengths observed in the center of NGC 1332. The strengths of Mg *b*, Fe, and NaD in the centers of the other galaxies of our sample are similar (e.g., Mg *b* $\sim 5.5\text{--}6 \text{ \AA}$, $\langle \text{Fe} \rangle \sim 3.5\text{--}3.7 \text{ \AA}$,

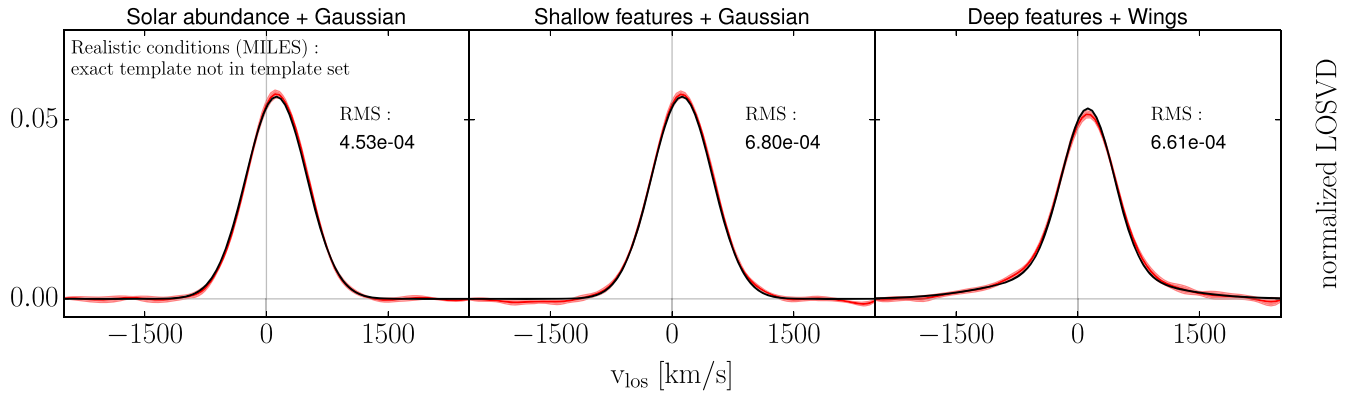


Figure 8. Summary of mock tests: nonparametric WINGFIT recoveries of the LOSVDs of the SOLAR mock (left column), DEEP mock (middle column), and the SHALLOW mock (right column) using our final fitting setup. All input LOSVDs are shown in solid black. The extent of the shaded areas indicates the spread of the recoveries from different noisy realizations of the corresponding mock spectrum. We used a fourth-order multiplicative polynomial and no additive polynomials in the fit.

and NaD $\sim 6\text{--}7\text{ \AA}$; Parikh et al. 2023, submitted). The only exception here is NGC 0307, the most lightweight ETG in our sample, which is markedly closer to solar (Mg $b \sim 4.7\text{ \AA}$, $\langle\text{Fe}\rangle \sim 3.2\text{ \AA}$, and NaD $\sim 4.5\text{ \AA}$). Furthermore, all galaxies, including NGC 1332 and NGC 0307, follow the same radial trends, moving closer to solar with increasing radius (in the outer parts of the galaxies Mg $b \sim 4.2\text{--}4\text{ \AA}$, $\langle\text{Fe}\rangle \sim 2.5\text{--}3.2\text{ \AA}$, and NaD $\sim 3\text{--}4.7\text{ \AA}$; Parikh et al. 2023, submitted). This reduces the amount of template mismatch with MILES templates and consequently the LOSVD distortions, as the SOLAR test shows. Hence, our tests are representative for our whole sample and probe the strongest template mismatch we expect to find in the galaxies. The lack of LOSVD distortions for these tests is particularly relevant given the fact that for both mocks there is actually some residual template mismatch between the effective MILES template and the true one, namely such that the effective template is α -deficient, relative to the α -enhanced DEEP and SHALLOW spectra. In Figure 4 we simulated the effects of this template mismatch on the shape of the LOSVD in a more isolated fashion, i.e., using a smaller wavelength region and fewer template stars. One particular difference is that our fiducial setup for real galaxies that we use here includes the NaD feature. We note that NaD is often very strong in ETGs (e.g., Conroy & van Dokkum 2012; Spiniello et al. 2012; van Dokkum & Conroy 2012). One could have expected that our effective template underpredicts NaD, resulting in a suppression of wing signal where genuine wings could exist. However, we do not find a mismatch of the $[\text{Na}/\text{H}]$ abundance in our effective MILES template with respect to the true one. Therefore, the inclusion of the NaD line did not bias the LOSVD recoveries in such a way that the distortion effects of the $[\text{Mg}/\text{Fe}]$ mismatch were merely compensated in the opposite direction. In this case we would have only accidentally recovered the correct LOSVD shape. Instead, it is the strength of NaD that provides a vital constraint on the shape of the LOSVD that made the fit more robust against the mismatch present in the other features.

We note that when we used the setup with minimum rms according to Table 3, which made extensive use of higher-order polynomials and where we masked NaD, the (symmetric) distortions of the LOSVDs were so strong that the recovered LOSVDs for both SHALLOW and DEEP were excessively winged and basically became indistinguishable from each other. Masking the second-strongest feature in our wavelength range,

Mg b , proved less critical but still significantly overpredicted the wings of the DEEP mock (raising the even-order Hermite moments, particularly $\Delta h_4 \sim 0.03$). Masking Mg b also increased σ (by $\sim 3\%$), but the effect of masking any feature also depends on the other features included in the fit and the particular mismatch of the templates that are used (e.g., Barth et al. 2002).

Instead, using our best setup from this section, we conclude that even though the centers of ETGs are often α -enriched by Type II supernovae as a consequence of rapid early star formation (e.g., Thomas et al. 1999, 2005; Conroy et al. 2014), our tests demonstrate that this is not an issue for an unbiased recovery of their LOSVD shapes.

We repeated these tests for S/Ns of 20, 50, and 80 without encountering any additional bias in the LOSVD recovery.⁶ At an S/N = 50, the recovery of the prograde wing of the DEEP mock LOSVD loses its statistical significance (by contrast, the more extended retrograde wing can be recovered with significance even at an S/N = 20 up to $\sim 1500\text{ km s}^{-1}$).

5. Results

In the previous sections we have demonstrated that the nonparametric shapes of LOSVDs can be measured with high accuracy and precision. We fitted nonparametric LOSVDs with WINGFIT for all spatial bins of our sample galaxies using the setup that turned out best in the previous sections. As an example of these fits, Figure 9 shows a kinematic fit to a Voronoi bin from the central regions of NGC 1332.

5.1. Nonparametric LOSVDs

In Figures 10 and 11, we show all nonparametric LOSVDs from our WINGFIT analysis grouped into fast and slow + intermediate rotators, respectively. We show individual LOSVDs in different spatial regions, together with their light-weighted average over these regions. While individual LOSVDs sometimes show oscillations larger than the statistical uncertainties from Monte Carlo simulations, the process of averaging LOSVDs over larger spatial regions helps to identify the most robust structures (in particular in the high-velocity tails of the LOSVDs). All galaxies, to a

⁶ This was the case even for the lowest S/N = 20, despite that the noise in this case is nominally larger than the differences between the mocks seen in Figure 6. This appears to be an effect of the large number of pixels used in the fit, which still provide enough constraints for the LOSVD.

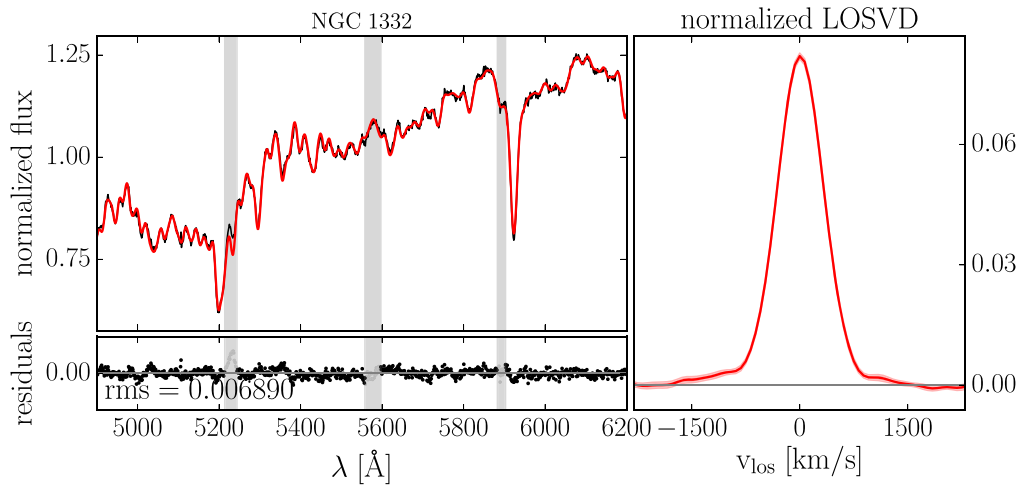


Figure 9. Left: kinematic fit (red) to the spectrum (black) of the central Voronoi bin of NGC 1332 using WINGFIT. Gray shaded areas indicate spectral regions that were masked during the fit. Right: nonparametric LOSVDs (solid red) recovered from these fits. The shaded envelope indicates the statistical uncertainties of the LOSVD from 100 Monte Carlo simulations. The line-of-sight velocities v_{los} are relative to the systemic velocity of the galaxy.

lesser or greater extent, show LOSVDs with wings. These are well defined in different parts of the galaxies but typically decrease from the center outward.

5.2. Parameterization of the LOSVDs: Higher-order Gauss–Hermite Moments and Large-scale Trends of Stellar Kinematics

Fitting the nonparametric LOSVDs from the previous section a posteriori with Gauss–Hermite polynomials, we also present the results of our stellar kinematic analysis in the form of 2D kinematic maps of the rotational velocity v_{rot} , velocity dispersion σ , and higher-order Gauss–Hermite coefficients h_3, h_4, h_5, \dots ; maps for the fast and the slow + intermediate rotators are shown in Figures 13 and 14, respectively. The maps help to highlight coherent stellar kinematic structures and patterns across the MUSE FOV. The highest order of Gauss–Hermite coefficients at which we can still visually identify coherent structures in the kinematic maps is larger for the fast rotators in our sample than for the slow + intermediate rotators. Therefore, we here present the kinematic maps of the fast rotators in our sample up to h_8 and the ones for the slow rotators up to h_6 . These orders should be regarded as the highest common order for either group. Individual galaxies show structures up to even higher-order moments.

In general, increasing orders of Gauss–Hermite moments permit an increase in the amount of signal at higher line-of-sight velocities, v_{los} , in units of σ , which can be generated for a parametric LOSVD. As a result, higher orders of coefficients are necessary to produce LOSVD wings. This is particularly important for power-law galaxies, as rotation increases the distance of the peak of the LOSVD from the terminal velocity of the tails/wings on the opposite side of the rotation. Consequently, higher orders and larger values of Hermite coefficients are needed to represent the full shape of their LOSVDs. Higher orders also add complexity to the shape of the distribution, which is, again, particularly relevant for the power-law galaxies in our sample, as they have LOSVDs with a stark contrast between dynamically cold, low-dispersion, disk or disk-like kinematic components and broader, high-

dispersion, bulge and wings components (J. Thomas et al. 2023, in preparation).

In NGC 6861, the kinematic maps show such spatially coherent patterns along its major axis up to even higher moments than shown here. We will present a detailed discussion of the kinematics of this galaxy in a separate paper (J. Thomas et al. 2023, in preparation).

5.2.1. Odd-order Hermite Moments

Figure 12 shows the higher-order Gauss–Hermite moments of the ETGs against v_{rot}/σ , separated into fast and slow +intermediate rotators by color.

Odd-order Hermite moments add asymmetries to the LOSVDs. In the first row of the figure, the $h_{3,5,6}$ profiles of fast-rotating power laws are spread out wide over v_{rot}/σ , with the profiles developing pronounced, curved, sometimes spiral-arm-like $v_{\text{rot}}-h_{2n+1}$ (anti)correlation patterns. Correlations or anticorrelations often reverse their order from one odd-order moment to the next, resulting in the oscillation of coefficients around zero between these moments seen in the kinematic maps. In general, odd-order Hermite moments are largely influenced by projection effects related to rotation, e.g., the famous anticorrelation between v_{rot} and h_3 in most axisymmetric galaxies. These typical hallmarks extend beyond h_3 to higher odd Hermite coefficients.

The spiral-arm shapes originate from the slope changes in the diagrams, most notably around $|v_{\text{rot}}/\sigma| \sim 1$ and $|v_{\text{rot}}/\sigma| \sim 0.5$. Typically, such slope changes are associated with transitions between different dynamical components, such as disks and bulges (e.g., Erwin et al. 2015; Veale et al. 2018). This is particularly visible for NGC 6861, where the h_{2n+1} (anti) correlations with v_{rot} become much steeper for the transition from the dynamically hot to the dynamically cold regime, $|v_{\text{rot}}/\sigma| > 1$. This is also clearly visible in the kinematic maps (see, e.g., NGC 6861 in Figure 13), where spatial regions with the strongest odd-order Hermite coefficients trace out the major axis of the galaxy.

NGC 1332 is a particularly interesting case: here, slope changes around $|v_{\text{rot}}/\sigma| \sim 0.5$ result in a transition from $v_{\text{rot}}-h_3$ correlation to anticorrelation, which then—via the oscillation of coefficients—reverberates to h_5 and, to a lesser extent, h_7 . The

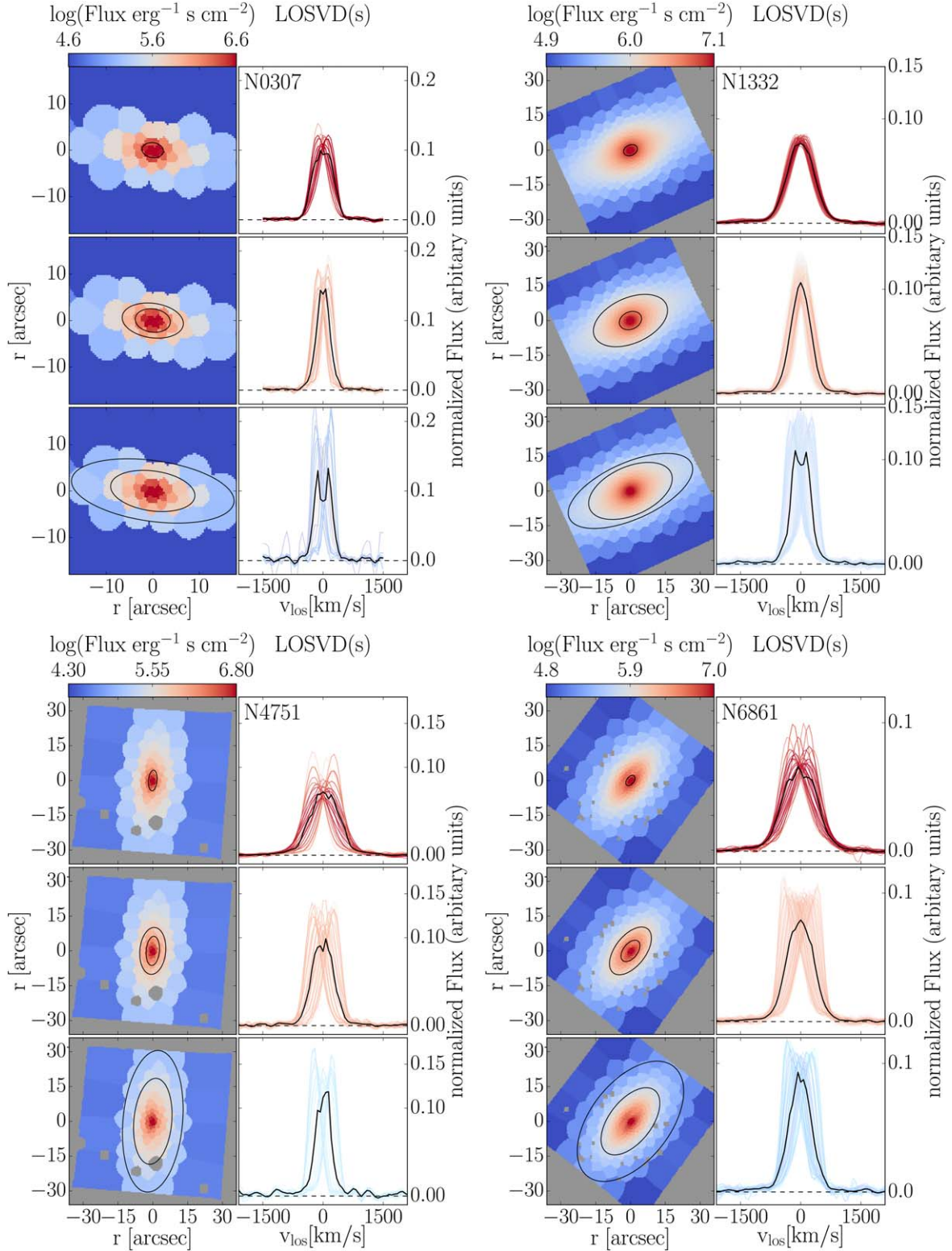


Figure 10. Nonparametric LOSVDs for fast-rotating ETGs NGC 0307, NGC 1332, NGC 4751, and NGC 6861. For each subfigure, LOSVDs are shown across three different spatial regions. Each region, in turn, is represented by one row and defined by all bins between two isophotes (black lines) shown in the left panels of the subfigures. The respective nonparametric LOSVDs from our WINGFIT analysis are shown in the right panels of the subfigures. Each LOSVD is colored according to the flux in the respective Voronoi bin. LOSVDs in solid black show the light-weighted average LOSVD in the respective area.

region of v_{rot} , h_3 correlation within $|v_{\text{rot}}/\sigma| \sim 0.5$ is also very noticeable in the h_3 map for the galaxy (see Figure 13), forming a “butterfly shape,” which, as we will argue later on, could be indicative of the presence of a bar component.

By contrast, slow + intermediate-rotating cores cluster around $v_{\text{rot}}/\sigma = 0$ and $h_{3,5,7} = 0$. There is only very minimal $v_{\text{rot}}-h_{2n+1}$ (anti)correlation and odd moment-to-moment oscillations, with the notable exception being the intermediate

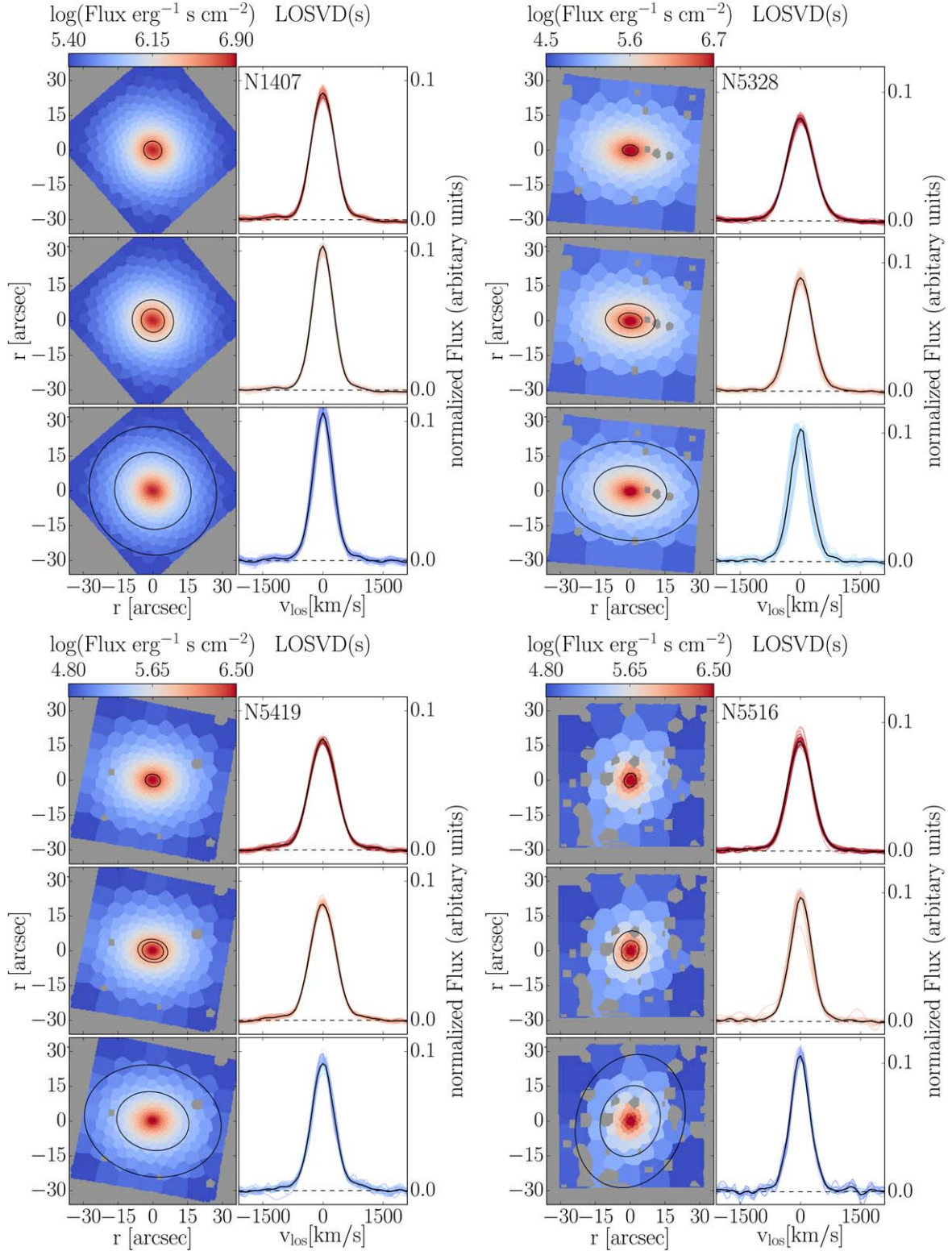


Figure 11. Nonparametric LOSVDs for slow-rotating ETGs NGC 1407, NGC 5328, NGC 5419, NGC 5516, and NGC 7619.

rotator NGC 7619, which shows steep $v_{\text{rot}}-h_3$ anticorrelation, which also features prominently in the galaxy’s kinematic maps (see Figure 14). None of the slow + intermediate-rotating galaxies have dynamically cold components, $|v_{\text{rot}}/\sigma| > 1$.

Overall, for all galaxies, the odd-order Hermite moments are largely unbiased, averaging out to zero over the FOV, which is also clearly visible in the kinematic maps, suggesting that any

residual asymmetric bias in the shape of the LOSVDs caused by template mismatch is likely very small.

5.2.2. Even-order Hermite Moments

Even-order Hermite moments add symmetric components to the LOSVDs. They are shown in the second row of

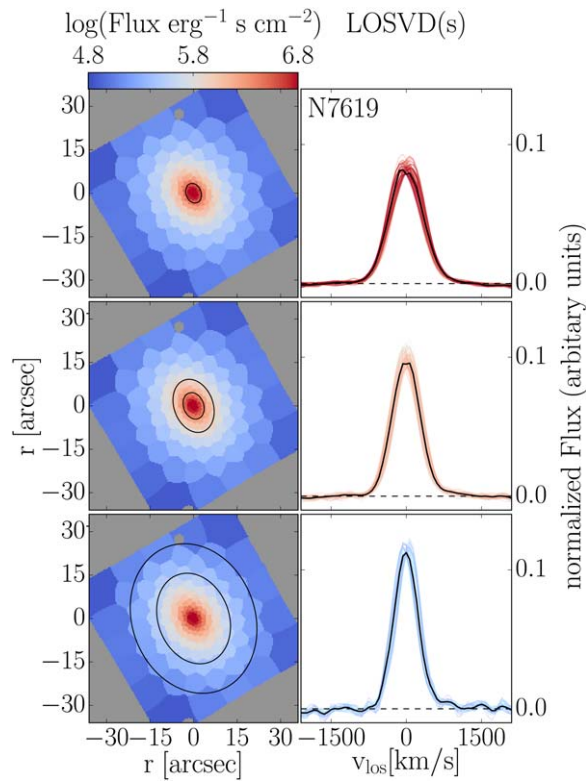


Figure 11. (Continued.)

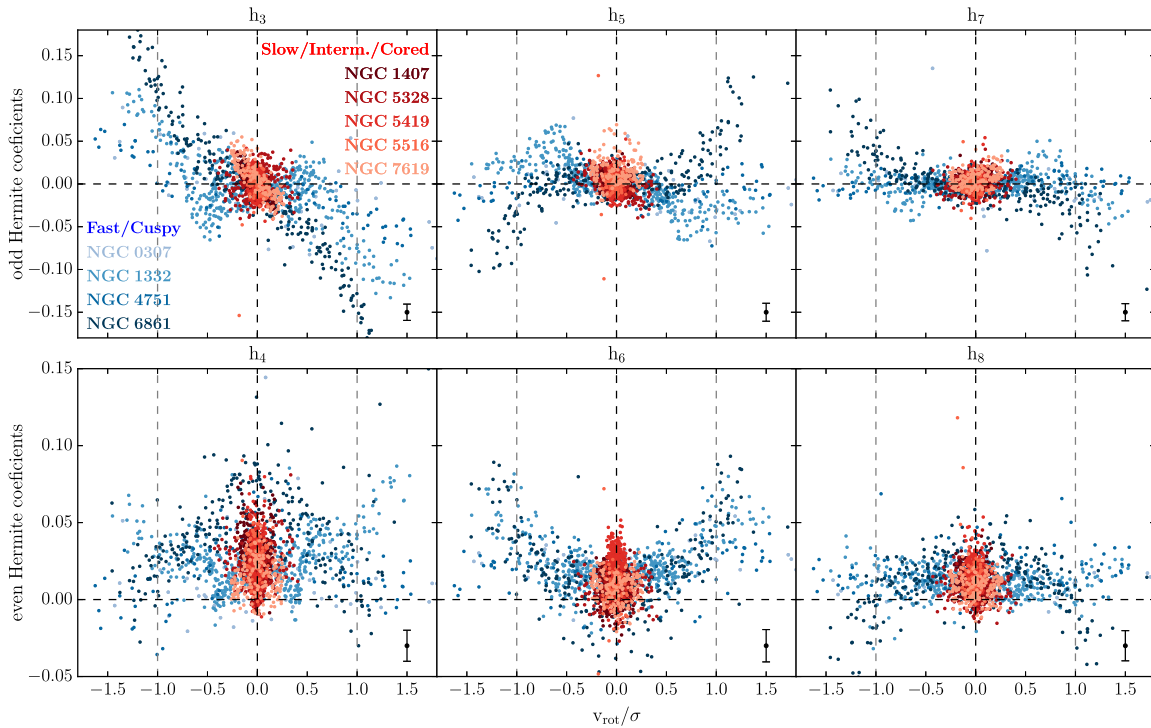


Figure 12. Higher-order Hermite moments h_3, \dots, h_8 against v_{rot}/σ , separated into odd-order (first row) and even-order moments (second row). The average error bar of each Hermite moment over all galaxies is indicated in black in each panel. The Hermite moments of fast-rotating, power-law ETGs (shades of blue) cover on average a larger dynamic range than those of slow- and intermediate-rotating, cored ETGs (shades of red). The even-order moments of both galaxy types are on average positive, while the odd moments are centered on zero. Lines at $v_{\text{rot}}/\sigma = \pm 1$ indicate transition points between dynamically hot and cold regions.

Figure 12. The most notable trend is that the coefficients are overall offset from zero toward $h_{2n+2} > 0$ for all types of galaxies—in contrast to the odd moments. The fast-rotating

power laws show mostly linear relations between $|v_{\text{rot}}|$ and $h_{4,6,8}$, which are, unsurprisingly, symmetric around $v_{\text{los}} = 0$. Just as with the odd-order coefficients, we find oscillations of

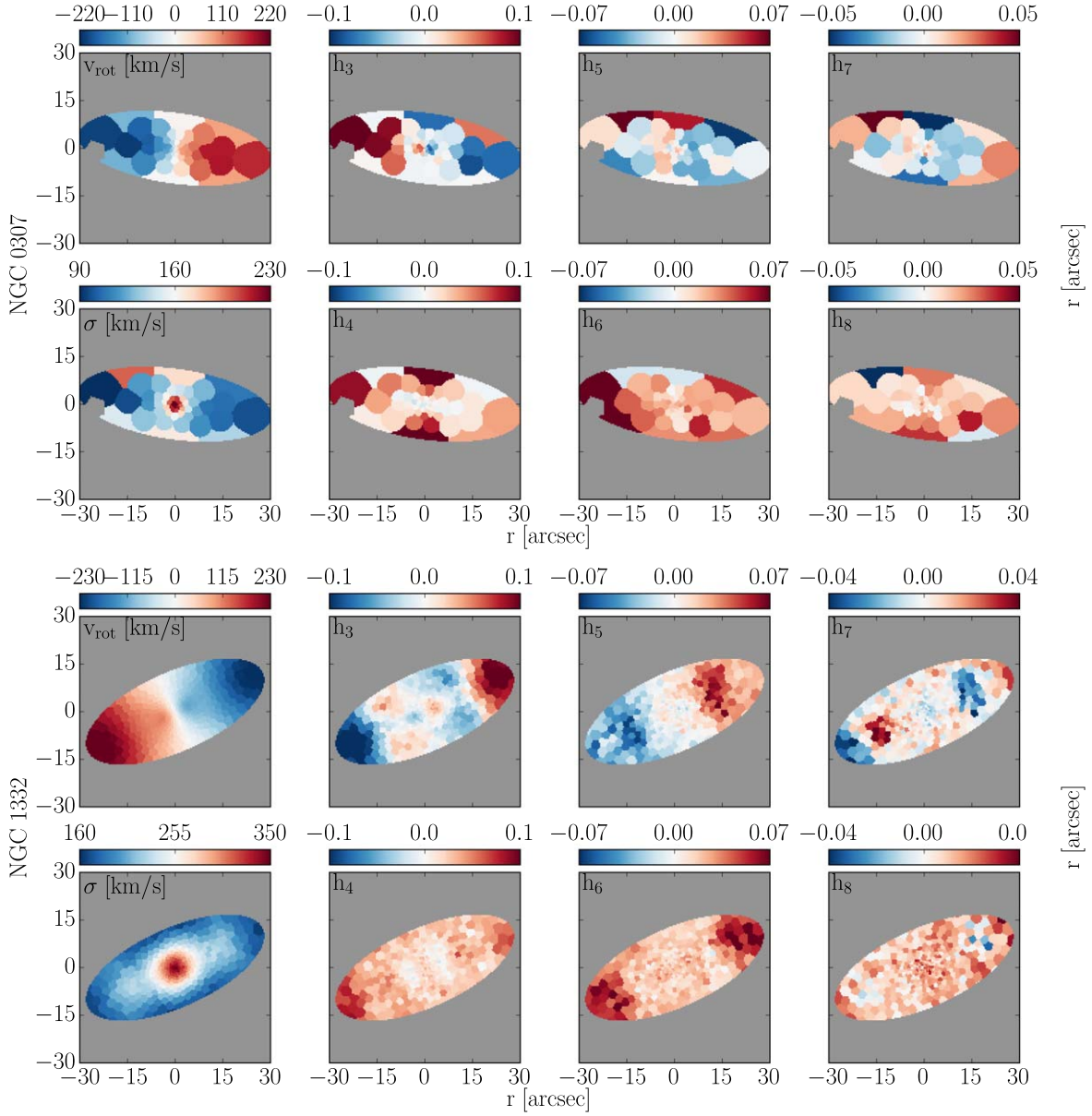


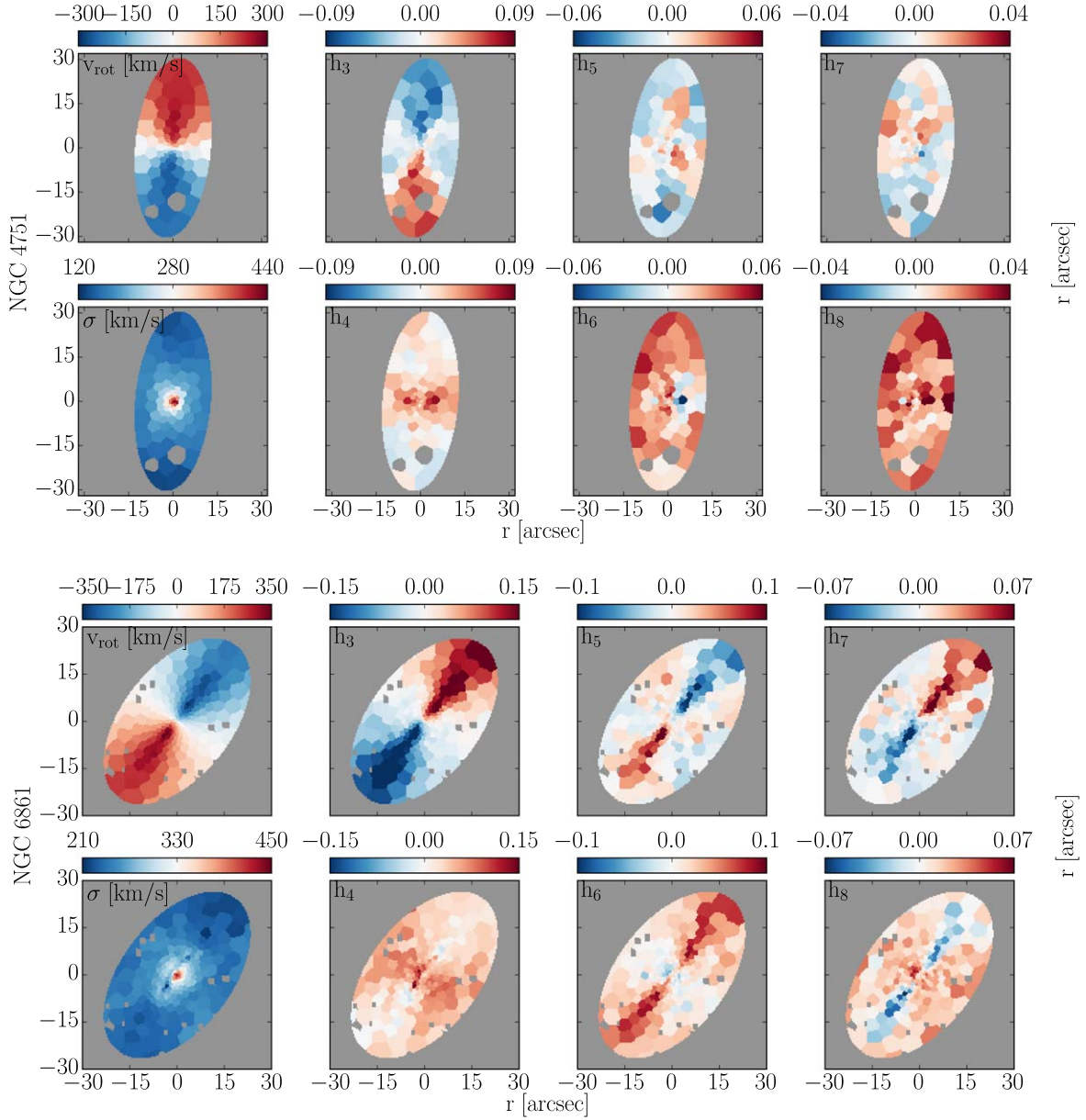
Figure 13. From left to right: MUSE-based 2D stellar kinematics of fast-rotating ETGs NGC 0307, NGC 1332, NGC 4751, and NGC 6861. In each subfigure, from top left to bottom right: maps of the rotational velocity v_{rot} , velocity dispersion σ , and higher-order Gauss–Hermite coefficients $h_3 - h_8$. We only show pixels inside the largest isophote that fits wholesale into the MUSE FOV (gray areas inside this region have been excluded from the binning). This implicitly indicates the positions of the major and minor axes and gives a general idea of each galaxy’s morphology.

the values of the coefficients from one even order to the next, albeit around values $h_{2n+2} > 0$ for most v_{rot}/σ .

For the slow + intermediate galaxies, there appears to be little or no correlation with rotation for the even-order moments. Instead, as can be seen in the kinematic maps, the even-order moments are more correlated with radius than with rotation, in the sense that the even-order coefficients typically increase/decrease at larger radii, while odd-order coefficients are generally strongest wherever the rotational velocity is strongest. Typically, the sign of the even moments does not change from one order to the next in the case of the slow rotators. These even moments are probably related to the contrasts between the widths of the narrower main part of the LOSVD and the broader wings.

However, neither h_4 nor other higher-order, even Gauss–Hermite moments can be used to parameterize the wings in a straightforward manner. This is because even-order moments govern not only the taillight and cutoff velocity but also the narrowing or flat-topping of the trunk of the LOSVD. Consequently, adding, e.g., wings to an LOSVD with a flat-topped or bimodal shape can result in an LOSVD with a net h_4 smaller than that of an LOSVD with a narrower peak but smaller wings.

We note that NGC 6861 seems to have particularly large values of h_4 within $|v_{\text{rot}}/\sigma| \sim 0.5$, compared to other fast rotators. This could be indicative of a larger, dynamically hot component in the galaxy contrasting against a narrower, more flattened component by way of h_4 . However, this is likely also


Figure 13. (Continued.)

partly due to dust, as the h_4 map of the galaxy (see Figure 13) shows its largest h_4 values in spatial regions associated with patchy dust bands within the galaxy’s disk. We discuss the effect of dust on the measurement of the stellar kinematics in the next section.

5.3. Radially Resolved Angular Momentum

Using our new kinematics, we create profiles of the angular momentum parameter λ of Emsellem et al. (2007, 2011) against radius, shown in Figure 15. As expected, the profiles are consistent with the typical fast/slow rotator dichotomy. However, three galaxies show trends that are worth singling out: NGC 7619, one of the intermediate-rotating galaxies, has a λ profile perfectly consistent with that of the fast rotators in our sample for small r/r_e , before shallowing out to a profile that is more similar to the slow rotators, but with overall larger λ at the same r/r_e . Here the “intermediate” classification seems to

be particularly apt. Both NGC 5328 and NGC 5419 have local maxima of λ around $r/r_e \sim 0.1$. This is due to the fact that both galaxies exhibit counterrotation in their central regions (see the v_{rot} maps in Figure 14). An inner maximum of the angular momentum—although weaker—is also present in NGC 1407. While the galaxy shows some kinematic twist in its center, there is no sign of counterrotation. All three galaxies appear to have double velocity dispersion peaks in their centers.

6. Discussion

6.1. Robustness of the Measurements

We are here, for the first time, investigating the full nonparametric shape of the LOSVDs of massive ETGs up to the highest bound stellar velocities. Our setup was specifically designed with the goal of bringing new, previously inaccessible kinematic aspects of ETGs to light. We have paid a lot of attention to possible sources of template mismatch and ways to

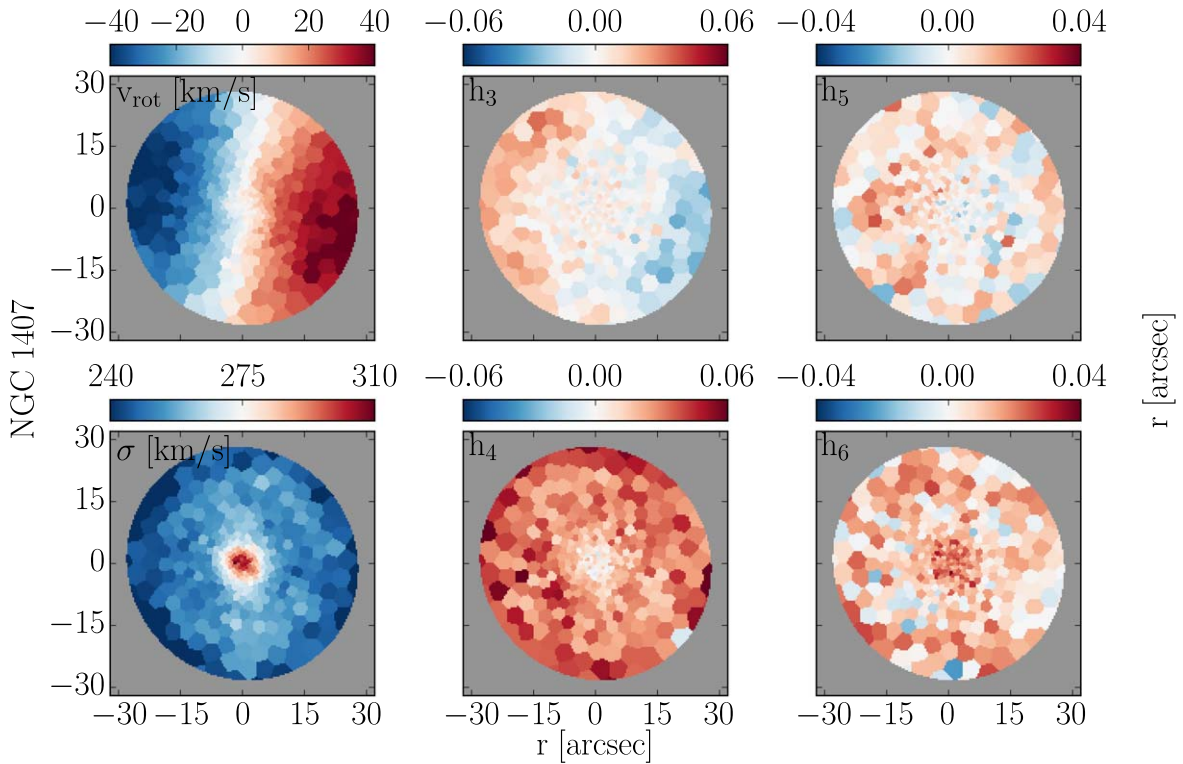


Figure 14. From left to right: MUSE-based 2D stellar kinematics of slow rotating ETGs NGC 1407, NGC 5328, NGC 5419, NGC 5516, and NGC 7619. In each subfigure, from top left to bottom right: maps of the rotational velocity v_{rot} , velocity dispersion σ , and higher-order Gauss–Hermite coefficients $h_3 - h_8$. We only show pixels inside the largest isophote that fits wholesale into the MUSE FOV (gray areas inside this region have been excluded from the binning). This implicitly indicates the positions of the major and minor axes and gives a general idea of each galaxy’s morphology.

minimize its effect on the shape of the recovered LOSVDs. In Section 4.2 we have discussed mock tests that have shown that our setup is robust against the expected forms of template mismatch. A posteriori, our measured LOSVDs for the observed galaxies confirm the robustness of our setup. Most significantly:

1. The Gauss–Hermite parameters derived from our LOSVDs give virtually no indication of template mismatch, given the almost complete lack of bias in h_3 and even, to a lesser extent, the other higher-order odd moments.
2. The high-velocity wings that we observe in many galaxies do not follow the velocity shifts of the LOSVD peaks in galaxies with rotation: while the main trunk of the LOSVD is centered on different v_{los} in different places of a rotating galaxy, the wings remain stationary relative to $v_{\text{los}} \sim 0$ (e.g., NGC 4751 and NGC 6861 in Figure 10). This makes template mismatch unlikely as the origin of the wings.
3. Template mismatch is likely strongest in the centers of our galaxies owing to increased metallicity and α elemental abundances there. However, we find LOSVD wings at both small and large radii.

We note that fitting the ETGs with the library of stars from Ivanov et al. (2019), which were observed with MUSE, produced the same winged LOSVDs as in our analysis. The wings are slightly less symmetric in this case, due to the smaller number of templates (only 35), which gives less flexibility to reduce the template mismatch in our preselection approach. This test excludes that the shape of the instrumental LSF of MUSE could bias the LOSVDs toward a winged shape.

Finally, in Appendix C we compare our kinematic measurements from the ETGs with previous published ones using different data and methods.

6.2. Origins of the LOSVD Wings

In this section we will speculate on the possible origin of extended, high-velocity wings for the nonparametric LOSVDs of ETGs. In addition to the LOSVDs presented here, the nonparametric kinematic study of the BCG Holm 15A with WINGFIT (Mehrgan et al. 2019) had also presented evidence for wings. Furthermore, there are examples of previous studies (e.g., van de Sande et al. 2017; Veale et al. 2018) noting increasing h_4 toward larger radii in massive ETGs. Veale et al. (2018), in particular, noted positive values of h_4 for most ETGs from the MASSIVE sample. While there is no one-to-one relation between h_4 and wings, wings always tend to increase h_4 .

6.2.1. LOSVD Wings at Small Radii: PSF Light?

The PSF redistributes light between different regions on scales on the order of a couple of times the FWHM. In the central regions, within the cusp or cuspy core of ETGs, especially approaching the central SMBH, the intrinsic stellar kinematics have very steep gradients with scales smaller than the PSF in this study (Rusli et al. 2013a, 2013b). Therefore, it is very likely that most of the light at large projected velocities—i.e., the wings—is light from the very center of the galaxy, possibly including contributions from within the sphere of influence (SOI) of the central black hole.

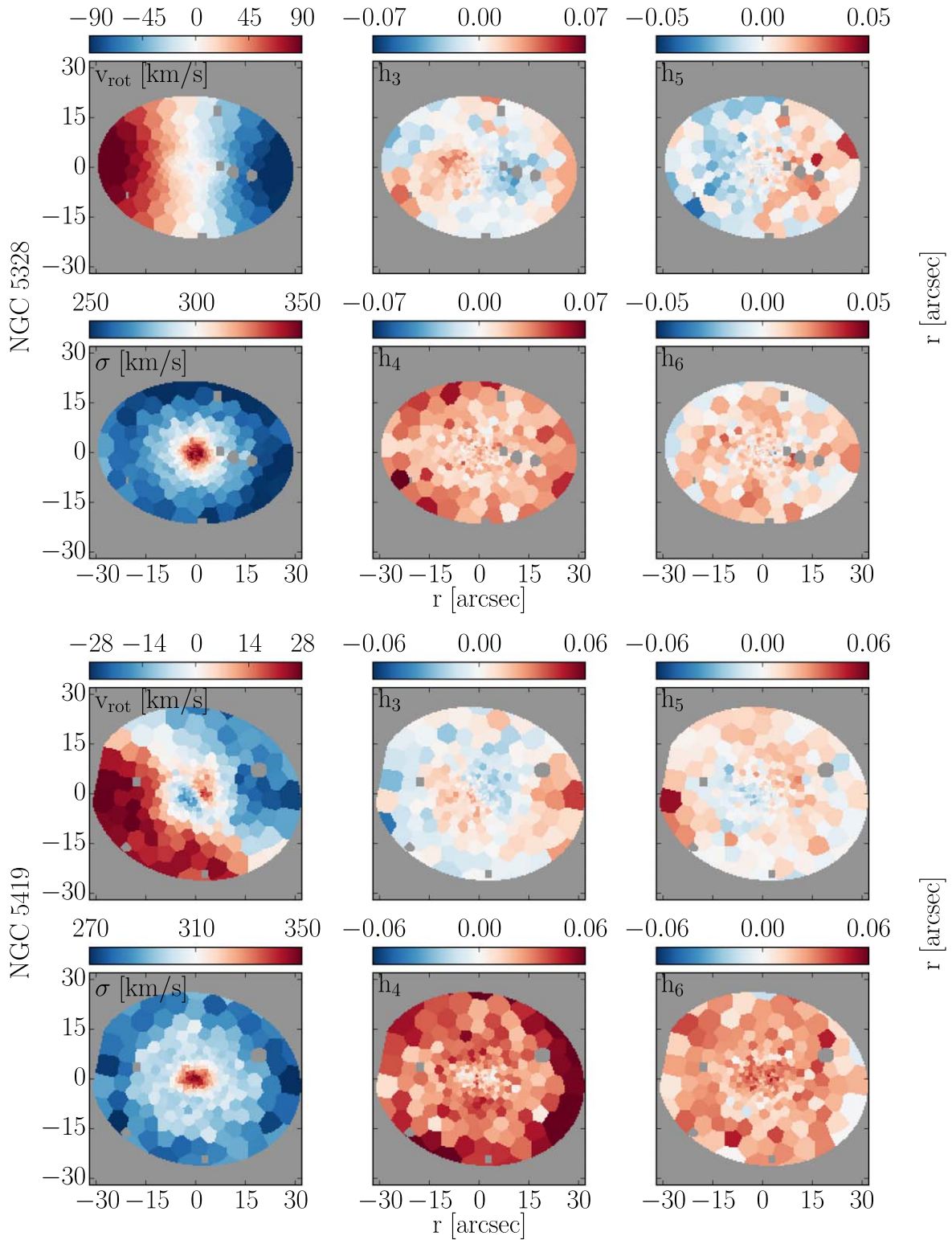


Figure 14. (Continued.)

If this is true, fitting nonparametric LOSVDs with the advanced accuracy, as we do here, might enable us to determine the masses of the central black holes from Schwarzschild dynamical modeling, even when the SOI is smaller than the PSF. We will investigate this possibility in our dynamical follow-up study of these ETGs (K. Mehrgan 2023, in preparation.).

Alternatively, or in addition, there could also be an overlap of two kinematically distinct stellar populations in the central parts of the MUSE FOV. Wings would then be produced by the contrast between a compact high- σ component and a brighter but narrower component that becomes more dominant with distance from the center of the galaxy.

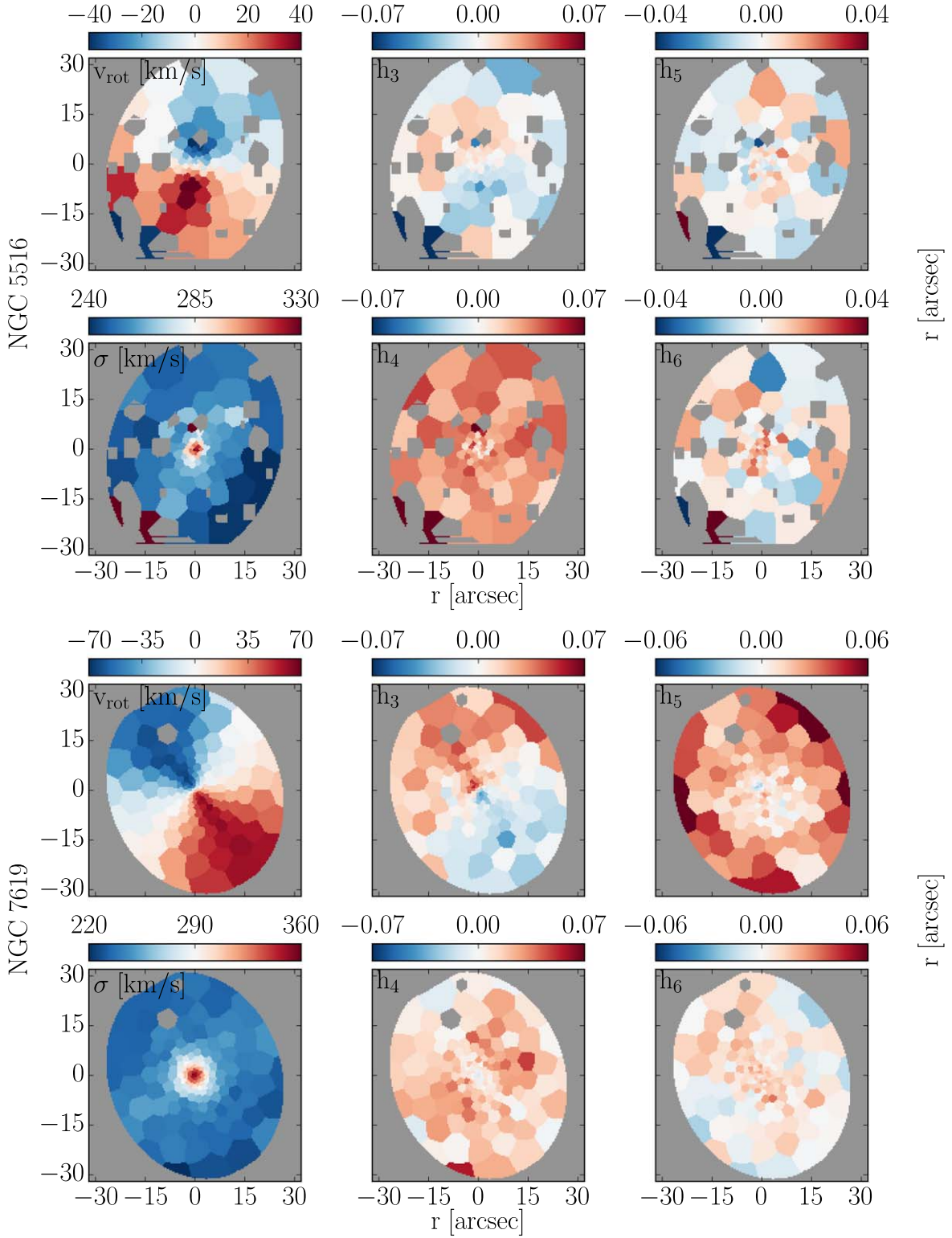


Figure 14. (Continued.)

6.2.2. LOSVD Wings at Large Radii: A Faint Stellar Envelope?

Wings outside the PSF region must have a different physical origin. Given the low signal but large stellar line-of-sight velocities in the wings $v_{\text{los}} \gtrsim 1000 \text{ km s}^{-1}$, it is likely that they originate from highly eccentric, loosely bound orbits that take the stars out to even larger radii. We therefore propose that these stars are to be associated with a faint, outer envelope of

weakly bound stars around the ETGs, similar to the much larger and brighter envelopes around BCGs.

In the latter galaxies, stellar envelopes are usually readily apparent in the stellar kinematics as a rise in the stellar velocity dispersion toward larger radii (e.g., Carter et al. 1981, 1985; Ventimiglia et al. 2010; Arnaboldi et al. 2012; Spiniello et al. 2018; Loubser et al. 2020). For NGC 6166, Bender et al. (2015)

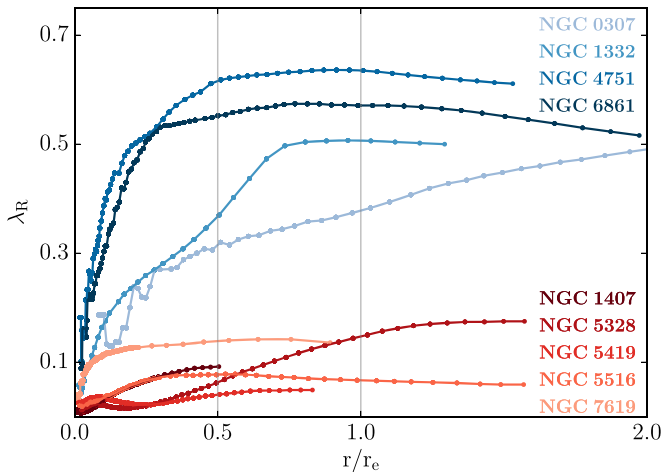


Figure 15. Angular momentum parameter λ over radius, scaled by the effective radius of each galaxy, r/r_e . Galaxies are separated into fast rotators (shades of blue) and slow rotators (shades of red).

found that this rising velocity dispersion profile increased toward larger radii, until it meets the dispersion of the cluster A2199. They concluded that the stellar envelope of the galaxy was more dominated by the gravity of the cluster than the central galaxy, to which it was only weakly bound, which was also evidenced by a growing bias in the rotation velocity toward larger radii. We propose a similar scenario for our ETGs, except for the stars being *necessarily* bound to a galaxy cluster.

Naturally, light from the outer envelopes of our ETGs would be much fainter than for the BCGs, which are at large radii entirely dominated by their envelopes. In our ETGs, in particular given our comparatively small spatial coverage with respect to the scales that are relevant here ($r > r_e$), we are in a regime where we only expect a faint high- σ LOSVD component superimposed on the dominant LOSVD associated with the inner parts of the galaxy—similar to how we have constructed the winged mock LOSVD (of the DEEP mock) in Section 4.3.

While in BCGs the velocity dispersion at large radius rises because the broader envelope component overshadows the main galaxy component, for the ETGs we would only expect to see an increase in the wing light with radius, while the broad component remains still the minor component. This could lead to an increase in h_4 with radius. By eye, we see increasing wing light toward larger radii in NGC 6861, NGC 1407, NGC 5328, and NGC 5419 (see Figures 10 and 11). In these same galaxies we also find an increase of h_4 (see Figures 13 and 14).

However, it must be noted that we are here only observing these ETGs at relatively small radii, $\lesssim 2r_e$ —we would need observations at larger radii to properly confirm this trend in these and perhaps also the other galaxies.

This scenario could also help explain the fact that in some galaxies the wings are slightly asymmetric. If the wings were an artifact related to template mismatch, we would expect them to be larger in the α -enriched galaxy centers rather than in the outskirts. But asymmetry between the narrower and broader components could reflect distortions in the dynamical equilibrium between the inner and the outer parts of the galaxies. For example, massive BCGs are often not properly settled in their respective cluster/envelope (see, e.g., the aforementioned

study of NGC 6166 by Bender et al. 2015, where the BCG’s central velocity is at odds with the cluster component on a scale of 50–100 km s^{−1})—we would expect this trend to be typically worse for our less massive ETGs. Hence, the asymmetry of the wings in our ETGs could originate from the broad LOSVD component of the envelope being shifted relative to the narrower component of the galaxy.

Of course, the analogy between such faint stellar envelopes and those of BCGs can only go so far, as for the latter the envelope is mostly a halo of stars ripped free, stripped, and accreted from other galaxies in the cluster (e.g., Bender et al. 2015; Kluge et al. 2020), while for our much less massive ETGs, which do not sit at the bottom of the gravitational well of some massive cluster, this probably cannot account for all of the envelope stars. Instead, we suggest a scenario in which the faint envelopes are mostly remnants of past mergers, wherein stars were placed on loose, higher-eccentricity orbits.

Here we have introduced the idea of the faint stellar envelope purely on kinematic grounds, but this is in itself not remarkable, as for BCGs there is typically no conclusive way of confirming an envelope from photometry alone, as in NGC 6166, where the impetus for the photometric decomposition by Bender et al. (2015) was derived from the increase in the velocity dispersion toward larger radii. Yet, for several of the galaxies in our sample, photometric decompositions require an outer stellar envelope component: this was the case for NGC 1407, NGC 5516 (Rusli et al. 2013a), and NGC 6861 (K. Mehrgan et al. 2023, in preparation). The last has been noted for being surrounded by an especially rich and dense globular cluster system (Escudero et al. 2015).

6.3. An End-on Hidden Bar Component in NGC 1332?

Some of the most striking kinematic patterns that we found for the kinematic maps that we produced for our sample are doubtlessly the ones for NGC 1332 (See Figure 13): the h_3 map shows X-shaped or butterfly-like regions of $v_{\text{rot}}-h_3$ correlation at roughly 45° angles to the major axis of the galaxy, interrupting the usual $v_{\text{rot}}-h_3$ anticorrelation regions at smaller and larger radii. At the same time, we find two lobes of lowered h_4 for the central regions of the h_4 map, as well as extended handles or lobes of relatively heightened σ along the major axis in the σ map.

These patterns look surprisingly similar to the 2D kinematic signatures of boxy/peanut bulges in simulated disk galaxies from Iannuzzi & Athanassoula (2015): the X-shaped $v_{\text{rot}}-h_3$ correlation regions in particular seem to be a good match for maps of an end-on bar shown in Figure 29 of Iannuzzi & Athanassoula (2015) for a disk inclination of $i = 80^\circ$. Intriguingly, a similar inclination of $i \sim 85^\circ$ has been found by ALMA observations of the circumnuclear disk of NGC 1332 by Barth et al. (2016).

We therefore cautiously suggest the presence of an end-on bar in NGC 1332. If this turns out to be true, this would likely lead to a bias in the determination of dynamical mass estimates of the galaxy if the bar component is not accounted for. This could potentially account for the discrepancy between the black hole mass measurements from dynamical models of the stars in the galaxy from Rusli et al. (2011) and those from emission from its circumnuclear disk observed with ALMA (Barth et al. 2016).

We note that Cretton & van den Bosch (1999) and Emsellem et al. (2011) have also suggested (but ultimately not favored)

the possibility of end-on bars in the massive ETGs NGC 4342 and NGC 1277, respectively, based on similar kinematic signals to what we have detected in NGC 1332.

6.4. Decoupled Cores in NGC 1407, NGC 5328, and NGC 5419?

Similarly striking in the kinematics maps are the decoupled cores that we found particularly for NGC 5328 and NGC 5419, as well as, to a lesser extent, NGC 1407 (see Figure 14). They are central regions where the rotation patterns of the galaxies suddenly flip and change signs. As previously discussed in Section 5.3, the three galaxies also seem to have central local maxima of their angular momentum parameter λ associated with the decoupled regions, which distinguish them from the other cored ETGs.

The counterrotation in the center of NGC 5419 was already reported by Mazzalay et al. (2016), who, using both HST and adaptive optics based SINFONI observations, found a double nucleus in the galaxy. For NGC 1407 Johnston et al. (2018) claimed a decoupled core from their analysis of the MUSE data from our proposal. It is not based on nonparametric LOSVDs, though, and the h_3 distribution is biased, likely indicating template mismatch.

Numerical simulations of merging ETGs from Rantala et al. (2019) and Frigo et al. (2021) produced rotation and dispersion patterns matching those we discuss here. Their simulations suggest that counterrotating decoupled cores are the products of binary SMBH mergers that occur during the mergers of ETGs that produce cored ETGs, such as NGC 1407, NGC 5328, and NGC 5419. Indeed, Mazzalay et al. (2016) suggested that there are two SMBHs at a distance of ~ 70 pc in the center of NGC 5419, which are associated with the double nuclei. In our central rotation map, the inner counterrotating regions appear to be connected to the larger velocity field in a way that suggests an inspiraling motion of the stars, which, in this scenario, would have been caused by dynamical drag of the sinking SMBHs/nuclei of the merging ETGs (Rantala et al. 2019; Frigo et al. 2021).

6.5. On the Inclusion of NaD

The 5890 and 5896 Å NaD absorption feature is commonly masked for stellar kinematics/populations owing to the danger of excess NaD absorption (or emission, but this only applies to low-mass galaxies, unlike our ETGs; Concas et al. 2019) from cold neutral gas in the interstellar medium (ISM). Such excess absorption would lead to an artificial template mismatch, whereby the template would appear to be more deficient in [Na/H] relative to the galaxy than it actually is. The result of this negative template mismatch would be a suppression of wing light (see Figure 3).

To investigate for the presence of cold, neutral gas, we performed a number of tests on the MUSE data of the galaxies. This included (i) inspecting the residuals of kinematic fits, which did not yield an excess beyond the local noise level, and (ii) using an isolated absorption-line doublet at 5890 and 5896 Å as an additional kinematic component in the fit that, using WINGFIT’s multicomponent fitting capabilities, was allowed to have its own kinematics LOSVD independent of that of the stars. This additional kinematic component, however, always yielded an LOSVD similar to that of the stars. Hence, we could not find evidence for an absorption

signal in the NaD lines that has a different kinematics than the stars. For galaxies with spatial regions with significant emission lines—which in the first place meant ionized gas in the cold disks of NGC 6861 and NGC 4751—we attempted to at first fit their spectra with a stellar and an emission component while masking NaD. Then, in a second step, we refitted the spectra with two components but added the extra NaD absorption component to the templates of the “emission” component and fixed its kinematics to the kinematics of the emission lines from the first step. Tying the extra absorption component to the kinematics of the cold disks in this way did not produce acceptable fits to the spectrum.

Thus, we could find no tangible evidence for excess absorption within the ISM of any of the galaxies in our sample. However, there is evidence for such absorption from the ISM of the Milky Way (which can be easily masked; Appendix B). Therefore, we saw no reason to discard this strong spectral feature from our analysis.

Including this feature in our mock tests (Section 3) consistently provided better recoveries of the LOSVD. For instance, expanding the upper limit of the wavelength range for our Mg and Fe mismatch tests (see Figure 4) to 6200 Å to include NaD reduced the dominant distortion effects of all tests. Most notably, for the test where our template was in excess of [Fe/H], the artificially produced wings decreased from $h_4 \sim 0.03$ to 0.01. The positive effect of including NaD is hardly surprising, as the continuum of the NaD absorption feature is especially smooth and featureless on both sides and the feature itself is usually the strongest in this wavelength range.

Positive h_4 values have been observed in several massive ETGs. Our tests suggest that a good indicator for the robustness of these measurements is their invariance under inclusion of the NaD region in the fit.

7. Summary and Conclusions

We have presented the first systematic study of the detailed LOSVD shapes of massive ETGs using nonparametric spectral fitting. Our sample encompasses nine galaxies, four of which are highly flattened, fast-rotating power-law galaxies. The remaining galaxies are massive slowly rotating galaxies with a depleted stellar core. The high signal of the MUSE observations allows us to extract 40–400 individual LOSVDs for each galaxy from binned spectra that still have an S/N > 100 per spectral bin. Our LOSVDs are determined with our recently developed spectral fitting code WINGFIT. It recovers the LOSVDs in a nonparametric fashion and uses a novel technique to adaptively optimize the smoothing (Thomas & Lipka 2022).

We have extensively discussed how well the detailed shapes of the LOSVDs can be measured and identified various types of LOSVD distortions related to potential template mismatch. Based on Monte Carlo simulations with stellar population models that allow us to vary the abundances of individual elements, we found an optimal strategy to avoid LOSVD distortions from template mismatch. Our setup combining the advanced LOSVD extraction method with very high S/N data was designed to measure the shapes of LOSVD with unprecedented precision.

Our most important findings concerning template mismatch are as follows:

1. Only when the exact template is among the candidate template spectra is the LOSVD recovery largely independent of the fitting setup, e.g., independent of the fitted wavelength range and of the applied additive or multiplicative polynomials.
2. Template mismatch that affects only individual stellar absorption features results in the long-known asymmetric LOSVD distortions, which are easily identifiable as template mismatch since they lead to a bias in h_3 .
3. Template mismatch that affects multiple features simultaneously or a particularly dominant feature results in symmetric LOSVD distortions, most often in the form of excess wings that bias h_4 and σ high.
4. Such artificial wings can easily “hide” template mismatch since their presence cannot unambiguously be attributed to template mismatch.
5. When the right template spectrum is not among the candidate spectra, liberal usage of polynomials makes this “hidden” mismatch more likely and amplifies its distorting effect on LOSVD shapes.
6. Our simulations of fitting massive ETGs in the optical regions without NaD almost always led to an over-prediction of light in the LOSVD wings.

To minimize template mismatch, we have developed a strategy that includes a proper preselection of template stars, minimal use of spectral masking and polynomials, and a wavelength basis that includes NaD. We carefully checked the NaD region in our sample of observed galaxies for contamination by an absorbing component with kinematics different from that of the stars. We do not find evidence for such a component. Fitting all the galaxies with our fiducial best setup, our main findings are as follows:

1. The complexity of observed nonparametrically derived LOSVD shapes of our ETGs requires Gauss–Hermite polynomials of at least sixth or eighth order to be represented well.
2. All galaxies show some kind of wings in their LOSVDs, which are unlikely an artifact of hidden template mismatch.
3. In the central regions of the galaxies the wings are always strongest and likely originate from light at the very centers of the galaxies, close to the central SMBH, which has been redistributed by the PSF. Additionally, a secondary, faint, and compact central high- σ stellar population could also produce a wing component in the LOSVD.
4. In some galaxies wings are also present at larger radii. We propose that these wings could be associated with faint stellar envelopes consisting of stars that are only loosely bound to the galaxies, similar to the cluster-bound stellar envelopes found in many BCGs.

In some of our ETGs photometric evidence for faint outer envelopes has been found (Rusli et al. 2013a). We are developing a decomposition method for LOSVDs to compare photometric and kinematic evidence for distinct stellar components in galaxies. In addition, deeper spectral observations, larger samples, and detailed dynamical models are required to follow up on the outer envelope of massive ETGs in the future.

The latter in particular will be important here: if extended LOSVD wings result to some degree from the overlap of

kinematically distinct stellar populations, stellar dynamical models with multiple kinematic components might be necessary to properly represent the galaxies. Furthermore, dynamical models together with independent mass constraints are crucial to determine the existence or absence of further systematic issues that affect the shape of the LOSVDs as we have recovered them here.

We acknowledge project/application support by the Max Planck Computing and Data Facility. Most kinematic computations were performed on the HPC system Raven and Cobra at the Max Planck Computing and Data Facility. We also made use of the computing facilities of the Computational Center for Particle and Astrophysics (C2PAP), and we are grateful for the support by A. Krukau and F. Beaujean through the C2PAP.

This study is based on observations collected at the European Organisation for Astronomical Research in the Southern Hemisphere under ESO program 095.B-0624(A), P.I. J. Thomas.

Appendix A Creating Mock Spectra and Templates Using *alf*

For the creation of mock galaxy spectra and synthetic stellar templates we used the software *alf* (v2.1), which is an implementation of the stellar population models first presented in Conroy & van Dokkum (2012), adapted for fitting the spectra of old stellar populations ($\gtrsim 1$ Gyr) in the optical to near-infrared (Sánchez-Blázquez et al. 2006; Choi et al. 2014; Conroy et al. 2014; Choi et al. 2016; Villaume et al. 2017; Conroy et al. 2018). The “spec_from_sum” subroutine of *alf* allows one to create model spectra by manually defining model parameters (instead of deriving them from fitted data), such as the metallicity or individual elemental abundances such as [Fe/H], but also the spectral broadening from an LOSVD, parameterized by Gauss–Hermite polynomials. By manually setting the LOSVD to a Gaussian with $v_{\text{los}} = 0 \text{ km s}^{-1}$ and $\sigma = 1 \text{ km s}^{-1}$, we created kinematically unbroadened template stellar spectra with an instrumental velocity resolution of $\sim 100 \text{ km s}^{-1}$ for our mock tests.

For the creation of the shallow features + Gaussian mock, specifically, from Section 4.3, for which we fitted the deep features + wings mock with *alf* using a Gaussian LOSVD, we required some additional tweaking of the code: the stellar population models are usually fit in several, same-sized wavelength sections of the full spectrum, as small as 100 \AA in extent, each with its own multiplicative polynomial for the normalization of the continuum. This however, results in a model that, even with the correct, intrinsic template, cannot be properly fit with WINGFIT, as the polynomial of the final model, which is “strung together” from the polynomials of all intervals, is too complex. This would have diluted the purpose of the mock tests based on this model, as the shape of the polynomial might then have interfered with the shape of the recovered LOSVD that would have been used to partially compensate for the mismatch in polynomials. Therefore, during this fit, we manually set up the fit such that the spectrum was not separated into intervals but fit as a whole. This resulted in a model with a lower-order multiplicative polynomial that could easily be reproduced with the multiplicative polynomial of our WINGFIT analysis. It should be noted that the *alf*-generated templates of our analysis do not include the polynomial and that these had to be multiplied after broadening with the

LOSVD to match the original model fit to the deep features + wings mock.

Appendix B Spectral Masking and Treatment of Emission

Apart from template mismatch, the true shape of the LOSVDs can also be distorted by (a) including spectral regions in the fit affected by systemic issues such as under- or oversubtracted skylines or regions in which the detector is affected by other instrumental issues, (b) excess absorption from neutral gas in the ISM, or (c) not properly treating emission lines from ionized gas.

Concerning issue (a), we spectrally masked or excluded from the wavelength interval of the fit all affected regions. This mostly meant spectrally masking the strong oxygen 5577 Å sky emission line and excluding wavelength regions bluer than 4800 Å, which are strongly affected by a sharp upturn of systemic uncertainties in the case of MUSE. In addition, we set the upper limit of the wavelength range at around 6200 Å, since, as we briefly described in Section 3, there were strong residuals from the telluric correction in between ~ 6200 and 6350 Å. The mock tests from that section showed that, for the recovery of the LOSVD, cutting off the wavelength interval to the exclusion of contaminated spectral regions is preferable to including large spectrally masked regions in the fit, which discontinuously section the spectrum. The particular wavelength interval and spectral masking we chose vary from galaxy to galaxy and were determined on a case-by-case basis, but we generally aimed to maximize the number of (good) spectral pixels in the fit, as per our prescription from Section 4.3.

For treating issue (b), we consider the 5890 and 5896 Å NaD absorption feature at the redshift of the galaxy for excess absorption from the ISM within the galaxy and in the rest frame $z=0$ for foreground absorption from within the Milky Way. The latter is frequently ignored in stellar population and kinematic analyses of galaxies but is readily apparent for most galaxies of our sample when inspecting the residuals of

kinematic fits to the galactic spectra (see NGC 5419 in Figure 16), varying in strength with the position of each galaxy on the night sky relative to the plane of the Milky Way. For the former, we could find no evidence of excess absorption within the ISM of any of the galaxies; see Section 6.5.

As for issue (c), we adopted a two-stage fitting procedure: First, we fit the stellar spectrum over a range wide enough to cover $H\beta$, as well as the strong $H\alpha$ and [N II] 6583 Å emission lines, using the in-built emission-line-fitting capabilities of WINGFIT to fit both absorption and emission features simultaneously. If we measure a flux large enough that the local S/N of the emission >3 for these emission lines, as well as the [O III] $\lambda 5007$ emission line, we treat the presence of ionized emission for the spectrum in question as “significant.” We include the [O III] emission lines in this S/N check to avoid an issue wherein the fit uses emission lines that, unlike [O III] emission, nominally lie on top of stellar absorption, as is the case, for example, for $H\beta$, to better “fill out” the absorption feature in the spectrum with an effective model consisting of an insufficiently deep stellar absorption + an emission component with an extremely broad LOSVD ($\sigma \gtrsim 500 \text{ km s}^{-1}$). This effect is in essence a compensation for template mismatch. In the second stage we narrow the fitted wavelength range to match that of the final WINGFIT analysis, which does not include the $H\alpha$ region, $\sim 4800\text{--}6200$ Å; mask all emission lines within this range where we judged the ionized emission of the concerned spectrum to be significant in the previous step; and fit only a stellar component (no emission). Where this was not the case, we did not apply any additional spectral masking in addition to the spectral masking from issues (a) and (b) to maximize the available constraints on the stellar abundances of the local template sets.

If, for fits from the first stage of the fitting approach of our template selection process (see Section 4.1), we detect emission with $S/N > 3$ for any elliptical ring section of a galaxy, we apply the same spatial masking—the spatial masking accounting for emission lines—to all spectra of that galaxy, even if some particular spectrum lies within an aperture for which we

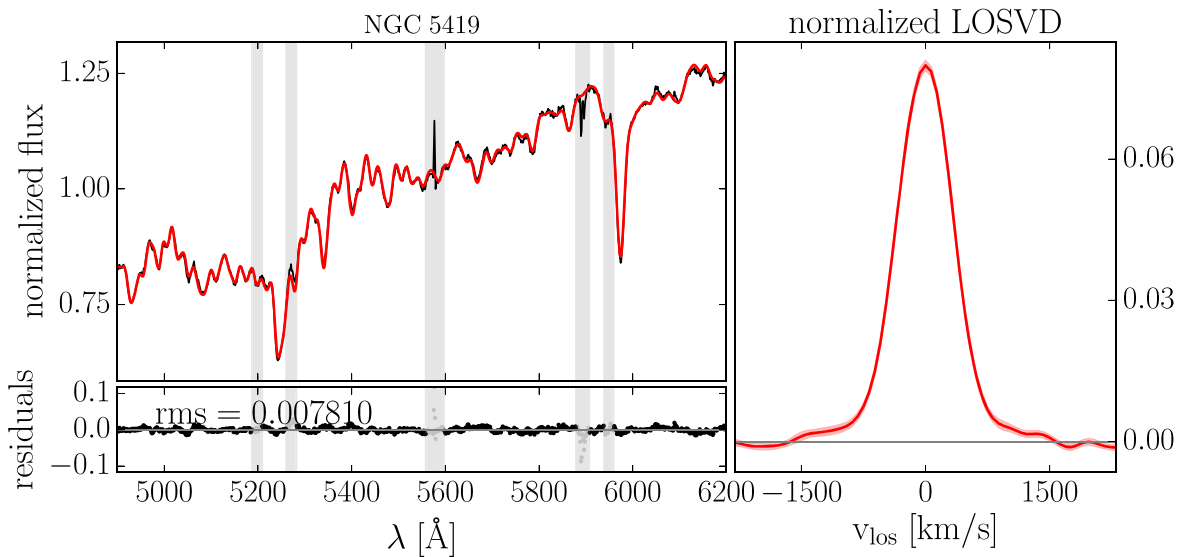


Figure 16. Left: kinematic fit (red) to the spectrum (black) of a Voronoi bin of NGC 5419 (bottom) using WINGFIT. At ~ 5890 Å the NaD absorption feature of the Milky Way ($z=0$) is clearly visible. Gray shaded areas indicate spectral regions that were masked during the fit—including this excess absorption from the Milky Way. Right: nonparametric LOSVDs (solid red) recovered from these fits. The shaded envelope indicates the statistical uncertainties of the LOSVD from 100 Monte Carlo simulations. The line-of-sight velocities v_{los} are relative to the systemic velocity of the galaxy.

did not find any significant emission. If we did not detect any significant emission for any of the elliptical sections of a galaxy, we do not apply any masking of ionized gas for any bins of that galaxy.

Appendix C Comparison with Previous Measurements

We here briefly compare our new kinematic measurements with those of previously published measurements, which were on similar spatial scales to the MUSE FOV, using different data and methods. For notable cases, we show the full kinematic measurements of the galaxies along their major axis and—where such data were available—the minor axis in comparison to ours. The observations with which we here compare our own were mostly long-slit data. In that case, for either axis, we plot our values of v_{rot} , σ , h_3 , and h_4 of all those bins that (a) included spaxel lying on the axis in question and (b) encompassed more spaxel within the slit width of the comparison data than outside (see Figures 17 and 18).

All comparison measurements were performed using the FCQ method, which, like for our WINGFIT code, produced nonparametric LOSVDs that were fit a posteriori with Gauss–Hermite polynomials, in this case of fourth order. For better comparison we refitted all of our nonparametric LOSVDs with only fourth-order Gauss–Hermite polynomials as well.

It should be kept in mind that for all these measurements the comparison data were binned for an S/N that was a factor 3–5 lower than our MUSE data.

1. *NGC 0307*: Our measurements for v_{rot} , σ , h_3 , and h_4 matched the measurements of Erwin et al. (2018), which were based on VLT-FORS1 data (see top panels of Figure 17).
2. *NGC 1332*: The measured kinematics from Rusli et al. (2011) seem to overall agree with our own (see bottom left panel of Figure 17). Their measurements were based on observations with the RCS at the Multiple Mirror telescope. The small differences between the measurements can be explained by differences in the PSF, which for Rusli et al. (2011) was likely smaller than our very large PSF = 2''12, resulting in a more smeared-out profile in our case (their PSF was unknown).
3. *NGC 4751 and NGC 5516*: for these two galaxies the available WiFes-based kinematics were based on observations with very poor signal (Rusli et al. 2013a). Therefore, both h_3 and h_4 were essentially not resolved. Nonetheless, within the uncertainties and for v_{rot} and σ , the kinematics match our own measurements.
4. *NGC 5328*: Most notably for the kinematic measurements of NGC 5328 from Rusli et al. (2013b), σ seems to be offset by 10%–15% from our own measurements (see top panels of Figure 18). The measurement from Rusli et al. (2013a) was based on spectra from the VIRUSW IFU spectrograph. Their kinematic fits were performed using only a single template star in contrast to our own preselected ~ 30 template stars for this galaxy. Refitting a

central bin from our own MUSE data using only one template star from MILES of the same class and spectral type as the one used in Rusli et al. (2013a), we were able to reproduce the 10%–15% offset in σ .

5. *NGC 5419*: With the exception of some outliers in σ at large radii, the kinematic measurements from Mazzalay et al. (2016), which were based on long-slit spectroscopy from the Southern African Large Telescope, agree well with our own measurements. Their h_3 , however, is much more strongly biased compared to our own—particularly for the aforementioned σ outliers—such that the differences can be explained by template mismatch.
6. *NGC 6861*: For the most part, the stellar kinematics from Rusli et al. (2013a), based on observations from the EMMI spectrograph at the ESO New Technology Telescope, agree with our measurements (see bottom right panel of Figure 17). However, there is a notable difference around $\pm 5''$ along the major axis: here our values of σ seem to “drop” by 20%–30%, relative to the values from Rusli et al. (2013a). Our study of the ionized emissions from the cold disk of the galaxy, which we will publish in a subsequent publication, reveals star-forming regions here, which bias σ low for our measurements. The measurements of Rusli et al. (2013a), on the other hand, were performed in a much redder region of the spectrum, namely around the CaT triplet. As a result, their measurements are more robust for the affected bins. These are in any case only a handful of bins out of the ~ 300 bins of our MUSE FOV. Furthermore, while for both measurements of h_3 there appears to be a similar amount of template mismatch, our own measurements of h_4 appear to be more asymmetric about the center of the galaxy.
7. *NGC 7619*: Along the major axis, within $\sim 5''$ the kinematics of Pu et al. (2010) match ours well (see bottom left panel of Figure 18). At larger radii, and along the minor axis, the σ and h_4 measured by Pu et al. (2010) (see bottom right panel of Figure 18) are larger than our measurements. Furthermore, their v_{rot} and σ profiles appear less symmetric about the center of the galaxy. Altogether, this could be symptomatic of template mismatch, as all forms of template mismatch we have encountered in this study (see Section 3) have invariably produced excess wing light. This, by necessity, biases σ and h_4 high. Our setup by comparison had specific precautions put in place to avoid this (see Sections 4.3.2 and 6.1). Furthermore, along the minor axis there is a significant amount of bias in $h_3 \sim -0.03$, larger than for our measurements, a dead giveaway for likely template mismatch. The data of Pu et al. (2010) were obtained with the Low Resolution Spectrograph (LRS) of the Hobby-Eberly Telescope (HET), and only a single template from the Vazdekis (1999) library of synthetic stellar spectra was used.

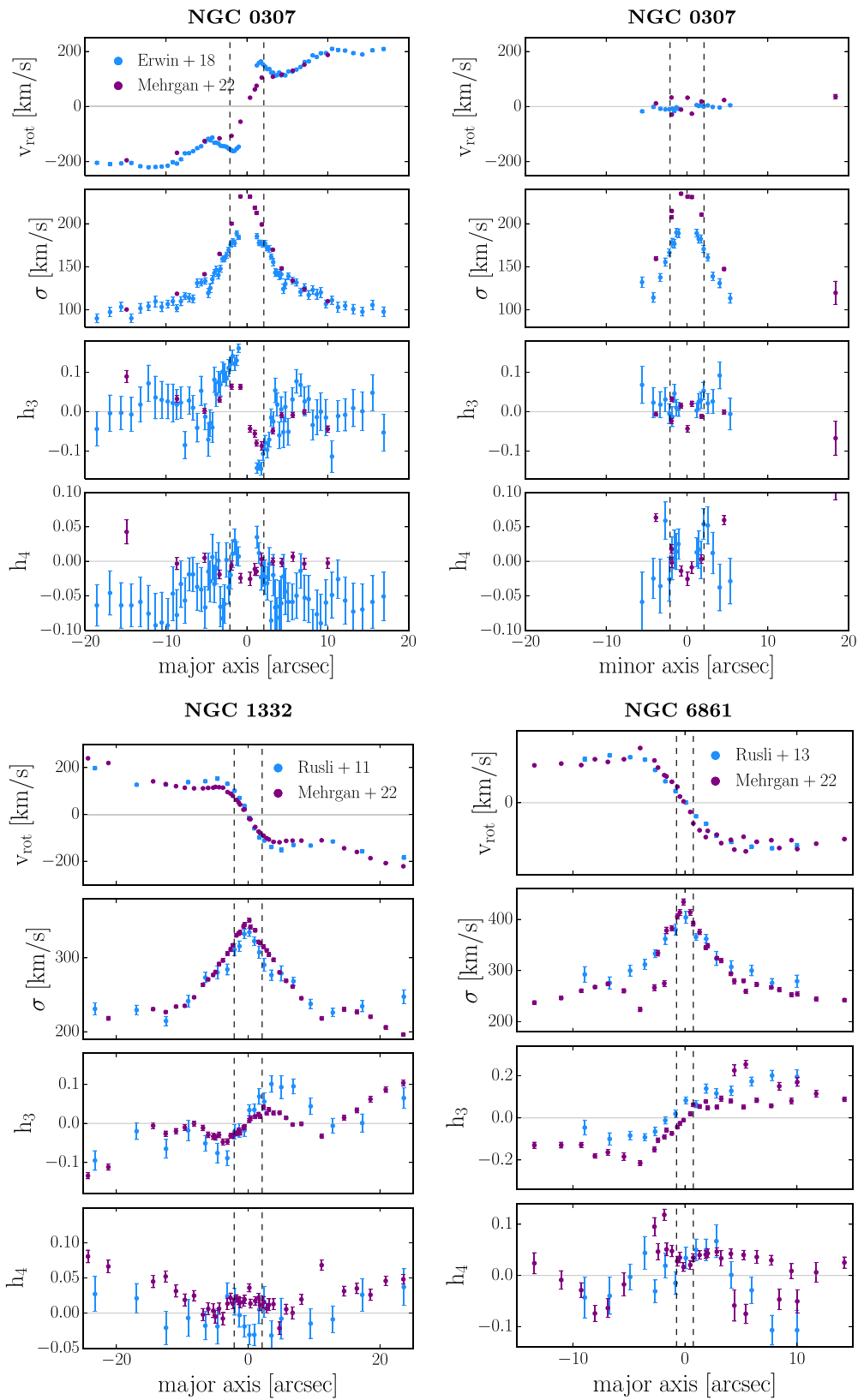


Figure 17. Stellar kinematics of NGC 0307, NGC 1332, and NGC 6861 parameterized by fourth-order Gauss–Hermite polynomials along the galaxies’ major and, in the case of NGC 0307, minor axes for nonparametric measurements of the LOSVDs from this study (purple circles) and from Rusli et al. (2011, 2013a) and Erwin et al. (2018) (blue circles). We show statistical uncertainties for all measurements. Vertical dashed lines show the FWHM of the PSF from our MUSE measurements.

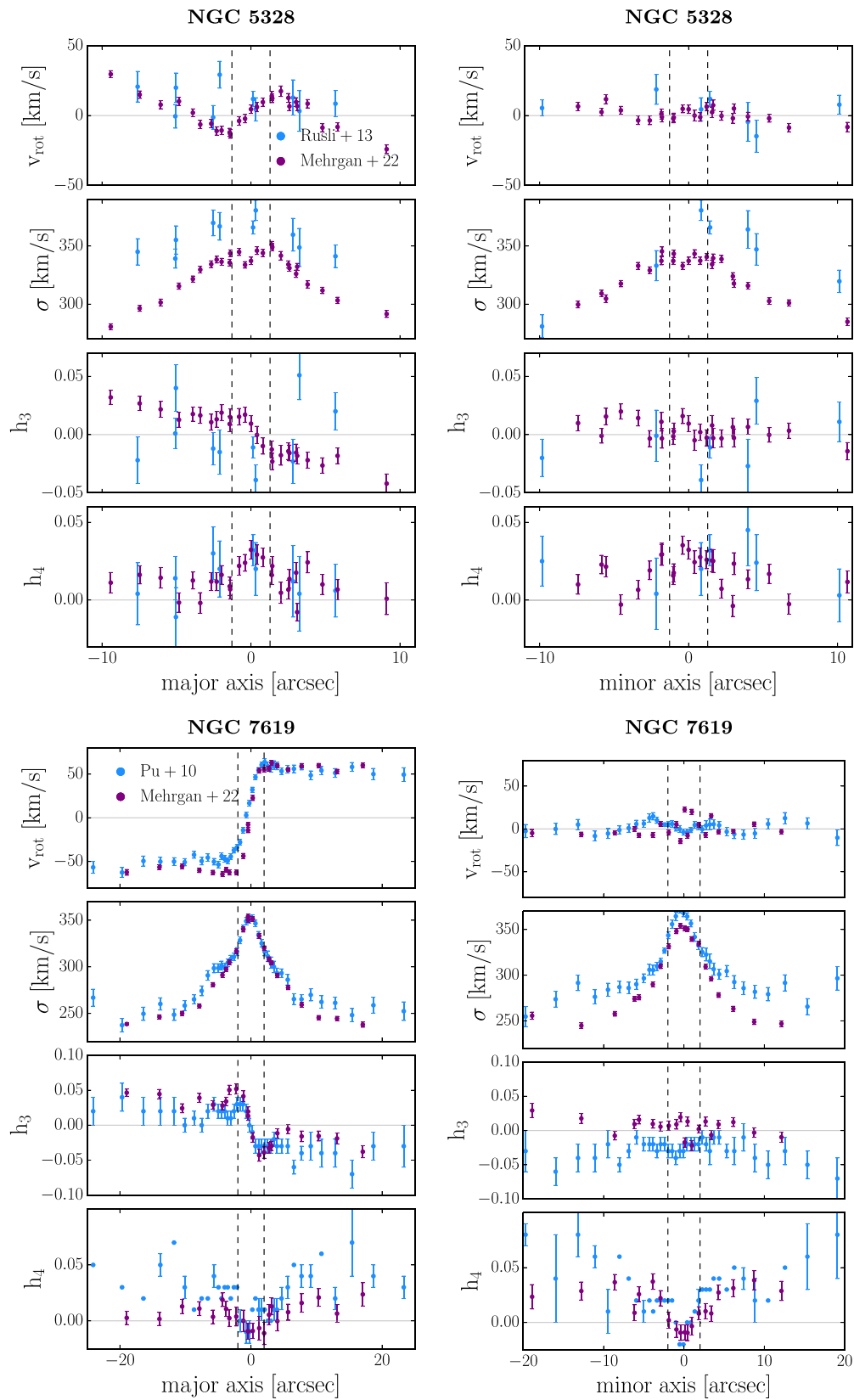


Figure 18. Stellar kinematics of NGC 5328 and NGC 7619 parameterized by fourth-order Gauss–Hermite polynomials along the galaxies’ major and minor axes for measurements from this study (purple circles) and from Rusli et al. (2013a) and Pu et al. (2010) (blue circles). We show statistical uncertainties for all measurements. Vertical dashed lines show the PSF from our measurements.

ORCID iDs

Kianusch Mehrgan  <https://orcid.org/0000-0002-9821-3535>
 Jens Thomas  <https://orcid.org/0000-0003-2868-9244>
 Roberto Saglia  <https://orcid.org/0000-0003-0378-7032>
 Taniya Parikh  <https://orcid.org/0000-0002-0621-6238>
 Ralf Bender  <https://orcid.org/0000-0001-7179-0626>

References

- Arnaboldi, M., Ventimiglia, G., Iodice, E., Gerhard, O., & Coccato, L. 2012, *A&A*, **545**, A37
- Barth, A. J., Boizelle, B. D., Darling, J., et al. 2016, *ApJL*, **822**, L28
- Barth, A. J., Ho, L. C., & Sargent, W. L. W. 2002, *AJ*, **124**, 2607
- Bender, R. 1990, *A&A*, **229**, 441
- Bender, R., Kormendy, J., Cornell, M. E., & Fisher, D. B. 2015, *ApJ*, **807**, 56
- Bender, R., Saglia, R. P., & Gerhard, O. E. 1994, *MNRAS*, **269**, 785
- Binney, J., & Mamon, G. A. 1982, *MNRAS*, **200**, 361
- Cappellari, M. 2008, *MNRAS*, **390**, 71
- Cappellari, M. 2016, *ARA&A*, **54**, 597
- Cappellari, M. 2020, *MNRAS*, **494**, 4819
- Cappellari, M., & Copin, Y. 2003, *MNRAS*, **342**, 345
- Cappellari, M., McDermid, R. M., Alatalo, K., et al. 2012, *Natur*, **484**, 485
- Carter, D., Efstathiou, G., Ellis, R. S., Inglis, I., & Godwin, J. 1981, *MNRAS*, **195**, 15P
- Carter, D., Inglis, I., Ellis, R. S., Efstathiou, G., & Godwin, J. G. 1985, *MNRAS*, **212**, 471
- Choi, J., Conroy, C., Moustakas, J., et al. 2014, *ApJ*, **792**, 95
- Choi, J., Dotter, A., Conroy, C., et al. 2016, *ApJ*, **823**, 102
- Concas, A., Popesso, P., Brusa, M., Mainieri, V., & Thomas, D. 2019, *A&A*, **622**, A188
- Conroy, C., Graves, G. J., & van Dokkum, P. G. 2014, *ApJ*, **780**, 33
- Conroy, C., & van Dokkum, P. G. 2012, *ApJ*, **760**, 71
- Conroy, C., Villaume, A., van Dokkum, P. G., & Lind, K. 2018, *ApJ*, **854**, 139
- Cretton, N., de Zeeuw, P. T., van der Marel, R. P., & Rix, H.-W. 1999, *ApJS*, **124**, 383
- Cretton, N., & van den Bosch, F. C. 1999, *ApJ*, **514**, 704
- de Lorenzi, F., Debattista, V. P., Gerhard, O., & Sambhus, N. 2007, *MNRAS*, **376**, 71
- de Nicola, S., Neureiter, B., Thomas, J., Saglia, R. P., & Bender, R. 2022, *MNRAS*, **517**, 3445
- de Nicola, S., Saglia, R. P., Thomas, J., Dehnen, W., & Bender, R. 2020, *MNRAS*, **496**, 3076
- Dejonghe, H., & Merritt, D. 1992, *ApJ*, **391**, 531
- Emsellem, E., Cappellari, M., Krajnović, D., et al. 2007, *MNRAS*, **379**, 401
- Emsellem, E., Cappellari, M., Krajnović, D., et al. 2011, *MNRAS*, **414**, 888
- Erwin, P., Saglia, R. P., Fabricius, M., et al. 2015, *MNRAS*, **446**, 4039
- Erwin, P., Thomas, J., Saglia, R. P., et al. 2018, *MNRAS*, **473**, 2251
- Escudero, C. G., Faifer, F. R., Bassino, L. P., Calderón, J. P., & Caso, J. P. 2015, *MNRAS*, **449**, 612
- Faber, S. M., Tremaine, S., Ajhar, E. A., et al. 1997, *AJ*, **114**, 1771
- Fabricius, M. H., Coccato, L., Bender, R., et al. 2014, *MNRAS*, **441**, 2212
- Falcón-Barroso, J., & Martig, M. 2021, *A&A*, **646**, A31
- Freudling, W., Romaniello, M., Bramich, D. M., et al. 2013, *A&A*, **559**, A96
- Frigo, M., Naab, T., Rantala, A., et al. 2021, *MNRAS*, **508**, 4610
- Gebhardt, K., Rich, R. M., & Ho, L. C. 2002, *ApJL*, **578**, L41
- Gebhardt, K., Richstone, D., Kormendy, J., et al. 2000, *AJ*, **119**, 1157
- Gerhard, O. E. 1993, *MNRAS*, **265**, 213
- Houghton, R. C. W., Magorrián, J., Sarzi, M., et al. 2006, *MNRAS*, **367**, 2
- Iannuzzi, F., & Athanassoula, E. 2015, *MNRAS*, **450**, 2514
- Ivanov, V. D., Coccato, L., Neeser, M. J., et al. 2019, *A&A*, **629**, A100
- Jethwa, P., Thater, S., Mair, T., & Van de Ven, G. 2020, DYNAMITE: DYNAMICS, AGE AND METALLICITY INDICATORS TRACING EVOLUTION, ASTROPHYSICS SOURCE CODE LIBRARY, [ascl:2011.007](https://doi.org/10.26434/chemrxiv-2021-007)
- Johnston, E. J., Hau, G. K. T., Coccato, L., & Herrera, C. 2018, *MNRAS*, **480**, 3215
- Kausch, W., Noll, S., Smette, A., et al. 2015, *A&A*, **576**, A78
- Kluge, M., Neureiter, B., Riffeser, A., et al. 2020, *ApJS*, **247**, 43
- Kormendy, J., & Bender, R. 1996, *ApJL*, **464**, L119
- Krajnović, D., Weibacher, P. M., Urrutia, T., et al. 2015, *MNRAS*, **452**, 2
- Lauer, T. R. 2012, *ApJ*, **759**, 64
- Liepold, C. M., Quenneville, M. E., Ma, C.-P., et al. 2020, *ApJ*, **891**, 4
- Lipka, M., & Thomas, J. 2021, *MNRAS*, **504**, 4599
- Loubser, S. I., Babul, A., Hoekstra, H., et al. 2020, *MNRAS*, **496**, 1857
- Mazzalay, X., Thomas, J., Saglia, R. P., et al. 2016, *MNRAS*, **462**, 2847
- Mehrgan, K., Thomas, J., Saglia, R., et al. 2019, *ApJ*, **887**, 195
- Mei, S., Blakeslee, J. P., Tonry, J. L., et al. 2005, *ApJ*, **625**, 121
- Merritt, D., & Saha, P. 1993, *ApJ*, **409**, 75
- Napolitano, N. R., Romanowsky, A. J., Capaccioli, M., et al. 2011, *MNRAS*, **411**, 2035
- Neureiter, B., de Nicola, S., Thomas, J., et al. 2023, *MNRAS*, **519**, 2004
- Neureiter, B., Thomas, J., Saglia, R., et al. 2021, *MNRAS*, **500**, 1437
- Parikh, T., Saglia, R., Thomas, J., Mehrgan, K., & Bender, R. 2023, submitted to MNRAS
- Parikh, T., Thomas, D., Maraston, C., et al. 2018, *MNRAS*, **477**, 3954
- Pinkney, J., Gebhardt, K., Bender, R., et al. 2003, *ApJ*, **596**, 903
- Pu, S. B., Saglia, R. P., Fabricius, M. H., et al. 2010, *A&A*, **516**, A4
- Quenneville, M. E., Liepold, C. M., & Ma, C.-P. 2021, *ApJS*, **254**, 25
- Quenneville, M. E., Liepold, C. M., & Ma, C.-P. 2022, *ApJ*, **926**, 30
- Rantala, A., Johansson, P. H., Naab, T., Thomas, J., & Frigo, M. 2019, *ApJL*, **872**, L17
- Rusli, S. P., Erwin, P., Saglia, R. P., et al. 2013a, *AJ*, **146**, 160
- Rusli, S. P., Thomas, J., Erwin, P., et al. 2011, *MNRAS*, **410**, 1223
- Rusli, S. P., Thomas, J., Saglia, R. P., et al. 2013b, *AJ*, **146**, 45
- Sánchez-Blázquez, P., Peletier, R. F., Jiménez-Vicente, J., et al. 2006, *MNRAS*, **371**, 703
- Sarazin, M., & Roddier, F. 1990, *A&A*, **227**, 294
- Schwarzschild, M. 1979, *ApJ*, **232**, 236
- Siopis, C., & Kandrump, H. E. 2000, *MNRAS*, **319**, 43
- Smette, A., Sana, H., Noll, S., et al. 2015, *A&A*, **576**, A77
- Spiniello, C., Koopmans, L. V. E., Trager, S. C., Czoske, O., & Treu, T. 2011, *MNRAS*, **417**, 3000
- Spiniello, C., Napolitano, N. R., Arnaboldi, M., et al. 2018, *MNRAS*, **477**, 1880
- Spiniello, C., Trager, S. C., Koopmans, L. V. E., & Chen, Y. P. 2012, *ApJL*, **753**, L32
- Syer, D., & Tremaine, S. 1996, *MNRAS*, **282**, 223
- Thater, S., Krajnović, D., Weibacher, P. M., et al. 2022, *MNRAS*, **509**, 5416
- Thomas, D., Greggio, L., & Bender, R. 1999, *MNRAS*, **302**, 537
- Thomas, D., Maraston, C., Bender, R., & Mendes de Oliveira, C. 2005, *ApJ*, **621**, 673
- Thomas, J., & Lipka, M. 2022, *MNRAS*, **514**, 6203
- Thomas, J., Saglia, R. P., Bender, R., et al. 2004, *MNRAS*, **353**, 391
- Thomas, J., Saglia, R. P., Bender, R., Erwin, P., & Fabricius, M. 2014, *ApJ*, **782**, 39
- Tonry, J. L., Dressler, A., Blakeslee, J. P., et al. 2001, *ApJ*, **546**, 681
- van de Sande, J., Bland-Hawthorn, J., Fogarty, L. M. R., et al. 2017, *ApJ*, **835**, 104
- van den Bosch, R. C. E., van de Ven, G., Verolme, E. K., Cappellari, M., & de Zeeuw, P. T. 2008, *MNRAS*, **385**, 647
- van der Marel, R. P., & Franx, M. 1993, *ApJ*, **407**, 525
- van Dokkum, P. G., & Conroy, C. 2012, *ApJ*, **760**, 70
- Vasiliev, E., & Valluri, M. 2020, *ApJ*, **889**, 39
- Vazdekis, A. 1999, *ApJ*, **513**, 224
- Veale, M., Ma, C.-P., Greene, J. E., et al. 2018, *MNRAS*, **473**, 5446
- Ventimiglia, G., Gerhard, O., Arnaboldi, M., & Coccato, L. 2010, *A&A*, **520**, L9
- Villaume, A., Conroy, C., Johnson, B., et al. 2017, *ApJS*, **230**, 23

Chapter 4

Dynamical stellar mass-to-light ratio gradients: Evidence for very centrally concentrated IMF variations in ETGs?

Bibliographic information

Kianusch Mehrgan, Jens Thomas, Roberto Saglia, Taniya Parikh, Bianca Neureiter, Peter Erwin, and Ralf Bender – Dynamical stellar mass-to-light ratio gradients: Evidence for very centrally concentrated IMF variations in ETGs?, ApJ, in press.

Author’s contribution

As first author, I wrote all sections of this manuscript myself, and generated all figures. Jens Thomas provided important support to this work in the form of frequent discussions, ideas, and revisions of text. Roberto Saglia provided further valuable corrections and discussions. The main input kinematics were adopted from Mehrgan et al. (2023a) (see Chapter 3). I generated the dynamical models of all seven galaxies appearing in this study, using our group’s axisymmetric Schwarzschild modeling code. For the implementation of Υ -gradients, I ran preliminary models of the galaxies to determine the most feasible setup. Jens Thomas and I developed the approach of defining and deriving the Υ -gradients together. Using these measurements, as well as Υ_{Kroupa} -profiles from SSP models provided by Taniya Parikh, I performed the comparison of our models with the literature of IMF probes on different spatial scales. I furthermore derived the updated $M_{BH} - \sigma$ relation for ETGs. I modified the triaxial N-body simulation from Rantala et al. (2018) to exhibit a mock- Υ -gradient. Bianca Neureiter generated LOSVDs and images from the modified simulation, which I dynamically modelled for our tests for systematic issues. Finally, I

4. Dynamical stellar mass-to-light ratio gradients: Evidence for very centrally concentrated IMF variations in ETGs?

analyzed the dust from the MUSE data of NGC 4751 and performed the deprojection of the photometry. The 2D photometric decomposition of the galaxy was performed by Peter Erwin. All authors provided feedback for the final version of the manuscript.

presented on pages 99 - 136.

Dynamical stellar mass-to-light ratio gradients:
Evidence for very centrally concentrated IMF variations in ETGs?

KIANUSCH MEHRGAN,^{1,2} JENS THOMAS,^{1,2} ROBERTO SAGLIA,^{1,2} TANIYA PARIKH,¹ BIANCA NEUREITER,^{1,2}
PETER ERWIN,¹ AND RALF BENDER^{1,2}

¹*Max-Planck-Institut für extraterrestrische Physik, Giessenbachstrasse, D-85748 Garching*

²*Universitäts-Sternwarte München, Scheinerstrasse 1, D-81679 München, Germany*

Submitted to ApJ

ABSTRACT

Evidence from different probes of the stellar initial mass function (IMF) of massive early-type galaxies (ETGs) has repeatedly converged on IMFs more bottom-heavy than in the Milky Way (MW). This consensus has come under scrutiny due to often contradictory results from different methods on the level of individual galaxies. In particular, a number of strong lensing probes are ostensibly incompatible with a non-MW IMF. Radial gradients of the IMF – related to gradients of the stellar mass-to-light ratio Υ – can potentially resolve this issue. We construct Schwarzschild models allowing for Υ -gradients in seven massive ETGs with MUSE and SINFONI observations. We find dynamical evidence that Υ increases towards the center for all ETGs. The gradients are confined to sub-kpc scales. Our results suggest that constant- Υ models may overestimate the stellar mass of galaxies by up to a factor 1.5. For all except one galaxy, we find a radius where the total dynamical mass has a minimum. This minimum places the strongest constraints on the IMF outside the center and appears at roughly 1 kpc. We consider the IMF at this radius characteristic for the main body of each ETG. In terms of the IMF mass-normalization α relative to a Kroupa IMF, we find on average a MW-like IMF $\langle \alpha_{\text{main}} \rangle = 1.03 \pm 0.19$. In the centers, we find concentrated regions with increased mass normalizations that are less extreme than previous studies suggested, but still point to a Salpeter-like IMF, $\langle \alpha_{\text{cen}} \rangle = 1.54 \pm 0.15$.

Keywords: galaxies: supermassive black holes – galaxies: ETG and lenticular, cD – galaxies: evolution
– galaxies: formation – stars: kinematics and dynamics – galaxies: center

1. INTRODUCTION

The question of how much stars contribute to the total mass of distant galaxies remains one of the fundamental issues of extragalactic astronomy. The answer is critical for mass decompositions of these objects into stellar components, dark matter (DM) and supermassive black holes (SMBHs), as well as for our understanding of galaxy formation histories. The difficulty lies in the fact that the unresolved stellar populations of these galaxies contain both low-luminosity dwarf stars and stellar remnants – both of which contribute to the galactic mass and follow the light of these galaxies, but contribute barely or not at all to the observed light.

The stellar initial mass function (IMF) describes the distribution function of stars as a function of stellar mass at the time of the star formation events in which the observed stellar populations of a galaxy were produced. It encompasses long-lived low-luminosity dwarf stars whose distribution essentially remains unchanged during galaxy evolution to the present epoch, and more massive stars which will have turned into remnants by the time of observation. Besides allowing an estimation of the total stellar mass, the IMF informs essentially every other part of galaxy evolution, such as star formation rates, stellar feedback, and heavy element production (e.g. Kennicutt 1998; Bastian et al. 2010).

Numerous studies have found that a Kroupa or Chabrier IMF can describe the IMF of the Milky Way (MW) across multiple different environments (e.g. Kroupa 2001, 2002; Chabrier 2003; Bastian et al. 2010),

as well as that of nearby spiral galaxies (e.g. [Kassin et al. 2006](#); [Brewer et al. 2012](#)). This prompts the question: is the IMF *universal* to all galaxies? If so, the proposed IMF models could be used to a priori separate the baryonic, DM and SMBH content of distant galaxies in dynamical models, which would greatly improve the accuracy of SMBH and DM measurements.

Individual star counts, as performed for IMF probes of the MW, are infeasible in other galaxies, as the stellar populations are unresolved. Therefore, different methods have to be used to extract IMF information from the observed stellar light. There are two dominant techniques in use:

1) Fitting of IMF-sensitive stellar absorption features whose strength is regulated by the ratio of dwarf to giant stars with models based on single stellar population (SSPs) synthesis libraries. These models output a stellar mass-to-light ratio Υ^{SSP} , as well as an IMF model. However, in this manner we can only probe the low-mass end of the IMF of early-type galaxies (ETGs), as on the high-mass end (without replenishment from star formation) most stars have turned into remnants, which are invisible to SSP modeling. 2) Measurements of the galactic gravitational potential, via stellar dynamics and/or gravitational lensing. These do not directly distinguish between DM, stars and the central SMBH of the galaxy, but produce a total mass-to-light ratio $(M^{\text{tot}}/L)^{\text{dyn}}$. From this, a stellar mass-to-light ratio Υ^{dyn} can be inferred relative to assumptions about the shape of the DM halo. Υ^{dyn} can be driven up either by the mass contributions of dwarfs or remnants from the high-mass end of the IMF.

For either approach, it is convenient to characterize the IMF probe by a mass normalization factor α of the stellar mass-to-light ratio relative to a reference $\Upsilon_{\text{ref}}^{\text{SSP}}$ with a reference IMF, which in this study will be a Kroupa IMF.

Many of the earliest dynamical probes of the stellar mass content of ETGs did not directly attempt to separate DM from stellar masses. These, most notably the SAURON project ([de Zeeuw et al. 2002](#); [Emsellem et al. 2004](#); [Cappellari et al. 2007a](#)), found that ETGs were fundamentally unlike spiral galaxies in their mass-light composition: Here, $(M^{\text{tot}}/L)^{\text{dyn}} > \Upsilon_{\text{Kroupa}}^{\text{SSP}}$, with the ratio for some galaxies being large enough that the total mass budget could accommodate a Salpeter or super-Salpeter IMF. Such an IMF produces larger Υ , due to a relative excess of low luminosity dwarf stars relative to a MW IMF, a phenomenon typically referred to as “bottom-heaviness”. At this point, there was still no consensus on whether or not the mass excess relative to a MW IMF was due to unaccounted DM or an enhanced

stellar contribution. However, even early (spherical) dynamical models with DM halo components found similar results for the remaining stellar contribution ([Gerhard et al. 2001](#)). Since then, a number of surveys and projects focused on dynamical and lensing models of ETGs have used a variety of DM models to produce measurements of the stellar mass-to-light Υ . These included the work of the SLACS group, which analyzed 56 massive lensing galaxies combining strong-lensing with simple spherical Jeans models ([Treu et al. 2010](#); [Auger et al. 2010](#)), and dynamical studies of the ETGS of the Coma cluster ([Thomas et al. 2007b, 2009, 2011](#)) and the cluster Abell 262 ([Wegner et al. 2012](#)) using sophisticated axisymmetric Schwarzschild orbit superposition models ([Schwarzschild 1979](#)). This was followed up by the ATLAS^{3D} project ([Cappellari et al. 2012, 2013a,b](#)), which analyzed 260 ETGs using Jeans anisotropic modeling (JAM; [Cappellari et al. 2007a](#); [Cappellari 2008](#)). These studies found galaxy-by-galaxy variation of the mass normalization α , which correlated with a number of galactic properties, particularly galactic velocity dispersion (e.g. equation 6 of [Posacki et al. 2015](#)). Notably, for massive ETGs with $\sigma_e \gtrsim 250$ km/s these studies predict a mass normalization at least twice the MW-level.

Various lensing studies have been used to more thoroughly investigate the central DM profiles of these galaxies, but found complementary trends of α , even where more concentrated DM profiles were used (e.g. [Spiniello et al. 2011](#); [Sonnenfeld et al. 2015](#); [Oldham & Auger 2018b](#); [Sonnenfeld et al. 2019](#)). [Napolitano et al. \(2011, 2014\)](#) used observations of globular clusters and planetary nebulae to derive dynamical constraints on the DM halos of massive ETGs out to several times the effective radius. With these constraints they found that unless the centers of the DM halos had undergone adiabatic contraction from baryonic infall, these galaxies required a Salpeter-level α .

At the same time as mass probes converged on a comprehensive picture of a variation in α , SSP modeling probes of the centers of ETGs, often from the same samples, supported the claim that the established trends of α indeed arise from variations of the IMF ([van Dokkum & Conroy 2010, 2011, 2012](#); [Smith et al. 2012](#); [Conroy & van Dokkum 2012](#); [Conroy et al. 2014](#); [Tortora et al. 2013](#); [Ferreras et al. 2013](#); [La Barbera et al. 2013](#)).

Since then, claims in favour of IMF variation among ETGs with mass and other properties, such as metallicity and [Mg/Fe] enrichment, have been accumulating ([Martín-Navarro et al. 2015b](#); [Lyubenova et al. 2016](#); [Li et al. 2017](#); [van Dokkum et al. 2017](#); [Parikh et al. 2018](#); [Poci et al. 2022](#); [Bernardi et al. 2019](#)).

However, a number of problems remain with this framework, which have yet to be resolved before the IMF can conclusively be determined to be non-universal. While the overall *trends* of the IMF found by dynamical/lensing and SSP measurements appear to be in agreement, on the level of individual galaxies, the measurements of α from the two methods often do not agree or not even correlate (Smith 2014; McDermid et al. 2014). Furthermore, recent lensing measurements from the SNELLS and MNELLS surveys (Smith et al. 2015; Newman et al. 2017; Collier et al. 2018, 2020), as well as a survey of 23 lensed ETGs by Sonnenfeld et al. (2019), and individual dynamical measurements (Rusli et al. 2013a; Thomas et al. 2016) have ruled out a mass normalisation α above the MW value for a number of very massive galaxies with $\sigma_e > 250$ kms.

Work by the CALIFA survey (Lyubenova et al. 2016) spanning all three methods suggested that the tension between different IMF probes can be partially alleviated by correcting for aperture effects. Consideration of aperture differences become crucial if ETGs possess intrinsic radial IMF gradients. Bernardi et al. (2018) and Domínguez Sánchez et al. (2019) suggested that if such gradients exist, they could bridge the difference between galaxy-gravitational and stellar population probes of the IMF. Radial gradients for massive ETGs would not be unexpected in a two-phase formation scenario where the central stars are mostly formed in-situ at high redshift while most of the outer material is accreted later on from smaller sub units with potentially different star-formation conditions.

A number of stellar population modeling studies have already claimed internal IMF gradients confined to small spatial scales on the order of a few kpc (Martín-Navarro et al. 2015a; van Dokkum et al. 2017; Parikh et al. 2018; La Barbera et al. 2019; Domínguez Sánchez et al. 2019). There exist only a few dynamical and lensing studies related to IMF gradients and these found similar results for the massive ETG M87 (Oldham & Auger 2018a; Li et al. 2020), the lensing galaxy ESO 325-G004 (Collett et al. 2018), as well as for several lensing galaxies from the samples of Oldham & Auger (2018b) and Newman et al. (2015).

Our goal in this study is to systematically investigate for the first time the possible existence of IMF-gradients with dynamical models. To this end we use our state-of-the-art orbit-based Schwarzschild dynamical modelling code which originally goes back to the code of Richstone & Tremaine (1988); Gebhardt et al. (2003); Thomas et al. (2004); Siopis et al. (2009). This code has been advanced since then in many respects, most notably it accounts for the overfitting problem and respective bi-

ases by using a generalised model selection technique (Lipka & Thomas 2021; Thomas & Lipka 2022).

Central gradients in the stellar mass-to-light ratio Υ can only be reliably determined if SMBHs are taken into account. For this reason, we are here studying a sample of seven massive ETGs with a combination of two sets of previously published non-parametric 2D stellar kinematics from a) the Multi-Unit Spectroscopic Explorer (MUSE), and b) the spectrograph Integral Field Observations in the Near Infrared (SINFONI). While the wide-field MUSE data have a high SNR (Mehrgan et al. 2023), the SINFONI data, which are concentrated on the central regions of the galaxies, are adaptive optics (AO) supported and resolve the sphere of influence (SOI) of the SMBHs (Rusli et al. 2011, 2013a,b; Erwin et al. 2018).

While our sample is relatively small, we combine several crucial advancements compared to previous studies: (i) we systematically probe for dynamical gradients in ETGs combining spectroscopic data which allows us to simultaneously constrain the wide-field mass distribution as well as central SMBHs; (ii) we use Schwarzschild models that do not require any a priori assumption on the anisotropy of the stellar orbits; (iii) we use a new generalised model selection technique that overcomes known limitations in Schwarzschild fits and allows for mass measurements with very high precision; (iv) we consistently use non-parametric LOSVDs both in the center and for the wide-field data. Points (ii) to (iv) have been demonstrated to be sufficient to break known degeneracies and avoid biases in dynamical models even for (more complex) triaxial galaxies and to allow for dynamical mass determinations with a precision at the 10%-level (Lipka & Thomas 2021; de Nicola et al. 2022; Neureiter et al. 2023a).

This study is structured as follows: in Section 2, we present our MUSE and SINFONI kinematics for the seven ETGs, as well as our Schwarzschild modeling approach. In Section 3, we present the derived gradients of Υ . Afterwards, in Section 4, we discuss them in terms of evidence for IMF gradients. Finally, we conclude our study in Section 6 by summing up our results and discussing their implications for future investigations of IMF variations in and between ETGs.

2. ORBITAL DYNAMICAL MODELING: TECHNIQUE AND DATA

We list the seven ETGs which we dynamically modeled for their Υ gradients in Table 1, together with some of their morphological properties and general information about the MUSE and SINFONI data which we used in this study. This sample is a sub-sample of the nine

ETGs analysed in [Mehrgan et al. \(2023\)](#). We have singled out the remaining two galaxies from that previous study, NGC 5419 and NGC 6861, for separate analysis elsewhere. NGC 5419 was modelled using our new tri-axial Schwarzschild dynamical modeling code SMART in [Neureiter et al. \(2023b\)](#). NGC 6861 will be presented in [Thomas et al.](#) in prep.

All seven galaxies under study here were modelled previously but using other data, mostly long-slit, for the outer parts rather than the new MUSE data ([Rusli et al. 2011, 2013a; Erwin et al. 2018](#), which we will refer to as R+11, R+13 and E+18).

Using the sequencing of ETGs first introduced by [Kormendy & Bender \(1996\)](#) and [Faber et al. \(1997\)](#) into luminous ETGs with shallow central surface brightness cores and less luminous ETGs with steep power-law surface brightness profiles (e.g. [Nieto et al. 1991; Crane et al. 1993; Kormendy et al. 1994; Ferrarese et al. 1994; Lauer et al. 1995; Gebhardt et al. 1996; Faber et al. 1997; Kormendy 1999; Lauer et al. 2007; Kormendy et al. 2009](#)), our sample can be partitioned into four cored ETGs and three power-law ETGs (R+11,13; E+18). We also classified these galaxies in our previous publication, [Mehrgan et al. \(2023\)](#) in accordance with the angular momentum classification scheme of [Emsellem et al. \(2007, 2011\)](#). As is typical for the core/power-law dichotomy (for review, see [Lauer 2012](#)), the three power-law ETGs are fast rotating and have either disc components or disc-like components, while the cored ETGs have no disc components and have less rotation. Two of the cored ETGs are typical slow rotators, while two have an angular momentum that could be considered “intermediate”

Below, in Section 2.1, we describe our implementation of the axisymmetric Schwarzschild dynamical models which we used on our sample. As inputs, these models use 3D deprojections of (2D) imaging data along the line-of-sight, which we describe in Section 2.2, and – importantly – stellar kinematics in the form of non-parametric line-of-sight velocity distributions (LOSVDs) derived from MUSE and SINFONI spectroscopy. These kinematics are described in Section 2.3.

2.1. Axisymmetric Schwarzschild modeling

2.1.1. Implementation of models with radial mass-to-light ratio gradients

We dynamically model the sample galaxies under the assumption that they are axisymmetric. We discuss this assumption later on in Section 4.3.

The dynamical models in this study consist of an advanced implementation of the axisymmetric

Schwarzschild orbit superposition code of [Thomas et al. \(2004\)](#). It allows for radial gradients of the stellar mass to light ratio, $\Upsilon(r)$. We here only briefly summarize the key features of this implementation and highlight new additions and those parts of our approach which are specific to the present study.

Following the Jeans theorem, in a stationary system, the phase-space density is constant along trajectories which typically obey three integrals of motion: E , L_z and the non-classical I_3 (for axisymmetric systems). Hence, we can think of stationary galaxies as the superposition of orbits which represent the system’s phase-space ([Schwarzschild 1979](#)) and constitute all possible solutions to the collisionless Boltzmann equation. A representative sampling of the integrals of motion E , L_z and I_3 in a model gravitational potential Φ enables us to construct any allowed configuration of orbits and match all kinds of observed galaxy shapes and kinematics. By linking Φ to different model mass (density) distributions via Poisson’s equation, we can thus optimize the mass model to best reproduce the observed stellar kinematics and imaging data of galaxies.

Here, we use the following parameterization for the mass composition $\rho(r, \theta)$:

$$\rho(r, \theta) = \rho_*(r, \theta) + M_{\text{BH}}\delta(r) + \rho_{\text{DM}}(r), \quad (1)$$

where θ is the polar angle, M_{BH} the mass of the central SMBH and ρ_{DM} the DM halo. For ρ_{DM} we initially chose to adopt the generalised NFW-halo derived from cosmological N-body simulations by [Navarro et al. \(1996\); Zhao \(1996\)](#), which is defined by three parameters, ρ_{10} , the DM density at 10 kpc, r_s , the scale radius of the halo and γ , the inner slope of the DM density profile. After extensive preliminary testing we found that for our sample galaxies the dynamical models always converged on cored DM-profiles, $\gamma = 0$ while r_s was always on similar scales ~ 100 kpc. We will discuss our DM halos and the implications of these findings in a different study. In the interest of avoiding parameter degeneracies with $\Upsilon(r)$ and saving computational time, we set γ to zero and r_s to a large value outside the spacial coverage of our kinematic data (in this case ~ 90 kpc, the average best-fit r_s of our preliminary models). Therefore, we only model one parameter for the DM halo, ρ_{10} .

The stellar mass-density distribution is tied to the three dimensional deprojection $\nu(r, \theta)$ of photometric imaging, as detailed in Section 2.2, via $\Upsilon(r)$,

$$\rho_*(r, \theta) = \Upsilon(r) \cdot \nu(r, \theta), \quad (2)$$

with $\nu(r, \theta)$, the 3D light density distribution, which is not a model parameter, but a constraint – it is fixed to

Galaxy	Morphology (M+23)	MUSE-PSF ["]	SINFONI SNR _{min} /Å	study for SINFONI
NGC 307	power-law/fast	2.10	30	E+18
NGC 1332	power-law/fast	2.12	83	R+11
NGC 1407	core/interm.	1.93	30	R+13
NGC 4751	power-law/fast	1.59	30	R+13
NGC 5328	core/slow	1.28	30	R+13
NGC 5516	core/slow	2.00	30	R+13
NGC 7619	core/interm.	2.00	30	R+13

Table 1. Selected properties of the observations and kinematic analysis of the sample galaxies with MUSE and SINFONI. The full width at half maximum (FWHM) of the point spread function (PSF) the MUSE observations are listed here as in Mehragan et al 2023 (M+23) for the sake of convenience. The SINFONI observations were adaptive optic based and have a FWHM of the PSF of roughly 0.15". We also list morphological classifications of the galaxies from M+23 according to their central regions and their angular momentum into fast, slow and intermediate rotating galaxies. In this study, we supplement our MUSE kinematics from M+23 with SINFONI kinematics from studies which are listed in the last column: [Rusli et al. \(2011\)](#) (R+11) [Rusli et al. \(2013a,b\)](#) (R+13), and [Erwin et al. \(2018\)](#) (M+18). We also list the minimum SNR of the SINFONI data. For all MUSE data SNR_{min}/Å ~ 100 (as described in M+23).

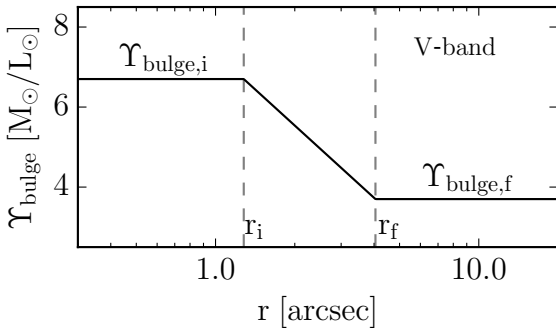


Figure 1. Example of our implementation of Υ_{bulge} gradients from the dynamical modeling of NGC 5328. We show best-fit values for one spatial quadrant of the galaxy (see Section 2.3). r_i is fixed to the MUSE PSF = 1.28", whereas r_f , $\Upsilon_{\text{bulge},i}$, $\Upsilon_{\text{bulge},f}$ are fit parameters.

the profiles derived from imaging data. Furthermore, our implementation allows for the modeling of multiple morphological components with separate $\Upsilon(r)$ (e.g. [Nowak et al. 2010](#), E+18). Therefore, for the fast rotating power-law galaxies, NGC 307, NGC 1332, and NGC 4751 we use a photometric decomposition to distinguish a bulge and a disc component. These are deprojected separately and have their own separate Υ_{bulge} and Υ_{disc} . Since the disc components fade into DM-dominated regions at larger radii and are outshone by the bulge components in the center, they are locally less well constrained and we decided to fit the disc components without gradients $\Upsilon_{\text{disc}}(r) \rightarrow \Upsilon_{\text{disc}}$. We fit the bulge components with gradients as with the cored ETGs, $\Upsilon_{\text{bulge}}(r)$.

Our implementation of mass-to-light ratio radial profiles operates by two values $\Upsilon_{i,f} = \Upsilon(r_{i,f})$ at different distances from the center of the galaxy, $r_{i,f}$. We show an example of this implementation in Figure 1. Between

r_i and r_f , $\Upsilon_{\text{bulge}}(r)$ is linearly interpolated over $\log(r)$. Outside r_i and r_f , $\Upsilon_{\text{bulge}}(r) = \Upsilon_{\text{bulge},i}$ for $r < r_i$, and $\Upsilon_{\text{bulge}}(r) = \Upsilon_{\text{bulge},f}$ for $r > r_f$.

Here, however, we face two challenges in particular: At both small and large radii, mass-contributions from the stars become much more difficult to differentiate from those of the “dark” components, i.e. the central SMBH and DM halo. Per definition, within the SOI of the central SMBH, the enclosed stellar mass is less than M_{BH} . Towards the center then, $\Upsilon(r)$ becomes overshadowed by M_{BH} in terms of its impact on the observed stellar kinematics. In the opposite direction, with increasing distance from the galactic center, as the luminous component of the galaxy becomes ever fainter and the DM halo more dominant, it becomes more difficult to determine Υ locally.

Therefore, after trying a number of different approaches for the galaxies, we settled on the following setup: We defined the inner value $\Upsilon_{\text{bulge},i}$ at r_i equalling one full width at half maximum (FWHM) of the point spread function (PSF) of the MUSE stellar kinematics (see the second column of Table 1) and the outer value, $\Upsilon_{\text{bulge},f}$ at a radius r_f , which in the fit is restricted to an interval between two times the FWHM of the PSF and two thirds of the MUSE FOV, i.e. up to $r = 20''$. Beyond this radius, the above mentioned problem with differentiating between DM and stellar mass contributions becomes too acute for a measurement. We also do not add another $\Upsilon_{\text{bulge},j}$ inside the PSF, instead keeping Υ_{bulge} constant, $\Upsilon_{\text{bulge}}(r) = \Upsilon_{\text{bulge},i}$, for $r < r_i = \text{PSF}$ since the AO-supported SINFONI data which cover these spatial scales generally have a much lower SNR than our MUSE data (see Table 1 and Section 2.3 below).

For NGC 307, the spatial extent of the bulge component is too small, $r_{e,bulge} \sim 2''$, to warrant gradient models in our approach. Therefore, for this galaxy alone we set $\Upsilon_{bulge,i} \equiv \Upsilon_{bulge,f}$.

Together with contributions from DM and the SMBH, and accounting for disk and bulge components where necessary, we fit a total of four to six parameters, depending on the galaxy: $M_{BH}, \Upsilon_{bulge,i}, \Upsilon_{bulge,f}, [\Upsilon_{disk},] r_f$ and ρ_{10} .

2.1.2. Model selection and Non-parametric LOSVD fits

Our modeling optimization entails sifting through different sets of $(M_{BH}, \Upsilon_{bulge,i}, \Upsilon_{bulge,f}, [\Upsilon_{disk},] r_f, \rho_{10})$ with the optimization software NOMAD (Audet & Denis, Jr. 2006; Le Digabel 2011; Audet & Hare 2017) and computing orbit libraries in the associated gravitational potentials $\Phi(M_{BH}, \Upsilon_{bulge,i}, \Upsilon_{bulge,f}, [\Upsilon_{disk},] r_f, \rho_{10})$. For each Φ , tens of thousands of orbits, which are assigned individual weights, are generated from different (E, L_z, I_3) . The Schwarzschild modeling code then optimizes these weights by maximizing

$$\hat{S} = S - \hat{\alpha} \cdot \chi^2, \quad (3)$$

where χ^2 is calculated from the model fit to the observed non-parametric LOSVDs, and S is the Boltzmann entropy (Thomas et al. 2004). The deprojected light-distributions are used as a constraint.

The parameter $\hat{\alpha}$ constitutes the smoothing of the models. Lipka & Thomas (2021) have shown that an optimal determination of $\hat{\alpha}$ is required for an unbiased dynamical recovery of the internal mass parameters. This can be achieved by taking the so-called effective degrees of freedom, m_{eff} , a generalised measure of the degrees of freedom in a penalized system, into account. To that end, we minimize the generalized Akaike Information Criterion $AIC_p = \chi^2 + 2 \times m_{\text{eff}}$ for penalized likelihood models (Thomas & Lipka 2022) over a grid of $\hat{\alpha}$ values.

After determination of the optimal $\hat{\alpha}$ -value for the current Φ the associated minimum AIC_p value is passed to NOMAD. NOMAD minimizes the AIC_p until the optimal $(M_{BH}, \Upsilon_{bulge,i}, \Upsilon_{bulge,f}, [\Upsilon_{disk},] r_f, \rho_{10})$ to fit the LOSVDs is found. This approach not only optimizes the smoothing in each trial potential but also takes into account that the mass optimisation in Schwarzschild models is actually a model selection problem rather than a simple parameter estimation (Lipka & Thomas 2021). The model selection allows for very accurate and unbiased mass- and anisotropy-recoveries (Lipka & Thomas 2021; Neureiter et al. 2023a; de Nicola et al. 2022).

2.2. Galaxy light density profiles

The 3D light distribution in our dynamical models, $\nu(r, \theta)$, is constrained by – or rather fixed to – deprojections of 2D imaging data of the galaxies along the line-of-sight. We here re-use the imaging data, bulge/disc decompositions (where applicable) and deprojections from the studies which are listed in the last column of Table 1, with one exception, NGC 4751.

For the power-law galaxies, the inclination i was assumed from the flattening of their discs at large radii (for an assumed intrinsic flattening $q = 0.2$): $i = 75$ for NGC 307 (E+18) and $i = 90$ for both NGC 1332 and NGC 4751. For the four disc-less cored galaxies, we assumed $i = 90$. Axisymmetric Schwarzschild models of realistic triaxial N-body simulations of core galaxies suggest that even using the AIC_p optimization technique, the models often fit the galaxies best at $i = 90$. These tests further suggest that the bias of the mass-to-light ratio that can arise from the assumption of axial symmetry (and $i = 90$) is on the order of 15% (Lipka et al. in prep).

All galaxies, including NGC 4751, have been assumed to be close-to or directly edge-on for the deprojections, based on their flattening at large radii

For NGC 4751, we performed a new disc/bulge decomposition (as none has been performed in R+13) based on the same HST NICMOS2 images we used in R+13, combined with K-Band observations with VIRCAM (Emerson et al. 2006; Dalton et al. 2006). We followed the same steps and approach as for the other galaxies to produce the disc/bulge decomposition and separate deprojections for both components. This is outlined in Appendix A.

2.3. Non-parametric stellar kinematics

MUSE data: The MUSE stellar kinematics of our sample were the result of the first systematic study of the detailed non-parametric shapes of the LOSVD of massive ETGs, which we published in Mehrgan et al. (2023), from here on M+23. They were derived using the new non-parametric spectral fitting code WINGFIT (Thomas et al. in prep.), which also uses the data-driven AIC_p -optimisation technique of Thomas & Lipka (2022). The details of the observations, derivation of the kinematics from them, as well as the resulting kinematics are presented in M+23.

The MUSE non-parametric LOSVDs are the main input for our orbital dynamical models: They cover a large $1' \times 1'$ field of view (FOV), encompassing half to a full effective radius r_e for each galaxy in our sample. Furthermore, the data were Voronoi binned using the Voronoi tessellation method of Cappellari & Copin (2003) for a very high SNR/ $\bar{A} > 100$ (as described in M+23).

For the dynamical models, we split the MUSE FOV into quadrants along the major and minor axes of each galaxy to ensure that we can provide a robust estimation of the error bars of the best-fit model parameters from the scatter between the quadrants. This resulted in roughly 15–100 spatial bins per quadrant per galaxy, each with its own non-parametric LOSVD.

We sampled the LOSVDs either with $N_{vel} = 15$ velocity bins out to 1500 km/s, or $N_{vel} = 17$ out to 1700 km/s, depending on where the LOSVDs of each galaxy terminate¹. Therefore, all in all, we end up with roughly 225 to 1500 kinematic MUSE-data points per galaxy per quadrant for our dynamical models.

SINFONI data: For the central regions of the galaxies, we also supply our dynamical models with non-parametric SINFONI stellar kinematics. These kinematics were derived earlier using the maximum pealized likelihood method (MP) from Gebhardt et al. (2000).

The SINFONI data was binned into radial and angular segments as in Rusli et al. (2013a). In Table 1, we list the SNR achieved with this binning. For the details surrounding the observations, binning, and kinematics, we refer to the studies listed in the last column of Table 1.

Though covering a much smaller FOV, $3'' \times 3''$, corresponding to the 100 mas-mode of SINFONI, these LOSVDs, which are adaptive-optics based, and thus not seeing limited, supply our models with vital constraints on the central mass-light profile of the galaxies as they can resolve the gravitational SOI of their central SMBHs (on a scale of $\lesssim 1''$). For these data we supply the PSF in the form of 2D images to the dynamical models. The images typically have a FWHM around $\sim 0.15''$.

We sampled the LOSVDs in the same way as the MUSE LOSVDs, resulting in $\sim 300 - 500$ kinematic data points per galaxy per quadrant for our dynamical models (~ 1000 in the case of NGC 1332).

Combining the kinematic data In Figure 2 we show, as an example, all the LOSVDs of NGC 7619, including both MUSE and SINFONI LOSVDs, divided into quadrants. For the dynamical models we also include LOSVDs from MUSE which spatially overlap with those from SINFONI.

2.4. Approach to deriving results

We compute at least 2500 models per quadrant. The best-fit model parameters in terms of AIC_p , as well as

¹ The sole exception here being NGC 307, the least massive ETG in our sample. Here, the LOSVDs terminate at $\sim \pm 1000$ km/s, and we used 21 velocity bins, to properly sample its much narrower distribution function

the associated mass profiles, including $\Upsilon(r)$, are averaged over all quadrants to produce one final set of model parameters and mass distribution per galaxy.

For NGC 1332, an independent black hole mass measurement was available from direct observation of the circumnuclear disk in the central 200 pc of the galaxy Barth et al. (2016), $M_{BH} = 6.64(-0.63, +0.65) \times 10^8 M_\odot$. We had previously dynamically determined a larger M_{BH} using Schwarzschild models in R+13. However the measurement from Barth et al. (2016) have a much higher spatial resolution of $0.044''$ (versus $\sim 0.15''$) and are derived from the kinematics of a cold disk within the SOI of the central SMBH – a simpler dynamical problem than our own models. Therefore we fixed M_{BH} for this galaxy to the measured value from Barth et al. (2016) and only varied the other model parameters to get better constraints on the central $\Upsilon(r)$.

For both NGC 1332, and NGC 1407 we had an especially large number of spatial bins available, with well over a 120 MUSE+SINFONI LOSVDs per Quadrant. The same assumption of axisymmetry that allowed us to split our dynamical models into quadrants and model those quadrants as “separate” galaxies, over which we average for the final results, allow us to sort all spatial bins in a quadrant according to radius and then group together every second spatial bin as a sub-quadrant to be modeled independently. Hence for these two galaxies, we model and average over eight instead of four dynamical best-fit models (for each sub-quadrant we also run at least 2500 models), which allows us to better sample the statistical uncertainties.

We here treat the values of $\Upsilon_{bulge,i,f}$ listed in Table 2 as *nuisance* parameters and not as the primary measures of the gradients which we detect: Firstly, if two photometric components are present, as is the case for NGC 307, NGC 1332 and NGC 4751, the final gradient $\Upsilon(r)$ emerges from the superposition of the light profiles of the bulge- and disk-components times their respective Υ -profiles, divided by the total light. In the case of NGC 1332 and NGC 4751, this produces a much more complex $\Upsilon(r)$ profile than for the bulge-component alone (for NGC 307, the gradient only emerges from the superposition of two constant- Υ components). Second, we take our Υ profiles as the average over the individual (sub-)quadrants of each galaxy at each radius. The resulting average profiles can be more complex than the parametric profiles of the individual quadrants.

Furthermore, for better comparison with stellar population models we project Υ along the line-of-sight. However, Υ as an intended purely *stellar* mass component, depends on assumptions in the mass decomposition. This is not so much of a concern in regions in

the center that are at the same time still outside the SOI. Here Υ is essentially identical to the total inner dynamical mass-to-light ratio, $(M^{\text{tot}}/L)(r)$, as the local mass-contribution of the DM-component is essentially drowned out by the stellar component. For all galaxies in our sample, except one (NGC 1407, see Section 4.3), the SOI is very small compared to the innermost radius of our gradient-models, $r_i/\text{SOI} \gtrsim 3$.

However, on scales of $0.5 - 1$ kpc from the center, $(M^{\text{tot}}/L)(r)$ starts to diverge from $\Upsilon(r)$ because DM begins to assert more influence on the dynamics of the stars and $(M^{\text{tot}}/L)(r)$ rises relative to $\Upsilon(r)$. At this point, disentangling DM from stars becomes more and more difficult and the derived $\Upsilon(r)$ will depend on the assumptions about DM (and vice versa).

In order to overcome the difficulty related to the mass decomposition in the outer parts, we try to determine the stellar $\Upsilon(r)$ focusing entirely on spatial scales where $\Upsilon \sim M^{\text{tot}}/L$, i.e. where the *stellar* Υ is least dependent on any assumption upon the mass decomposition. It turns out that this is possible, because the stellar dynamical gradients all fall very quickly with galactocentric radius (see next Section) and at larger radius the DM halo “takes over”. As a consequence, the $(M^{\text{tot}}/L)(r)$ profiles are effectively valley-shaped (see next Section and Figure 5), with a global minimum in between the two regimes. This minimum is not only a characteristic property related to the central gradients but it is also key to determine the stellar mass-to-light ratio in the main body of the galaxies in a way that depends only little on the assumed DM profile: under the only assumption that the stellar mass-to-light ratio does not increase towards the outer parts, the minimum in the total $(M^{\text{tot}}/L)(r)$ is the point of strongest constraint for the stellar mass-to-light ratio in the main body of the galaxy. More specifically, it sets an upper limit for this ratio. We therefore treat the stellar mass-to-light ratio $\Upsilon_{\text{main}} = \Upsilon(r_{\text{main}})$ associated to the radius r_{main} where the minimum in $(M^{\text{tot}}/L)(r)$ occurs as the mass-to-light ratio of the galaxy main body. For the central stellar mass-to-light ratio, we define Υ_{cen} simply as $\Upsilon(r)$ within the MUSE PSF ($r_{\text{cen}} = r_i = \text{PSF}$).

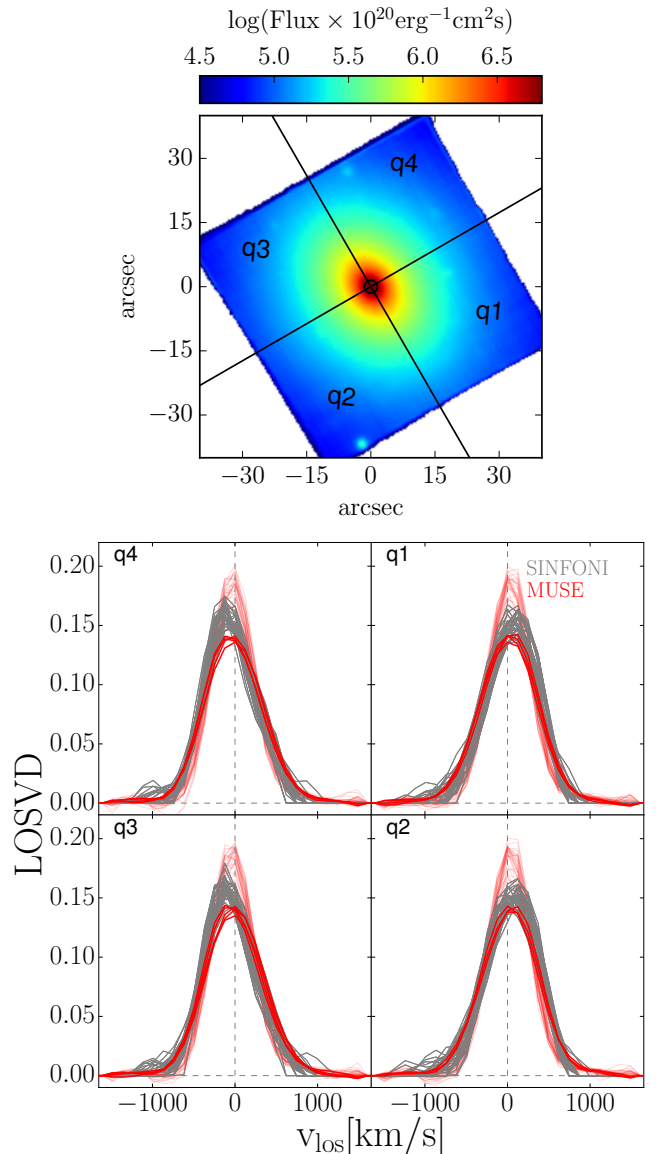


Figure 2. Example of the kinematic data used in this study. Top: Flux map of the MUSE data (north is up, east is left). Black lines show the major axis (position angle = 30°) and minor axis. The small black circle in the center ($r = 1.5''$) indicates the SINFONI FOV. Bottom: Non-parametric LOSVDs from MUSE (red) and SINFONI (grey) for NGC 7619, separated into the spatial quadrants indicated in the top panel. MUSE-LOSVDs from bins that spatially overlap with the SINFONI FOV are shown in solid red, whereas all other LOSVDs are shown in a fainter red. The stellar rotation of NGC 7619 increases towards the center (Figure 15 of M+23). This trend continues into the spatial regions resolved by SINFONI (i.e. the SINFONI LOSVDs are more strongly shifted in $\pm v_{\text{los}}$.)

3. RESULTS

The best-fit model parameters for all galaxies are listed in Table 2. The best-fit models have on average

Galaxy	Band	$\Upsilon_{\text{bulge},i}$	$\Upsilon_{\text{bulge},f}$	r_f	Υ_{disk}	M_{BH}	ρ_{10}	$\langle (\chi^2 + m_{\text{eff}})/N \rangle$
		$[\text{M}_{\odot}/\text{L}_{\odot}]$	$[\text{M}_{\odot}/\text{L}_{\odot}]$	$[\text{kpc}]$	$[\text{M}_{\odot}/\text{L}_{\odot}]$	$[10^9 \text{M}_{\odot}]$	$[10^8 \text{M}_{\odot}/\text{kpc}^3]$	
NGC 307	K	1.13 ± 0.04	1.13 ± 0.04	–	0.63 ± 0.27	0.22 ± 0.04	1.9 ± 0.4	0.72
NGC 1332	R	8.50 ± 0.83	1.38 ± 0.89	1.0 ± 0.4	2.31 ± 1.62	0.66*	5.0 ± 0.9	0.76
NGC 1407	B	11.10 ± 2.86	1.04 ± 1.08	1.2 ± 0.5	–	5.50 ± 1.58	2.7 ± 0.4	0.78
NGC 4751	K	2.17 ± 0.24	0.83 ± 0.47	1.3 ± 0.6	0.58 ± 0.13	1.75 ± 0.34	5.5 ± 0.6	1.39
NGC 5328	V	6.57 ± 0.51	4.28 ± 0.43	1.9 ± 1.4	–	1.63 ± 0.89	1.1 ± 0.2	0.99
NGC 5516	R	6.16 ± 0.60	2.83 ± 1.91	2.9 ± 1.8	–	2.50 ± 0.53	0.8 ± 0.1	0.95
NGC 7619	I	4.00 ± 0.79	2.00 ± 1.28	2.0 ± 0.6	–	3.25 ± 1.40	0.8 ± 0.2	0.62

Table 2. Results of Schwarzschild dynamical modeling using mass-to-light gradient models. Photometric bands, as well as extinction corrections for Υ -values for all galaxies were taken over from R+11, R+13, and E+18, according to Table 1, except for NGC 4751. Model parameters are averages with standard deviations over all quadrants or sub-quadrants. $\Upsilon_{\text{bulge},i}$ was fitted at a set radius $r_i = \text{PSF}$, whereas r_f , the radius of $\Upsilon_{\text{bulge},f}$ was a free parameter in the fit. We also list (sub-)quadrant averages of $\langle (\chi^2 + m_{\text{eff}})/N \rangle$ of the fits to the non-parametric LOSVDs. (*) For NGC 1332, we used the M_{BH} -value measured by Barth et al. (2016) as a fixed parameter.

Galaxy	Υ_{cen}	Υ_{main}	$(M^{\text{tot}}/L)_{\text{main}}$	r_{main}	α_{cen}	α_{main}	$\alpha_{\text{main}}^{\text{tot}}$
	$[\text{M}_{\odot}/\text{L}_{\odot}]$	$[\text{M}_{\odot}/\text{L}_{\odot}]$	$[\text{M}_{\odot}/\text{L}_{\odot}]$	$[\text{kpc}]$			
NGC 307	4.65 ± 0.04	4.12 ± 0.09	4.64 ± 0.04	1.0	1.23 ± 0.06	1.23 ± 0.06	1.23 ± 0.06
NGC 1332	9.69 ± 0.46	2.54 ± 0.34	3.72 ± 0.3	0.9	2.20 ± 0.26	0.59 ± 0.20	0.86 ± 0.14
NGC 1407	7.69 ± 1.54	1.29 ± 0.71	2.00 ± 0.61	1.1	1.76 ± 0.45	0.30 ± 0.18	0.47 ± 0.17
NGC 4751	9.54 ± 0.25	4.12 ± 0.22	5.40 ± 0.25	0.8	2.35 ± 0.26	1.246 ± 0.28	1.63 ± 0.32
NGC 5328	6.56 ± 0.11	4.54 ± 0.13	4.88 ± 0.12	1.3	1.62 ± 0.13	1.12 ± 0.15	1.21 ± 0.14
NGC 5516	7.83 ± 0.16	4.66 ± 0.43	5.00 ± 0.42	1.3	1.90 ± 0.19	1.22 ± 0.51	1.29 ± 0.50
NGC 7619	5.81 ± 0.29	3.96 ± 0.42	4.12 ± 0.42	1.1	1.55 ± 0.31	0.92 ± 0.37	0.97 ± 0.36

Table 3. V-band stellar and total mass-to-light ratios, Υ , M^{tot}/L measured from our best-fit dynamical models. These values are projected along the line-of-sight for later comparison with SSP models. Therefore, these values should not be confused with the modeling-parameters in Table 2. Inner Υ_{cen} -values are essentially identical to inner $(M^{\text{tot}}/L)_{\text{cen}}$. The stellar mass-to-light ratios of the main body of the galaxy, Υ_{main} are defined at the global minimum of $(M^{\text{tot}}/L)(r)$, $M^{\text{tot}}/L(r_{\text{main}}) = \min(M^{\text{tot}}/L) = (M^{\text{tot}}/L)_{\text{main}}$, for all galaxies except NGC 307, where we manually set $r_{\text{main}} = 1 \text{ kpc}$. Finally we also show these mass-light values relative to the stellar mass-to-light ratio assuming a Kroupa IMF for these galaxies from the SSP analysis of Parikh et al. submitted to MNRAS, in the form of the excess parameter α .

$\chi^2/N \sim 0.6$ over all (sub-)quadrants. Such low χ^2/N values for best-fit models have long been typical for Schwarzschild models, due to the large number of the degrees of freedom involved. Taking the effective degrees of freedom, m_{eff} into account, $\langle (\chi^2 + m_{\text{eff}})/N \rangle \sim 0.9$ (see last column of Table 2). The remaining difference between $\langle (\chi^2 + m_{\text{eff}}) \rangle$ and N likely originates from covariances between the individual velocity bins of the LOSVDs.

For all intents and purposes our $\langle (\chi^2 + m_{\text{eff}})/N \rangle$ values demonstrate that our dynamical models produced good fits to the kinematic data – At least for all galaxies except NGC 4751. Here $\langle (\chi^2 + m_{\text{eff}})/N \rangle \sim 1.4$ was larger than for the other galaxies, due to the presence of dust-lanes covering almost the entirety of the major axis within r_e (see Appendix A) We also had to exclude one quadrant entirely for this galaxy as we could not find a good fit to the data $\langle (\chi^2 + m_{\text{eff}})/N \rangle \sim 3$. We treat the

results for this galaxy with some added caution. This is discussed later in Section 4.2.1.

We show one example-fit to central LOSVDs of NGC 1407 in Figure 3. LOSVD- and radial kinematic fits for all galaxies are included in Appendix B.

We show AIC_p model selection curves converging on the best-fit parameters of the (sub-)quadrants of the galaxies in Figure 4.

In the following we examine the mass-to-light ratio gradients $\Upsilon(r)$ and discuss the effect of gradients M_{BH} measurements.

3.1. Mass-to-light ratio gradients

The main result of our study is that we have found stellar dynamical evidence in favour of radial gradients of the stellar mass-to-light ratio, $\Upsilon(r)$ for all galaxies in our sample. These gradients are confined to the very centers of the galaxies and occur on spatial scales of

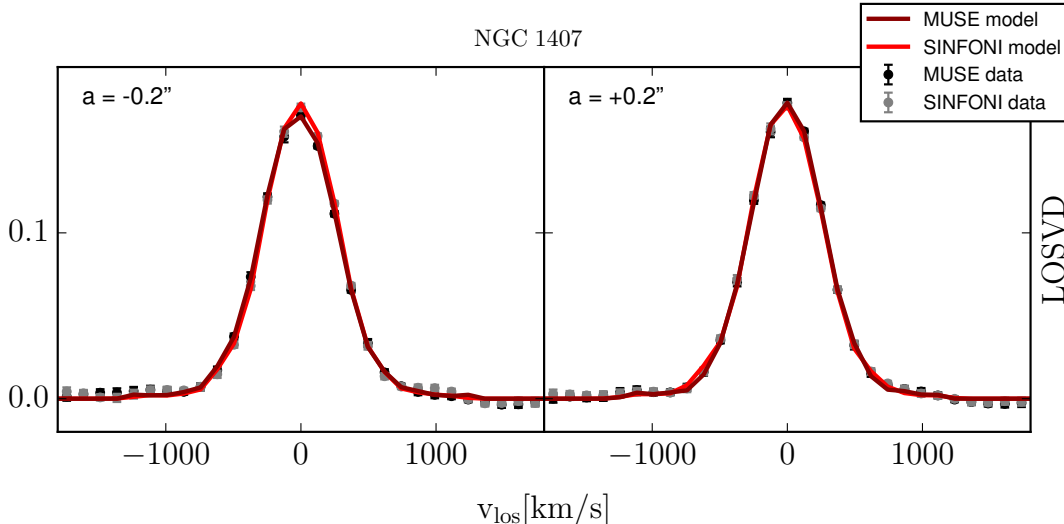


Figure 3. Dynamical fits to the non-parametric LOSVDs from the center of NGC 1407. We show fits at two positions near the major-axis a on opposite sites of the minor axis of the galaxy. MUSE and SINFONI data spatially overlap at these positions. The MUSE data LOSVDs with statistical uncertainties are shown as black points with error bars, whereas the respective best-fit dynamical model is shown as a solid dark red line. Analogously, we show the SINFONI data and model LOSVDs in grey and light red. The best-fit LOSVDs are here shown at the full MUSE velocity resolution.

$r \sim 1$ kpc. For all galaxies, Υ becomes larger towards the center of the galaxy (Figure 5).

Moreover, in all our galaxies a well-defined global minimum of the total dynamical mass-to-light ratio $(M^{\text{tot}}/L)(r)$ occurs. We call the radius where this minimum occurs r_{main} . As explained above, the mass-to-light ratio at this radius poses strong constraints on the mass-to-light ratio of the stars in the main body of the galaxy largely independent of the detailed assumptions upon the mass decomposition.

NGC 307 is an exception since the galaxy does not show a minimum in (M^{tot}/L) . Here we set $r_{\text{main}} \sim 1$ kpc, which coincides roughly with the point where $(M^{\text{tot}}/L)(r)$ begins to rise from the center.

For a few individual (sub-)quadrants of the galaxies the AIC_p -curves of the outer $\Upsilon_{\text{bulge},f}$, (and/or Υ_{disk}) did not converge to a minimum, but instead hit the lower boundary of our sampling range. This amounts to the mass contribution of the DM component displacing mass contribution of the stellar component, and $\Upsilon_{\text{bulge},f}$ getting as close to zero as our models allow. As explained, this does not concern us since $r_{\text{main}} < r_f$ (cf. Tables 2 and 3) for all galaxies, and in our approach we focus on the parts of the galaxies least affected by DM, while treating the mass decomposition past r_{main} as a curtain we do not look behind – the dynamical mass of our models can reproduce the kinematics in this region without us knowing the details of the mass decomposition.

For the gradient-plots in Figure 5, we normalized all gradients relative to Υ_{main} to illustrate by how much

the stellar mass-to-light ratio appears to increase in the centers of the individual galaxies.

For the four core galaxies in our sample we supplement our gradient models with models that assume a spatially constant stellar Υ both as a consistency check and for better comparison with previous measurements (Appendix C). These models without gradients were worse fits to the kinematic data for all (sub-)quadrants and galaxies. Compared to their counterparts with gradients the $\Delta\text{AIC}_p \sim 10 - 20$ is significant. In general, the best-fit Υ derived from models without a gradient lie between Υ_{cen} and Υ_{main} . Note that because the actual gradients occur on very small spatial scales, this means that the models without gradients tend to overestimate the stellar mass in the main body of the galaxy by a factor of 1.5 on average. This effect of overestimating Υ when such gradients remain unaccounted for had also previously been suggested by Bernardi et al. (2018); Domínguez Sánchez et al. (2019).

In Table 3, we list the characteristic inner and main-body mass-to-light ratios of our models in the V-band, as well as the IMF normalization α relative to a Kroupa IMF for these values. We discuss the mass normalisation in Section 4.

We briefly describe the Υ -gradients of the galaxies.

NGC 307: As stated above, the bulge of this galaxy was too small to warrant the implementation of gradients. There is, however, a weak composite $\Upsilon(r)$ gradient from the superposition of the two constant Υ_{bulge} , Υ_{disk} . The increase of our composite $\Upsilon(r)$ within 1 kpc is con-

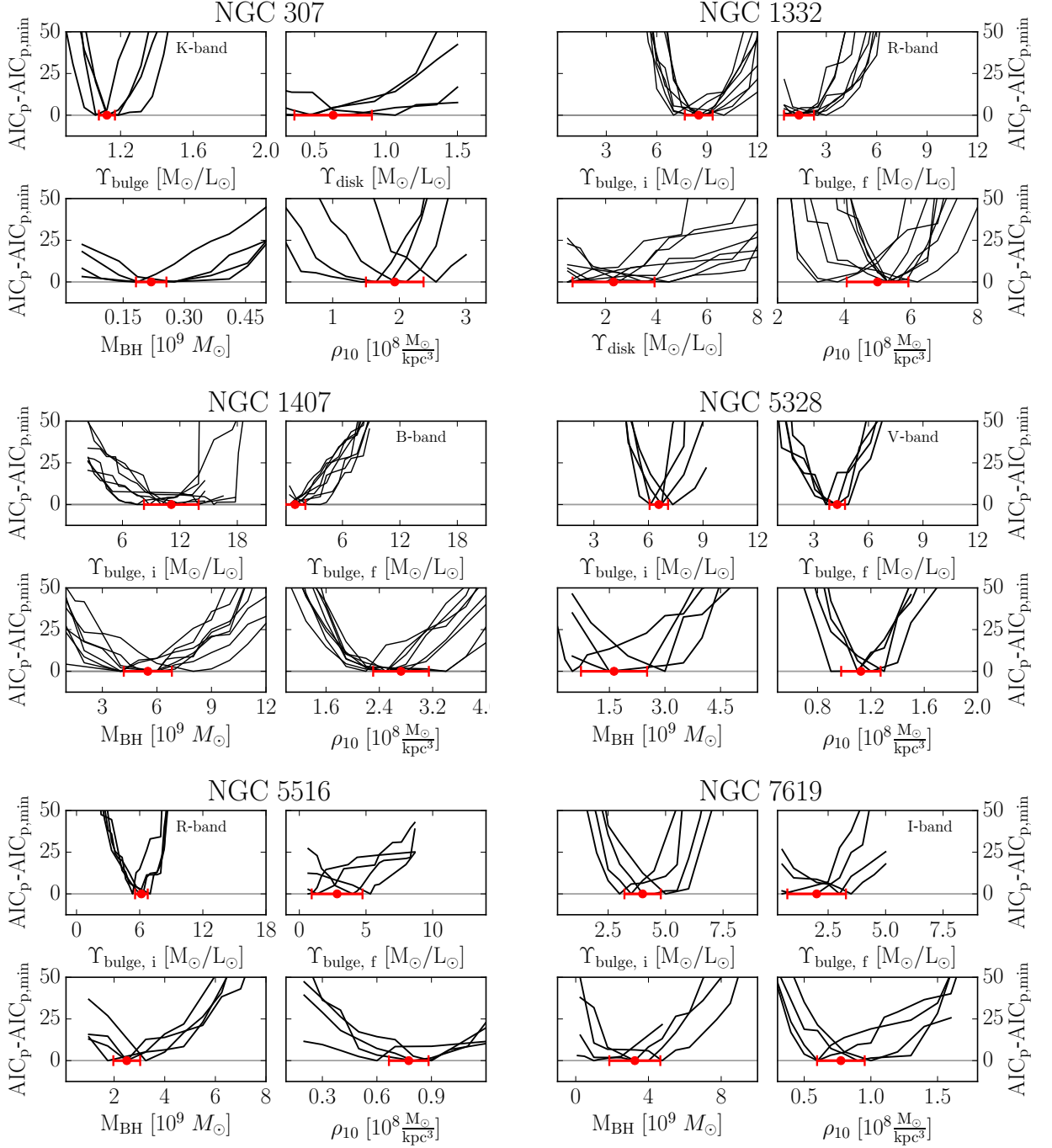


Figure 4. AIC_p model selection curves, the equivalent of the classical χ^2 curves for Schwarzschild models. Each curve represents the (independent) modelling result of one quadrant/sub-quadrant and is derived from the lowest AIC_p value of each sampling point of the corresponding modeling parameter. The best-fit values (red points with errorbars) are determined at the minima of the AIC_p and the variation between the AIC_p minima represents the statistical uncertainties of each measurement for each galaxy.

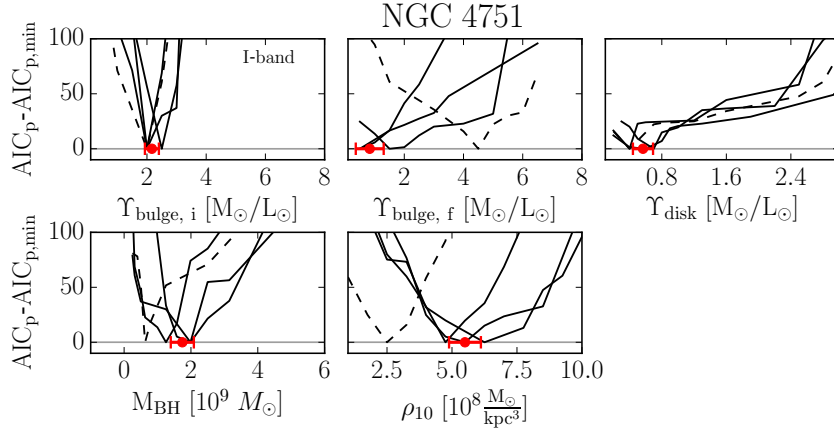


Figure 4. (continued) For NGC 4751 one of the quadrants (dashed curve), was not used for the calculation of the best-fit parameters or any other modeling results.

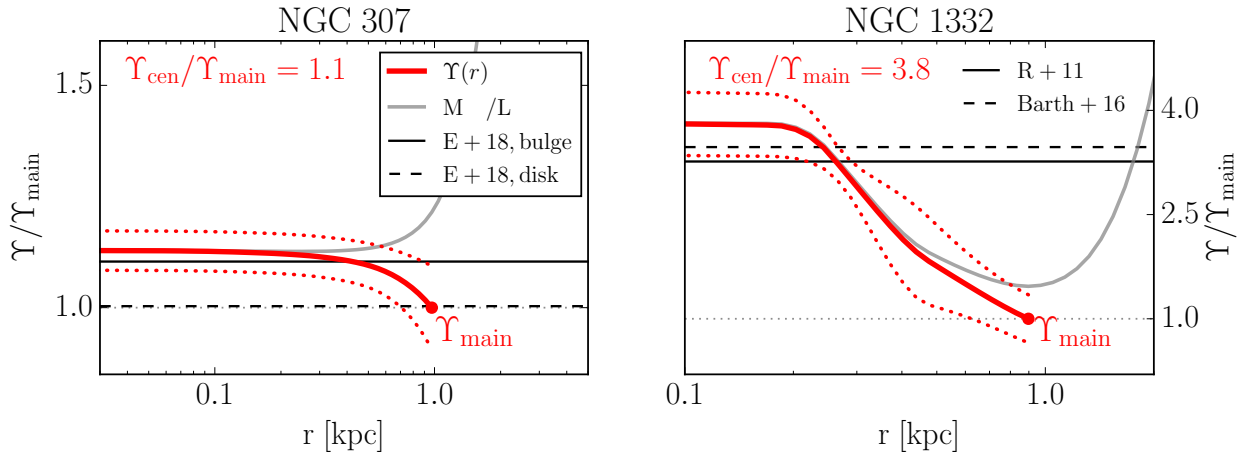


Figure 5. Mass-to-light ratio profiles of the sample galaxies. The best-fit stellar $\Upsilon(r)$ (solid red lines, uncertainties indicated by dotted red lines) of the galaxies are shown relative to the values of the galaxy main body, $\Upsilon_{\text{main}} = \Upsilon(r_{\text{main}})$. The radius r_{main} is defined at the minimum of the *total* mass-to-light ratio $(M^{\text{tot}}/L)(r)$, for all galaxies except NGC 307 (see text). While the *stellar* $\Upsilon(r)$ depends on assumptions upon the mass decomposition, $(M^{\text{tot}}/L)(r)$ is directly derived from the observations. We indicate $(M^{\text{tot}}/L)(r)$ and its uncertainties by solid grey lines and grey shaded areas, respectively. Note that $\Upsilon(r)$ profiles are projected along the line-of-sight (differences to the non-projected profiles are small). The figure includes comparisons with previous dynamical models without gradients (R+11,13; E+18 and Barth et al. 2016). For the four core galaxies we run comparison models without gradients as well (denoted as “ $\Upsilon = \text{const.}$ ”). Models without gradients are worse fits to the kinematic data and tend to overestimate the mass in the main body of the galaxy.

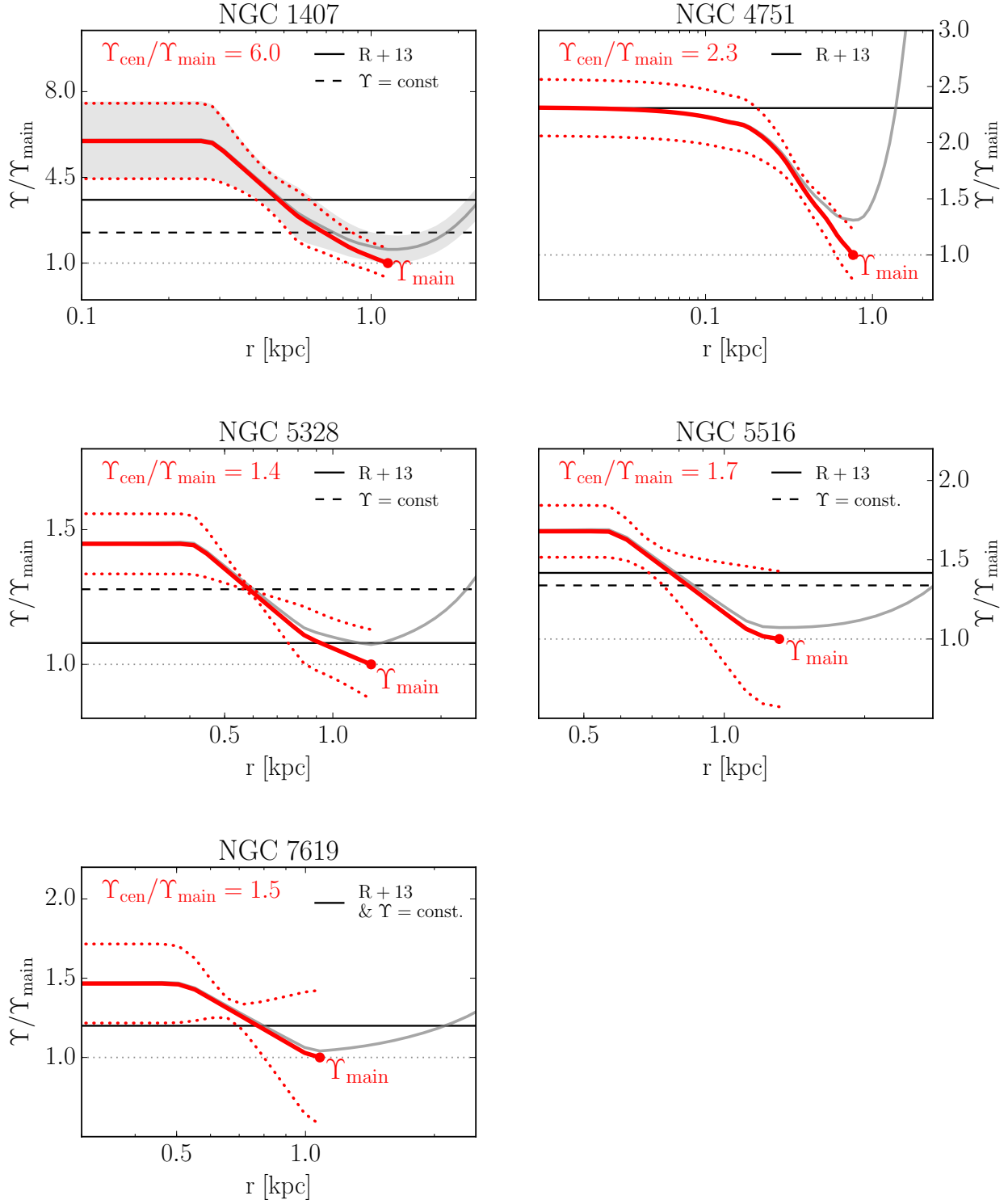


Figure 5. (continued)

sistent with the one found by E+18, $\Upsilon_{\text{bulge}}/\Upsilon_{\text{disk}} = 1.1$ (their values). Considering our Υ_{bulge} , Υ_{disk} best-fit model parameters, our Υ_{bulge} -value is identical to the one from E+18. For the disk component, our value is overall lower, but still roughly consistent with theirs within the uncertainties: $\Upsilon_{\text{disk}} \sim 0.63 \pm 0.27$ versus 1.0 ± 0.1 in E+18 (I-band).

NGC 1332: We find a significant, almost factor-of-four increase towards the center of this galaxy from the superposition of the disk and bulge components. The central parts of this gradient ($r \lesssim 0.3$ kpc) have a slightly larger Υ than our constant- Υ models from R+11. Over most of the galaxy’s spatial extent, however, our new models produce significantly lower Υ . Our central Υ is furthermore in agreement with the models by Barth et al. (2016) for the central 0.2 kpc.

NGC 1407: This galaxy has by far the most notable Υ -gradient in our sample, with a factor six increase towards the center. This is the only galaxy in our sample for which the SOI of the central SMBH, $r_{\text{SOI}} = (0.34 \pm 0.076)$ kpc, extends to scales larger than the inner part of the Υ -gradient, $r_{\text{cen}} \sim 0.3$ kpc. Furthermore, the outer mass-to-light ratio is surprisingly low, $\Upsilon'_f = 1.29 \pm 0.71$ in V-band. Even accounting for uncertainties in the mass decomposition, the total $(M^{\text{tot}}/L)_{\text{main}} \sim 2$ is by far the lowest in our sample. However, the comparison models without gradient yield $\Upsilon = 3.0 \pm 0.20$ closer to our outer mass-light profile and lower than measured by R+13 (~ 4.6 in V-band). The latter appears consistent with a radial average of our Υ -gradient, roughly bisecting our mass-light profile in the middle in Figure 5.

NGC 4751: As with NGC 1332, we find a Υ -gradient within the bulge component, which in superposition with the constant- Υ disc component produces an effective total Υ -gradient of slightly more than a factor two. The maximum of the gradient, within $r < 0.1$ kpc, matches our previously published constant- Υ value from R+13.

NGC 5328: For this galaxy, the constant- Υ measurement is roughly an average over radius of our gradient model $\Upsilon(r)$. At the point where our gradient intersects with the constant Υ -model ($\Upsilon \sim 5.8$ in V-band, $r \sim 0.6$ kpc), it is also the most well defined with respect to the uncertainties. Our previously published Υ -measurement from R+13 appears to be consistent with our Υ_{main} , but a factor ~ 1.3 smaller than Υ_{cen} .

NGC 5516 & 7619: For both of these galaxies we find gradients of a similar magnitude as for NGC 5328, and for which both our new constant- Υ models and previous measurements from R+13, are roughly averages over radius.

3.2. SMBH measurements

Unless one has kinematic data that resolve the SOI of a central SMBH very well, there is always some covariance between dynamically determined stellar mass-to-light ratios and the respective black hole mass, M_{BH} (e.g. Rusli et al. 2013a). Our previous SMBH mass measurements for the galaxies studied here were based on models without gradients hence we expect that after allowing for gradients the SMBH masses will change to some extent. However, a direct comparison is difficult, since the previous measurements used older (mostly long-slit) kinematic data outside the central regions. If we directly compare the SMBH masses from the old (gradient-free) and the new (gradient) models then we find two galaxies where M_{BH} goes up and two where it goes down². The difference can be up to 50%. This is surprising, since our new, central stellar mass-to-light ratios Υ_{cen} are always larger than the previous Υ from the gradient-free models. However, if we take our new comparison models without gradients as reference (which are based on the same data and modelled with the same advanced Schwarzschild code) then we find that in the gradient models, M_{BH} is *always* smaller than in the gradient-free models – as expected. The average decrease is 25%.

The remaining scatter when comparing the old (gradient-free) models with the new (gradient) models stems from the fact that the new MUSE data and advancements in the dynamical modelling have a non-negligible effect on our SMBH mass measurements. Still, our new values of M_{BH} are consistent with those found in R+13 and E+18 within the uncertainties for all galaxies except NGC 5328 (see Section 4.2.1 and also the discussion in Appendix C of M+23).

In Figure 6 we compare our new dynamical models to established trends between M_{BH} and galaxy velocity dispersion σ . We take the data for galaxies from Saglia et al. (2016) but use the updated values for the seven galaxies of this study. We also added a number of the most recent Schwarzschild-based measurements from the literature: From our own work we include axisymmetric Schwarzschild modeling results for the massive ETGs NGC 1600 Thomas et al. (2016) and Holm 15A Mehrgan et al. (2019), which were both noted for their particularly massive SMBHs, as well as NGC 5419, which was modeled with our new triaxial modeling code SMART (Neureiter et al. 2021). More-

² We restrict the discussion to the four core galaxies where we ran comparison models without gradients. For NGC 1332 we took M_{BH} from Barth et al. (2016) and for NGC 307 and NGC 4751 the new and old M_{BH} are almost identical.

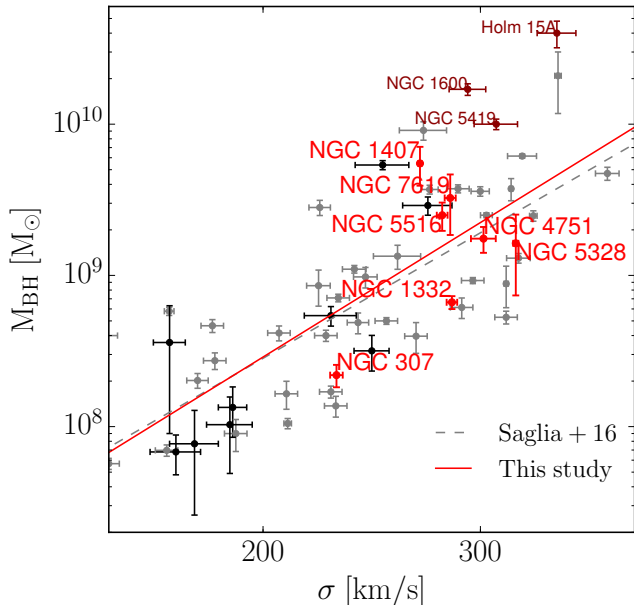


Figure 6. Our new dynamical M_{BH} measurements from the Schwarzschild models with gradients of this study (red) compared to the ETGs in Saglia et al. (2016) (grey) and new SMBH measurements from Thomas et al. (2016); Mehrgan et al. (2019) and Neureiter et al. (2023b) (all in dark red) and Thater et al. (2019, 2022); Quenneville et al. (2022); Liepold et al. (2023) (black). The $M_{\text{BH}} - \sigma$ relation of Saglia et al. (2016) is shown as a dashed grey line. We re-fitted the relation using all of the above measurements (solid red). For the same galaxy, using the same data and modelling codes we find that M_{BH} from models that allow for gradients are 25% smaller than in models without gradients.

over we add results from triaxial Schwarzschild modeling of NGC 1453 from Quenneville et al. (2022), using the σ_e value from Veale et al. (2018), as well as triaxial models for M87 from Liepold et al. (2023). Finally, we add seven more axisymmetric Schwarzschild measurements for low-mass fast-rotating ETGs from Thater et al. (2019) and Thater et al. (2022).

With all of these new measurements added, we find the following relation:

$$\log\left(\frac{M_{\text{BH}}}{M_{\odot}}\right) = (5.05 \pm 0.41) \cdot \log\left(\frac{\sigma}{200 \text{ km/s}}\right) + (8.46 \pm 0.06) \quad (4)$$

This updated $M_{\text{BH}} - \sigma$ relation for ETGs is consistent with the relation of Saglia et al. (2016) (“CorePowerE” in Table 11 of that study) within the uncertainties, though slightly steeper.

4. DISCUSSION

4.1. On the stellar IMF

In this section we evaluate our measured radial mass-light gradients in the context of a potential IMF varia-

tion within galaxies. To this end we calculate the mass normalization of our $\Upsilon(r)$ and $M^{\text{tot}}/L(r)$ profiles relative to SSP-based measurements assuming a Kroupa IMF, $\Upsilon_{\text{Kroupa}}^{\text{SSP}}$ (Parikh et al. submitted to MNRAS). While this is not a direct measurement of the shape of the IMF itself, it allows us to explore what level of bottom-heaviness is compatible with the dynamics of the galaxies, since the presence of low-luminosity dwarf stars is expected to be the main driver of IMF variation in ETGs (van Dokkum & Conroy 2010).

4.1.1. Radial IMF gradients

The radius r_{main} is particularly relevant for our IMF-probes. The total-mass profiles from our dynamics effectively serve as upper-limits for the bottom-heaviness of the IMF: Formally all IMF models which produce $\Upsilon_{\text{IMF}}(r)$ below our derived $(M^{\text{tot}}/L)^{\text{dyn}}(r)$ are consistent with our analysis – we only need to account for the difference between $\Upsilon_{\text{IMF}}(r)$ and $(M^{\text{tot}}/L)^{\text{dyn}}(r)$ by local mass-density corrections to our DM-halo models. Thus, at r_{main} , the radial position of the global minimum of $(M^{\text{tot}}/L)(r)$, the constraints on the maximum bottom-heaviness of the IMF are strongest. We here formulate the IMF mass normalization for a Kroupa IMF for both our $\Upsilon(r)$ and $(M^{\text{tot}}/L)(r)$, and refer to them as $\alpha(r)$ and $\alpha^{\text{tot}}(r)$, respectively. As explained above Υ depends on the mass decomposition but is projected along the line-of-sight (as the SSP measurements are). The directly measured quantity $(M^{\text{tot}}/L)(r)$ is independent of any mass decomposition but its projection is useless as it carries all the DM in the outskirts of the galaxy/model with it.

Values of the main body of each ETG, α_{main} , $\alpha_{\text{main}}^{\text{tot}}$, as well as of the inner regions, α_{cen} are listed in Table 3. As stated before, towards the center, the Υ -gradients become essentially identical to $(M^{\text{tot}}/L)(r)$, and this carries over to α . We show the full $\alpha(r)$ profiles up to r_{main} for all galaxies in Figure 7.

At roughly 1 kpc our dynamical models are on average consistent with the Υ from a Kroupa or Chabrier IMF, $\langle \alpha_{\text{main}} \rangle = 0.94 \pm 0.16$ ($\Upsilon_{\text{Chabrier}} = 0.9 \times \Upsilon_{\text{Kroupa}}$). Considering our total mass profiles, at 1 kpc, a local IMF with a Salpeter level bottom-heaviness is inconsistent with the fits at a level between one and two sigma for all galaxies except NGC 5516 and NGC 4751. We find $\langle \alpha_{\text{main}}^{\text{tot}} \rangle = 1.16 \pm 0.14$.

Interior to 0.3 kpc our dynamical models are on average consistent with the Υ of a Salpeter IMF, $\langle \alpha_{\text{cen}} \rangle = 1.61 \pm 0.15$ ($\Upsilon_{\text{Salpeter}} \sim 1.55 \times \Upsilon_{\text{Kroupa}}$). A Salpeter-level bottom-heaviness is consistent with our dynamical models for all but one galaxy, the least massive galaxy in our sample, NGC 307. For more than half of the sample

levels of bottom-heaviness up to a “heavyweight” $\alpha = 2$, are consistent with the fits at a one sigma level.

4.1.2. IMF variation with galaxy σ

Many previous studies of the IMF using various methods found a trend between α and galaxy velocity dispersion σ which suggests that galaxies with higher σ have higher α . The majority of existing α determinations are based on models without gradients. Different measurements are also derived over different spatial scales. SSP probes typically focus on the very center of a galaxy, i.e. within $r_e/8$. Dynamical probes, by tendency try to capture as much of the galaxy as possible within r_e . Apertures of gravitational lensing probes are identical to the observed Einstein rings, θ_{Ein} , and lie usually in between SSP and dynamics measurements in terms of spatial coverage. Lyubenova et al. (2016) found that part of the tension between different IMF probes could be alleviated by matching apertures. Here we address the question what trends with σ our α -gradient models produce for different apertures.

To this end we compare light-weighted averages of our α profiles³ and σ to different IMF probes from the literature while adapting our aperture sizes to the respective comparison sample.

First, in Figure 8 we compare our α measurements on both small and large spatial scales. In the left panel of the Figure we consider the “overall” IMF of the galaxy. By this we mean the light-weighted average α within an isophote with a circularized radius $r_{ap} > r_{main}$ (see below). We compare this α to stellar dynamical α -measurements from ATLAS^{3D} (Cappellari et al. 2013b) and dynamics+lensing measurements from SLACS, as well as lensing measurements from the SNELLS lensing survey (Smith et al. 2015; Newman et al. 2017). For the SLACS sample we use the updated values from Posacki et al. (2015). We also show the quadratic $\alpha - \sigma$ relation from Posacki et al. (2015) which simultaneously fits the ATLAS^{3D} and updated SLACS measurements.

The ATLAS^{3D} values were determined for an aperture of $r_{ap} = r_e$. The SLACS values are a combination of stellar dynamics and strong lensing constraints and the average θ_{Ein} is roughly $r_e/2$. Thus, they still probe similar spatial scales. The SNELLS lens-measurements on the other hand probe more confined absolute scales, $\theta_{Ein} \sim 2$ kpc, which translates into $\sim 20 - 70\%$ of r_e depending on the galaxy’s distance.

For the comparison with our measurements, these varying spatial scales are not a problem, however. The gradients which we found are so spatially concentrated,

that between $r_{ap} = 1$ kpc and $r_{ap} = r_e$, the integrated α changes on average by less than 4% for all galaxies in our sample (we find similarly small changes with aperture past 1 kpc for σ). Since $\alpha(r)$ seems to correlate well with physical radius we here use $r_{ap} = 2$ kpc (average extent of the SNELLS lenses).

On the $\alpha - \sigma$ diagram for the overall galaxy-wide IMF, our gradient models appear to follow a different, much less bottom-heavy trend than the ATLAS^{3D} and SLACS galaxies. Six out of seven of our sample galaxies are more massive than $\sigma = 250$ km/s, yet our sample scatters around a MW IMF normalization $\alpha = 1.03 \pm 0.33$ (or $\alpha = 1.15 \pm 0.17$ if we do not count the outlier NGC 1407), whereas the relation of Posacki et al. (2015) predicts a Salpeter or above-Salpeter level bottom-heaviness, $\alpha \gtrsim 1.55$ for $\sigma > 250$ km/s. However, our gradient models agree well with the SNELLS lensing results, which find a MW-level normalization even for ETGs with $\sigma > 250$ km/s.

In the right panel of Figure 8, we compare the bottom-heavy centers $r_{ap} = r_{cen}$ of our models to SSP IMF probes from the MASSIVE survey (Gu et al. 2022), as well as from Conroy & van Dokkum (2012), since their probes are also focused on the centers of the ETGs. van Dokkum et al. (2017) also measured radial IMF gradients for a set of six ETGs using SSP models. We here add the centermost α values from these gradients to the diagram.

For the most part, within the uncertainties our central α -values seem to be consistent with the SSP trends of the MASSIVE, Conroy & van Dokkum (2012) and van Dokkum et al. (2017) samples, which also agree with the dynamics-based trend of Posacki et al. (2015) (despite the latter originating from measurements from much larger apertures).

There is, however, a distinct band of galaxies with extremely bottom-heavy SSP measurements $\alpha \gtrsim 2.5$. Among these galaxies is also NGC 1407 whose SSP-measured $\alpha = 3$ is much larger than our central $\alpha = 1.76 \pm 0.516$. Since on the relevant spatial scales uncertainties in the mass decomposition are insignificant, the dynamical and SSP measurements are hard to reconcile. This is indicative of a still unresolved broader problem of matching SSP and dynamical measurements of Υ on the level of individual galaxies (Smith 2014; McDermid et al. 2014).

Nonetheless, considering the overall trends, the two panels of Figure 8 could be seen to imply that our models are in agreement with SNELLS lensing results (at large scales) and SSP modeling results (at small scales) and at tension with dynamical measurements from ATLAS^{3D}

³ We here assume that $\alpha(r) = \alpha_{main}$ for $r > r_{main}$

and SLACS. However, there are unaccounted differences between the measurements which we discuss in Figure 9.

As we stated in the previous section (and as also discussed by Bernardi et al. 2018; Domínguez Sánchez et al. 2019), if $\Upsilon(r)$ intrinsically rises towards the center, this biases α high for models without gradients. With the exception of the SSP measurements by van Dokkum et al. (2017), all of the literature measurements we showed here were based on the assumption of gradient-free Υ .

Hence, for a more consistent comparison, the left-hand panel of Figure 9 compares the dynamical measurements from ATLAS^{3D}, SLACS, and SNELLS to our own gradient-free models. As stated above, these models provide worse fits to the kinematics than models with gradients and are here used merely to understand where the differences between the various IMF determinations could arise from. We also add recent Schwarzschild-based constant- Υ measurements of the ETGs NGC 1600, Holm 15A and NGC 5419 (Thomas et al. 2016; Mehrgan et al. 2019; Neureiter et al. 2023b). The figure confirms that models with a spatially constant Υ lead to higher α . Thus they are more consistent with the measurements from ATLAS^{3D} and SLACS, as expected. However, our measurements are still on the lower side of those distributions. This may be an artefact of our small sample size. It may also be due to the differences in the modelling approach. The ATLAS^{3D} and SLACS measurements were determined using Jeans an-isotropic modeling (JAM; Cappellari et al. 2007a; Cappellari 2008) while we use Schwarzschild models. Schwarzschild models provide the most general solutions to the Collisionless Boltzmann Equation which governs the dynamics of stars in galaxies. We have shown that using adaptive regularisation, our generalised model selection and non-parametric LOSVDs, Schwarzschild models allow for very accurate mass reconstructions (Lipka & Thomas 2021; Thomas & Lipka 2022; Neureiter et al. 2023a; de Nicola et al. 2022).

Considering the central regions of our models, in the right-hand panel of Figure 9 we repeat the same diagram as in the right panel of Figure 8 but take the *exact* aperture of the SSP measurements, $r_{ap} = r_e/8$. Over this aperture, our gradient models for all galaxies except NGC 4751 are similarly offset with respect to the SSP measurements from MASSIVE and Conroy & van Dokkum (2012) as they are for a 2kpc aperture to the dynamical measurements from SLACS and ATLAS^{3D} (cf. left panel of Figure 8). This demonstrates again how concentrated our gradients are. Adding once again the *actual* constant- Υ models for our galaxies to the diagram, we find the same results as for the dynamical, galaxy-wide comparison: Broadly consistent with pre-

vious trends within the uncertainties, but with α that tend to be lower overall.

We might summarize the contents of Figures 8 and 9 as follows: In the centers of the galaxies, our Schwarzschild dynamical Υ -measurements reveal increased levels of stellar mass that confirm and agree with previously suggested mass normalization factors larger than that of a Kroupa IMF in ETGs. Most likely, this mass excess points to a bottom heavy IMF in the centers (but see Section 4.4). The gradients are so centrally concentrated, however, that already for apertures of only $r_{ap} = 2$ kpc the mass enhancement disappears and the IMF converges to a Kroupa level, consistent with measurements in nearby lenses. This largely alleviates the differences between previous studies. Not accounting for existing centrally rising gradients of Υ biases α high – for some galaxies high enough to ostensibly yield a Salpeter-level α . However, there remain some inconsistencies. Even when compared on equivalent spatial scales and when matching the use of constant- Υ models, for both small and large apertures, our α values are overall less extreme than previous probes.

4.1.3. Comparison with SSP-based gradients

After having compared the central values of α from our dynamical Υ -gradient models to the central values of the SSP-based Υ -gradient models from van Dokkum et al. (2017), we will now compare the full radial α -gradients with each other. In Figure 10, we show all seven models from our study together with the average α gradient determined by van Dokkum et al. (2017) over the six ETGs of their sample. One galaxy, NGC 1407, is mutual to both studies.

The figure confirms many of the trends we have found in the previous subsections. Both our dynamical models and the SSP models show radial profiles that at large radii converge on a MW-like IMF normalization on average. Both approaches yield an increased mass normalisation near the center around the Salpeter level. However, the dynamical masses are about 1.6 times smaller than the SSP models of van Dokkum et al. (2017) imply. This difference can not be explained by uncertainties in the dynamical mass decomposition, as $\alpha \sim \alpha^{\text{tot}}$ in the center.

For NGC 1407 the discrepancy is even larger: At no radius is the dynamical profile consistent with the extremely bottom-heavy α profile measured by van Dokkum et al. (2017). At the radius where the total dynamical mass-to-light ratio reaches its minimum, the dynamical models yield a very low stellar mass normalisation $\alpha_{\text{main}} = 0.30 \pm 0.19$ whereas the SSP models produce a “heavyweight” normalisation of $\alpha \sim 2.5$.

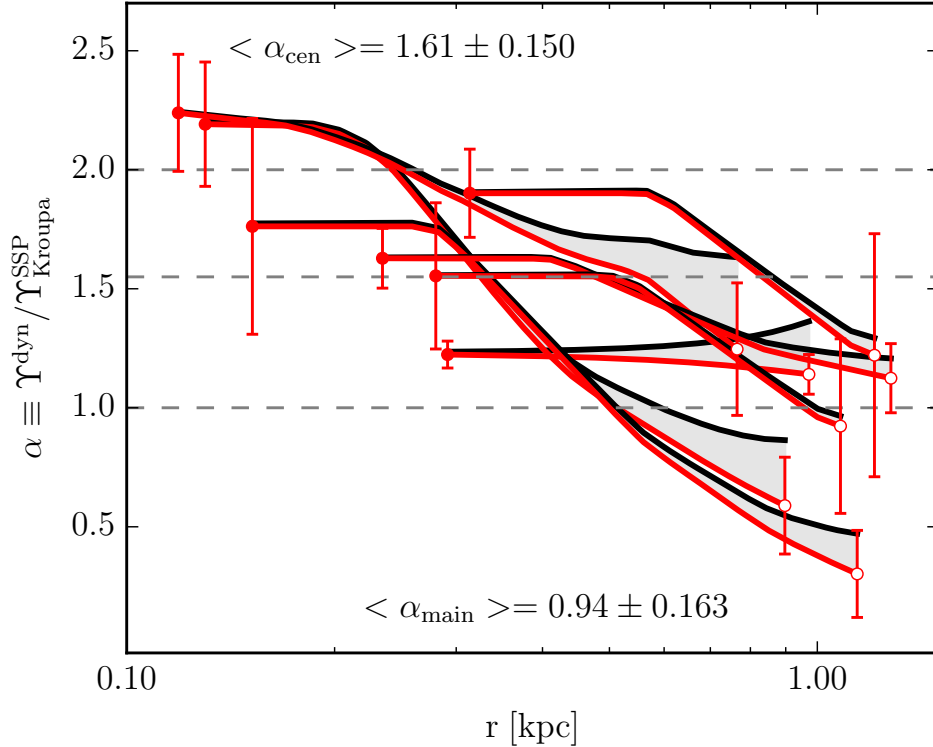


Figure 7. Profiles of the mass normalization $\alpha(r)$ of our dynamical mass-to-light ratio profiles relative to a Kroupa IMF. Normalization profiles of the stellar mass component Υ are shown in red and those relative to the entire dynamical M^{tot}/L in black. Stellar and total α profiles for the same galaxy are connected by grey shaded areas. Grey horizontal dashed lines indicate Kroupa, Salpeter and “heavyweight” IMFs ($\alpha = 1, 1.55$ and 2 , respectively). We highlight the two ends of the gradients, α_{cen} and α_{main} (Table 3), with (red) filled and open symbols, respectively. Uncertainties of the total mass profiles are comparable to those of the stellar component. The gradients are spatially very concentrated and confined to the central kpc of the galaxies. The gradients are plotted up to the point where the total dynamical M^{tot}/L has its minimum. This point constrains the α_{main} of the main body of the galaxy strongest (see text for details).

Even considering the total dynamical mass, this value remains surprisingly high compared to the dynamical $\alpha_{\text{main}}^{\text{tot}} = 0.48 \pm 0.18$. This does not appear to be a problem originating from our gradient models per-se, as even our dynamical models without gradient result in a low $\alpha = 0.66 \pm 0.044$ consistent with the gradient models within the uncertainties. In principle, the lower dynamical Υ could be matched with the very bottom-heavy IMF of van Dokkum et al. (2017) by increasing the low-mass cut-off of the IMF. However, the central IMF of the galaxy was also studied with non-parametric IMF-models in a companion SSP analysis (Conroy et al. 2017). This study suggests that the low-mass IMF slope remains very steep down to $0.1 M_{\odot} (dN/dM_{\star} \propto M_{\star}^{-2.7})$.

In Section 4.2 we suggest that our dynamical models of NGC 1407 could be partly biased by the galaxy being triaxial. On the other hand, however, we already noted that NGC 1407 is among the handful of galaxies for which the SSP analysis results in distinctly high mass normalizations (Figure 8). Even if triaxiality might bias the dynamical analysis by up to factor of 2 in extreme

cases (Thomas et al. 2007a) it seems unlikely that this can explain the entire difference between our dynamical models and the SSP analysis (which amounts to a factor of ~ 5).

A similar case is the massive ETG NGC 1600: the Schwarzschild models of Thomas et al. (2016) produce a MW-like $\alpha = 1.1 \pm 0.24$ which is consistent with our results for similar core galaxies presented here (though the models of Thomas et al. 2016 are without gradients). However, this low mass normalisation is at tension with the gradient SSP-models of van Dokkum et al. (2017) that point to a Salpeter-level or higher bottom-heaviness at most radii and with the gradient-free models of Gu et al. (2022) (who found a super-Salpeter normalisation $\alpha = 1.67 \pm 0.16$).

4.2. Evaluation of uncertainties

Our new state-of-the-art dynamical models yield very spatially concentrated gradients together with an almost Kroupa-like mass normalisation for the galaxies outside the center. We have seen that taking into account aper-

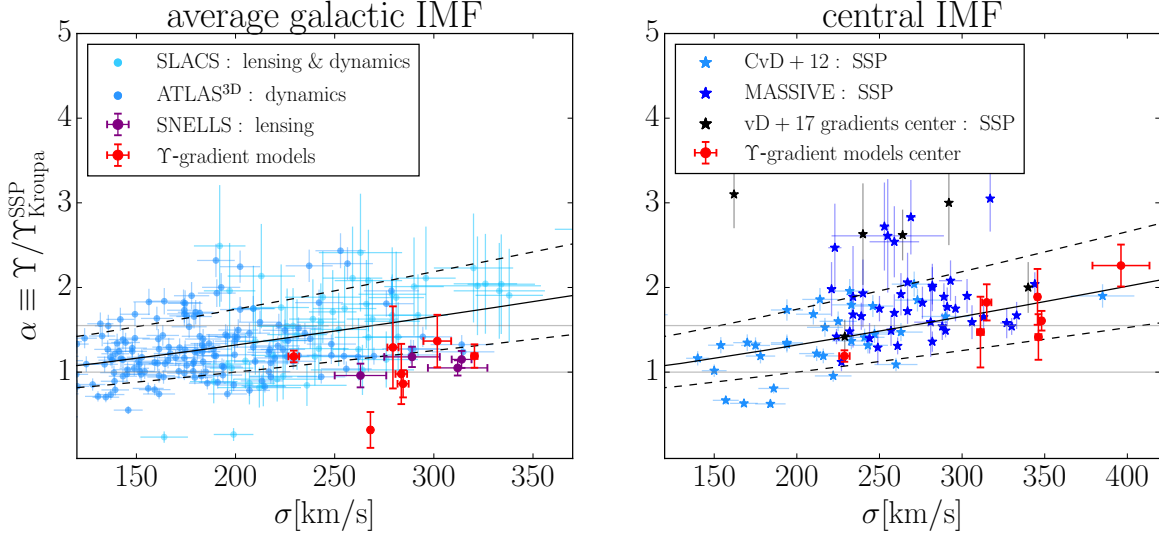


Figure 8. Comparison of our dynamical $\alpha(r)$ and velocity dispersion σ within different apertures (red), compared to different IMF probes. Left: Light-weighted averages of our $\alpha(r)$ and σ for an aperture of 2 kpc compared to α measurements from the ATLAS^{3D} (Cappellari et al. 2013b), SLACS (Treu et al. 2010; Auger et al. 2010; Posacki et al. 2015), and SNELLS (Smith et al. 2015; Newman et al. 2017) surveys. Right: the innermost α and σ of our models compared to the SSP measurements of (Conroy & van Dokkum 2012) and from the MASSIVE survey (Gu et al. 2022). We also show central α -measurements from the α -gradient models of van Dokkum et al. (2017). In both panels the solid/dashed black lines shows the quadratic $\alpha - \sigma$ relation from Posacki et al. (2015) and its scatter. Horizontal light-grey lines indicate Kroupa- and Salpeter-levels of bottom-heaviness. Both panels taken together illustrate how spatially concentrated the detected gradients are: already over scales of only 2 kpc (left panel) the central high α seen in the right panel are washed out and the IMF becomes Kroupa-like, consistent with nearby strong lenses.

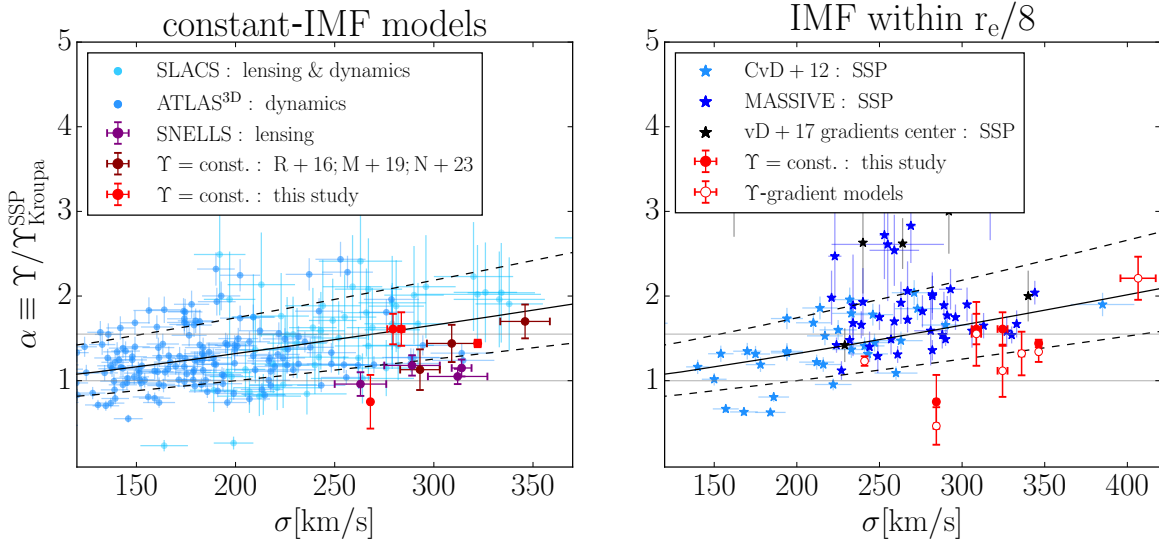


Figure 9. Same as Figure 8, but for comparison models without gradients (left, only for the four galaxies for which we generated constant- Υ models), to which we add recent constant- Υ Schwarzschild models of Thomas et al. (2016); Mehrgan et al. (2019), and Neureiter et al. (2023b) (here T+16, M+19, and N+23). For NGC 5328 from our new models (at $\sigma \sim 325$ km/s), the errorbars are of similar size as the scatter point. For the right-hand panel we consider an aperture of $r_e/8$, instead of r_{cen} for α and σ for our models (the literature data remains unchanged from the right panel of Figure 8). Models without gradients not only fit the data worse but lead to an overestimation of the stellar mass. Still, even without gradients our stellar mass normalisation α derived with state-of-the-art Schwarzschild models is on the low side of previously found distributions. Within $r_e/8$ the spatially very confined dynamical gradients are already partly washed out and the mass normalisation is on average lower than in Figure 8 (right).

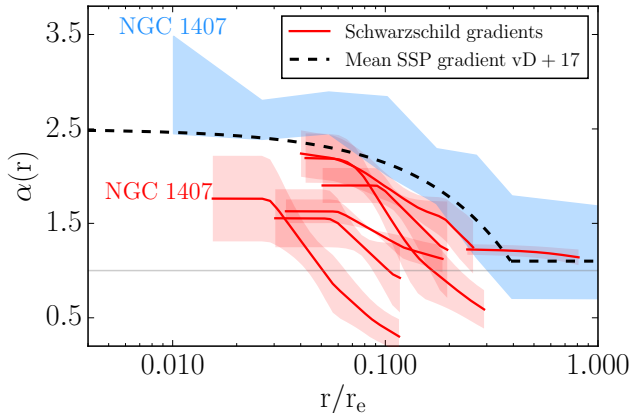


Figure 10. Comparison of the IMF normalization α of our Schwarzschild dynamical Υ -gradients (red lines, with red shaded areas indicating uncertainties) to the mean SSP-based gradient of van Dokkum et al. (2017, black dashed curve). We also show the SSP-based gradient with uncertainties for NGC 1407 (light blue area), which is also in our sample. While the resolved dynamical and SSP gradients both indicate an increase in α towards the center, the dynamical gradients are steeper, more centrally concentrated, and have a lower mass normalisation. For NGC 1407 the two approaches yield inconsistent results.

ture effects and gradients can bring different IMF probes closer together that at first glance seem to yield inconsistent results. In this section we discuss some of the possible systematics which could contribute to the remaining inconsistencies between methods.

Generally, there is the potential of a bias towards high α in some of the SSP models to which we have compared our dynamical results here. Such a bias could arise from incomplete stellar libraries. If for instance, elemental abundances associated with certain IMF-sensitive features such as Na I were underrepresented in the stellar modeling libraries of low-mass dwarf stars, more of them would be needed to reproduce this feature in observed spectra, driving up the measured bottom-heaviness. A more detailed discussion of stellar population uncertainties will be given in the companion paper by Parikh et al. (submitted to MNRAS). We here focus only on our own dynamical models, though a complete evaluation of the discrepancies of different IMF probes among each other has to take into account the combined effects of biases of all methods.

4.2.1. Input stellar kinematics

As discussed in Section 2.1, MUSE and SINFONI LOSVDs are generally consistent with each other within the uncertainties. Differences still arise due to spatial, spectral, and seeing differences, particularly as the SINFONI kinematics are supported by adaptive optics,

while the MUSE kinematics are limited by natural seeing. We expect the stellar dynamical models to be able to fit both sets equally well as they take the above mentioned differences into account.

Overall, our models were successful in fitting both sets of non-parametric LOSVDs for six out of the seven galaxies, as the values of $(\chi^2 + m_{\text{eff}})/N$ for the fits in Table 2 show (with NGC 4751 being the exception). In particular, the models were generally able to fit MUSE and SINFONI kinematics simultaneously in areas where they spatially overlap, $r \leq 1.5''$. We show individual LOSVD fits for all galaxies in such overlapping regions in Appendix B. In our kinematics paper, M+23, we had noted forms of “hidden template-mismatch” which can not be unambiguously diagnosed from the spectral analysis alone. Since our models were mostly able to reproduce both (independent) LOSVD sets simultaneously at the same spatial locations, it seems that the hidden template-mismatch in our data was low. In M+23 we had taken deliberate steps to render this outcome more likely, as is detailed in that study. Nonetheless we faced some problems for a few galaxies, which we briefly describe here:

NGC 4751: This was the only galaxy in our sample for which $(\chi^2 + m_{\text{eff}})/N > 1$. Moreover, one of the four quadrants even produced a $(\chi^2 + m_{\text{eff}})/N > 3$. This anomalous quadrant was also an outlier in terms of the best-fit model parameters (see the last plot of Figure 5). We therefore excluded this quadrant from our analysis entirely. However, the large $(\chi^2 + m_{\text{eff}})/N$ value in Table 2 was already derived without this quadrant. The main limitation here appears to be dust contamination of the LOSVD signal. As described in Section 2.2 and Appendix A, most of the major axis of the galaxy is covered with dust all the way to the effective radius on both sides of the center of the galaxy. Our imaging data was derived in the K-band and the most severely contaminated regions were masked before the photometric decomposition. The SINFONI LOSVDs were derived in the infrared. The MUSE kinematics by contrast were measured in the optical and therefore potentially more affected by dust. In general, the presence of dust in a galaxy should not affect the symmetry of the LOSVDs, only emphasise the LOSVD signal from some part of the galaxy more than others – those parts of the LOSVD which originate from behind the dust along the line-of-sight being dampened. This is consistent with both asymmetric spatial variation and biases of even order Hermite moments if the LOSVDs are parameterized with Gauss-Hermite polynomials. In Appendix B, we discuss to to what extent the LOSVDs are likely distorted by the dust in terms of h_4 .

To what extent our dynamical models of NGC 4751 might be biased by dust cannot be evaluated easily. To be conservative, we quote our sample-averaged IMF normalization measurements *without* NGC 4751: $\langle \alpha_{\text{cen}} \rangle = 1.54 \pm 0.15$, $\langle \alpha_{\text{main}} \rangle = 0.91 \pm 0.172$, and $\langle \alpha_{\text{main}}^{\text{tot}} \rangle = 1.13 \pm 0.142$. However, our previous conclusions on IMF gradients remain essentially the same even without NGC 4751.

NGC 7619 (and NGC 5516): While we can successfully fit the MUSE and SINFONI kinematics for NGC 7619 for the majority of our spatial coverage, there are some small problems at the largest and smallest radii of the MUSE data (the SINFONI data is reproduced well over the full SINFONI coverage, see Figure 13). At large radii ($r > 20''$) the h_4 of our models rises towards the edges of the MUSE FOV, whereas the MUSE data appears to follow the opposite trend. Within $2''$, our models underpredict the dispersion of the MUSE data (while reproducing all of the SINFONI data correctly). This could be indicative of a bias in the MUSE LOSVDs arising from the aforementioned hidden template mismatch. Whatever the cause of these differences between the model and the MUSE data, they are comparatively small as evidenced by non-parametric LOSVDs themselves, as seen in Figure 12 (which, after all are the target and deciding factor of our dynamical models). Furthermore, the reduced χ^2 for our dynamical fits are still favourable (see Table 2). Similarly, but less significantly the dynamical models for NGC 5516 underpredict the centermost MUSE σ value, and h_4 within 3 arcsecond. However, once again, the difference in the nonparametric LOSVDs themselves is small.

NGC 5328 is a galaxy where fitting both data sets, MUSE and SINFONI, simultaneously turned out to be particularly difficult. For this galaxy one of two CO band-heads – the spectral features on which the SINFONI kinematics for all galaxies were based – was obstructed by residual OH emission, limiting the accuracy of the SINFONI LOSVDs to an extent such that the central LOSVDs were assumed to have a Gaussian shape (R+13). We thus used the Gaussian fits from R+13 as the input SINFONI LOSVDs and not the original non-parametric LOSVDs. That the shape of these LOSVDs (Gaussian) is not consistent with the measured shape of the MUSE LOSVDs is not surprising. This could have biased our determination of M_{BH} , but the inclusion of the SINFONI kinematics (basically the velocity dispersion scale) still provided vital constraints on the recovery of the $\Upsilon(r)$ profile (Appendix B).

4.2.2. Assumption of Axisymmetry

We have here dynamically modeled the sample galaxies under the assumption that they are axisymmetric systems. For galaxies with strongly ordered velocity fields like the fast rotating power-law galaxy NGC 307 or even the “intermediate” rotator NGC 7619, which has the most symmetric velocity field of all our cored ETGs, this assumption is generally justified. However, cored ETGs as a whole must have triaxial shapes in general (e.g. Bender 1988; Kormendy & Bender 1996; Cappellari et al. 2007b; Emsellem et al. 2007).

The potentially negative effects of triaxiality on the accuracy of axisymmetric models are generally viewing angle and shape dependant (e.g. Thomas et al. 2007a; van den Bosch & de Zeeuw 2010). Thomas et al. (2007a) find that the mass-to-light ratio of triaxial galaxies can be underestimated in axisymmetric models by as much as a factor two. The effects of triaxiality in the case of mass-to-light ratio gradients have not been investigated yet. However, a factor of two bias holds only in extreme cases. For example, axisymmetric Schwarzschild models of the triaxial galaxy M87 from Gebhardt & Thomas (2009), using an earlier version of our modeling code, determined a SMBH mass of $M_{\text{BH}} = (6.4 \pm 0.4) \times 10^9 M_{\odot}$, which was later confirmed by direct imaging of the shadow of the SMBH by the Event Horizon telescope ($M_{\text{BH}} = (6.5 \pm 0.8) \times 10^9 M_{\odot}$, Event Horizon Telescope Collaboration et al. 2019).

While M87 might be special (it appears nearly round in its central regions) such an accuracy is not entirely surprising. Numerical merger simulations suggest that core-formation, which involves the ejection of stars from the center of a forming core by binary SMBHs, preferentially ejects stars on box-orbits from the center of merger remnants, which essentially “removes” triaxiality from within the core break-radius r_b (Frigo et al. 2021). This means that even in the centers of core galaxies there is no a priori reason to expect axisymmetric gradient models to be particularly biased.

In addition to triaxiality, allowing for Υ -gradients poses new challenges. E.g. the extended parameter space and the larger freedom in the stellar mass distribution might cause degeneracies or complications that were not yet encountered in models assuming only a single galaxy-wide Υ for the stars.

In order to test for potential systematics in our fits we have fitted mock data based on a realistic numerical N-body simulation from Rantala et al. (2018). Since this simulation was tuned to resemble NGC 1600, it represents quite realistically a massive triaxial elliptical galaxy with a DM halo and SMBH. Specifically, the simulation, as we have set it up here, is a cored ETG with a SMBH of $8.5 \times 10^9 M_{\odot}$ and a $\Upsilon(r)$ gradient that

resembles the gradients of real galaxies. I.e. it consists of an increased $\Upsilon_{\text{cen}}^{\text{sim}} = 2$ inside $r \sim 1 - 2$ kpc that is two times larger than the main-body $\Upsilon_{\text{main}}^{\text{sim}} = 1$ (see Appendix D for details). We model this mock galaxy with exactly the same approach that we use for our observed galaxies.

We find that the input main-body Υ could be successfully recovered ($\Upsilon_{\text{main}} = 0.93 \pm 0.11$ at $r_{\text{main}} = 1.9$ kpc). We have already argued above that we do not expect too strong biases of axisymmetric models around the core region of massive galaxies. This is supported by the result of these mock tests. In addition, the tests show that even when modelling a steep DM halo with a cored profile (i) the main-body mass-to-light ratio is highly robust and (ii) the spatial confinement of the gradient can be well recovered.

The central mass-to-light ratio of the simulation was overestimated by a factor of roughly 1.6 ($\Upsilon_{\text{cen}} = 3.16 \pm 1.13$). As argued above, triaxiality may not be the main driver behind this bias. There are several other reasons, why the central Υ_{cen} is more difficult to measure than the mass in the main body. First, the central potential is dominated by the black hole (in this case $r_{\text{SOI}} \sim 0.5$ kpc $\sim r_{\text{cen}}$) and the stars contribute less and less to the total mass. Second, the line-of-sight is more and more dominated by foreground and background light while the signal from the region physically close to the center is weak. Hence the increased uncertainty in the very central parts of the gradient is not entirely surprising. However, where the bias comes from is not clear yet. We note that the black hole is recovered within one sigma ($M_{\text{BH}} = (7.4 \pm 2.7) \times 10^9 M_{\odot}$). Likewise, the central DM halo mass of the simulation is recovered within 10%.

Overall this stress test leaves the possibility that the central Salpeter mass normalization which we inferred for our sample might actually be an upper limit. We plan fully triaxial gradient models for our galaxies as well as more extended tests with simulations to clarify this issue.

Nonetheless, our finding that the IMF of the sample galaxies becomes MW-like at 1 kpc is a very robust result. As we have seen in Section 4.1, this in itself is already an important step in potentially closing the gap between different IMF probes.

4.2.3. Uncertain cases: NGC 1407 and NGC 1332

Two galaxies in our sample deserve deeper consideration. Firstly, while our axisymmetric dynamical models provided good fits to all available data for all galaxies, there was an problem with fitting our 2D kinematic data for NGC 1407, which we encountered for none of

the other seven galaxies: As shown in Figure 14, our dynamical models, while producing overall excellent fits to the kinematics (see also Table 2 and Figure 3), were unable to reproduce the velocity signal $|v_{\text{rot}}| > 0$ along the minor axis of the galaxy (the y-axis of the maps in the Figure). As a counterexample, in Figure 15, we show kinematic maps of NGC 307, for which the full 2D rotation signal is captured by our dynamical models. The difference lies in the fact that the velocity field of NGC 1407 is visibly distorted, the peaks of v_{rot} not being aligned with the major axis (M+23) and the $v_{\text{rot}} = 0$ line not being aligned with the minor axis but pointing along a diagonal direction outside the central few arcseconds. The full extent of this kinematic pattern cannot be captured by axisymmetric models. Nonetheless, the kinematic signal in each quadrant can be *individually* reproduced by the axisymmetric models. The only exception to this is the rotation directly on the minor axis, which cannot be reproduced with tube orbits. However, in NGC 1407 as well as in all other core galaxies in our sample, the velocity signal is overall very weak and thus carries little of the galaxy’s energy. Hence, mismatch in the rotation can be expected to result only in a small mass bias.

The velocity pattern could be well caused by the galaxy being triaxial. However, the velocity signal is not very strong and we have seen above from the simulation test that triaxiality is not necessarily a driver for strong biases. In fact, our measured SMBH corresponds to a $r_{\text{SOI}} = (2.41 \pm 0.546)''$ consistent with $r_b = 2.01''$ (R+13), as is expected for cored ETGs (Thomas et al. 2016). Furthermore, the core of this ETG (as well as that of the other cored ETGs in our sample), shows the characteristic orbit structure of a core, with the orbital anisotropy parameter β transitioning from positive, i.e. radial anisotropy, $\beta \sim 0.55$ outside the core region to negative, i.e. tangential anisotropy, $\beta \sim -0.55$ within the core. This is predicted by numerical simulations of core formation (Rantala et al. 2018). We therefore consider the central $\langle \alpha_{\text{cen}} \rangle$ of NGC 1407 robust.

However, at large radii the IMF normalisation in NGC 1407 is worryingly low, even considering uncertainties in the mass decomposition, $\alpha_{\text{main}}^{\text{tot}} = 0.44 \pm 0.18$. “Worrying”, because the outer parts of massive galaxies are thought to be assembled from material of less massive galaxies and satellites – objects for which a MW-like IMF is strongly expected. Therefore, either we have accidentally detected a rare bottom-light IMF at r_{main} and $\Upsilon(r)$ rises again past r_{main} to $\alpha \sim 1$ (so that the Υ profile rises at both ends), or – more likely – our dynamical model is somewhat biased. Strong triaxiality (stronger than in the tested simulation) could

in principle explain such a low mass normalisation. Another possibility might be that the distortions in the velocity field do not originate from triaxiality but instead the galaxy might be slightly out of equilibrium (e.g. due to a recent merger). In any case, we revise the sample-average of the outer IMF normalization from Section 4.1 by excluding this ETG from the calculation, $\langle \alpha_{\text{main}} \rangle = 1.05 \pm 0.18$ ($\langle \alpha_{\text{main}}^{\text{tot}} \rangle = 1.25 \pm 0.15$). Excluding also NGC 4751, we find $\langle \alpha_{\text{main}} \rangle = 1.03 \pm 0.19$ ($\langle \alpha_{\text{main}}^{\text{tot}} \rangle = 1.23 \pm 0.15$). However, the conclusions of our study remain unchanged.

The second galaxy that deserves closer inspection is NGC 1332. While we have tested our setup on a (static) triaxial merger remnant, real galaxies can be even more complex and involve a rotating gravitational potential. Specifically for NGC 1332, we had inferred the possible presence of an end-on bar from a comparison of the galaxy’s 2D stellar kinematics with the kinematical signature of boxy/peanut bulges of simulated disk galaxies from Iannuzzi & Athanassoula (2015) (see Section 6.3 of M+23 for a detailed discussion).

For the dynamical fits, we did not encounter any significant issues with reproducing both the MUSE and SINFONI LOSVDs for this galaxy (see Figs. 12 and 13), which is also evidenced by the value of $\langle (\chi^2 + m_{\text{eff}})/N \rangle = 0.76$.

While the main body $\alpha_{\text{main}} \sim 0.6$ is also somewhat low for this galaxy, considering the total $\alpha_{\text{main}}^{\text{tot}} \sim 0.9$, the difference to a MW IMF can easily be attributed to the uncertainties of the dynamical mass decomposition.

We have here used the M_{BH} of Barth et al. (2016) from the circumnuclear gas disc detected with ALMA, for which they measured $v_{\text{disk}} \sim 450 - 400 \text{ km/s}$ at $r \sim 1''$. Not fixing the central black hole to the value of Barth et al. (2016) produces a $M_{\text{BH}} = (1.58 \pm 0.43) \times 10^9 M_{\odot}$, which would be consistent with our results from R+13, but in excess of the ALMA M_{BH} by a factor of two. At $1''$ this higher- M_{BH} model would imply a circular velocity $v_{\text{circ}} \gtrsim 500 \text{ km/s}$ which is higher than the ALMA measurements and a central stellar mass normalisation that would be smaller by a factor 1.3, though still above Salpeter, $\alpha_{\text{cen}} = 1.65 \pm 0.49$. While it is possible that the ALMA measurement is biased low, the higher spatial resolution of the ALMA data makes it more plausible that the mismatch is due to an end-on bar which our current models do not account for.

However, for the models which we present here and use the ALMA M_{BH} , the circular velocity at $1''$, $v_{\text{circ}} = (459 \pm 43.3) \text{ km/s}$ is consistent with the ALMA data. Moreover, the stellar Υ derived by Barth et al. (2016) is consistent with the central value of our gradient models (Figure 5). For all these reasons from our dynamical

point-of-view, we see little reason to discount our measurements of Υ_{cen} at this stage.

4.2.4. Can DM explain the Gradients?

In our simulation tests in Section 4.2.2, we have demonstrated that our assumption about the inner slope of the DM halo has no significant influence on the recovered stellar mass-to-light ratio. Cappellari et al. (2012) also found that the dynamically inferred increased stellar mass normalizations of massive elliptical galaxies do not depend strongly on the assumed DM halo profile.

Of course, under extreme assumptions this independence breaks down. In particular, if one considers a component of dark matter that follows the light and thus would become indistinguishable from stellar mass. Such a component could explain our central measured mass excess $\langle \alpha \rangle \sim 1.5$ while the IMF would still be Kroupa in all galaxies at all radii. On average, the fraction of mass in our fitted DM components is about three percent at $r_{\text{main}} \sim 1 \text{ kpc}$. Considering the values of $\alpha_{\text{main}}^{\text{tot}}$ at that radius (see Table 3), we can see that even if we assume that all the dynamical mass in excess of a Kroupa stellar mass would be dark matter, the DM fraction would still remain low. Hence, if we also assume that the IMF is Kroupa in the very centre, the DM fraction would have to rise from three to almost *fifty* percent over a mere 1 kpc towards the galactic center. This would be difficult to explain.

In summary, there is no reason to believe that our dynamical gradients are biased towards a centrally increasing stellar mass-to-light ratio due to our adopted DM halo profiles. In case of an exotic DM component that follows the light, a Kroupa IMF in all galaxies at all radii would still be consistent with the data though unlikely (but see Section 4.4).

4.3. Origins of bottom-heavy galactic centers

In the following, we briefly speculate as to possible origins of the bottom-heavy IMF which we have potentially measured in the centers of the galaxies.

If the IMF is different in the centers of ETGs, necessarily, the conditions and/or mechanisms of the originating starbursts of the stellar populations had to be very different from those found in any environment in the MW.

Recent studies have proposed that the conditions in the centers of ETGs when they were first assembled, $z \gtrsim 2$ were unlike any environment found in the MW. In this picture, massive compact galaxies, which are up to 60 times denser than local ETGs and virtually absent from the local universe are the progenitors of the centers of massive ETGs. It is proposed that they

have formed on very short times scales from the in-fall and compaction of cold gas triggering intense in-situ star-formation, followed by extreme quenching from stellar- and/or AGN feedback, turning them into “red nuggets”. Around these nuggets stellar components accumulate via merger- and accretion-driven inside-out-growth, forming what will become local ETGs (Bezanson et al. 2009; Oser et al. 2010; Barro et al. 2013; Nelson et al. 2014; van Dokkum et al. 2015; Zolotov et al. 2015; Barro et al. 2016). It has been suggested that the intense nature of the starbursts which formed these red nuggets, meaning the exceptional intensity of the gravito-turbulent fragmentation of the in-falling gas, where radiation pressure is ramped up by the rate of star-formation, competing with gravitational collapse, could have created a relative excess of low-mass dwarf stars in the centers of ETGs (e.g. Lasker et al. 2013; Chabrier et al. 2014; Belli et al. 2014; van de Sande et al. 2013).

While this matter remains speculative, the fact that the correlation of α with [Mg/Fe] has been found to be tighter than with σ (Conroy & van Dokkum 2012), has been seen as indication that rapid starbursts are correlated with the excess production of dwarf stars, as the above scenario also suggests. In our companion paper (Parikh et al. submitted to MNRAS), however, we show that while all galaxies in our sample are strongly enriched in [Mg/Fe], [Mg/Fe] $\sim 0.3 - 0.4$, we do not find radial gradients for this abundance. The [Mg/Fe] - α correlation has also been called into question by other studies (Smith 2014; La Barbera et al. 2015).

On the other hand, if the above formation scenario for ETGs holds true, we would expect central gradients of the IMF to correlate more with physical radius than radius relative to r_e (as the outer parts were assembled later on), which, as we have shown, is the case for our models. This had also previously been suggested by van Dokkum et al. (2017).

The main conceptual problem with this framework is our understanding of the merger hierarchies of massive ETGs: High-mass ETGs are thought to have assembled from dry major mergers of less massive ETGs (e.g. Niето & Bender 1989; Kormendy & Bender 1996; Hopkins et al. 2009; van der Wel et al. 2009; Lauer 2012; Kormendy & Bender 2013). Numerical merger simulations suggest that in dry major mergers the compact central regions of the progenitors sink to the center where a SMBH binary sling-shots stars to larger radii and forms a (cuspy) core Rantala et al. (2018, 2019). If the merger is wet, the new-born core is “covered up” by new star formation, which we expect to produce stars in line with a MW IMF (since the conditions around nugget-formation

have past at this point). If the merger is dry, the diluted core remains as-is (e.g. Kormendy & Bender 1996; Kormendy 1999; Kormendy et al. 2009). Either way therefore, we expect that IMF gradients in massive galaxies become less steep the more they merge. We note that the two galaxies with the highest central mass normalizations in our sample, NGC 1332 and NGC 4751, are both power-law galaxies. On the other hand the least massive galaxy in our sample, NGC 307, has the smallest α_{cen} . It remains to be seen if larger samples of galaxies modelled with Υ -gradients support the implied dichotomy between cored and power-law ETGs.

Finally, the fact that our gradients seem to all have the same spatial scale of ~ 1 kpc could point to a characteristic size for the detectable remnants of red nuggets in the centers of ETGs. As of now, it is unclear what physical processes are the driver for the spatial size of our measured IMF gradients.

4.4. On the possibility of top-heavy galactic centers

Similar to the “DM following stars” scenario, BHs could follow the luminous component and explain the high mass normalizations α_{cen} which we found. The only difference here would be that the IMF would then no longer be MW-like, as the BHs would be the remnants of a population of giant stars which made up a much larger fraction of the IMF than in the MW, i.e. the IMF would be top-heavy. This scenario is rarely considered since SSP models cannot probe for top-heaviness, as once the massive stars become remnants they become invisible to spectral analysis. But not to dynamical modeling, which simply measures (enclosed) mass as a function of radius. As such, our results are fully consistent with a central top-heavy IMF – any mass decomposition follows from other assumptions.

There is yet no consensus on the possible origins of this kind of IMF in the centers of ETGs. However, first-epoch JWST NIRCам imaging from the *Cosmic Evolution Early Release Science* (CEERS) Survey has provided some insight into the possibility of an early-universe IMF evolution in this direction: For a sample of galaxies with $z \gtrsim 9$, Finkelstein et al. (2023) have found an excess of UV luminosity per unit halo mass at $z \sim 11$ relative to extrapolations of the UV luminosity function at lower redshifts. They argue that this excess could be accounted for if star formation in these galaxies was dominated by a top-heavy IMF. This, in principle, would be compatible with predictions of the fragmentation of metal-less gas into stars (Bromm & Larson 2004), i.e. with predictions of the IMF in a very low-metallicity environment. Since these galaxies are very compact, $r_e \sim 0.5$ kpc, some of the arguments

that we have used for the possibility of bottom-heavy red nuggets ending up in the centers of massive ETGs would apply for top-heavy progenitors. But would these top-heavy populations remain intact in the centers of ETGs? As with the bottom-heavy centers some level of dilution of the IMF is expected. Particularly if core scouring events on similar spatial scales as these centers are sustained. It is also unclear why the excess of black holes from these populations would not be driven to the very center by dynamical friction and merge with the central SMBH. Nonetheless it will be interesting to see what further probes of the early-universe IMF from the JWST era will uncover on this matter.

5. SUMMARY AND CONCLUSIONS

We have constructed state-of-the-art axisymmetric Schwarzschild models to systematically probe for the existence of IMF variations within seven massive early-type galaxies. Our study utilises novel dynamical techniques to improve the accuracy of the results:

- We consistently use non-parametric LOSVDs both in the center (from AO-based SINFONI data with high spatial resolution to resolve the central SMBHs) and for the galaxy main body (from high-SNR MUSE spectroscopy, [Mehrgan et al. 2023](#)).
- We use mass models that allow for radial gradients of the stellar mass-to-light ratio $\Upsilon(r)$.
- We use a generalized model selection technique to account for the varying model flexibility of Schwarzschild models [Lipka & Thomas \(2021\)](#); [Thomas & Lipka \(2022\)](#).

In previous papers we have shown that using non-parametric LOSVDs and the generalised model selection allows us to break known degeneracies and to avoid potential biases in dynamical models even in the more complex case of triaxial galaxies ([de Nicola et al. 2022](#); [Neureiter et al. 2023a](#)). We showed that with the above improvements dynamical mass determinations at the 10% precision level are possible.

Applying these models, we have found radial gradients of Υ in all seven galaxies, with $\Upsilon(r)$ always increasing towards the center of the galaxies. We have found the following results concerning these gradients:

- Gradients of $\Upsilon(r)$ are concentrated on very small spatial scales of less than ~ 1 kpc.
- The total dynamical mass-to-light of the galaxies has a minimum and this minimum occurs at roughly $r_{\text{main}} \sim 1$ kpc from the center. Under

the assumption that the stellar mass-to-light ratio does not increase with radius this point provides a strong constraint for Υ_{main} in the main body of the galaxies.

- Relative to the stellar mass-to-light ratio of the main body of the galaxy, Υ_{main} , the inner Υ_{cen} increases on average by a factor 2.6.
- Models without gradients fit the data worse and yield Υ -values between the Υ_{cen} and Υ_{main} of gradient models. Since gradients occur on small spatial scales, models without gradients can lead to an overestimation of the stellar mass content of a galaxy by up to a factor of ~ 1.5 .
- Models with gradients yielded M_{BH} that are on average 25% smaller than for constant- Υ models in our sample.

In order to probe for gradients of the IMF, we calculated radial profiles of the IMF mass normalization α relative to SSP measurements assuming a Kroupa IMF. Our probes revealed the following IMF trends:

- At $r_{\text{main}} \sim 1$ kpc we find an IMF normalization which is on average Kroupa-like $\langle \alpha_{\text{main}} \rangle = 1.03 \pm 0.19$. Considering the total mass at this radius, which is independent of any assumption related to the mass decomposition, we find $\langle \alpha_{\text{main}}^{\text{tot}} \rangle = 1.23 \pm 0.15$. A Salpeter-level bottom-heaviness is inconsistent with the dynamics for five out of seven galaxies in our sample at a one- to two-sigma level at this radius.
- In the center of the galaxies we find concentrated regions of increased mass normalizations with Υ -gradients rising to roughly a Salpeter-like normalization, $\langle \alpha_{\text{cen}} \rangle = 1.54 \pm 0.15$.
- In the center, the DM contribution essentially vanishes. Therefore, for many galaxies, there is a spatial interval that is still central enough for DM to be insignificant, but is at the same time outside the SOI of the central SMBH, so that $\alpha \sim \alpha^{\text{tot}}$, i.e. α becomes independent of any assumption related to the mass decomposition. Considering this total dynamical mass, five out of seven galaxies in our sample are consistent with a Salpeter- or higher-level bottom-heaviness of the IMF in the very center.
- Taking into account aperture effects and the difference between models with and without gradients our results produce similar, but overall less

extreme levels of bottom-heaviness compared to many previous studies.

- Not taking into account gradients biases α high.
- The dynamically detected gradients are so spatially concentrated that even within central apertures as small as $r_e/8$ (typical for SSP measurements) aperture effects can affect the comparison.

Our study confirms previous claims in favor of the non-universality of the IMF. The main issue with this claim is that while the different SSP, dynamics and lensing studies all agree on the fact of non-universality, and sometimes the same IMF-trends, they often do not produce consistent results for individual galaxies. [Bernardi et al. \(2018\)](#) and [Lyubenova et al. \(2016\)](#) already suggested that gradients play a crucial role in matching different IMF probes. Our dynamical evidence for very concentrated Υ -gradients makes the necessity of match-

ing spatial apertures for comparisons between different works even more crucial. Moreover, the gradients that we find are so spatially concentrated that taking into account central SMBHs is important.

Modelling larger samples of galaxies with next-generation Schwarzschild models similar to the ones used here and direct comparisons with SSP models galaxy-by-galaxy will be important to constrain the IMF better. We plan to do this in a future paper, also combining gradient models with triaxial symmetry ([Neureiter et al. 2021](#); [de Nicola et al. 2022](#); [Neureiter et al. 2023b](#)).

ACKNOWLEDGEMENT

We acknowledge project/application support by the Max Planck Computing and Data Facility. All dynamic computations were performed on the HPC system Raven and Cobra at the Max Planck Computing and Data Facility.

APPENDIX

A. BULGE/DISC DECOMPOSITION AND DEPROJECTION OF NGC 4751

While we used the same NICMOS2 high resolution imaging as in [Rusli et al. \(2013b\)](#), we supplemented this with more recent large scale K-band imaging from the near infrared camera VIRCAM at the 4m VISTA telescope at La Silla ([Emerson et al. 2006](#); [Dalton et al. 2006](#)). The imaging data consists of two 180 second exposures taken in the context of the VISTA hemisphere survey (Program ID 179.A-2010) and was taken from the ESO archive.

The decomposition was derived from simultaneous fits to the VISTA and HST images using the “multifit” extension of imfit ([Erwin 2015](#)) which allows us to fit the same model to multiple images. There was also very strong dust contamination in the nuclear region and along the major axis (see Figure 11), which we masked during the fit with imfit. The dust disproportionately affects one side from the major axis of the galaxy more than the other. Due to the extent of the dusty regions, covering most of the galaxy’s major axis within r_e , some of the LOSVDs from M+23 for this galaxy, which were derived in the MgB region, are likely affected by them. This is discussed in Section 4.2.1.

Our best fit was formally constructed from 4 components, which are listed in Table 4. We decided to make component 3 the “disc”, as it was the most flattened component, and we combined components 1, 2 and 4 into one “bulge” component.

During the dynamical modeling-process, we sample Υ_{disc} on the same grid as $\Upsilon_{\text{bulge},i,f}$. Therefore, if our decomposition was in error, in the sense of there not being two distinct morphological components in the same way as there are in the other two power-law galaxies in our sample, the modeling can still find a solution which essentially amounts to just fitting one (bulge) component.

As with the other galaxies, we used the algorithm of [Magorrian \(1999\)](#), which utilizes a penalized log-likelihood function to produce 3D non-parametric axisymmetric luminosity density distributions $\nu_{\text{depro}}(\mathbf{r})$ which are consistent

Component	ϵ	PA [°]	n	r_e ["]	% of total light	description
1	0.21	179	3.2	1.1	22.6	nuclear component
2	0.44	175	0.8	3.5	15.9	inner part of the main body
3	0.62	176	1.7	21.9	48.3	outer part of the main body
4	0.23	176	0.8	73.8	13.1	outer envelope

Table 4. Photometric decomposition of NGC 4751 with imfit, showing the ellipticity, position angle, effective radius, and fraction of the total galaxy light for each component. The position angle of the fourth component was fixed to the one of the third.

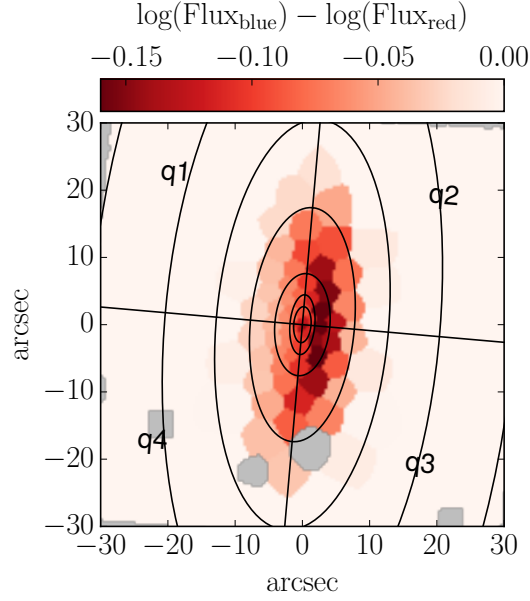


Figure 11. Dust map of NGC 4751, derived from the binned MUSE datacube (M+23) by computing the difference between the logarithms of the integrated flux between $7870 - 8500 \text{ \AA}$ and $4870 - 5500 \text{ \AA}$. Grey areas indicate regions spatially masked during the kinematic analysis (cf. Figure 13 in M+23). The line at $PA = 176^\circ$ indicates the major axis, the line orthogonal to this, the minor axis, while $q1 - q4$ are labels for the quadrants used in the modeling. We also show exemplary isophotal ellipses. The figure shows that every spatial bin of our kinematic input data which lies on the major axis is contaminated by dust all the way to the effective radius $r_e = 22.76''$. The western (right) regions are affected more significantly than the eastern. The south-side of the major axis (bottom) appears to be slightly worse affected than the north-side major axis. This makes q3 the quadrant which is the most affected by dust.

with the 2D input surface brightness profiles, under the assumed viewing angle i . We deprojected NGC 4751 which is close to edge on for $i = 90^\circ$, with the bulge and disc components treated separately.

B. KINEMATIC FITS

In Figure 12 we present LOSVD fits to central MUSE and SINFONI LOSVDs in spatially overlapping regions for all galaxies, except NGC 1407 which we present separately in Figure 3. As discussed in Section 2.1, MUSE and SINFONI LOSVD-sets are generally consistent with each other within the uncertainties. Differences in the shapes of the LOSVDs arise due to spatial, spectral, and seeing differences, particularly as the SINFONI kinematics are supported by adaptive optics. Baring fundamental kinematic inconsistencies with either set, we expect the stellar dynamical models to be able to fit both sets equally well at the same spatial location as the models take the above mentioned differences into account. Fortunately this is the case for our sample, and we produced good fits to both kinematic data sets, $\langle \chi^2 + m_{\text{eff}} \rangle / N \sim 0.8$ (see Table 2), which indicates a low amount of template-mismatch in the MUSE data from M+23, as we discuss in Section 4.2.1.

In Figure 13 we show the full radial kinematic profiles of the MUSE, SINFONI, and dynamical model LOSVDs parameterized by fourth order Gauss-Hermite polynomials for all galaxies. We here add some special notes on the kinematics and kinematic fits of NGC 1332, 4751 and 5328:

NGC 1332: The radial kinematic profiles for NGC 1332 show that we can simultaneously reproduce both the MUSE and SINFONI kinematics over the full spatial coverage of our data, despite the bar-like kinematic signatures noted in M+23. There we had noted a particular h_3 butterfly-shape, which we can see in the radial profile as the crisscrossing of the h_3 -model lines from two sides of the galaxy at around $r \sim 6''$ and $15''$. The only outliers are within $\sim 0.5''$. Here the models slightly underpredict the h_4 of the MUSE data. While the difference appears significant in these figures, it is in fact minuscule when considering the underlying non-parametric LOSVDs (the actual concern of our dynamical models). The LOSVDs belonging to NGC 1332 which we present in Figure 12, are from this problematic region.

NGC 5328: For this galaxy, radial kinematic profiles are also overall good, but within the SINFONI coverage, $r = 1.5''$, the h_4 of the MUSE data is significantly underpredicted by our models, much more so than for NGC 1332. This is due to the obstruction of one of the two CO band-heads from which the SINFONI kinematics were measured. This produced spurious h_3 , indicating that there were either not enough constraints on the *full* LOSVD-shape in the face of possible contamination from sky emission. Therefore R+13 corrected the LOSVDs such that they subtracted the higher order h_3 and h_4 signal, resulting in a suppression of light at higher velocities, which is very much present in our MUSE kinematics. These differences are shown for the non-parametric LOSVDs in Figure 12. There, these differences are also relatively small, but nonetheless show that the MUSE-model LOSVD-signal is suppressed around $v_{\text{los}} \sim \pm 1000$ km/s. This slightly biased the fit to MUSE LOSVDs in the center, as seen in Figure 13, whereas the SINFONI LOSVDs were fit well (since there were more SINFONI LOSVDs within $r = 1.5''$ the latter dominated the fits in the central regions.): Within the SINFONI FOV our MUSE data has $h_4 \sim 0.03 \pm 0.01$. The models however, produce a h_4 that is roughly zero, which corresponds to the h_4 of the SINFONI data/models. As a consequence, the $\langle \chi^2 + m_{\text{eff}} \rangle / N = 0.99$ while still good, is the largest in our sample. The SOI of the SMBH, $r_{\text{SOI}} = (0.50 \pm 0.12)''$, is also the only one amongst our four cored galaxies which is inconsistent with the break-radius of the core, $r_b = (0.85 \pm 0.04)''$. Typically in cored galaxies $r_b \sim r_{\text{SOI}}$ (Thomas et al. 2016). For dynamical models without SINFONI LOSVDs, $\langle \chi^2 + m_{\text{eff}} \rangle / N = 0.93$ becomes lower. However, this produces spurious results: The SMBH and SOI become even less consistent with r_b as M_{BH} becomes significantly smaller, $M_{\text{BH}} \sim 0.7 \times 10^9 M_{\odot}$. The Υ -gradient, at the same time, becomes much steeper, $\Upsilon_{\text{cen}} \sim 9$, $\Upsilon_{\text{main}} \sim 0.6$ (V-Band). This essentially amounts to $\Upsilon(r)$ vanishing entirely into the DM. Put in terms of the IMF, this would mean a far below-MW bottom-light IMF normalization $\alpha_{\text{main}} \sim 0.2$, compared of the perfectly MW-like IMF $\alpha_{\text{main}} \sim 1$ which we found for our full models (see Table 3). As we argue for NGC 1407, such a bottom light outer IMF is extremely unlikely to be physical. We therefore suggest that the use of the AO-assisted SINFONI data might have biased our SMBH measurement, but still provided *necessary* constraints on the larger shape of the Υ -profile, via constraints on the central orbital anisotropy and SMBH. Finally, in M+23, we had noted a small counter-rotating region in the central few arcseconds of our MUSE FOV. Closer inspection of Figure 13 shows that the lines tracking our model- v_{rot} for the MUSE kinematics from two sides of the galaxy cross and switch signs at around $r \sim 3''$ to fit this counter rotating region correctly.

NGC 4751: Considering the distribution of the dust in NGC 4751 (see Figure 11), the dust appears to be somewhat evenly distributed within r_e . However, the distribution of dust is slightly more extended on the south and west side from the center. The quadrant which we had to exclude, q3, is the south western quadrant of the galaxy. The effects of the dust on the kinematics could potentially explain why the $\langle \chi^2 + m_{\text{eff}} \rangle / N$ of our fits was higher in this galaxy. Considering the radial profiles of the dynamic fits parameterized by Gauss-Hermite polynomials (see Figure 13), the

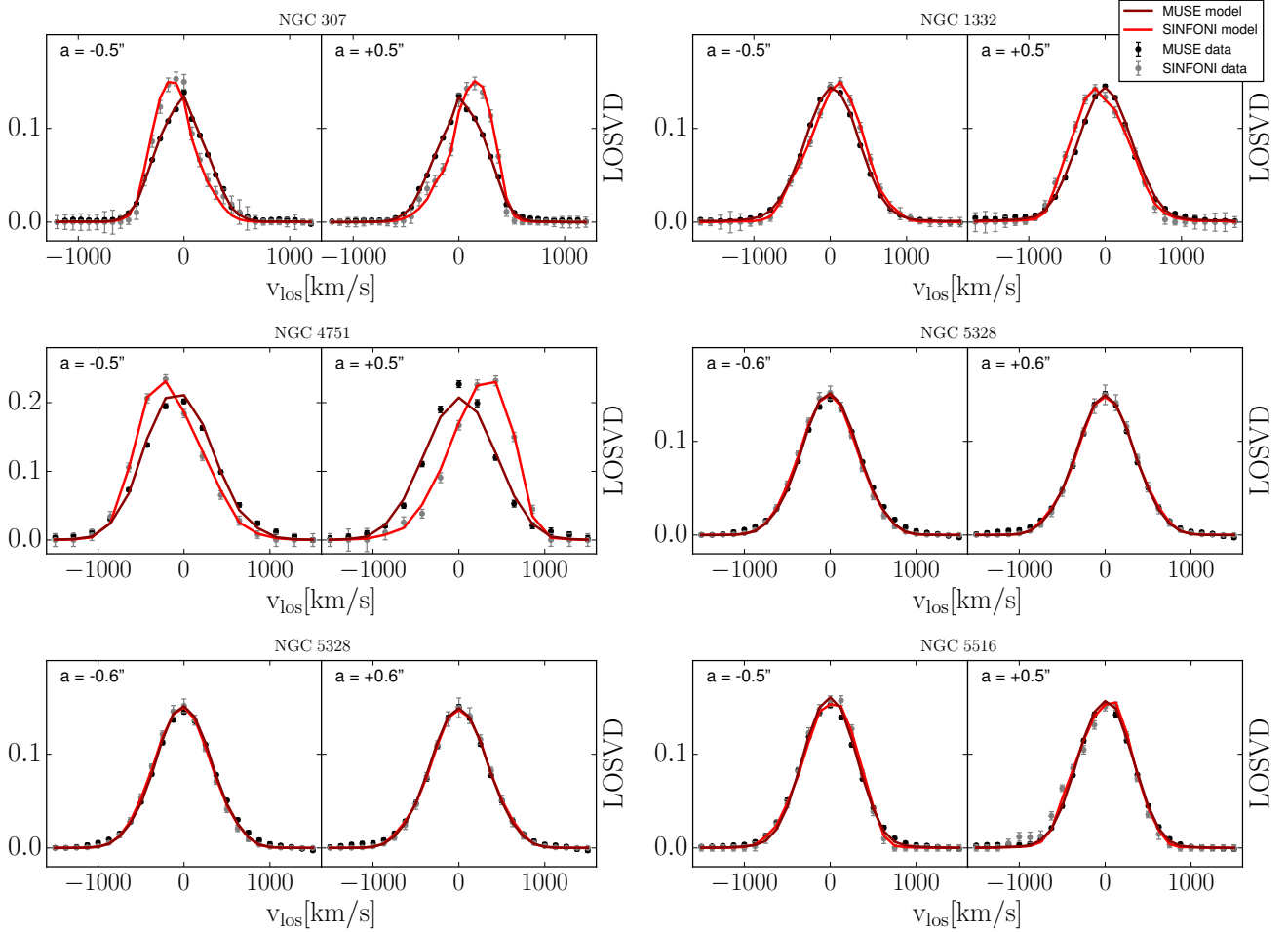


Figure 12. Non-parametric LOSVD fits from the centers of the sample galaxies except NGC 1407, which we present separately in Figure 3. We show spatially overlapping fits to the MUSE and SINFONI LOSVDs along the major axis for a distance a from the center. MUSE data- and model-LOSVDs are shown in black and dark red, respectively, SINFONI data- and model-LOSVDs in grey and light red. All data-LOSVDs are non-parametric, except the SINFONI data of NGC 5328, whose losvds are simple Gaussian LOSVDs (see Section 4.2.1). The uncertainties of these LOSVDs are adopted from the original non-parametric LOSVDs of the SINFONI data for this galaxy.

main problem with the fits appears to be an elevated h_4 signal within the central $4''$ for the MUSE data which the models cannot reproduce. Considering the non-parametric LOSVDs from this region (see Figure 12), we can see that while the fit to the SINFONI LOSVDs is quite good, the models have problems reproducing the LOSVD signal of the peak of the MUSE LOSVDs (roughly between ± 250 km/s). This problem appears to be worse on the side where $v_{\text{rot}} < 0$ (right side), which corresponds to the southern, dustier side of the galaxy. At large radii ($r \sim 20 - 30''$ in Figure 13), there also appears to be some bias in h_3 – a telltale sign of template-mismatch. At the same time h_4 at radii large than $10''$ are biased somewhat low. In the kinematic maps shown in Figure 13 of M+23 it can be seen that this bias towards low h_4 originates from one side of the galaxy, where h_4 becomes overall negative, the south side, whereas the north side has overall positive h_4 . This again makes dust the likely candidate. The large radius template mismatch could also be associated with this, as the template selection was performed in the same spectral region as the main kinematic fits (M+23).

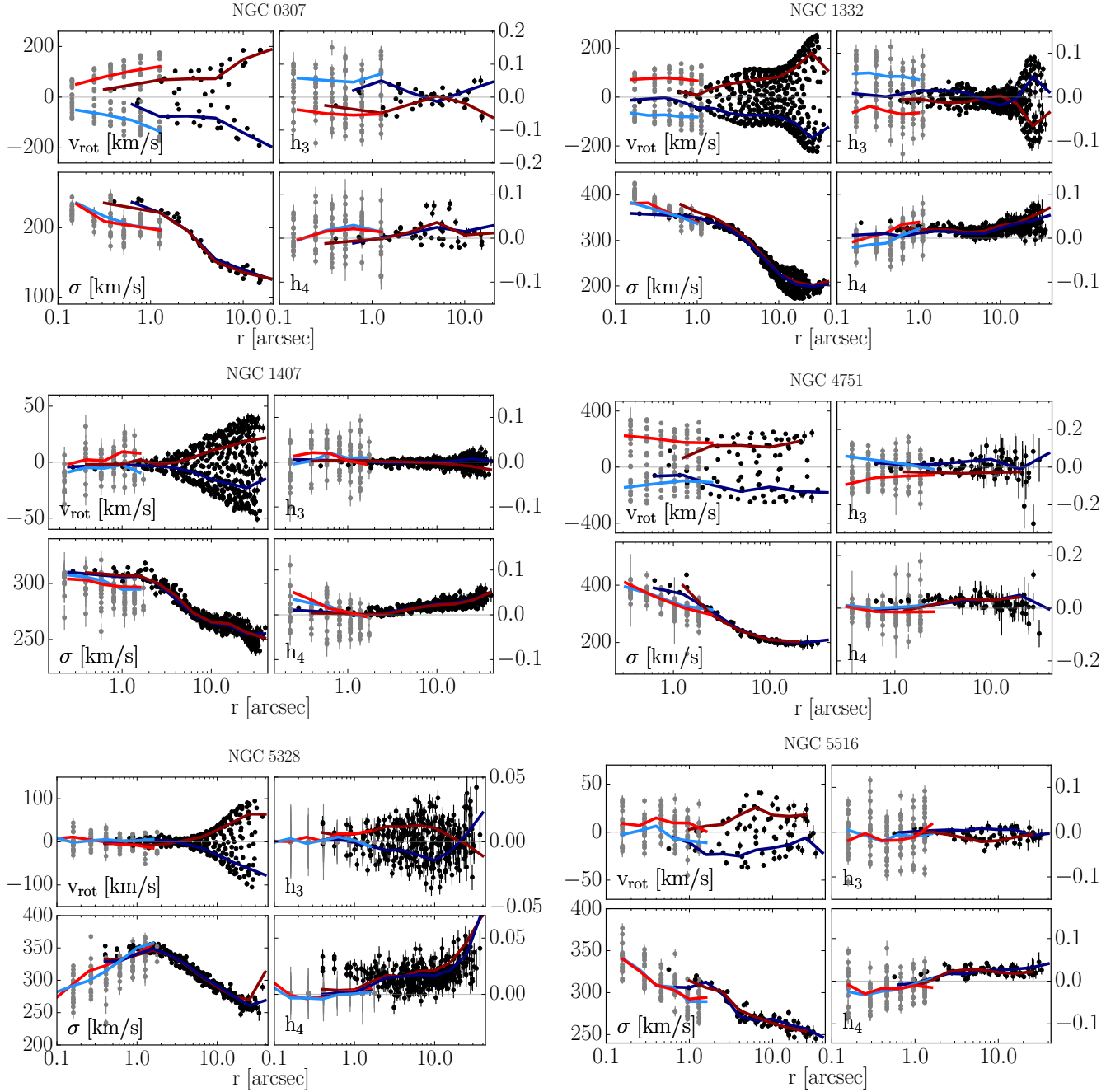


Figure 13. Dynamic fits to MUSE and SINFONI kinematics shown as radial profiles of Gauss-Hermite parameters. Gauss-Hermite parameters were derived from 8th order Gauss-Hermite polynomial fits to the non-parametric data and model LOSVDs – though we only show the first four orders here. The MUSE data kinematics are shown as black points with error bars. Since our dynamical models fit all LOSVDs there should be one model LOSVD point per data LOSVD point, but for the sake of visibility we show our models as radial averages split into two for the two sides of rotation of each galaxy (red and blue lines). The dynamical fits to the MUSE data are shown as solid dark red and dark blue lines. Analogously, we show the SINFONI data in grey and the SINFONI model LOSVDs in light blue and light red. Points without visible errorbars have statistical uncertainties smaller than the symbols. For NGC 5328, the SINFONI kinematic data points all have $h_3 = h_4 = 0$, since only for this galaxy we used simple Gaussian LOSVDs which were derived from fits to the non-parametric LOSVDs (see Section 4.2.1). The errorbars of the data points were derived from fitting noisy realisations of these LOSVDs based on the noise of the original non-parametric LOSVDs.

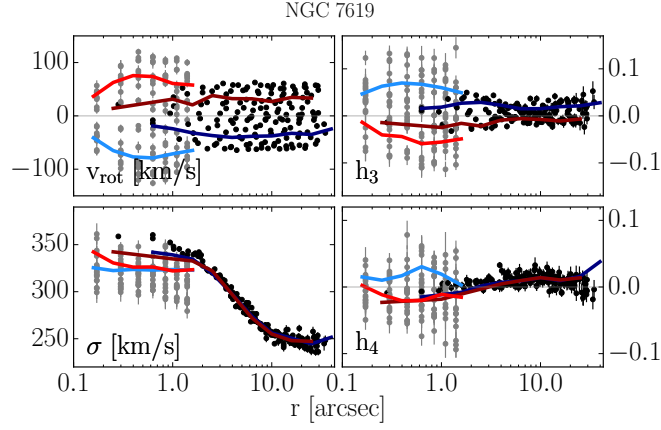


Figure 13. (continued)

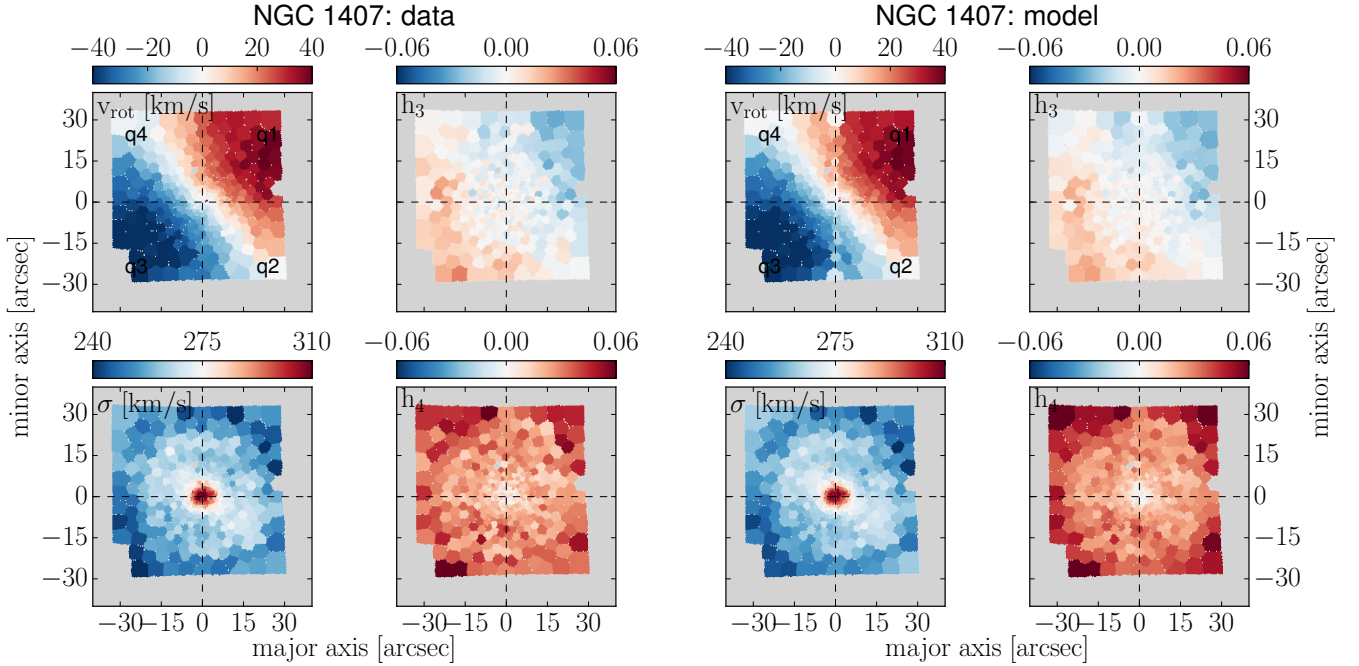


Figure 14. MUSE data-kinematics (left) and dynamical models (right) of NGC 1407 shown as 2D kinematic maps of Gauss-Hermite parameters. X- and Y-axes are aligned with the major and minor axes of the galaxy. Gauss-Hermite parameters were derived from 8th order Gauss-Hermite polynomial fits to the non-parametric data and model LOSVDs – though we only show the first four orders here. The model-map for v_{rot} shows a low-velocity artefact along the minor axis.

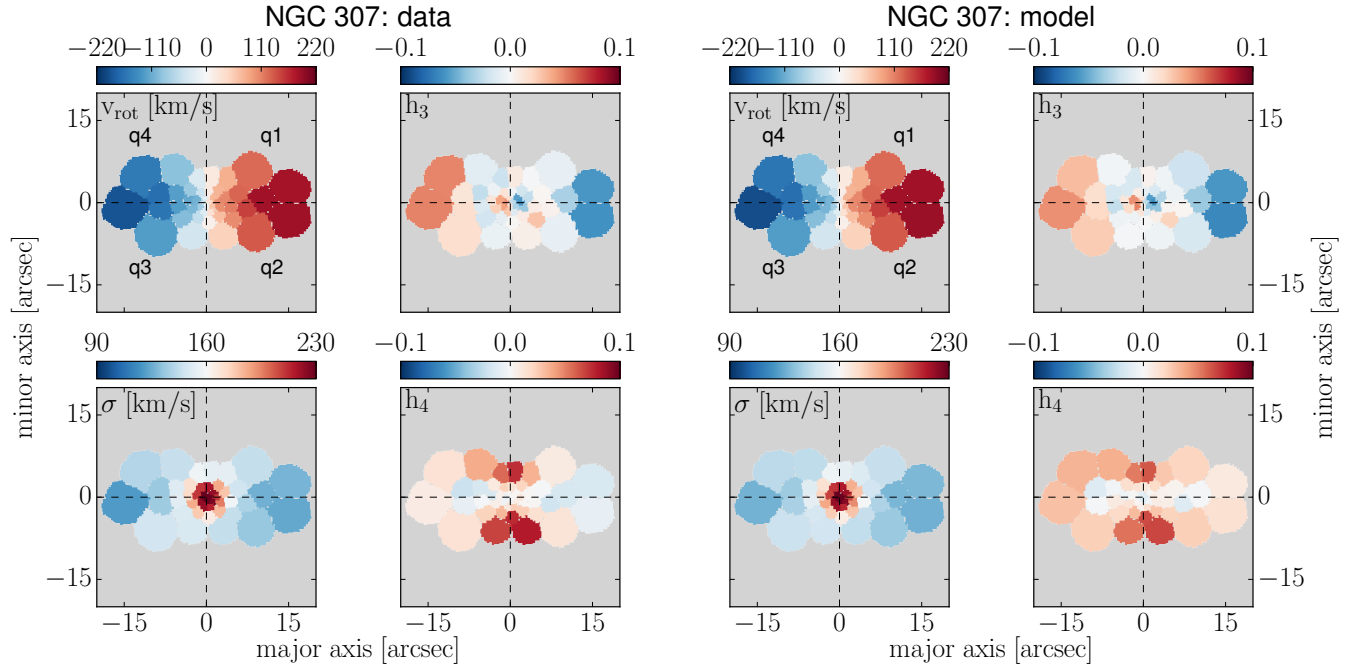


Figure 15. MUSE data-kinematics (left) and dynamical models (right) of NGC 307, same as Figure 14.

C. CONSTANT- Υ MODELS

In Table 5 we list the best-fit modeling parameters from our best-fit constant- Υ models. These models were *fully* encompassed in the parameter space of our Υ -gradient models. Best-fit Υ -gradient models were in all cases better fits to the data than constant- Υ models, with an AIC_p -difference of around 10 – 20, slightly larger than the typical threshold for a black hole measurement, which is easily explained by the fact that the differences between the models primarily concern the central kiloparsec of the galaxies, which almost entirely accounts for the difference in AIC_p . This also indicates that outside this radius the slightly larger Υ of the constant- Υ models is taken out of the mass-budget of the DM component of the total dynamical mass profile.

Galaxy	Band	Υ [M_\odot/L_\odot]	M_{BH} [$10^9 M_\odot$]	ρ_{10} [$10^8 M_\odot/\text{kpc}^3$]	α
NGC 1407	B	4.14 ± 0.28	8.50 ± 0.87	2.13 ± 0.13	0.75 ± 0.32
NGC 5328	V	5.81 ± 0.31	2.25 ± 0.43	0.85 ± 0.15	1.44 ± 0.04
NGC 5516	R	4.83 ± 0.83	2.88 ± 1.13	0.60 ± 0.05	1.61 ± 0.18
NGC 7619	I	3.00 ± 0.50	4.38 ± 0.38	0.65 ± 0.05	1.61 ± 0.20

Table 5. Results of Schwarzschild dynamical modeling using constant mass-to-light models. Photometric bands, as well as extinction corrections for Υ -values for all galaxies were taken over from R+13, according to Table 1. Modeling parameters are listed as averages and standard deviations of values over all quadrants or sub-quadrants of each galaxy. In addition to the modeling parameters we also list the IMF mass normalization parameters relative to a Kroupa IMF.

D. TESTING OUR AXISYMMETRIC MODELS WITH A TRIAXIAL N-BODY SIMULATION

As a stress test, we applied our axisymmetric models with Υ gradients to a numerical N-body originally from Rantala et al. (2018). It is the same simulation that we have used to test our triaxial Schwarzschild code SMART and details about how we extract mock LOSVDs and images can be found in the respective papers (de Nicola et al. 2022; Neureiter et al. 2023a). We model the projection of the simulation along its intermediate axis. To match the simulation with the average galaxy in our sample we shrunk it in radius and mass by a factor of two, such that all particle velocities stay the same. Originally, the stellar particles all have the same mass. To introduce a gradient we have to assign a mass-to-light ratio to each particle. In a steady state system, a stable mass-to-light ratio gradient needs to be a function of the integrals of motion. Simply defining a Υ gradient as a function of radius is not a good option. Instead, we define the gradient as a function of energy. To do so we first fit a polynomial to the distribution $E(r)$ of the particle energies. Then we determine the average particle energies E_{main} at 2 kpc and E_{cen} at 0.5 kpc. For all particles with $E < E_{\text{cen}}$ we set the mass-to-light ratio equal to two and for all particles with $E > E_{\text{main}}$ we set the mass-to-light ratio to one. In between, we interpolated the mass-to-light ratios log-linearly over E . With the mass-to-light ratio defined for each particle, we can assign a luminosity to each particle and derive LOSVDs and images respectively. The mock galaxy that we have constructed in this way has a stellar mass-to-light ratio gradient that is similar to our observed gradients, but somewhat steeper, a bit more extended, and without a central Υ -plateau – Υ increases to $\Upsilon_{\text{cen}}^{\text{sim}}$ essentially in the very center. This can be seen in Figure 16.

To prepare the simulation for Schwarzschild dynamical modeling we set out to generate mock kinematic data in analogy to the data we used in this study (see Section 2.3). We adopt the simulated MUSE and SINFONI binning from Neureiter et al. (2023b), assuming a distance of $D = 56.2$ Mpc (about the largest in our sample). The LOSVDs were generated over $v_{\text{los}} = \pm 1500$ km/s with $N_{\text{vel}} = 15$ for both mock-data sets, in analogy to the sample galaxies. Dividing the galaxy in the spatial quadrants along the major and minor axis (aligned with the x and y axis of the FOVs), we derive a total of ~ 80 mock SINFONI plus MUSE LOSVDs per quadrant.

Finally we generated images, in a way that mimics our use of HST and ground-based imaging for the sample galaxies: One $30'' \times 30''$ image with a pixel size of 0.05 arcsec, and one $300'' \times 300''$ image with a pixel size of $0.2''$. For the photometric analysis and combination of the images we proceed as with the sample galaxies (see Section 2.2).

The dynamical models of the simulated galaxy use exactly the same setup as was used for the other sample galaxies.

The best-fit models achieved a good $(\chi^2 + m_{\text{eff}})/N \sim 0.96$. The models recovered the mass of the central SMBH within one sigma, $M_{\text{BH}} = (7.38 \pm 2.68) \times 10^9 M_{\odot}$. As for the sample galaxies we used a cored NFW halo with just one parameter, ρ_{10} , which necessarily under-predicts the central DM density of the simulation, which has an inner logarithmic density slope of $\gamma \sim -0.7$. Nonetheless, when comparing the enclosed mass within $r_{\text{cen}} = \text{FWHM}_{\text{PSF}} = 1.5''$, we find that our models recover the enclosed central DM mass within 8%, $M_{\text{DM}}(r \leq r_{\text{cen}}) = (4.02 \pm 1.12) \times 10^8 M_{\odot}/\text{kpc}^3$, versus $M_{\text{DM}}^{\text{sim}}(r \leq r_{\text{cen}}) \sim 5.56 \times 10^8 M_{\odot}/\text{kpc}^3$. We also correctly recover the main-body mass-to-light ratio of the stars within one sigma $\Upsilon_{\text{main}} = 0.93 \pm 0.11$. This precision in the SMBH mass, DM recovery and main-body stellar mass is quite remarkably in view of the fact that the simulation is triaxial but our models assume axial symmetry.

The central mass-to-light ratio is more uncertain. On average, we overestimate its value by a factor of roughly 1.6, $\Upsilon_{\text{main}} = 3.16 \pm 1.13$, as shown in Figure 16. This bias could have been caused by the fact that the simulation is triaxial. As triaxial effects are viewing angle dependant, with just one viewing angle tested it is difficult to draw a final conclusion at this point.

The test presented here should be considered a stress test for our approach. We have shown that even under difficult conditions (triaxial object, large sphere of influence) the main-body mass-to-light ratio and the spatial scale of the gradient are very robust. The central amplitude of the gradient – if any – could be shallower than inferred. We plan a more thorough and comprehensive investigation of how accurate stellar mass-to-light ratio gradients can be recovered dynamically in a future paper.

REFERENCES

- Audet, C., & Dennis, Jr., J. 2006, SIAM Journal on Optimization, 17, 188, doi: [doi:10.1137/040603371](https://doi.org/10.1137/040603371)
- Audet, C., & Hare, W. 2017, Derivative-Free and Blackbox Optimization, Springer Series in Operations Research and Financial Engineering (Springer International Publishing), 302, doi: [10.1007/978-3-319-68913-5](https://doi.org/10.1007/978-3-319-68913-5)

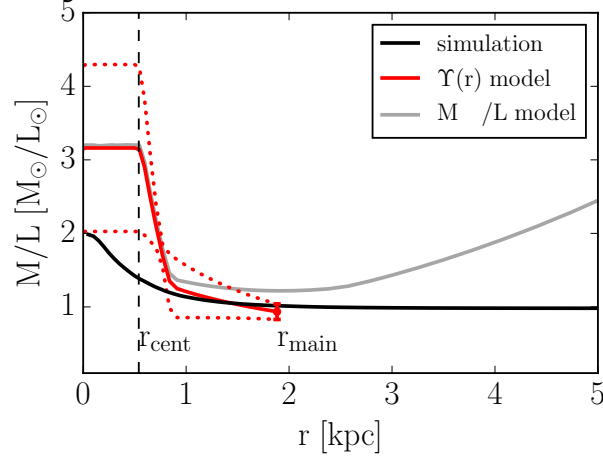


Figure 16. Mass-to-light ratio profile of our dynamical fits (solid red, the uncertainties are indicated by dotted red lines) to the triaxial Υ -gradient galaxy simulation (black). Even though the simulation is triaxial, our axisymmetric models can correctly recover Υ_{main} . However, the stellar mass-to-light ratio inside r_{cent} , Υ_{cent} is overestimated by a factor of roughly 1.6.

- Auger, M. W., Treu, T., Gavazzi, R., et al. 2010, *ApJL*, 721, L163, doi: [10.1088/2041-8205/721/2/L163](https://doi.org/10.1088/2041-8205/721/2/L163)
- Barro, G., Faber, S. M., Pérez-González, P. G., et al. 2013, *ApJ*, 765, 104, doi: [10.1088/0004-637X/765/2/104](https://doi.org/10.1088/0004-637X/765/2/104)
- Barro, G., Kriek, M., Pérez-González, P. G., et al. 2016, *ApJL*, 827, L32, doi: [10.3847/2041-8205/827/2/L32](https://doi.org/10.3847/2041-8205/827/2/L32)
- Barth, A. J., Boizelle, B. D., Darling, J., et al. 2016, *ApJL*, 822, L28, doi: [10.3847/2041-8205/822/2/L28](https://doi.org/10.3847/2041-8205/822/2/L28)
- Bastian, N., Covey, K. R., & Meyer, M. R. 2010, *ARA&A*, 48, 339, doi: [10.1146/annurev-astro-082708-101642](https://doi.org/10.1146/annurev-astro-082708-101642)
- Belli, S., Newman, A. B., & Ellis, R. S. 2014, *ApJ*, 783, 117, doi: [10.1088/0004-637X/783/2/117](https://doi.org/10.1088/0004-637X/783/2/117)
- Bender, R. 1988, *A&A*, 193, L7
- Bernardi, M., Domínguez Sánchez, H., Brownstein, J. R., Drory, N., & Sheth, R. K. 2019, *Monthly Notices of the Royal Astronomical Society*, 489, 5633
- Bernardi, M., Sheth, R. K., Fischer, J. L., et al. 2018, *MNRAS*, 475, 757, doi: [10.1093/mnras/stx3171](https://doi.org/10.1093/mnras/stx3171)
- Bezanson, R., van Dokkum, P. G., Tal, T., et al. 2009, *ApJ*, 697, 1290, doi: [10.1088/0004-637X/697/2/1290](https://doi.org/10.1088/0004-637X/697/2/1290)
- Brewer, B. J., Dutton, A. A., Treu, T., et al. 2012, *MNRAS*, 422, 3574, doi: [10.1111/j.1365-2966.2012.20870.x](https://doi.org/10.1111/j.1365-2966.2012.20870.x)
- Bromm, V., & Larson, R. B. 2004, *ARA&A*, 42, 79, doi: [10.1146/annurev.astro.42.053102.134034](https://doi.org/10.1146/annurev.astro.42.053102.134034)
- Cappellari, M. 2008, *MNRAS*, 390, 71, doi: [10.1111/j.1365-2966.2008.13754.x](https://doi.org/10.1111/j.1365-2966.2008.13754.x)
- Cappellari, M., & Copin, Y. 2003, *MNRAS*, 342, 345, doi: [10.1046/j.1365-8711.2003.06541.x](https://doi.org/10.1046/j.1365-8711.2003.06541.x)
- Cappellari, M., Emsellem, E., Bacon, R., et al. 2007a, *MNRAS*, 379, 418, doi: [10.1111/j.1365-2966.2007.11963.x](https://doi.org/10.1111/j.1365-2966.2007.11963.x)
- . 2007b, *MNRAS*, 379, 418, doi: [10.1111/j.1365-2966.2007.11963.x](https://doi.org/10.1111/j.1365-2966.2007.11963.x)
- Cappellari, M., McDermid, R. M., Alatalo, K., et al. 2012, *Nature*, 484, 485, doi: [10.1038/nature10972](https://doi.org/10.1038/nature10972)
- Cappellari, M., Scott, N., Alatalo, K., et al. 2013a, *MNRAS*, 432, 1709, doi: [10.1093/mnras/stt562](https://doi.org/10.1093/mnras/stt562)
- Cappellari, M., McDermid, R. M., Alatalo, K., et al. 2013b, *MNRAS*, 432, 1862, doi: [10.1093/mnras/stt644](https://doi.org/10.1093/mnras/stt644)
- Chabrier, G. 2003, *PASP*, 115, 763, doi: [10.1086/376392](https://doi.org/10.1086/376392)
- Chabrier, G., Hennebelle, P., & Charlot, S. 2014, *ApJ*, 796, 75, doi: [10.1088/0004-637X/796/2/75](https://doi.org/10.1088/0004-637X/796/2/75)
- Collett, T. E., Oldham, L. J., Smith, R. J., et al. 2018, *Science*, 360, 1342, doi: [10.1126/science.aao2469](https://doi.org/10.1126/science.aao2469)
- Collier, W. P., Smith, R. J., & Lucey, J. R. 2018, *MNRAS*, 478, 1595, doi: [10.1093/mnras/sty1188](https://doi.org/10.1093/mnras/sty1188)
- . 2020, *MNRAS*, 494, 271, doi: [10.1093/mnras/staa602](https://doi.org/10.1093/mnras/staa602)
- Conroy, C., Graves, G. J., & van Dokkum, P. G. 2014, *ApJ*, 780, 33, doi: [10.1088/0004-637X/780/1/33](https://doi.org/10.1088/0004-637X/780/1/33)
- Conroy, C., & van Dokkum, P. G. 2012, *ApJ*, 760, 71, doi: [10.1088/0004-637X/760/1/71](https://doi.org/10.1088/0004-637X/760/1/71)
- Conroy, C., van Dokkum, P. G., & Villaume, A. 2017, *ApJ*, 837, 166, doi: [10.3847/1538-4357/aa6190](https://doi.org/10.3847/1538-4357/aa6190)
- Crane, P., Stiavelli, M., King, I. R., et al. 1993, *AJ*, 106, 1371, doi: [10.1086/116733](https://doi.org/10.1086/116733)
- Dalton, G. B., Caldwell, M., Ward, A. K., et al. 2006, in *Society of Photo-Optical Instrumentation Engineers (SPIE) Conference Series*, Vol. 6269, Society of Photo-Optical Instrumentation Engineers (SPIE) Conference Series, ed. I. S. McLean & M. Iye, 62690X, doi: [10.1117/12.670018](https://doi.org/10.1117/12.670018)
- de Nicola, S., Neureiter, B., Thomas, J., Saglia, R. P., & Bender, R. 2022, *MNRAS*, 517, 3445, doi: [10.1093/mnras/stac2852](https://doi.org/10.1093/mnras/stac2852)
- de Zeeuw, P. T., Bureau, M., Emsellem, E., et al. 2002, *MNRAS*, 329, 513, doi: [10.1046/j.1365-8711.2002.05059.x](https://doi.org/10.1046/j.1365-8711.2002.05059.x)

- Domínguez Sánchez, H., Bernardi, M., Brownstein, J. R., Drory, N., & Sheth, R. K. 2019, *MNRAS*, 489, 5612, doi: [10.1093/mnras/stz2414](https://doi.org/10.1093/mnras/stz2414)
- Emerson, J., McPherson, A., & Sutherland, W. 2006, *The Messenger*, 126, 41
- Emsellem, E., Cappellari, M., Peletier, R. F., et al. 2004, *MNRAS*, 352, 721, doi: [10.1111/j.1365-2966.2004.07948.x](https://doi.org/10.1111/j.1365-2966.2004.07948.x)
- Emsellem, E., Cappellari, M., Krajnović, D., et al. 2007, *MNRAS*, 379, 401, doi: [10.1111/j.1365-2966.2007.11752.x](https://doi.org/10.1111/j.1365-2966.2007.11752.x)
- . 2011, *MNRAS*, 414, 888, doi: [10.1111/j.1365-2966.2011.18496.x](https://doi.org/10.1111/j.1365-2966.2011.18496.x)
- Erwin, P. 2015, *ApJ*, 799, 226, doi: [10.1088/0004-637X/799/2/226](https://doi.org/10.1088/0004-637X/799/2/226)
- Erwin, P., Thomas, J., Saglia, R. P., et al. 2018, *MNRAS*, 473, 2251, doi: [10.1093/mnras/stx2499](https://doi.org/10.1093/mnras/stx2499)
- Event Horizon Telescope Collaboration, Akiyama, K., Alberdi, A., et al. 2019, *ApJL*, 875, L1, doi: [10.3847/2041-8213/ab0ec7](https://doi.org/10.3847/2041-8213/ab0ec7)
- Faber, S. M., Tremaine, S., Ajhar, E. A., et al. 1997, *AJ*, 114, 1771, doi: [10.1086/118606](https://doi.org/10.1086/118606)
- Ferrarese, L., van den Bosch, F. C., Ford, H. C., Jaffe, W., & O'Connell, R. W. 1994, *AJ*, 108, 1598, doi: [10.1086/117180](https://doi.org/10.1086/117180)
- Ferreras, I., La Barbera, F., de La Rosa, I. G., et al. 2013, *MNRAS*, 429, L15, doi: [10.1093/mnrasl/sls014](https://doi.org/10.1093/mnrasl/sls014)
- Finkelstein, S. L., Bagley, M. B., Ferguson, H. C., et al. 2023, *ApJL*, 946, L13, doi: [10.3847/2041-8213/acade4](https://doi.org/10.3847/2041-8213/acade4)
- Frigo, M., Naab, T., Rantala, A., et al. 2021, *MNRAS*, 508, 4610, doi: [10.1093/mnras/stab2754](https://doi.org/10.1093/mnras/stab2754)
- Gebhardt, K., & Thomas, J. 2009, *ApJ*, 700, 1690, doi: [10.1088/0004-637X/700/2/1690](https://doi.org/10.1088/0004-637X/700/2/1690)
- Gebhardt, K., Richstone, D., Ajhar, E. A., et al. 1996, *AJ*, 112, 105, doi: [10.1086/117992](https://doi.org/10.1086/117992)
- Gebhardt, K., Richstone, D., Kormendy, J., et al. 2000, *AJ*, 119, 1157, doi: [10.1086/301240](https://doi.org/10.1086/301240)
- Gebhardt, K., Richstone, D., Tremaine, S., et al. 2003, *ApJ*, 583, 92, doi: [10.1086/345081](https://doi.org/10.1086/345081)
- Gerhard, O., Kronawitter, A., Saglia, R. P., & Bender, R. 2001, *AJ*, 121, 1936, doi: [10.1086/319940](https://doi.org/10.1086/319940)
- Gu, M., Greene, J. E., Newman, A. B., et al. 2022, *ApJ*, 932, 103, doi: [10.3847/1538-4357/ac69ea](https://doi.org/10.3847/1538-4357/ac69ea)
- Hopkins, P. F., Lauer, T. R., Cox, T. J., Hernquist, L., & Kormendy, J. 2009, *ApJS*, 181, 486, doi: [10.1088/0067-0049/181/2/486](https://doi.org/10.1088/0067-0049/181/2/486)
- Iannuzzi, F., & Athanassoula, E. 2015, *MNRAS*, 450, 2514, doi: [10.1093/mnras/stv764](https://doi.org/10.1093/mnras/stv764)
- Kassin, S. A., de Jong, R. S., & Pogge, R. W. 2006, *ApJS*, 162, 80, doi: [10.1086/498394](https://doi.org/10.1086/498394)
- Kennicutt, Robert C., J. 1998, in *Astronomical Society of the Pacific Conference Series*, Vol. 142, *The Stellar Initial Mass Function (38th Herstmonceux Conference)*, ed. G. Gilmore & D. Howell, 1
- Kormendy, J. 1999, in *Astronomical Society of the Pacific Conference Series*, Vol. 182, *Galaxy Dynamics - A Rutgers Symposium*, ed. D. R. Merritt, M. Valluri, & J. A. Sellwood, 124
- Kormendy, J., & Bender, R. 1996, *ApJL*, 464, L119, doi: [10.1086/310095](https://doi.org/10.1086/310095)
- . 2013, *ApJL*, 769, L5, doi: [10.1088/2041-8205/769/1/L5](https://doi.org/10.1088/2041-8205/769/1/L5)
- Kormendy, J., Dressler, A., Byun, Y. I., et al. 1994, in *European Southern Observatory Conference and Workshop Proceedings*, Vol. 49, *European Southern Observatory Conference and Workshop Proceedings*, 147
- Kormendy, J., Fisher, D. B., Cornell, M. E., & Bender, R. 2009, *ApJS*, 182, 216, doi: [10.1088/0067-0049/182/1/216](https://doi.org/10.1088/0067-0049/182/1/216)
- Kroupa, P. 2001, *MNRAS*, 322, 231, doi: [10.1046/j.1365-8711.2001.04022.x](https://doi.org/10.1046/j.1365-8711.2001.04022.x)
- . 2002, *Science*, 295, 82, doi: [10.1126/science.1067524](https://doi.org/10.1126/science.1067524)
- La Barbera, F., Ferreras, I., & Vazdekis, A. 2015, *MNRAS*, 449, L137, doi: [10.1093/mnrasl/slv029](https://doi.org/10.1093/mnrasl/slv029)
- La Barbera, F., Ferreras, I., Vazdekis, A., et al. 2013, *Monthly Notices of the Royal Astronomical Society*, 433, 3017, doi: [10.1093/mnras/stt943](https://doi.org/10.1093/mnras/stt943)
- La Barbera, F., Vazdekis, A., Ferreras, I., et al. 2019, *MNRAS*, 489, 4090, doi: [10.1093/mnras/stz2192](https://doi.org/10.1093/mnras/stz2192)
- Lasker, R., van den Bosch, R. C. E., van de Ven, G., et al. 2013, *MNRAS*, 434, L31, doi: [10.1093/mnrasl/slt070](https://doi.org/10.1093/mnrasl/slt070)
- Lauer, T. R. 2012, *ApJ*, 759, 64, doi: [10.1088/0004-637X/759/1/64](https://doi.org/10.1088/0004-637X/759/1/64)
- Lauer, T. R., Ajhar, E. A., Byun, Y. I., et al. 1995, *AJ*, 110, 2622, doi: [10.1086/117719](https://doi.org/10.1086/117719)
- Lauer, T. R., Gebhardt, K., Faber, S. M., et al. 2007, *ApJ*, 664, 226, doi: [10.1086/519229](https://doi.org/10.1086/519229)
- Le Digabel, S. 2011, *ACM Transactions on Mathematical Software*, 37, 1
- Li, C., Zhu, L., Long, R. J., et al. 2020, *MNRAS*, 492, 2775, doi: [10.1093/mnras/staa027](https://doi.org/10.1093/mnras/staa027)
- Li, H., Ge, J., Mao, S., et al. 2017, *ApJ*, 838, 77, doi: [10.3847/1538-4357/aa662a](https://doi.org/10.3847/1538-4357/aa662a)
- Liebold, E. R., Ma, C.-P., & Walsh, J. L. 2023, *ApJL*, 945, L35, doi: [10.3847/2041-8213/acbbcf](https://doi.org/10.3847/2041-8213/acbbcf)
- Lipka, M., & Thomas, J. 2021, *MNRAS*, 504, 4599, doi: [10.1093/mnras/stab1092](https://doi.org/10.1093/mnras/stab1092)
- Lyubenova, M., Martín-Navarro, I., van de Ven, G., et al. 2016, *MNRAS*, 463, 3220, doi: [10.1093/mnras/stw2434](https://doi.org/10.1093/mnras/stw2434)
- Magorrian, J. 1999, *MNRAS*, 302, 530, doi: [10.1046/j.1365-8711.1999.02135.x](https://doi.org/10.1046/j.1365-8711.1999.02135.x)

- Martín-Navarro, I., La Barbera, F., Vazdekis, A., Falcón-Barroso, J., & Ferreras, I. 2015a, *MNRAS*, 447, 1033, doi: [10.1093/mnras/stu2480](https://doi.org/10.1093/mnras/stu2480)
- Martín-Navarro, I., Vazdekis, A., La Barbera, F., et al. 2015b, *ApJL*, 806, L31, doi: [10.1088/2041-8205/806/2/L31](https://doi.org/10.1088/2041-8205/806/2/L31)
- McDermid, R. M., Cappellari, M., Alatalo, K., et al. 2014, *ApJL*, 792, L37, doi: [10.1088/2041-8205/792/2/L37](https://doi.org/10.1088/2041-8205/792/2/L37)
- Mehrgan, K., Thomas, J., Saglia, R., et al. 2019, *ApJ*, 887, 195, doi: [10.3847/1538-4357/ab5856](https://doi.org/10.3847/1538-4357/ab5856)
- Mehrgan, K., Thomas, J., Saglia, R., Parikh, T., & Bender, R. 2023, *ApJ*, 948, 79, doi: [10.3847/1538-4357/acbf2e](https://doi.org/10.3847/1538-4357/acbf2e)
- Napolitano, N. R., Pota, V., Romanowsky, A. J., et al. 2014, *MNRAS*, 439, 659, doi: [10.1093/mnras/stt2484](https://doi.org/10.1093/mnras/stt2484)
- Napolitano, N. R., Romanowsky, A. J., Capaccioli, M., et al. 2011, *MNRAS*, 411, 2035, doi: [10.1111/j.1365-2966.2010.17833.x](https://doi.org/10.1111/j.1365-2966.2010.17833.x)
- Navarro, J. F., Frenk, C. S., & White, S. D. M. 1996, *ApJ*, 462, 563, doi: [10.1086/177173](https://doi.org/10.1086/177173)
- Nelson, E., van Dokkum, P., Franx, M., et al. 2014, *Nature*, 513, 394, doi: [10.1038/nature13616](https://doi.org/10.1038/nature13616)
- Neureiter, B., de Nicola, S., Thomas, J., et al. 2023a, *MNRAS*, 519, 2004, doi: [10.1093/mnras/stac3652](https://doi.org/10.1093/mnras/stac3652)
- Neureiter, B., Thomas, J., Rantala, A., et al. 2023b, *arXiv e-prints*, arXiv:2305.03078, doi: [10.48550/arXiv.2305.03078](https://doi.org/10.48550/arXiv.2305.03078)
- Neureiter, B., Thomas, J., Saglia, R., et al. 2021, *MNRAS*, 500, 1437, doi: [10.1093/mnras/staa3014](https://doi.org/10.1093/mnras/staa3014)
- Newman, A. B., Ellis, R. S., & Treu, T. 2015, *ApJ*, 814, 26, doi: [10.1088/0004-637X/814/1/26](https://doi.org/10.1088/0004-637X/814/1/26)
- Newman, A. B., Smith, R. J., Conroy, C., Villaume, A., & van Dokkum, P. 2017, *ApJ*, 845, 157, doi: [10.3847/1538-4357/aa816d](https://doi.org/10.3847/1538-4357/aa816d)
- Nieto, J. L., & Bender, R. 1989, *A&A*, 215, 266
- Nieto, J.-L., Bender, R., & Surma, P. 1991, *A&A*, 244, L37
- Nowak, N., Thomas, J., Erwin, P., et al. 2010, *MNRAS*, 403, 646, doi: [10.1111/j.1365-2966.2009.16167.x](https://doi.org/10.1111/j.1365-2966.2009.16167.x)
- Oldham, L., & Auger, M. 2018a, *MNRAS*, 474, 4169, doi: [10.1093/mnras/stx2969](https://doi.org/10.1093/mnras/stx2969)
- Oldham, L. J., & Auger, M. W. 2018b, *MNRAS*, 476, 133, doi: [10.1093/mnras/sty065](https://doi.org/10.1093/mnras/sty065)
- Oser, L., Ostriker, J. P., Naab, T., Johansson, P. H., & Burkert, A. 2010, *ApJ*, 725, 2312, doi: [10.1088/0004-637X/725/2/2312](https://doi.org/10.1088/0004-637X/725/2/2312)
- Parikh, T., Thomas, D., Maraston, C., et al. 2018, *MNRAS*, 477, 3954, doi: [10.1093/mnras/sty785](https://doi.org/10.1093/mnras/sty785)
- Poci, A., McDermid, R. M., Lyubenova, M., et al. 2022, *MNRAS*, 514, 3660, doi: [10.1093/mnras/stac1514](https://doi.org/10.1093/mnras/stac1514)
- Posacki, S., Cappellari, M., Treu, T., Pellegrini, S., & Ciotti, L. 2015, *MNRAS*, 446, 493, doi: [10.1093/mnras/stu2098](https://doi.org/10.1093/mnras/stu2098)
- Quenneville, M. E., Liepold, C. M., & Ma, C.-P. 2022, *ApJ*, 926, 30, doi: [10.3847/1538-4357/ac3e68](https://doi.org/10.3847/1538-4357/ac3e68)
- Rantala, A., Johansson, P. H., Naab, T., Thomas, J., & Frigo, M. 2018, *ApJ*, 864, 113, doi: [10.3847/1538-4357/aada47](https://doi.org/10.3847/1538-4357/aada47)
- . 2019, *ApJL*, 872, L17, doi: [10.3847/2041-8213/ab04b1](https://doi.org/10.3847/2041-8213/ab04b1)
- Richstone, D. O., & Tremaine, S. 1988, *ApJ*, 327, 82, doi: [10.1086/166171](https://doi.org/10.1086/166171)
- Rusli, S. P., Erwin, P., Saglia, R. P., et al. 2013b, *AJ*, 146, 160, doi: [10.1088/0004-6256/146/6/160](https://doi.org/10.1088/0004-6256/146/6/160)
- Rusli, S. P., Thomas, J., Erwin, P., et al. 2011, *MNRAS*, 410, 1223, doi: [10.1111/j.1365-2966.2010.17610.x](https://doi.org/10.1111/j.1365-2966.2010.17610.x)
- Rusli, S. P., Thomas, J., Saglia, R. P., et al. 2013a, *AJ*, 146, 45, doi: [10.1088/0004-6256/146/3/45](https://doi.org/10.1088/0004-6256/146/3/45)
- Saglia, R. P., Opitsch, M., Erwin, P., et al. 2016, *ApJ*, 818, 47, doi: [10.3847/0004-637X/818/1/47](https://doi.org/10.3847/0004-637X/818/1/47)
- Schwarzschild, M. 1979, *ApJ*, 232, 236, doi: [10.1086/157282](https://doi.org/10.1086/157282)
- Siopis, C., Gebhardt, K., Lauer, T. R., et al. 2009, *ApJ*, 693, 946, doi: [10.1088/0004-637X/693/1/946](https://doi.org/10.1088/0004-637X/693/1/946)
- Smith, R. J. 2014, *MNRAS*, 443, L69, doi: [10.1093/mnras/lu082](https://doi.org/10.1093/mnras/lu082)
- Smith, R. J., Lucey, J. R., & Carter, D. 2012, *MNRAS*, 426, 2994, doi: [10.1111/j.1365-2966.2012.21922.x](https://doi.org/10.1111/j.1365-2966.2012.21922.x)
- Smith, R. J., Lucey, J. R., & Conroy, C. 2015, *MNRAS*, 449, 3441, doi: [10.1093/mnras/stv518](https://doi.org/10.1093/mnras/stv518)
- Sonnenfeld, A., Jaelani, A. T., Chan, J., et al. 2019, *A&A*, 630, A71, doi: [10.1051/0004-6361/201935743](https://doi.org/10.1051/0004-6361/201935743)
- Sonnenfeld, A., Treu, T., Marshall, P. J., et al. 2015, *ApJ*, 800, 94, doi: [10.1088/0004-637X/800/2/94](https://doi.org/10.1088/0004-637X/800/2/94)
- Spiniello, C., Koopmans, L. V. E., Trager, S. C., Czoske, O., & Treu, T. 2011, *MNRAS*, 417, 3000, doi: [10.1111/j.1365-2966.2011.19458.x](https://doi.org/10.1111/j.1365-2966.2011.19458.x)
- Thater, S., Krajnović, D., Cappellari, M., et al. 2019, *A&A*, 625, A62, doi: [10.1051/0004-6361/201834808](https://doi.org/10.1051/0004-6361/201834808)
- Thater, S., Krajnović, D., Weilbacher, P. M., et al. 2022, *MNRAS*, 509, 5416, doi: [10.1093/mnras/stab3210](https://doi.org/10.1093/mnras/stab3210)
- Thomas, J., Jesseit, R., Naab, T., et al. 2007a, *MNRAS*, 381, 1672, doi: [10.1111/j.1365-2966.2007.12343.x](https://doi.org/10.1111/j.1365-2966.2007.12343.x)
- Thomas, J., & Lipka, M. 2022, *MNRAS*, doi: [10.1093/mnras/stac1581](https://doi.org/10.1093/mnras/stac1581)
- Thomas, J., Ma, C.-P., McConnell, N. J., et al. 2016, *Nature*, 532, 340, doi: [10.1038/nature17197](https://doi.org/10.1038/nature17197)
- Thomas, J., Saglia, R. P., Bender, R., et al. 2007b, *MNRAS*, 382, 657, doi: [10.1111/j.1365-2966.2007.12434.x](https://doi.org/10.1111/j.1365-2966.2007.12434.x)
- . 2009, *ApJ*, 691, 770, doi: [10.1088/0004-637X/691/1/770](https://doi.org/10.1088/0004-637X/691/1/770)
- . 2004, *MNRAS*, 353, 391, doi: [10.1111/j.1365-2966.2004.08072.x](https://doi.org/10.1111/j.1365-2966.2004.08072.x)

- . 2011, *MNRAS*, 415, 545,
doi: [10.1111/j.1365-2966.2011.18725.x](https://doi.org/10.1111/j.1365-2966.2011.18725.x)
- Tortora, C., Romanowsky, A. J., & Napolitano, N. R. 2013, *ApJ*, 765, 8, doi: [10.1088/0004-637X/765/1/8](https://doi.org/10.1088/0004-637X/765/1/8)
- Treu, T., Auger, M. W., Koopmans, L. V. E., et al. 2010, *ApJ*, 709, 1195, doi: [10.1088/0004-637X/709/2/1195](https://doi.org/10.1088/0004-637X/709/2/1195)
- van de Sande, J., Kriek, M., Franx, M., et al. 2013, *ApJ*, 771, 85, doi: [10.1088/0004-637X/771/2/85](https://doi.org/10.1088/0004-637X/771/2/85)
- van den Bosch, R. C. E., & de Zeeuw, P. T. 2010, *MNRAS*, 401, 1770, doi: [10.1111/j.1365-2966.2009.15832.x](https://doi.org/10.1111/j.1365-2966.2009.15832.x)
- van der Wel, A., Rix, H.-W., Holden, B. P., Bell, E. F., & Robaina, A. R. 2009, *ApJL*, 706, L120, doi: [10.1088/0004-637X/706/1/L120](https://doi.org/10.1088/0004-637X/706/1/L120)
- van Dokkum, P., Conroy, C., Villaume, A., Brodie, J., & Romanowsky, A. J. 2017, *ApJ*, 841, 68, doi: [10.3847/1538-4357/aa7135](https://doi.org/10.3847/1538-4357/aa7135)
- van Dokkum, P. G., & Conroy, C. 2010, *Nature*, 468, 940, doi: [10.1038/nature09578](https://doi.org/10.1038/nature09578)
- . 2011, *ApJL*, 735, L13, doi: [10.1088/2041-8205/735/1/L13](https://doi.org/10.1088/2041-8205/735/1/L13)
- . 2012, *ApJ*, 760, 70, doi: [10.1088/0004-637X/760/1/70](https://doi.org/10.1088/0004-637X/760/1/70)
- van Dokkum, P. G., Nelson, E. J., Franx, M., et al. 2015, *ApJ*, 813, 23, doi: [10.1088/0004-637X/813/1/23](https://doi.org/10.1088/0004-637X/813/1/23)
- Veale, M., Ma, C.-P., Greene, J. E., et al. 2018, *MNRAS*, 473, 5446, doi: [10.1093/mnras/stx2717](https://doi.org/10.1093/mnras/stx2717)
- Wegner, G. A., Corsini, E. M., Thomas, J., et al. 2012, *AJ*, 144, 78, doi: [10.1088/0004-6256/144/3/78](https://doi.org/10.1088/0004-6256/144/3/78)
- Zhao, H. 1996, *MNRAS*, 278, 488, doi: [10.1093/mnras/278.2.488](https://doi.org/10.1093/mnras/278.2.488)
- Zolotov, A., Dekel, A., Mandelker, N., et al. 2015, *MNRAS*, 450, 2327, doi: [10.1093/mnras/stv740](https://doi.org/10.1093/mnras/stv740)

Chapter 5

Conclusions and outlook

In this thesis, I address a number of pertinent issues of the dynamical mass decomposition of ETGs. The high mass end of the mass function of black holes in ETGs is poorly understood. At the same time, without strong constraints on the shape of the IMF, the mass separation of stars and DM in ETGs is uncertain.

The high mass end of the black hole mass function is tied to the centers of massive ETGs, as the largest SMBHs are expected in the largest and faintest shallow surface brightness cores. In Mehrgan et al. (2019), I generate detailed axisymmetric Schwarzschild models for the massive BCG Holm 15A, which possesses the largest and faintest known core so far ($r_\gamma \sim 4$ kpc, $\mu_{0,V} \sim 20$ mag/arcsec²). I base these models on stellar kinematic data derived from high-resolution, wide-field observations with MUSE. The data resolve the kinematic structure of the core of the galaxy in great detail, with more than a hundred non-parametric LOSVDs from within the core region, derived from spectra with a SNR/ $\text{\AA} \sim 50$, each. I generate these kinematics using our spectral fitting code WINGFIT, which enables us to derive non-parametric LOSVDs capturing the full shape of the distribution all way to the escape velocity. This study constitutes the first time that this advanced kinematic fitting code has been utilized for dynamical modeling. The dynamical analysis yields the following results:

- Holm 15A hosts the largest dynamically detected SMBH so far, $M_{\text{BH}} = (4.0 \pm 0.8) \times 10^{10} M_\odot$. This makes it one of only four UMBHs ($M_{\text{BH}} \geq 10^{10} M_\odot$) that have been dynamically detected thus far.
- Following the predictions of core-scaling relations, the core radius corresponds roughly to the SOI of the black hole, $r_{\text{SOI}} = (3.8 \pm 0.37)$ kpc.
- I establish two new core scaling relations, $M_{\text{BH}}-\mu_{0,V}$, and $M_{\text{BH}}-\Sigma_0$, describing empirical relations between SMBH mass and central surface brightness/mass-density of cored ETGs.
- Comparison of the details of the orbit structure and light profile of the core with N-body merger simulations of Rantala et al. (2018, 2019) suggest that the galaxy is the outcome of a merger between two ETGs with *pre-existing* cores.

The newly established scaling relations $M_{\text{BH}}-\mu_{0,V}$, and $M_{\text{BH}}-\Sigma_0$, together with the $r_{\text{SOI}}-r_b$, and $M_{\text{BH}}-r_b$ relations, have the potential of replacing classical, “global” scaling laws such as $M_{\text{BH}}-\sigma$ for massive ETGs, as these generally break down at the high-mass end. The $M_{\text{BH}}-\mu_{0,V}$ relation relies on a simple photometric measurement, which can be used for a targeted investigation of the high-mass end of the local black hole mass function with dynamical models. E.g. ESO program 105.20PX.001(A) (P.I. K. Mehrgan) consists of a sample of eight cored BCGs which are UMBH-host candidates based on these relations.

The main part of this thesis focuses on investigating ETGs for intrinsic gradients of the IMF. To derive strong constraints on the stellar mass-to-light ratio $\Upsilon(r)$ needed for this analysis, we require non-parametric stellar kinematics with exceptional accuracy. Therefore in Mehrgan et al. (2023a), using WINGFIT, I kinematically analyze a unique high-resolution data set consisting of nine ETGs observed with MUSE, which spatially covers each galaxy up to at least $r_e/2$. To improve the accuracy of WINGFIT even further, we for the first time adopt the generalized AIC_p model selection approach from Lipka and Thomas (2021) and Thomas and Lipka (2022) for the smoothing of the non-parametric LOSVDs. Furthermore, I perform an extensive series of mock-tests with simulated galaxy spectra to investigate the effects of template-mismatch on LOSVD recoveries under realistic conditions. The results of this kinematic analysis are as follows:

- We generate complex nonparametric 2D kinematics from spectra with a very high $\text{SNR}/\text{\AA} \gtrsim 100$ per galaxy per spatial bin for all nine ETGs
- Through our tests we identify the possibility of “hidden” template-mismatch, which cannot be diagnosed from a kinematic analysis alone, as it distorts LOSVDs in a symmetric fashion.
- We develop a recipe for template selection which can be applied to any galaxy to effectively minimize template-mismatch.
- Most galaxies in our sample show high-velocity LOSVD “wings” in the central spatial regions and towards the edges of the FOV.
- We propose that LOSVD wings in the centers of galaxies originate from signal close to the SMBH which has been spread out by the PSF. We suggest the possibility that wings found at larger radii originate from loose, weakly bound envelopes of stars around ETGs.

To probe for internal IMF gradients, I use the above kinematic data for seven ¹ of the galaxies for a Schwarzschild dynamical analysis in Mehrgan et al. (in press 2023b). To further strengthen the constraints on spatial IMF variation in the galaxies we require strong constraints on M_{BH} and Υ -gradient models. The SMBH dominates the central regions of the gravitational potential within r_{SOI} . We combine the MUSE kinematics

¹The two remaining galaxies, NGC 5419 and NGC 6861 were singled out for separate analysis in Neureiter et al. (2023b) and Thomas in prep.

with previously published AO-supported SINFONI kinematics covering the central $1.5''$ of each ETG (Rusli et al., 2011, 2013a,b; Erwin et al., 2018), which can resolve their respective SOIs. With few exceptions, IMF probes of ETGs in the literature assumed a single, spatially constant Υ for each LOSVD. We here, for the first time, augment our axisymmetric Schwarzschild modeling code with Υ -gradient models. Furthermore, we also adopt the AIC_p model selection approach for our Schwarzschild models, which helps to break down known degeneracies in the mass decomposition (Neureiter et al., 2021; Lipka and Thomas, 2021; de Nicola et al., 2022). After I dynamically model the seven galaxies, I use stellar mass-to-light ratios from a SSP analysis for an assumed Kroupa IMF (Parikh et al. submitted to MNRAS), to generate radial profiles of $\alpha(r) = \Upsilon^{dyn}(r)/\Upsilon_{Kroupa}^{SSP}(r)$ for each galaxy to characterize the IMF variations. The dynamical analysis yields the following insights:

- All seven ETGs have $\Upsilon(r)$ which increase towards their centers (on average by a factor of 2.6)
- The gradients are very centrally concentrated within 1 kpc.
- Constant- Υ models *overestimate* the total stellar mass of the galaxies relative to Υ -gradient models (by up to a factor 1.5)
- The average central IMF mass normalization is consistent with a Salpeter IMF, $\langle \alpha_{cen} \rangle = 1.54 \pm 0.15$
- For all except one galaxy, the total mass-to-light ratio $(M^{tot}/L)(r)$ has a global minimum at $r_{main} \sim 1$ kpc. Υ_{main} places the strongest constraints on the IMF of the main-body of each galaxy. On average we find a MW-like IMF normalization, $\langle \alpha_{main} \rangle = 1.03 \pm 0.19$.
- Many previous IMF probes (e.g. Posacki et al., 2015; Conroy and van Dokkum, 2012) suggested a spatially constant Salpeter or super-Salpeter α for massive ETGs. But even considering the most conservative mass-decomposition $\alpha^{tot} = (M^{tot}/L)/\Upsilon_{Kroupa}^{SSP}$, we find main-body IMFs that are more MW-like $\langle \alpha_{main}^{tot} \rangle = 1.23 \pm 0.15$.
- We show that light-averaging profiles of $\alpha(r)$ over a ~ 2 kpc radius “washes out” high central α -values to produce MW-like $\langle \alpha \rangle = 1.03 \pm 0.33$, similar to the lensing results of the SNELLS and MNELLS surveys for massive ETGs for roughly the same aperture size (Smith et al., 2015; Newman et al., 2017; Collier et al., 2018, 2020)

Our dynamical results are an important step in the direction of facilitating a consistency between different methods of probing the IMF, which is thus far lacking (Smith, 2014; McDermid et al., 2014). But there are significant differences between our dynamical measurements and SSP probes. To determine the origin of this issue, one needs to consider a sample of ETGs which uses gradient models both for the dynamical analysis, and the SSP

modeling, and for which the two methods can be directly compared *for the same galaxies*. We perform such an analysis in a companion paper, Parikh et al (submitted to MNRAS).

The dawn of the JWST era could drastically change the way that our results are to be interpreted: First epoch JWST NIRCAM observations of galaxies at very high redshifts $z \gtrsim 9$ suggest a relative excess of UV luminosity compared to galaxies at smaller redshifts, which Finkelstein et al. (2023) claim as evidence for the top-heaviness of the IMF. These galaxies are likely progenitors of the centers of ETGs. If the IMF becomes top-heavy in the centers of galaxies, the consequent relative excess of remnants over a Kroupa IMF would lead to an increase of Υ^{dyn} , but not of Υ^{SSP} , since the former is sensitive to the full integrated mass of the IMF, whereas the latter is only sensitive to the low-mass end of the IMF. As regions of the universe at higher redshifts become accessible for IMF probes, IMF-gradient probes from the local universe have to be placed in a consistent framework of galaxy evolution which can explain why different regions of galaxies were produced with different IMFs.

Moreover, triaxial Schwarzschild dynamical models are now becoming increasingly available (e.g. Neureiter et al., 2021). Currently, these are resource-intensive to such an extent that they are only suitable to the study of individual galaxies. However, this situation is expected to change in the future, in which case samples of comparable size to the one presented here should be studied using triaxial models with Υ -gradients for cored ETGs. It will be interesting to see how and if the constraints on radial profiles of the IMF change for cored ETGs if triaxiality is accounted for.

Bibliography

- M. W. Auger, T. Treu, R. Gavazzi, A. S. Bolton, L. V. E. Koopmans, and P. J. Marshall. Dark Matter Contraction and the Stellar Content of Massive Early-type Galaxies: Disfavoring “Light” Initial Mass Functions. *ApJ*, 721(2):L163–L167, October 2010. doi: 10.1088/2041-8205/721/2/L163.
- Joshua E. Barnes and Lars Hernquist. Transformations of Galaxies. II. Gasdynamics in Merging Disk Galaxies. *ApJ*, 471:115, November 1996. doi: 10.1086/177957.
- Nate Bastian, Kevin R. Covey, and Michael R. Meyer. A Universal Stellar Initial Mass Function? A Critical Look at Variations. *ARA&A*, 48:339–389, September 2010. doi: 10.1146/annurev-astro-082708-101642.
- M. C. Begelman, R. D. Blandford, and M. J. Rees. Massive black hole binaries in active galactic nuclei. *Nature*, 287(5780):307–309, September 1980. doi: 10.1038/287307a0.
- R. Bender. Unraveling the kinematics of early-type galaxies. Presentation of a new method and its application to NGC 4621. *A&A*, 229:441–451, March 1990.
- R. Bender, S. Doebereiner, and C. Moellenhoff. Isophote shapes of elliptical galaxies. I. The data. *A&AS*, 74:385–426, September 1988.
- R. Bender, R. P. Saglia, and O. E. Gerhard. Line-of-sight velocity distributions of elliptical galaxies. *MNRAS*, 269:785–813, August 1994. doi: 10.1093/mnras/269.3.785.
- Ralf Bender and Claus Moellenhoff. Elliptische Galaxien. *Sterne und Weltraum*, 26:264–271, May 1987.
- Ralf Bender, David Burstein, and S. M. Faber. Dynamically Hot Galaxies. I. Structural Properties. *ApJ*, 399:462, November 1992. doi: 10.1086/171940.
- M. Bernardi, R. K. Sheth, J. L. Fischer, A. Meert, K. H. Chae, H. Dominguez-Sanchez, M. Huertas-Company, F. Shankar, and V. Vikram. Stellar mass functions and implications for a variable IMF. *MNRAS*, 475(1):757–771, March 2018. doi: 10.1093/mnras/stx3171.

- Matthew A. Bershad, Thomas P. K. Martinsson, Marc A. W. Verheijen, Kyle B. Westfall, David R. Andersen, and Rob A. Swaters. Galaxy Disks are Submaximal. *ApJ*, 739(2): L47, October 2011. doi: 10.1088/2041-8205/739/2/L47.
- J. Binney and G. de Vaucouleurs. The apparent and true ellipticities of galaxies of different Hubble types in the Second Reference Catalogue. *MNRAS*, 194:679–691, February 1981. doi: 10.1093/mnras/194.3.679.
- J. Binney and G. A. Mamon. M/L and velocity anisotropy from observations of spherical galaxies, of must M 87 have a massive black hole ? *MNRAS*, 200:361–375, July 1982. doi: 10.1093/mnras/200.2.361.
- James Binney and Michael Merrifield. *Galactic Astronomy*. 1998.
- James Binney and Scott Tremaine. *Galactic Dynamics: Second Edition*. 2008.
- Michael Boylan-Kolchin, Chung-Pei Ma, and Eliot Quataert. Red mergers and the assembly of massive elliptical galaxies: the fundamental plane and its projections. *MNRAS*, 369 (3):1081–1089, July 2006. doi: 10.1111/j.1365-2966.2006.10379.x.
- Brendon J. Brewer, Aaron A. Dutton, Tommaso Treu, Matthew W. Auger, Philip J. Marshall, Matteo Barnabè, Adam S. Bolton, David C. Koo, and Léon V. E. Koopmans. The SWELLS survey - III. Disfavouring 'heavy' initial mass functions for spiral lens galaxies. *MNRAS*, 422(4):3574–3590, June 2012. doi: 10.1111/j.1365-2966.2012.20870.x.
- Y. I. Byun, C. J. Grillmair, S. M. Faber, E. A. Ajhar, A. Dressler, J. Kormendy, T. R. Lauer, D. Richstone, and S. Tremaine. The Centers of Early-Type Galaxies With HST. II. Empirical Models and Structural Parameters. *AJ*, 111:1889, May 1996. doi: 10.1086/117927.
- N. Caon, M. Capaccioli, and M. D’Onofrio. On the shape of the light profiles of early-type galaxies. *MNRAS*, 265:1013–1021, December 1993. doi: 10.1093/mnras/265.4.1013.
- M. Cappellari. Improving the full spectrum fitting method: accurate convolution with Gauss-Hermite functions. *MNRAS*, 466:798–811, April 2017. doi: 10.1093/mnras/stw3020.
- Michele Cappellari. Measuring the inclination and mass-to-light ratio of axisymmetric galaxies via anisotropic Jeans models of stellar kinematics. *MNRAS*, 390(1):71–86, October 2008. doi: 10.1111/j.1365-2966.2008.13754.x.
- Michele Cappellari, Eric Emsellem, R. Bacon, M. Bureau, Roger L. Davies, P. T. de Zeeuw, Jesús Falcón-Barroso, Davor Krajnović, Harald Kuntschner, Richard M. McDermid, Reynier F. Peletier, Marc Sarzi, Remco C. E. van den Bosch, and Glenn van de Ven. The SAURON project - X. The orbital anisotropy of elliptical and lenticular galaxies: revisiting the $(V/\sigma, \epsilon)$ diagram with integral-field stellar kinematics. *MNRAS*, 379(2): 418–444, August 2007. doi: 10.1111/j.1365-2966.2007.11963.x.

- Michele Cappellari, Richard M. McDermid, Katherine Alatalo, Leo Blitz, Maxime Bois, Frédéric Bournaud, M. Bureau, Alison F. Crocker, Roger L. Davies, Timothy A. Davis, P. T. de Zeeuw, Pierre-Alain Duc, Eric Emsellem, Sadegh Khochfar, Davor Krajnović, Harald Kuntschner, Pierre-Yves Lablanche, Raffaella Morganti, Thorsten Naab, Tom Oosterloo, Marc Sarzi, Nicholas Scott, Paolo Serra, Anne-Marie Weijmans, and Lisa M. Young. Systematic variation of the stellar initial mass function in early-type galaxies. *Nature*, 484(7395):485–488, April 2012. doi: 10.1038/nature10972.
- Michele Cappellari, Richard M. McDermid, Katherine Alatalo, Leo Blitz, Maxime Bois, Frédéric Bournaud, M. Bureau, Alison F. Crocker, Roger L. Davies, Timothy A. Davis, P. T. de Zeeuw, Pierre-Alain Duc, Eric Emsellem, Sadegh Khochfar, Davor Krajnović, Harald Kuntschner, Raffaella Morganti, Thorsten Naab, Tom Oosterloo, Marc Sarzi, Nicholas Scott, Paolo Serra, Anne-Marie Weijmans, and Lisa M. Young. The ATLAS^{3D} project - XX. Mass-size and mass- σ distributions of early-type galaxies: bulge fraction drives kinematics, mass-to-light ratio, molecular gas fraction and stellar initial mass function. *MNRAS*, 432(3):1862–1893, July 2013a. doi: 10.1093/mnras/stt644.
- Michele Cappellari, Richard M. McDermid, Katherine Alatalo, Leo Blitz, Maxime Bois, Frédéric Bournaud, M. Bureau, Alison F. Crocker, Roger L. Davies, Timothy A. Davis, P. T. de Zeeuw, Pierre-Alain Duc, Eric Emsellem, Sadegh Khochfar, Davor Krajnović, Harald Kuntschner, Raffaella Morganti, Thorsten Naab, Tom Oosterloo, Marc Sarzi, Nicholas Scott, Paolo Serra, Anne-Marie Weijmans, and Lisa M. Young. The ATLAS^{3D} project - XX. Mass-size and mass- σ distributions of early-type galaxies: bulge fraction drives kinematics, mass-to-light ratio, molecular gas fraction and stellar initial mass function. *MNRAS*, 432(3):1862–1893, July 2013b. doi: 10.1093/mnras/stt644.
- Michele Cappellari, Nicholas Scott, Katherine Alatalo, Leo Blitz, Maxime Bois, Frédéric Bournaud, M. Bureau, Alison F. Crocker, Roger L. Davies, Timothy A. Davis, P. T. de Zeeuw, Pierre-Alain Duc, Eric Emsellem, Sadegh Khochfar, Davor Krajnović, Harald Kuntschner, Richard M. McDermid, Raffaella Morganti, Thorsten Naab, Tom Oosterloo, Marc Sarzi, Paolo Serra, Anne-Marie Weijmans, and Lisa M. Young. The ATLAS^{3D} project - XV. Benchmark for early-type galaxies scaling relations from 260 dynamical models: mass-to-light ratio, dark matter, Fundamental Plane and Mass Plane. *MNRAS*, 432(3):1709–1741, July 2013c. doi: 10.1093/mnras/stt562.
- C. Marcella Carollo, I. John Danziger, R. Michael Rich, and Xinzhong Chen. Nuclear Properties of Kinematically Distinct Cores. *ApJ*, 491(2):545–560, December 1997. doi: 10.1086/304979.
- Gilles Chabrier. Galactic Stellar and Substellar Initial Mass Function. *PASP*, 115(809): 763–795, July 2003. doi: 10.1086/376392.
- Thomas E. Collett, Lindsay J. Oldham, Russell J. Smith, Matthew W. Auger, Kyle B. Westfall, David Bacon, Robert C. Nichol, Karen L. Masters, Kazuya Koyama, and

- Remco van den Bosch. A precise extragalactic test of General Relativity. *Science*, 360 (6395):1342–1346, June 2018. doi: 10.1126/science.aao2469.
- William P. Collier, Russell J. Smith, and John R. Lucey. A new strong-lensing galaxy at $z=0.066$: another elliptical galaxy with a lightweight IMF. *MNRAS*, 478(2):1595–1600, August 2018. doi: 10.1093/mnras/sty1188.
- William P. Collier, Russell J. Smith, and John R. Lucey. MNELLS: the MUSE nearby early-type galaxy lens locator survey. *MNRAS*, 494(1):271–292, May 2020. doi: 10.1093/mnras/staa602.
- Charlie Conroy. Modeling the Panchromatic Spectral Energy Distributions of Galaxies. *ARA&A*, 51(1):393–455, August 2013. doi: 10.1146/annurev-astro-082812-141017.
- Charlie Conroy and Pieter G. van Dokkum. The Stellar Initial Mass Function in Early-type Galaxies From Absorption Line Spectroscopy. II. Results. *ApJ*, 760(1):71, November 2012. doi: 10.1088/0004-637X/760/1/71.
- Charlie Conroy, Genevieve J. Graves, and Pieter G. van Dokkum. Early-type Galaxy Archeology: Ages, Abundance Ratios, and Effective Temperatures from Full-spectrum Fitting. *ApJ*, 780(1):33, January 2014. doi: 10.1088/0004-637X/780/1/33.
- Charlie Conroy, Alexa Villaume, Pieter G. van Dokkum, and Karin Lind. Metal-rich, Metal-poor: Updated Stellar Population Models for Old Stellar Systems. *ApJ*, 854(2):139, February 2018. doi: 10.3847/1538-4357/aaab49.
- P. Crane, M. Stiavelli, I. R. King, J. M. Deharveng, R. Albrecht, C. Barbieri, J. C. Blades, A. Boksenberg, M. J. Disney, P. Jakobsen, T. M. Kamperman, F. Machetto, C. D. Mackay, F. Paresce, G. Weigelt, D. Baxter, P. Greenfield, R. Jedrzejewski, A. Nota, and W. B. Sparks. High Resolution Imaging of Galaxy Cores. *AJ*, 106:1371, October 1993. doi: 10.1086/116733.
- N. Cretton, P. T. de Zeeuw, R. P. van der Marel, and H.-W. Rix. Axisymmetric Three-Integral Models for Galaxies. *ApJS*, 124:383–401, October 1999. doi: 10.1086/313264.
- Timothy A. Davis and Richard M. McDermid. Spatially resolved variations of the IMF mass normalization in early-type galaxies as probed by molecular gas kinematics. *MNRAS*, 464(1):453–468, January 2017. doi: 10.1093/mnras/stw2366.
- R. S. de Jong and E. F. Bell. Stellar Mass-to-Light Ratios and the Tully-Fisher Relation. In José G. Funes and Enrico Maria Corsini, editors, *Galaxy Disks and Disk Galaxies*, volume 230 of *Astronomical Society of the Pacific Conference Series*, pages 555–556, January 2001. doi: 10.48550/arXiv.astro-ph/0008056.
- Stefano de Nicola, Bianca Neureiter, Jens Thomas, Roberto P. Saglia, and Ralf Bender. Accuracy and precision of triaxial orbit models - II. Viewing angles, shape, and orbital structure. *MNRAS*, 517(3):3445–3458, December 2022. doi: 10.1093/mnras/stac2852.

- Gerard de Vaucouleurs. Recherches sur les Nebuleuses Extragalactiques. *Annales d'Astrophysique*, 11:247, January 1948.
- Gerard de Vaucouleurs. Classification and Morphology of External Galaxies. *Handbuch der Physik*, 53:275, January 1959. doi: 10.1007/978-3-642-45932-0_7.
- P. T. de Zeeuw, M. Bureau, Eric Emsellem, R. Bacon, C. M. Carollo, Y. Copin, Roger L. Davies, Harald Kuntschner, Bryan W. Miller, G. Monnet, Reynier F. Peletier, and E. K. Verolme. The SAURON project - II. Sample and early results. *MNRAS*, 329(3):513–530, January 2002. doi: 10.1046/j.1365-8711.2002.05059.x.
- Tim de Zeeuw and Marijn Franx. Structure and dynamics of elliptical galaxies. *ARA&A*, 29:239–274, January 1991. doi: 10.1146/annurev.aa.29.090191.001323.
- Herwig Dejonghe and David Merritt. Inferring the Mass of Spherical Stellar Systems from Velocity Moments. *ApJ*, 391:531, June 1992. doi: 10.1086/171368.
- S. Djorgovski and Marc Davis. Fundamental Properties of Elliptical Galaxies. *ApJ*, 313:59, February 1987. doi: 10.1086/164948.
- H. Domínguez Sánchez, M. Bernardi, J. R. Brownstein, N. Drory, and R. K. Sheth. Galaxy properties as revealed by MaNGA - I. Constraints on IMF and M_*/L gradients in ellipticals. *MNRAS*, 489(4):5612–5632, November 2019. doi: 10.1093/mnras/stz2414.
- T. Ebisuzaki, J. Makino, and S. K. Okumura. Merging of two galaxies with central black holes. *Nature*, 354:212–214, November 1991. doi: 10.1038/354212a0.
- Eric Emsellem, Michele Cappellari, Reynier F. Peletier, Richard M. McDermid, R. Bacon, M. Bureau, Y. Copin, Roger L. Davies, Davor Krajnović, Harald Kuntschner, Bryan W. Miller, and P. Tim de Zeeuw. The SAURON project - III. Integral-field absorption-line kinematics of 48 elliptical and lenticular galaxies. *MNRAS*, 352(3):721–743, August 2004. doi: 10.1111/j.1365-2966.2004.07948.x.
- Eric Emsellem, Michele Cappellari, Davor Krajnović, Glenn van de Ven, R. Bacon, M. Bureau, Roger L. Davies, P. T. de Zeeuw, Jesús Falcón-Barroso, Harald Kuntschner, Richard McDermid, Reynier F. Peletier, and Marc Sarzi. The SAURON project - IX. A kinematic classification for early-type galaxies. *MNRAS*, 379(2):401–417, August 2007. doi: 10.1111/j.1365-2966.2007.11752.x.
- Eric Emsellem, Michele Cappellari, Davor Krajnović, Katherine Alatalo, Leo Blitz, Maxime Bois, Frédéric Bournaud, Martin Bureau, Roger L. Davies, Timothy A. Davis, P. T. de Zeeuw, Sadegh Khochfar, Harald Kuntschner, Pierre-Yves Lablanche, Richard M. McDermid, Raffaella Morganti, Thorsten Naab, Tom Oosterloo, Marc Sarzi, Nicholas Scott, Paolo Serra, Glenn van de Ven, Anne-Marie Weijmans, and Lisa M. Young. The ATLAS^{3D} project - III. A census of the stellar angular momentum within the effective radius of early-type galaxies: unveiling the distribution of fast and slow rotators. *MNRAS*, 414(2):888–912, June 2011. doi: 10.1111/j.1365-2966.2011.18496.x.

- Peter Erwin, Jens Thomas, Roberto P. Saglia, Maximilian Fabricius, Stephanie P. Rusli, Stella Seitz, and Ralf Bender. NGC 307 and the effects of dark-matter haloes on measuring supermassive black holes in disc galaxies. *MNRAS*, 473(2):2251–2274, January 2018. doi: 10.1093/mnras/stx2499.
- Peter Erwin, Anil Seth, Victor P. Debattista, Marja Seidel, Kianusch Mehrgan, Jens Thomas, Roberto Saglia, Adriana de Lorenzo-Cáceres, Witold Maciejewski, Maximilian Fabricius, Jairo Méndez-Abreu, Ulrich Hopp, Matthias Kluge, John E. Beckman, Ralf Bender, Niv Drory, and Deanne Fisher. Composite bulges - II. Classical bulges and nuclear discs in barred galaxies: the contrasting cases of NGC 4608 and NGC 4643. *MNRAS*, 502(2):2446–2473, April 2021. doi: 10.1093/mnras/stab126.
- Event Horizon Telescope Collaboration, K. Akiyama, A. Alberdi, W. Alef, K. Asada, R. Azulay, A.-K. Baczko, D. Ball, M. Baloković, J. Barrett, and et al. First M87 Event Horizon Telescope Results. I. The Shadow of the Supermassive Black Hole. *ApJ*, 875(1):L1, April 2019. doi: 10.3847/2041-8213/ab0ec7.
- S. M. Faber, A. Dressler, R. L. Davies, D. Burstein, D. Lynden Bell, R. Terlevich, and G. Wegner. Global Scaling Relations for Elliptical Galaxies and Implications for Formation. In Sandra M. Faber, editor, *Nearly Normal Galaxies. From the Planck Time to the Present*, page 175, January 1987.
- S. M. Faber, Scott Tremaine, Edward A. Ajhar, Yong-Ik Byun, Alan Dressler, Karl Gebhardt, Carl Grillmair, John Kormendy, Tod R. Lauer, and Douglas Richstone. The Centers of Early-Type Galaxies with HST. IV. Central Parameter Relations. *AJ*, 114:1771, November 1997. doi: 10.1086/118606.
- L. Ferrarese, F. C. van den Bosch, H. C. Ford, W. Jaffe, and R. W. O’Connell. Hubble Space Telescope Photometry of the Central Regions of Virgo Cluster Elliptical Galaxies. III. Brightness Profiles. *AJ*, 108:1598, November 1994. doi: 10.1086/117180.
- Laura Ferrarese, Patrick Cote, John P. Blakeslee, Simona Mei, David Merritt, and Michael J. West. The Inner Workings of Early-Type Galaxies: Cores, Nuclei and Supermassive Black Holes (Including a Critical Comparison of Nuker and core-Sersic/Sersic models). *arXiv e-prints*, art. astro-ph/0612139, December 2006. doi: 10.48550/arXiv.astro-ph/0612139.
- I. Ferreras, F. La Barbera, I. G. de La Rosa, A. Vazdekis, R. R. de Carvalho, J. Falcon-Barroso, and E. Ricciardelli. Systematic variation of the stellar initial mass function with velocity dispersion in early-type galaxies. *MNRAS*, 429:L15–L19, February 2013. doi: 10.1093/mnras/sls014.
- Steven L. Finkelstein, Micaela B. Bagley, Henry C. Ferguson, Stephen M. Wilkins, Jeyhan S. Kartaltepe, Casey Papovich, L. Y. Aaron Yung, Pablo Arrabal Haro, Peter Behroozi, Mark Dickinson, Dale D. Kocevski, Anton M. Koekemoer, Rebecca L. Larson, Aurélien Le Bail, Alexa M. Morales, Pablo G. Pérez-González, Denis Burgarella,

- Romeel Davé, Michaela Hirschmann, Rachel S. Somerville, Stijn Wuyts, Volker Bromm, Caitlin M. Casey, Adriano Fontana, Seiji Fujimoto, Jonathan P. Gardner, Mauro Giavalisco, Andrea Grazian, Norman A. Grogin, Nimish P. Hathi, Taylor A. Hutchison, Saurabh W. Jha, Shardha Jogee, Lisa J. Kewley, Allison Kirkpatrick, Arianna S. Long, Jennifer M. Lotz, Laura Pentericci, Justin D. R. Pierel, Nor Pirzkal, Swara Ravindranath, Russell E. Ryan, Jonathan R. Trump, Guang Yang, Rachana Bhatawdekar, Laura Bisigello, Véronique Buat, Antonello Calabrò, Marco Castellano, Nikko J. Cleri, M. C. Cooper, Darren Croton, Emanuele Daddi, Avishai Dekel, David Elbaz, Maximilien Franco, Eric Gawiser, Benne W. Holwerda, Marc Huertas-Company, Anne E. Jaskot, Gene C. K. Leung, Ray A. Lucas, Bahram Mobasher, Viraj Pandya, Sandro Tacchella, Benjamin J. Weiner, and Jorge A. Zavala. CEERS Key Paper. I. An Early Look into the First 500 Myr of Galaxy Formation with JWST. *ApJ*, 946(1):L13, March 2023. doi: 10.3847/2041-8213/acade4.
- Marijn Franx, Garth Illingworth, and Tim de Zeeuw. The Ordered Nature of Elliptical Galaxies: Implications for Their Intrinsic Angular Momenta and Shapes. *ApJ*, 383:112, December 1991. doi: 10.1086/170769.
- M. Frigo, T. Naab, A. Rantala, P. H. Johansson, B. Neureiter, J. Thomas, and F. Rizzuto. The two phases of core formation - orbital evolution in the centres of ellipticals with supermassive black hole binaries. *MNRAS*, 508(3):4610–4624, December 2021. doi: 10.1093/mnras/stab2754.
- Karl Gebhardt and Jens Thomas. The Black Hole Mass, Stellar Mass-to-Light Ratio, and Dark Halo in M87. *ApJ*, 700(2):1690–1701, August 2009. doi: 10.1088/0004-637X/700/2/1690.
- Karl Gebhardt, Douglas Richstone, Edward A. Ajhar, Tod R. Lauer, Yong-Ik Byun, John Kormendy, Alan Dressler, S. M. Faber, Carl Grillmair, and Scott Tremaine. The Centers of Early-Type Galaxies With HST. III. Non-Parametric Recovery of Stellar Luminosity Distribution. *AJ*, 112:105, July 1996. doi: 10.1086/117992.
- Karl Gebhardt, Douglas Richstone, Scott Tremaine, Tod R. Lauer, Ralf Bender, Gary Bower, Alan Dressler, S. M. Faber, Alexei V. Filippenko, Richard Green, Carl Grillmair, Luis C. Ho, John Kormendy, John Magorrian, and Jason Pinkney. Axisymmetric Dynamical Models of the Central Regions of Galaxies. *ApJ*, 583(1):92–115, January 2003. doi: 10.1086/345081.
- O. E. Gerhard. Line-of-sight velocity profiles in spherical galaxies: breaking the degeneracy between anisotropy and mass. *MNRAS*, 265:213, November 1993. doi: 10.1093/mnras/265.1.213.
- Alister W. Graham, Peter Erwin, I. Trujillo, and A. Asensio Ramos. A New Empirical Model for the Structural Analysis of Early-Type Galaxies, and A Critical Review of the Nuker Model. *AJ*, 125(6):2951–2963, June 2003. doi: 10.1086/375320.

- Meng Gu, Jenny E. Greene, Andrew B. Newman, Christina Kreisch, Matthew E. Quenneville, Chung-Pei Ma, and John P. Blakeslee. The MASSIVE Survey. XVI. The Stellar Initial Mass Function in the Center of MASSIVE Early-type Galaxies. *ApJ*, 932(2):103, June 2022. doi: 10.3847/1538-4357/ac69ea.
- Alessia Gualandris and David Merritt. Ejection of Supermassive Black Holes from Galaxy Cores. *ApJ*, 678(2):780–797, May 2008. doi: 10.1086/586877.
- M. L. P. Gunawardhana, A. M. Hopkins, R. G. Sharp, S. Brough, E. Taylor, J. Bland-Hawthorn, C. Maraston, R. J. Tuffs, C. C. Popescu, D. Wijesinghe, D. H. Jones, S. Croom, E. Sadler, S. Wilkins, S. P. Driver, J. Liske, P. Norberg, I. K. Baldry, S. P. Bamford, J. Loveday, J. A. Peacock, A. S. G. Robotham, D. B. Zucker, Q. A. Parker, C. J. Conselice, E. Cameron, C. S. Frenk, D. T. Hill, L. S. Kelvin, K. Kuijken, B. F. Madore, B. Nichol, H. R. Parkinson, K. A. Pimbblet, M. Prescott, W. J. Sutherland, D. Thomas, and E. van Kampen. Galaxy and Mass Assembly (GAMA): the star formation rate dependence of the stellar initial mass function. *MNRAS*, 415(2):1647–1662, August 2011. doi: 10.1111/j.1365-2966.2011.18800.x.
- Patrick Hennebelle and Gilles Chabrier. Analytical Theory for the Initial Mass Function: CO Clumps and Prestellar Cores. *ApJ*, 684(1):395–410, September 2008. doi: 10.1086/589916.
- J. G. Hills and L. W. Fullerton. Computer simulations of close encounters between single stars and hard binaries. *AJ*, 85:1281–1291, September 1980. doi: 10.1086/112798.
- Michael Hilz, Thorsten Naab, Jeremiah P. Ostriker, Jens Thomas, Andreas Burkert, and Roland Jesseit. Relaxation and stripping - The evolution of sizes, dispersions and dark matter fractions in major and minor mergers of elliptical galaxies. *MNRAS*, 425(4):3119–3136, October 2012. doi: 10.1111/j.1365-2966.2012.21541.x.
- Philip F. Hopkins. The stellar initial mass function, core mass function and the last-crossing distribution. *MNRAS*, 423(3):2037–2044, July 2012. doi: 10.1111/j.1365-2966.2012.20731.x.
- Philip F. Hopkins, Lars Hernquist, Thomas J. Cox, Suvendra N. Dutta, and Barry Rothberg. Dissipation and Extra Light in Galactic Nuclei. I. Gas-Rich Merger Remnants. *ApJ*, 679(1):156–181, May 2008. doi: 10.1086/587544.
- Philip F. Hopkins, Thomas J. Cox, Suvendra N. Dutta, Lars Hernquist, John Kormendy, and Tod R. Lauer. Dissipation and Extra Light in Galactic Nuclei. II. “Cusp” Ellipticals. *ApJS*, 181(1):135–182, March 2009a. doi: 10.1088/0067-0049/181/1/135.
- Philip F. Hopkins, Tod R. Lauer, Thomas J. Cox, Lars Hernquist, and John Kormendy. Dissipation and Extra Light in Galactic Nuclei. III. “Core” Ellipticals and “Missing” Light. *ApJS*, 181(2):486–532, April 2009b. doi: 10.1088/0067-0049/181/2/486.

- Erik A. Hoversten and Karl Glazebrook. Evidence for a Nonuniversal Stellar Initial Mass Function from the Integrated Properties of SDSS Galaxies. *ApJ*, 675(1):163–187, March 2008. doi: 10.1086/524095.
- E. P. Hubble. *Realm of the Nebulae*. 1936.
- J. H. Jeans. Bakerian Lecture, 1917: The Configurations of Rotating Compressible Masses. *Philosophical Transactions of the Royal Society of London Series A*, 218:157–210, January 1919. doi: 10.1098/rsta.1919.0003.
- R. D. Joseph and G. S. Wright. Recent star formation in interacting galaxies - II. Super starbursts in merging galaxies. *MNRAS*, 214:87–95, May 1985. doi: 10.1093/mnras/214.2.87.
- Susan A. Kassin, Roelof S. de Jong, and Richard W. Pogge. Dark and Baryonic Matter in Bright Spiral Galaxies. I. Near-Infrared and Optical Broadband Surface Photometry of 30 Galaxies. *ApJS*, 162(1):80–96, January 2006. doi: 10.1086/498394.
- G. Kauffmann, S. D. M. White, and B. Guiderdoni. The formation and evolution of galaxies within merging dark matter haloes. *MNRAS*, 264:201–218, September 1993. doi: 10.1093/mnras/264.1.201.
- Jr. Kennicutt, R. C. The rate of star formation in normal disk galaxies. *ApJ*, 272:54–67, September 1983. doi: 10.1086/161261.
- Jr. Kennicutt, Robert C. Overview: The Initial Mass Function in Galaxies. In Gary Gilmore and Debbie Howell, editors, *The Stellar Initial Mass Function (38th Herstmonceux Conference)*, volume 142 of *Astronomical Society of the Pacific Conference Series*, page 1, January 1998.
- M. Kluge, B. Neureiter, A. Riffeser, R. Bender, C. Goessl, U. Hopp, M. Schmidt, C. Ries, and N. Brosch. Structure of Brightest Cluster Galaxies and Intracluster Light. *ApJS*, 247(2):43, April 2020. doi: 10.3847/1538-4365/ab733b.
- Matthias Kluge and Ralf Bender. Minor Mergers are not enough: The importance of Major Mergers during Brightest Cluster Galaxy assembly. *arXiv e-prints*, art. arXiv:2304.03527, April 2023. doi: 10.48550/arXiv.2304.03527.
- J. Kormendy. Brightness profiles of the cores of bulges and elliptical galaxies. *ApJ*, 292:L9–L13, May 1985. doi: 10.1086/184463.
- J. Kormendy, A. Dressler, Y. I. Byun, S. M. Faber, C. Grillmair, T. R. Lauer, D. Richstone, and S. Tremaine. HST Photometry of the Cores of Early-Type Galaxies. In *European Southern Observatory Conference and Workshop Proceedings*, volume 49 of *European Southern Observatory Conference and Workshop Proceedings*, page 147, January 1994.

- John Kormendy. The Central Structure of Elliptical Galaxies and the Stellar-Dynamical Search for Supermassive Black Holes. In David R. Merritt, Monica Valluri, and J. A. Sellwood, editors, *Galaxy Dynamics - A Rutgers Symposium*, volume 182 of *Astronomical Society of the Pacific Conference Series*, page 124, August 1999.
- John Kormendy and Ralf Bender. A Proposed Revision of the Hubble Sequence for Elliptical Galaxies. *ApJ*, 464:L119, June 1996. doi: 10.1086/310095.
- John Kormendy and Ralf Bender. Correlations between Supermassive Black Holes, Velocity Dispersions, and Mass Deficits in Elliptical Galaxies with Cores. *ApJ*, 691(2):L142–L146, February 2009. doi: 10.1088/0004-637X/691/2/L142.
- John Kormendy and Ralf Bender. A Revised Parallel-sequence Morphological Classification of Galaxies: Structure and Formation of S0 and Spheroidal Galaxies. *ApJS*, 198(1):2, January 2012. doi: 10.1088/0067-0049/198/1/2.
- John Kormendy and Ralf Bender. The $L_{\nu} \text{prop} \sigma^8$ Correlation for Elliptical Galaxies with Cores: Relation with Black Hole Mass. *ApJ*, 769(1):L5, May 2013. doi: 10.1088/2041-8205/769/1/L5.
- John Kormendy and Luis C. Ho. Coevolution (Or Not) of Supermassive Black Holes and Host Galaxies. *ARA&A*, 51(1):511–653, August 2013. doi: 10.1146/annurev-astro-082708-101811.
- John Kormendy and Douglas Richstone. Inward Bound—The Search For Supermassive Black Holes In Galactic Nuclei. *ARA&A*, 33:581, January 1995. doi: 10.1146/annurev.aa.33.090195.003053.
- John Kormendy and David B. Sanders. Ultraluminous IRAS Galaxies: Formation of Elliptical Galaxies by Merger-induced Dissipative Collapse. *ApJ*, 390:L53, May 1992. doi: 10.1086/186370.
- John Kormendy, David B. Fisher, Mark E. Cornell, and Ralf Bender. Structure and Formation of Elliptical and Spheroidal Galaxies. *ApJS*, 182(1):216–309, May 2009. doi: 10.1088/0067-0049/182/1/216.
- Davor Krajnović, Peter M. Weilbacher, Tanya Urrutia, Eric Emsellem, C. Marcella Carollo, Maryam Shirazi, Roland Bacon, Thierry Contini, Benoît Epinat, Sebastian Kamann, Thomas Martinsson, and Matthias Steinmetz. Unveiling the counter-rotating nature of the kinematically distinct core in NGC 5813 with MUSE. *MNRAS*, 452(1):2–18, September 2015. doi: 10.1093/mnras/stv958.
- Pavel Kroupa. On the variation of the initial mass function. *MNRAS*, 322(2):231–246, April 2001. doi: 10.1046/j.1365-8711.2001.04022.x.
- Pavel Kroupa. The Initial Mass Function of Stars: Evidence for Uniformity in Variable Systems. *Science*, 295(5552):82–91, January 2002. doi: 10.1126/science.1067524.

- Mark R. Krumholz. On the Origin of Stellar Masses. *ApJ*, 743(2):110, December 2011. doi: 10.1088/0004-637X/743/2/110.
- F. La Barbera, I. Ferreras, A. Vazdekis, I. G. de la Rosa, R. R. de Carvalho, M. Trevisan, J. Falcón-Barroso, and E. Ricciardelli. SPIDER VIII – constraints on the stellar initial mass function of early-type galaxies from a variety of spectral features. *Monthly Notices of the Royal Astronomical Society*, 433(4):3017–3047, 06 2013. ISSN 0035-8711. doi: 10.1093/mnras/stt943. URL <https://doi.org/10.1093/mnras/stt943>.
- F. La Barbera, A. Vazdekis, I. Ferreras, A. Pasquali, C. Allende Prieto, I. Martín-Navarro, D. S. Aguado, R. R. de Carvalho, S. Rembold, J. Falcón-Barroso, and G. van de Ven. IMF radial gradients in most massive early-type galaxies. *MNRAS*, 489(3):4090–4110, November 2019. doi: 10.1093/mnras/stz2192.
- T. R. Lauer. Boxy isophotes, discs and dust lanes in elliptical galaxies. *MNRAS*, 216: 429–438, September 1985. doi: 10.1093/mnras/216.2.429.
- T. R. Lauer, E. A. Ajhar, Y. I. Byun, A. Dressler, S. M. Faber, C. Grillmair, J. Kormendy, D. Richstone, and S. Tremaine. The Centers of Early-Type Galaxies with HST.I.An Observational Survey. *AJ*, 110:2622, December 1995. doi: 10.1086/117719.
- Tod R. Lauer, S. M. Faber, Karl Gebhardt, Douglas Richstone, Scott Tremaine, Edward A. Ajhar, M. C. Aller, Ralf Bender, Alan Dressler, Alexei V. Filippenko, Richard Green, Carl J. Grillmair, Luis C. Ho, John Kormendy, John Magorrian, Jason Pinkney, and Christos Siopis. The Centers of Early-Type Galaxies with Hubble Space Telescope. V. New WFPC2 Photometry. *AJ*, 129(5):2138–2185, May 2005. doi: 10.1086/429565.
- Tod R. Lauer, S. M. Faber, Douglas Richstone, Karl Gebhardt, Scott Tremaine, Marc Postman, Alan Dressler, M. C. Aller, Alexei V. Filippenko, Richard Green, Luis C. Ho, John Kormendy, John Magorrian, and Jason Pinkney. The Masses of Nuclear Black Holes in Luminous Elliptical Galaxies and Implications for the Space Density of the Most Massive Black Holes. *ApJ*, 662(2):808–834, June 2007a. doi: 10.1086/518223.
- Tod R. Lauer, S. M. Faber, Douglas Richstone, Karl Gebhardt, Scott Tremaine, Marc Postman, Alan Dressler, M. C. Aller, Alexei V. Filippenko, Richard Green, Luis C. Ho, John Kormendy, John Magorrian, and Jason Pinkney. The Masses of Nuclear Black Holes in Luminous Elliptical Galaxies and Implications for the Space Density of the Most Massive Black Holes. *ApJ*, 662(2):808–834, Jun 2007b. doi: 10.1086/518223.
- Tod R. Lauer, Karl Gebhardt, S. M. Faber, Douglas Richstone, Scott Tremaine, John Kormendy, M. C. Aller, Ralf Bender, Alan Dressler, Alexei V. Filippenko, Richard Green, and Luis C. Ho. The Centers of Early-Type Galaxies with Hubble Space Telescope. VI. Bimodal Central Surface Brightness Profiles. *ApJ*, 664(1):226–256, July 2007c. doi: 10.1086/519229.

- Chao Li, Ling Zhu, R. J. Long, Shude Mao, Eric W. Peng, Marc Sarzi, Glenn van de Ven, Hongxin Zhang, Rui Guo, Xiangxiang Xue, Alessia Longobardi, Patrick Côté, Laura Ferrarese, Chengze Liu, Stephen Gwyn, Sungsoon Lim, and Youkyung Ko. A discrete chemo-dynamical model of M87's globular clusters: Kinematics extending to ~ 400 kpc. *MNRAS*, 492(2):2775–2795, February 2020. doi: 10.1093/mnras/staa027.
- Hongyu Li, Junqiang Ge, Shude Mao, Michele Cappellari, R. J. Long, Ran Li, Eric Emsellem, Aaron A. Dutton, Cheng Li, Kevin Bundy, Daniel Thomas, Niv Drory, and Alexandre Roman Lopes. SDSS-IV MaNGA: Variation of the Stellar Initial Mass Function in Spiral and Early-type Galaxies. *ApJ*, 838(2):77, April 2017. doi: 10.3847/1538-4357/aa662a.
- Emily R. Liepold, Chung-Pei Ma, and Jonelle L. Walsh. Keck Integral-field Spectroscopy of M87 Reveals an Intrinsically Triaxial Galaxy and a Revised Black Hole Mass. *ApJ*, 945(2):L35, March 2023. doi: 10.3847/2041-8213/acbbcf.
- Mathias Lipka and Jens Thomas. A novel approach to optimize the regularization and evaluation of dynamical models using a model selection framework. *MNRAS*, 504(3):4599–4625, July 2021. doi: 10.1093/mnras/stab1092.
- D. Lynden-Bell. Galactic Nuclei as Collapsed Old Quasars. *Nature*, 223(5207):690–694, August 1969. doi: 10.1038/223690a0.
- M. Lyubenova, I. Martín-Navarro, G. van de Ven, J. Falcón-Barroso, L. Galbany, A. Galazzi, R. García-Benito, R. González Delgado, B. Husemann, F. La Barbera, R. A. Marino, D. Mast, J. Mendez-Abreu, R. F. P. Peletier, P. Sánchez-Blázquez, S. F. Sánchez, S. C. Trager, R. C. E. van den Bosch, A. Vazdekis, C. J. Walcher, L. Zhu, S. Zibetti, B. Ziegler, J. Bland-Hawthorn, and CALIFA Collaboration. IMF shape constraints from stellar populations and dynamics from CALIFA. *MNRAS*, 463(3):3220–3225, December 2016. doi: 10.1093/mnras/stw2434.
- John Magorrian, Scott Tremaine, Douglas Richstone, Ralf Bender, Gary Bower, Alan Dressler, S. M. Faber, Karl Gebhardt, Richard Green, Carl Grillmair, John Kormendy, and Tod Lauer. The Demography of Massive Dark Objects in Galaxy Centers. *AJ*, 115(6):2285–2305, June 1998. doi: 10.1086/300353.
- Junichiro Makino and Toshikazu Ebisuzaki. Merging of Galaxies with Central Black Holes. I. Hierarchical Mergings of Equal-Mass Galaxies. *ApJ*, 465:527, July 1996. doi: 10.1086/177439.
- Junichiro Makino and Yoko Funato. Evolution of Massive Black Hole Binaries. *ApJ*, 602(1):93–102, February 2004. doi: 10.1086/380917.
- C. Maraston, L. Hill, D. Thomas, R. Yan, Y. Chen, J. Lian, T. Parikh, J. Neumann, S. Meneses-Goytia, M. Bershadsky, N. Drory, D. Bizyaev, A. Concas, J. Brownstein, D. Lazarz, G. Stringfellow, and K. Stassun. Stellar population models based on the

- SDSS-IV MaStar library of stellar spectra - I. Intermediate-age/old models. *MNRAS*, 496(3):2962–2997, August 2020. doi: 10.1093/mnras/staa1489.
- Claudia Maraston. Evolutionary synthesis of stellar populations: a modular tool. *MNRAS*, 300(3):872–892, November 1998. doi: 10.1046/j.1365-8711.1998.01947.x.
- Ignacio Martín-Navarro, Francesco La Barbera, Alexandre Vazdekis, Jesús Falcón-Barroso, and Ignacio Ferreras. Radial variations in the stellar initial mass function of early-type galaxies. *MNRAS*, 447(2):1033–1048, February 2015a. doi: 10.1093/mnras/stu2480.
- Ignacio Martín-Navarro, Alexandre Vazdekis, Francesco La Barbera, Jesús Falcón-Barroso, Mariya Lyubenova, Glenn van de Ven, Ignacio Ferreras, S. F. Sánchez, S. C. Trager, R. García-Benito, D. Mast, M. A. Mendoza, P. Sánchez-Blázquez, R. González Delgado, C. J. Walcher, and CALIFA Team. IMF&ndashMetallicity: A Tight Local Relation Revealed by the CALIFA Survey. *ApJ*, 806(2):L31, June 2015b. doi: 10.1088/2041-8205/806/2/L31.
- Nicholas J. McConnell and Chung-Pei Ma. Revisiting the Scaling Relations of Black Hole Masses and Host Galaxy Properties. *ApJ*, 764(2):184, February 2013. doi: 10.1088/0004-637X/764/2/184.
- Nicholas J. McConnell, Chung-Pei Ma, Jeremy D. Murphy, Karl Gebhardt, Tod R. Lauer, James R. Graham, Shelley A. Wright, and Douglas O. Richstone. Dynamical Measurements of Black Hole Masses in Four Brightest Cluster Galaxies at 100 Mpc. *ApJ*, 756(2):179, Sep 2012. doi: 10.1088/0004-637X/756/2/179.
- Richard M. McDermid, Michele Cappellari, Katherine Alatalo, Estelle Bayet, Leo Blitz, Maxime Bois, Frédéric Bournaud, Martin Bureau, Alison F. Crocker, Roger L. Davies, Timothy A. Davis, P. T. de Zeeuw, Pierre-Alain Duc, Eric Emsellem, Sadegh Khochfar, Davor Krajnović, Harald Kuntschner, Raffaella Morganti, Thorsten Naab, Tom Oosterloo, Marc Sarzi, Nicholas Scott, Paolo Serra, Anne-Marie Weijmans, and Lisa M. Young. Connection between Dynamically Derived Initial Mass Function Normalization and Stellar Population Parameters. *ApJ*, 792(2):L37, September 2014. doi: 10.1088/2041-8205/792/2/L37.
- Kianusch Mehrgan, Jens Thomas, Roberto Saglia, Ximena Mazzalay, Peter Erwin, Ralf Bender, Matthias Kluge, and Maximilian Fabricius. A 40 Billion Solar-mass Black Hole in the Extreme Core of Holm 15A, the Central Galaxy of Abell 85. *ApJ*, 887(2):195, December 2019. doi: 10.3847/1538-4357/ab5856.
- Kianusch Mehrgan, Jens Thomas, Roberto Saglia, Taniya Parikh, and Ralf Bender. Detailed Shapes of the Line-of-sight Velocity Distributions in Massive Early-type Galaxies from Nonparametric Spectral Models. *ApJ*, 948(2):79, May 2023a. doi: 10.3847/1538-4357/acbf2e.

- Kianusch Mehrgan, Jens Thomas, Roberto Saglia, Taniya Parikh, and Ralf Bender. Dynamical stellar mass-to-light ratio gradients: Evidence for very centrally concentrated IMF variations in ETGs? *ApJ*, in press 2023b.
- D. Merritt. *Dynamics and Evolution of Galactic Nuclei*. July 2013.
- D. Merritt and M. Milosavljević. Massive Black Hole Binary Evolution. *Living Reviews in Relativity*, 8, November 2005. doi: 10.12942/lrr-2005-8.
- David Merritt. Mass Deficits, Stalling Radii, and the Merger Histories of Elliptical Galaxies. *ApJ*, 648(2):976–986, Sep 2006. doi: 10.1086/506139.
- David Merritt and Prasenjit Saha. Mapping Spherical Potentials with Discrete Radial Velocities. *ApJ*, 409:75, May 1993. doi: 10.1086/172643.
- David Merritt, Seppo Mikkola, and Andras Szell. Long-Term Evolution of Massive Black Hole Binaries. III. Binary Evolution in Collisional Nuclei. *ApJ*, 671(1):53–72, December 2007. doi: 10.1086/522691.
- J. Christopher Mihos and Lars Hernquist. Dense Stellar Cores in Merger Remnants. *ApJ*, 437:L47, December 1994. doi: 10.1086/187679.
- M. Milosavljević and D. Merritt. Formation of Galactic Nuclei. *ApJ*, 563:34–62, December 2001. doi: 10.1086/323830.
- Miloš Milosavljević, David Merritt, Armin Rest, and Frank C. van den Bosch. Galaxy cores as relics of black hole mergers. *MNRAS*, 331(4):L51–L55, April 2002. doi: 10.1046/j.1365-8711.2002.05436.x.
- Julio F. Navarro, Carlos S. Frenk, and Simon D. M. White. The Structure of Cold Dark Matter Halos. *ApJ*, 462:563, May 1996. doi: 10.1086/177173.
- B. Neureiter, J. Thomas, R. Saglia, R. Bender, F. Finozzi, A. Krukau, T. Naab, A. Rantala, and M. Frigo. SMART: a new implementation of Schwarzschild’s Orbit Superposition technique for triaxial galaxies and its application to an N-body merger simulation. *MNRAS*, 500(1):1437–1465, January 2021. doi: 10.1093/mnras/staa3014.
- B. Neureiter, S. de Nicola, J. Thomas, R. Saglia, R. Bender, and A. Rantala. Accuracy and precision of triaxial orbit models I: SMBH mass, stellar mass, and dark-matter halo. *MNRAS*, 519(2):2004–2016, February 2023a. doi: 10.1093/mnras/stac3652.
- Bianca Neureiter, Jens Thomas, Antti Rantala, Thorsten Naab, Kianusch Mehrgan, Roberto Saglia, Stefano de Nicola, and Ralf Bender. The isotropic center of NGC 5419 – A core in formation? *arXiv e-prints*, art. arXiv:2305.03078, May 2023b. doi: 10.48550/arXiv.2305.03078.

- Andrew B. Newman, Richard S. Ellis, and Tommaso Treu. Luminous and Dark Matter Profiles from Galaxies to Clusters: Bridging the Gap with Group-scale Lenses. *ApJ*, 814 (1):26, November 2015. doi: 10.1088/0004-637X/814/1/26.
- Andrew B. Newman, Russell J. Smith, Charlie Conroy, Alexa Villaume, and Pieter van Dokkum. The Initial Mass Function in the Nearest Strong Lenses from SNELLS: Assessing the Consistency of Lensing, Dynamical, and Spectroscopic Constraints. *ApJ*, 845 (2):157, August 2017. doi: 10.3847/1538-4357/aa816d.
- J. L. Nieto and R. Bender. Boxiness in elliptical galaxies. *A&A*, 215:266–271, May 1989.
- J. L. Nieto, R. Bender, J. Arnaud, and P. Surma. The shape of central regions in elliptical galaxies. *A&A*, 244:L25, April 1991a.
- Jean-Luc Nieto, R. Bender, and P. Surma. Central brightness profiles and isophotal shapes in elliptical galaxies. *A&A*, 244:L37, April 1991b.
- Lindsay Oldham and Matthew Auger. Galaxy structure from multiple tracers - III. Radial variations in M87's IMF. *MNRAS*, 474(3):4169–4185, March 2018a. doi: 10.1093/mnras/stx2969.
- Lindsay J. Oldham and Matthew W. Auger. Dark matter contraction and stellar-mass-to-light ratio gradients in massive early-type galaxies. *MNRAS*, 476(1):133–150, May 2018b. doi: 10.1093/mnras/sty065.
- Ludwig Oser, Jeremiah P. Ostriker, Thorsten Naab, Peter H. Johansson, and Andreas Burkert. The Two Phases of Galaxy Formation. *ApJ*, 725(2):2312–2323, December 2010. doi: 10.1088/0004-637X/725/2/2312.
- Taniya Parikh, Daniel Thomas, Claudia Maraston, Kyle B. Westfall, Daniel Goddard, Jianhui Lian, Sofia Meneses-Goytia, Amy Jones, Sam Vaughan, Brett H. Andrews, Matthew Bershad, Dmitry Bizyaev, Jonathan Brinkmann, Joel R. Brownstein, Kevin Bundy, Niv Drory, Eric Emsellem, David R. Law, Jeffrey A. Newman, Alexandre Roman-Lopes, David Wake, Renbin Yan, and Zheng Zheng. SDSS-IV MaNGA: the spatially resolved stellar initial mass function in ~ 400 early-type galaxies. *MNRAS*, 477(3):3954–3982, July 2018. doi: 10.1093/mnras/sty785.
- A. Poci, R. M. McDermid, M. Lyubenova, I. Martín-Navarro, G. van de Ven, L. Coccato, E. M. Corsini, K. Fahrion, J. Falcón-Barroso, D. A. Gadotti, E. Iodice, F. Pinna, M. Sarzi, P. T. de Zeeuw, and L. Zhu. The Fornax3D project: intrinsic correlations between orbital properties and the stellar initial mass function. *MNRAS*, 514(3):3660–3669, August 2022. doi: 10.1093/mnras/stac1514.
- Silvia Posacki, Michele Cappellari, Tommaso Treu, Silvia Pellegrini, and Luca Ciotti. The stellar initial mass function of early-type galaxies from low to high stellar velocity dispersion: homogeneous analysis of ATLAS^{3D} and Sloan Lens ACS galaxies. *MNRAS*, 446 (1):493–509, January 2015. doi: 10.1093/mnras/stu2098.

- Matthew E. Quenneville, Christopher M. Liepold, and Chung-Pei Ma. Triaxial Orbit-based Dynamical Modeling of Galaxies with Supermassive Black Holes and an Application to Massive Elliptical Galaxy NGC 1453. *ApJ*, 926(1):30, February 2022. doi: 10.3847/1538-4357/ac3e68.
- Gerald D. Quinlan. The dynamical evolution of massive black hole binaries I. Hardening in a fixed stellar background. *New A*, 1(1):35–56, July 1996a. doi: 10.1016/S1384-1076(96)00003-6.
- Gerald D. Quinlan. The dynamical evolution of massive black hole binaries I. Hardening in a fixed stellar background. *New A*, 1(1):35–56, July 1996b. doi: 10.1016/S1384-1076(96)00003-6.
- Antti Rantala, Peter H. Johansson, Thorsten Naab, Jens Thomas, and Matteo Frigo. The Formation of Extremely Diffuse Galaxy Cores by Merging Supermassive Black Holes. *ApJ*, 864(2):113, September 2018. doi: 10.3847/1538-4357/aada47.
- Antti Rantala, Peter H. Johansson, Thorsten Naab, Jens Thomas, and Matteo Frigo. The Simultaneous Formation of Cored, Tangentially Biased, and Kinematically Decoupled Centers in Massive Early-type Galaxies. *ApJ*, 872(2):L17, February 2019. doi: 10.3847/2041-8213/ab04b1.
- E. Ricciardelli, A. Vazdekis, A. J. Cenarro, and J. Falcón-Barroso. MIUSCAT: extended MILES spectral coverage - II. Constraints from optical photometry. *MNRAS*, 424(1):172–189, July 2012. doi: 10.1111/j.1365-2966.2012.21178.x.
- D. Richstone, E. A. Ajhar, R. Bender, G. Bower, A. Dressler, S. M. Faber, A. V. Filippenko, K. Gebhardt, R. Green, L. C. Ho, J. Kormendy, T. R. Lauer, J. Magorrian, and S. Tremaine. Supermassive black holes and the evolution of galaxies. *Nature*, 385(6701):A14, October 1998. doi: 10.48550/arXiv.astro-ph/9810378.
- D. O. Richstone and S. Tremaine. A general method for constructing spherical galaxy models. *ApJ*, 286:27–37, November 1984. doi: 10.1086/162572.
- D. O. Richstone and S. Tremaine. Maximum-entropy models of galaxies. *ApJ*, 327:82–88, April 1988. doi: 10.1086/166171.
- Hans-Walter Rix, P. Tim de Zeeuw, Nicolas Cretton, Roeland P. van der Marel, and C. Marcella Carollo. Dynamical Modeling of Velocity Profiles: The Dark Halo around the Elliptical Galaxy NGC 2434. *ApJ*, 488(2):702–719, October 1997. doi: 10.1086/304733.
- S. P. Rusli, J. Thomas, P. Erwin, R. P. Saglia, N. Nowak, and R. Bender. The central black hole mass of the high- σ but low-bulge-luminosity lenticular galaxy NGC 1332. *MNRAS*, 410(2):1223–1236, January 2011. doi: 10.1111/j.1365-2966.2010.17610.x.

- S. P. Rusli, J. Thomas, R. P. Saglia, M. Fabricius, P. Erwin, R. Bender, N. Nowak, C. H. Lee, A. Riffeser, and R. Sharp. The Influence of Dark Matter Halos on Dynamical Estimates of Black Hole Mass: 10 New Measurements for High- σ Early-type Galaxies. *AJ*, 146:45, September 2013a. doi: 10.1088/0004-6256/146/3/45.
- S. P. Rusli, P. Erwin, R. P. Saglia, J. Thomas, M. Fabricius, R. Bender, and N. Nowak. Depleted Galaxy Cores and Dynamical Black Hole Masses. *AJ*, 146:160, December 2013b. doi: 10.1088/0004-6256/146/6/160.
- R. P. Saglia, M. Opitsch, P. Erwin, J. Thomas, A. Beifiori, M. Fabricius, X. Mazzalay, N. Nowak, S. P. Rusli, and R. Bender. The SINFONI Black Hole Survey: The Black Hole Fundamental Plane Revisited and the Paths of (Co)evolution of Supermassive Black Holes and Bulges. *ApJ*, 818(1):47, February 2016. doi: 10.3847/0004-637X/818/1/47.
- E. E. Salpeter. Accretion of Interstellar Matter by Massive Objects. *ApJ*, 140:796–800, August 1964. doi: 10.1086/147973.
- Edwin E. Salpeter. The Luminosity Function and Stellar Evolution. *ApJ*, 121:161, January 1955. doi: 10.1086/145971.
- Allan Sandage, Kenneth C. Freeman, and N. R. Stokes. The Intrinsic Flattening of e , so , and Spiral Galaxies as Related to Galaxy Formation and Evolution. *ApJ*, 160:831, June 1970. doi: 10.1086/150475.
- M. Schwarzschild. A numerical model for a triaxial stellar system in dynamical equilibrium. *ApJ*, 232:236–247, August 1979. doi: 10.1086/157282.
- F. Schweizer. Interactions in our time. In Roland Wielen, editor, *Dynamics and Interactions of Galaxies*, pages 60–71. 1990.
- Jose Luis Sersic. *Atlas de Galaxias Australes*. 1968.
- Christos Siopis, Karl Gebhardt, Tod R. Lauer, John Kormendy, Jason Pinkney, Douglas Richstone, S. M. Faber, Scott Tremaine, M. C. Aller, and Ralf Bender. A Stellar Dynamical Measurement of the Black Hole Mass in the Maser Galaxy NGC 4258. *ApJ*, 693(1):946–969, Mar 2009. doi: 10.1088/0004-637X/693/1/946.
- R. J. Smith. Variations in the initial mass function in early-type galaxies: a critical comparison between dynamical and spectroscopic results. *MNRAS*, 443:L69–L73, September 2014. doi: 10.1093/mnrasl/slu082.
- Russell J. Smith, John R. Lucey, and David Carter. The stellar initial mass function in red-sequence galaxies: 1- μ m spectroscopy of Coma cluster galaxies with Subaru/FMOS. *MNRAS*, 426(4):2994–3007, November 2012. doi: 10.1111/j.1365-2966.2012.21922.x.

- Russell J. Smith, John R. Lucey, and Charlie Conroy. The SINFONI Nearby Elliptical Lens Locator Survey: discovery of two new low-redshift strong lenses and implications for the initial mass function in giant early-type galaxies. *MNRAS*, 449(4):3441–3457, June 2015. doi: 10.1093/mnras/stv518.
- Alessandro Sonnenfeld, Tommaso Treu, Philip J. Marshall, Sherry H. Suyu, Raphaël Gavazzi, Matthew W. Auger, and Carlo Nipoti. The SL2S Galaxy-scale Lens Sample. V. Dark Matter Halos and Stellar IMF of Massive Early-type Galaxies Out to Redshift 0.8. *ApJ*, 800(2):94, February 2015. doi: 10.1088/0004-637X/800/2/94.
- Alessandro Sonnenfeld, Anton T. Jaelani, James Chan, Anupreeta More, Sherry H. Suyu, Kenneth C. Wong, Masamune Oguri, and Chien-Hsiu Lee. Survey of gravitationally-lensed objects in HSC imaging (SuGOHI). III. Statistical strong lensing constraints on the stellar IMF of CMASS galaxies. *A&A*, 630:A71, October 2019. doi: 10.1051/0004-6361/201935743.
- C. Spiniello, L. V. E. Koopmans, S. C. Trager, O. Czoske, and T. Treu. The X-Shooter Lens Survey - I. Dark matter domination and a Salpeter-type initial mass function in a massive early-type galaxy. *MNRAS*, 417(4):3000–3009, November 2011. doi: 10.1111/j.1365-2966.2011.19458.x.
- Chiara Spiniello, Scott Trager, Léon V. E. Koopmans, and Charlie Conroy. The stellar IMF in early-type galaxies from a non-degenerate set of optical line indices. *MNRAS*, 438(2):1483–1499, February 2014. doi: 10.1093/mnras/stt2282.
- Matthias Steinmetz and Julio F. Navarro. The hierarchical origin of galaxy morphologies. *New A*, 7(4):155–160, June 2002. doi: 10.1016/S1384-1076(02)00102-1.
- Sabine Thater, Davor Krajnović, Peter M. Weilbacher, Dieu D. Nguyen, Martin Bureau, Michele Cappellari, Timothy A. Davis, Satoru Iguchi, Richard McDermid, Kyoko Onishi, Marc Sarzi, and Glenn van de Ven. Cross-checking SMBH mass estimates in NGC 6958 - I. Stellar dynamics from adaptive optics-assisted MUSE observations. *MNRAS*, 509(4):5416–5436, February 2022. doi: 10.1093/mnras/stab3210.
- Daniel Thomas, Claudia Maraston, and Ralf Bender. Stellar population models of Lick indices with variable element abundance ratios. *MNRAS*, 339(3):897–911, March 2003. doi: 10.1046/j.1365-8711.2003.06248.x.
- J. Thomas, R. P. Saglia, R. Bender, D. Thomas, K. Gebhardt, J. Magorrian, and D. Richstone. Mapping stationary axisymmetric phase-space distribution functions by orbit libraries. *MNRAS*, 353:391–404, September 2004. doi: 10.1111/j.1365-2966.2004.08072.x.
- J. Thomas, R. P. Saglia, R. Bender, D. Thomas, K. Gebhardt, J. Magorrian, E. M. Corsini, and G. Wegner. Dynamical modelling of luminous and dark matter in 17 Coma early-type galaxies. *MNRAS*, 382(2):657–684, December 2007. doi: 10.1111/j.1365-2966.2007.12434.x.

- J. Thomas, R. P. Saglia, R. Bender, D. Thomas, K. Gebhardt, J. Magorrian, E. M. Corsini, and G. Wegner. Dark Matter Scaling Relations and the Assembly Epoch of Coma Early-Type Galaxies. *ApJ*, 691(1):770–782, January 2009. doi: 10.1088/0004-637X/691/1/770.
- J. Thomas, R. P. Saglia, R. Bender, D. Thomas, K. Gebhardt, J. Magorrian, E. M. Corsini, G. Wegner, and S. Seitz. Dynamical masses of early-type galaxies: a comparison to lensing results and implications for the stellar initial mass function and the distribution of dark matter. *MNRAS*, 415(1):545–562, July 2011. doi: 10.1111/j.1365-2966.2011.18725.x.
- J. Thomas, R. P. Saglia, R. Bender, P. Erwin, and M. Fabricius. The Dynamical Fingerprint of Core Scouring in Massive Elliptical Galaxies. *ApJ*, 782:39, February 2014. doi: 10.1088/0004-637X/782/1/39.
- Jens Thomas and Mathias Lipka. A simple data-driven method to optimise the penalty strengths of penalised models and its application to non-parametric smoothing. *MNRAS*, June 2022. doi: 10.1093/mnras/stac1581.
- Jens Thomas, Chung-Pei Ma, Nicholas J. McConnell, Jenny E. Greene, John P. Blakeslee, and Ryan Janish. A 17-billion-solar-mass black hole in a group galaxy with a diffuse core. *Nature*, 532(7599):340–342, April 2016. doi: 10.1038/nature17197.
- A. Toomre. Theories of spiral structure. *ARA&A*, 15:437–478, January 1977. doi: 10.1146/annurev.aa.15.090177.002253.
- S. Tremaine. Summary. In Pieter Timotheus de Zeeuw, editor, *Structure and Dynamics of Elliptical Galaxies*, volume 127, pages 367–373, January 1987. doi: 10.1007/978-94-009-3971-4_30.
- Benoit Tremblay and David Merritt. The Frequency Function of Elliptical Galaxy Intrinsic Shapes. *AJ*, 110:1039, September 1995. doi: 10.1086/117584.
- Tommaso Treu, Matthew W. Auger, Léon V. E. Koopmans, Raphaël Gavazzi, Philip J. Marshall, and Adam S. Bolton. The Initial Mass Function of Early-Type Galaxies. *ApJ*, 709(2):1195–1202, February 2010. doi: 10.1088/0004-637X/709/2/1195.
- I. Trujillo, P. Erwin, A. Asensio Ramos, and A. W. Graham. Evidence for a New Elliptical-Galaxy Paradigm: Sérsic and Core Galaxies. *AJ*, 127:1917–1942, April 2004a. doi: 10.1086/382712.
- I. Trujillo, Peter Erwin, A. Asensio Ramos, and Alister W. Graham. Evidence for a New Elliptical-Galaxy Paradigm: Sérsic and Core Galaxies. *AJ*, 127(4):1917–1942, April 2004b. doi: 10.1086/382712.
- R. C. E. van den Bosch, G. van de Ven, E. K. Verolme, M. Cappellari, and P. T. de Zeeuw. Triaxial orbit based galaxy models with an application to the (apparent) decoupled core

- galaxy NGC 4365. *MNRAS*, 385(2):647–666, April 2008. doi: 10.1111/j.1365-2966.2008.12874.x.
- Roeland P. van der Marel and Marijn Franx. A New Method for the Identification of Non-Gaussian Line Profiles in Elliptical Galaxies. *ApJ*, 407:525, April 1993. doi: 10.1086/172534.
- Pieter van Dokkum, Charlie Conroy, Alexa Villaume, Jean Brodie, and Aaron J. Romanowsky. The Stellar Initial Mass Function in Early-type Galaxies from Absorption Line Spectroscopy. III. Radial Gradients. *ApJ*, 841(2):68, June 2017. doi: 10.3847/1538-4357/aa7135.
- Pieter G. van Dokkum and Charlie Conroy. A substantial population of low-mass stars in luminous elliptical galaxies. *Nature*, 468(7326):940–942, December 2010. doi: 10.1038/nature09578.
- Pieter G. van Dokkum and Charlie Conroy. Confirmation of Enhanced Dwarf-sensitive Absorption Features in the Spectra of Massive Elliptical Galaxies: Further Evidence for a Non-universal Initial Mass Function. *ApJ*, 735(1):L13, July 2011. doi: 10.1088/2041-8205/735/1/L13.
- Pieter G. van Dokkum and Charlie Conroy. The Stellar Initial Mass Function in Early-type Galaxies from Absorption Line Spectroscopy. I. Data and Empirical Trends. *ApJ*, 760(1):70, November 2012. doi: 10.1088/0004-637X/760/1/70.
- A. Vazdekis, E. Casuso, R. F. Peletier, and J. E. Beckman. A New Chemo-evolutionary Population Synthesis Model for Early-Type Galaxies. I. Theoretical Basis. *ApJS*, 106:307, October 1996. doi: 10.1086/192340.
- A. Vazdekis, E. Ricciardelli, A. J. Cenarro, J. G. Rivero-González, L. A. Díaz-García, and J. Falcón-Barroso. MIUSCAT: extended MILES spectral coverage - I. Stellar population synthesis models. *MNRAS*, 424(1):157–171, July 2012. doi: 10.1111/j.1365-2966.2012.21179.x.
- Melanie Veale, Chung-Pei Ma, Jenny E. Greene, Jens Thomas, John P. Blakeslee, Jonelle L. Walsh, and Jennifer Ito. The MASSIVE survey - VIII. Stellar velocity dispersion profiles and environmental dependence of early-type galaxies. *MNRAS*, 473(4):5446–5467, February 2018. doi: 10.1093/mnras/stx2717.
- M. Volonteri, F. Haardt, and P. Madau. The Assembly and Merging History of Supermassive Black Holes in Hierarchical Models of Galaxy Formation. *ApJ*, 582:559–573, January 2003. doi: 10.1086/344675.
- G. A. Wegner, E. M. Corsini, J. Thomas, R. P. Saglia, R. Bender, and S. B. Pu. Further Evidence for Large Central Mass-to-light Ratios in Early-type Galaxies: The Case of Ellipticals and Lenticulars in the A262 Cluster. *AJ*, 144(3):78, September 2012. doi: 10.1088/0004-6256/144/3/78.

- S. D. M. White and M. J. Rees. Core condensation in heavy halos: a two-stage theory for galaxy formation and clustering. *MNRAS*, 183:341–358, May 1978. doi: 10.1093/mnras/183.3.341.
- Xue-Bing Wu, Feige Wang, Xiaohui Fan, Weimin Yi, Wenwen Zuo, Fuyan Bian, Linhua Jiang, Ian D. McGreer, Ran Wang, Jinyi Yang, Qian Yang, David Thompson, and Yuri Beletsky. An ultraluminous quasar with a twelve-billion-solar-mass black hole at redshift 6.30. *Nature*, 518(7540):512–515, February 2015. doi: 10.1038/nature14241.
- H. Zhao. Analytical models for galactic nuclei. *MNRAS*, 278:488–496, January 1996. doi: 10.1093/mnras/278.2.488.
- Simon Zieleniewski, Ryan C. W. Houghton, Niranjan Thatte, Roger L. Davies, and Sam P. Vaughan. Radial gradients in initial mass function sensitive absorption features in the Coma brightest cluster galaxies. *MNRAS*, 465(1):192–212, February 2017. doi: 10.1093/mnras/stw2712.